GRAVITY SPREADING AND DISPERSION OF DENSE GAS CLOUDS RELEASED SUDDENLY INTO A TURBULENT BOUNDARY LAYER

by

Robert N. Meroney*
and
Achim Lohmeyer[Δ]

Fluid Mechanics and Wind Engineering Program
Civil Engineering Department
Colorado State University
Fort Collins, Colorado

for

Gas Research Institute
Contract No. 5014-352-0203
GRI Project Manager
Steve J. Wiersma
Environment and Safety Research Department

* Von Humboldt Awardee, Colorado State University Fort Collins, CO USA
Δ Institut Wasserbau III, Universitat Karlsruhe, BRD

August 1982

MARCH 1983, AND SEPTEMBER 1987
ERRATA
GRI-81-0025
CER82-83RNM-AL-7

CORRECTIONS FOR "Gravity Spreading and Dispersion of Desne Gas Clouds Released Suddenly Into a Turbulent Boundary Layer," by R.N. Meroney and A. Lohmeyer.

The following errors occured when the computer converted FORTRAN code into wordprocessor text. At the time the report was published we were unaware statements had been scrambled.

1) Page 194 (Appendix A):
After the 20th line down from the top of the page, please insert:

```
 34    CONTINUE
```

2) Page 209 (Appendix B):
Replace the first 12 lines with the following:

```
      DT1=DT
      GO TO 61
29    K=K+1
30    CONTINUE
      LCNT=LCNT+1
C     CALCULATE A,B,C,D TO PERMIT CALCUATION OF HA
C******************
C
      DO 305 I=2,100
305   UW(I)=(U(I)+U(I-1)*RW(I)**BM/2.0
      DO 301 I=2,99
      CFP=CFF+DELTA*ABS(U(I))
      DA=B1*RHO(I)*ABS(U(I+1)-U(I))*RW(I+1)**BM
      DC=B1*RHO(I)*ABS(U(I)-U(I-1))*RW(I)**BM
      A(I)=AMAX1(-UW(I+1),DA-UW(I+1)/2.0,0.0)*DT/DR/R(I)**BM
      CC(I)=AMAX1(UW(I),DC+UW(I)/2.0,0.0)*DT/DR/R(I)**BM
      B(I)=1.0+A(I)+CC(I)+(UW(I+1)-UW(I))*DT/DR/R(I)**BM
      D(I)=HA(I)
      IF(BM.EQ.0) GO TO 43
```

3) Page 210 (Appendix B):
Insert:

```
      DT4=DR/(UMAX+ROHMX)
```

before the 7th line from the bottom of the page

4) Page 211 (Appendix B):

a) Delete: the 12th and 16th lines from the bottom of the page

b) Line 14 from the bottom of the page should read:

```
      IF(K.GT.MTOT) GO TO 1
```

5) Page 212 (Appendix B):

a) Ten lines up from bottom of text add space between DO and 401

b) Replace last 3 lines of text on page with:

```
      DO 402 MK=1,MM
      M=MD-MK
402   W(M)=E(M)*W(M+1)+F(M)
      RETURN
      END
```

GRI DISCLAIMER

LEGAL NOTICE This report was prepared by Colorado State University as account of work sponsored by the Gas Research Institute (GRI). Neither GRI, members of GRI, not any person acting on behalf of either:

a. Makes any warranty of representation, expressed or implied with respect to the accuracy, completeness, or usefulness of the information contained in this report, or that the use of any information, apparatus, method or process disclosed in this report may not infringe privately owned rights; or

b. Assumes any liability with respect to the use of, or for damages resulting from the use of, any information, apparatus, method, or process disclosed in this report.

50272-101

REPORT DOCUMENTATION PAGE	1. REPORT NO. GRI - 82/0025	2.	3. Recipient's Accession No.

4. Title and Subtitle
GRAVITY SPREADING AND DISPERSION OF DENSE GAS CLOUDS RELEASED SUDDENLY INTO A TURBULENT BOUNDARY LAYER

5. Report Date
August 1982

6.

7. Author(s)
R. N. Meroney and A. Lohmeyer

8. Performing Organization Rept. No.
CER82-83RNM-AL-7

9. Performing Organization Name and Address

Civil Engineering Department
Colorado State University
Fort Collins, Colorado 80523

10. Project/Task/Work Unit No.

11. Contract(C) or Grant(G) No.
(C)
(G) 5014-352-0203

12. Sponsoring Organization Name and Address

Gas Research Institute
8600 West Bryn Mawr Avenue
Chicago, Illinois 60631

13. Type of Report & Period Covered
Topical (June 1980-July 1981)

14.

15. Supplementary Notes

16. Abstract (Limit: 200 words)

Wind tunnel concentration data were obtained from modeling tests of the dispersion of three different source volumes released in five wind field conditions. Multiple replication of each experiment provided statistics of cloud behavior. Results were compared against numerical box and depth averaged models to specify entrainment constants and evaluate behavior. Extrapolation of the results to sudden spills of quantities of Propane suggest that current Gaussian-plume predictions using the CHRIS approach are incorrect.

17. Document Analysis a. Descriptors

Liquefied Natural Gas, wind tunnel, dispersion of heavy plumes, vapor cloud dispersion

b. Identifiers/Open-Ended Terms

c. COSATI Field/Group

18. Availability Statement:	19. Security Class (This Report)	21. No. of Pages
Distribution Unlimited	Unclassified	220
	20. Security Class (This Page) Unclassified	22. Price

RESEARCH SUMMARY

Title	Gravity Spreading and Dispersion of Dense Gas Clouds Released Suddenly into a Turbulent Boundary Layer
	Accession Code: GRI-82/0025
Contractor	Colorado State University Fort Collins, Colorado 80523
	GRI Contract 5014-352-0203
Principal Investigators	Robert N. Meroney and Achim Lohmeyer
Report Period	June 1980 - July 1982 Topical Report
Objectives	The objective of this study was to simulate in a wind tunnel the behavior of instantaneous releases of dense gas volumes emitted in the atmospheric boundary layer. These data would be used to evaluate numerical box and slab models and the associated entrainment assumptions.
Technical Perspective	When small to medium size containers of pressurized heavy gases or cryogenic liquids are suddenly ruptured the dense gas clouds produced may present severe toxic and flammability hazards. Techniques to predict the extent of the hazard zones are needed to assist in developing siting criteria, plant layout design, and hazard response procedures.
Results	Wind Tunnel concentration data were obtained from modeling tests of the dispersion of three different source volumes released in five wind field conditions. Multiple replication of each experiment provided statistics of cloud behavior. Results were compared against numerical box and depth-averaged models to specify entrainment constants and evaluate behavior. Extrapolation of the results to sudden spills of propane suggest that current Gaussian-plume predictions using the CHRIS approach are incorrect.
Project Implications	This work presents data on the wind-tunnel modeling of the dispersion of instaneous releases of dense gases. The research complements previously reported results (Report Number GRI-80/0145) on wind-tunnel modeling of continuous-spill LNG plume dispersion by

Colorado State University. GRI will use the results of both studies in future research assessing the applicability of theoretical models in predicting vapor dispersion from potential accidental spills of LNG.

GRI Project Manager
Steve J. Wiersma
Manager, Safety Research

ACKNOWLEDGEMENTS

The authors wish to gratefully acknowledge the friendship and support of Dr. E. Plate, Professor, Institute Wasserbau III, University of Karlsruhe, FRG, who provided fiscal support to construct the wind tunnel and calibration facilities required for this research. The senior author was the recipient of a senior U.S. Scientist Award from the Alexander von Humboldt Stiftung, FRG, during the tenure of this cooperative research program. Many of the technical staff of the Institute Wasserbau III at the University of Karlsruhe provided valuable assistance during the preparation of research equipment and numerical programs. The careful typing and editing of Mrs. Gloria Burns has resulted in an attractive report. Finally the decision of the Gas Research Institute to support report preparation and distribution of these research results is appreciated.

Table of Contents

LIST OF TABLES

LIST OF FIGURES

List of Symbols

Symbols	Definition	Dimension
a	Constants in Equation B-3	-
b	Constants in Equation B-3	-
B	Buoyancy, $B = g'V$, or Constant in Eq. (2.2)	$(L^4\ T^{-2})$
c	Wave speed, $c = \sqrt{g'h}$	(LT^{-1})
c_r, c_z	Entrainment coefficients	-
C	Mass fraction	-
$C_f/2$	Skin friction coefficient, $\frac{C_f}{2} = (\frac{u_*}{u_\delta})^2$	-
E	Hot wire mean voltage	(volts)
E_o	Hot wire mean voltage, zero flow	(volts)
e'	Fluctuating hotwire voltage	(volts)
f	Probability distribution	-
g	Gravitational constant	$(L\ T^{-2})$
g'	Modified gravitational constant $g' = g\ (\rho - \rho_a)/\rho_a$	$(L\ T^{-2})$
h, H or H	Height of cloud	(L)
	Shape factor, $H = \frac{\theta}{\delta^*}$	-
k	von Karman's constant	-
k	Sensitivity measure of hot wire to along wire flow (See Eq. 3-2)	-
L	Length scale or dimension of source cup	(L)

Symbols	Definition	Dimension
L_{H_o}	Maximum width of dense cloud at x = 0	(L)
L_o	Monin Obukhov Similarity Length	(L)
L_u	Maximum upwind extent of dense cloud from origin	(L)
ℓ_b	Buoyancy length scale	(L)
n	Frequency	(T^{-1})
N	Number of test replications	-
p	Power law coefficient	-
r, R	Cloud dimension in cylindrical coordinates	(L)
Re	Reynolds number $Re = V_i^{1/2} (g_i')^{1/2} / \nu$	-
Re_*	$Re_* = u_* z_o / \nu$	-
Re_R	$Re_R = u_R V_i^{1/3} / \nu$	-
Ri	Richardson number $Ri = g_i' V_i^{1/3} / u_R^2$ or $= g_i' L / u^2$	-
Ri_*	$Ri_* = g_i' (V_i)^{1/3} / u_*^2$	-
t	Time	(T)
t_a	Cloud arrival time	(T)
T_c	Characteristic acceleration time (Eq. 4-4)	(T)
t_d	Cloud departure time	(T)
t_m	Arrival of Maximum Concentration time	(T)
t_s	Cloud slump time	(T)
t	Time to significant viscous effects	(T)
$t_{I/B}$	Time after which cloud entrainment is significant due to buoyancy driven velocities	(T)
T	Time scale	(T)

Symbols	Definition	Dimension
T_E	Eulerian turbulent time scale	(T)
$S_u(n)$	Spectral energy density, longitudinal component	(L^2T^{-1})
u, v, w	Velocity components in coordinate directions x, y, z	(LT^{-1})
u_e	Wind shear velocity	(LT^{-1})
u_F	Wave frontal velocity	(LT^1)
u_*	Friction velocity	(LT^{-1})
u_g	Velocity in cloud due to bouyancy effects only	(LT^{-1})
u', v', w'	Fluctuating velocity components	(LT^{-1})
U	Velocity scale	(LT^{-1})
V, $\forall$	Cloud volume	(L^3)
V_g	Twice volume of a propylene release	(L^3)
w_e	Entrainment velocity	(LT^{-1})
x, y, z	Coordinate system, origin at source center	(L)
y^+	Dimensionless height yu_*/ν	(-)
z_o	Roughness length	(L)
z_{SL}	Sublayer depth	(L)

Greek Symbols

α	Constants in various equations	-
α_1	"	-
α_2	"	-
α_4	"	-
α_6	"	-
α_7	"	-
β	"	-

Symbols	Definition	Dimension
β_1	Constants in various equations	-
β_2	"	-
γ	"	-
δ	Boundary layer thickness (δ = 20 cm)	(L)
δ^*	Displacement thickness (Eq. 4-1)	(L)
θ	Momentum thickness (Eq. 4-1)	(L)
λ_p	Peak of n S(n) distribution	(L)
Λ	Eulerian turbulent integral length scale	(L)
ρ	Cloud density	(ML^{-3})
σ_a	Standard deviation of a quantity A	-
χ	Plume dilution, mole fraction, or volume fraction	-
τ_o	Shear stress at wall	$(ML^{-1}T^{-2})$
τ_H	Shear stress at cloud top	$(ML^{-1}T^{-2})$

Subscripts

i	Initial cloud property	-
a	Property of ambient fluid	-
R	Evaluated at reference height (z_R = 10 cm)	-
L	Evaluated at length scale height	-

Superscripts

*	Dimensionless quantity (Eq. 2-6)	-
~	Dimensionless quantity (Eq. 2-10)	-
≈	Dimensionless quantity (Eq. 4-6 to 10)	-

Symbols	Definition	Dimension
Misc. Acronyms		
SG	Specific gravity	-
LNG	Liquified natural gas	-
Freon-12	Trade name for CCl_2F_2	-
STP	Standard Temperature and Pressure	-

1.0 INTRODUCTION

Modern use and transport of combustible hydrocarbon fuels having boiling points below ambient temperatures (liquefied natural gas (LNG), ethane, propane or butane (LPG)) or similar storage and handling of toxic gases (ammonia, chlorine, sulfur dioxide, or hydrogen sulfide) invites questions concerning the consequences resulting from accidental release. Often such gases have molecular or temperature characteristics which result in negatively buoyant gas clouds which hug the ground and extend the hazard zone in time and space.

This report considers the results of experiments performed to examine the behavior of dense plumes during periods of gravity spread/air entrainment dominance. The experiments include a broad examination of source size and shear layer intensity. The transient phenomenon is emphasized; hence, plume statistics are examined by multiple replication of each release scenario.

An initial description of dense gas kinematics and the status of other research complete this section. Scaling methods employed during physical modeling of atmospheric and plume motion are discussed in Chapter 2. The details of the experimental measurements are described in Chapter 3. Chapter 4 lists the laboratory tests and the data obtained. Chapter 5 analyzes the transient gas cloud data presented in Chapter 4 with respect to various scaling arguments. Data are also compared with a numerical box model described in Appendix A and a numerical depth averaged diffusion model presented in Appendix B. Chapter 6 summarizes the conclusions obtained from this study and gives recommendations for future work.

1.1 DENSE GAS KINEMATICS

The extreme volatility of many of the liquified gases permits the formation of very large vapor clouds in very short times. Havens (1977) suggested that a spill of 25,000 m^3 of liquified methane (LNG) on the sea surface would evaporate in about 300 sec resulting in a dense (SG = 1.55) gas cloud 5.8 x 10^6 m^3 in volume. van Ulden (1974) described an experiment where 1000 kg of Freon-12 was evaporated on water in about 5 sec resulting in a 2400 m^3 dense (SG = 1.25) cloud. Jagger and Kaiser (1980) examined the sudden release of gases from pressurized containment. For example, propylene, liquified under pressure, produces vigorous bulk boiling after a vessel bursts and between 50 to 65% of the material vaporizes in a flash. The remainder is thrown into the air as fine liquid droplets. The flash expansion is over extremely quickly (0.001 $V_g^{1/3}$ seconds, where V_g (m^3) is twice the volume of propylene released at STP) during which there is little or no entrainment of air. In the sudden failure of a pressurized LPG rail car of 40 m^3 volume, the flash vaporization of the decompressed liquid requires only the seconds needed to evacuate the tank. For these reasons the vapor release is often modeled as a sudden formation of the full volume of vapor, following which the cloud drifts and disperses. In some cases the source configuration induces its own rapid dilution; in other cases the cloud appears essentially undiluted.

Sudden release of a dense gas near the ground is accompanied by horizontal spreading caused by gravitational forces. Such clouds will drift downwind from the source location at ground level, providing an opportunity for ignition if the gas is flammable or perhaps for acute toxic effects to life in its path. An initially cylindrical or hemispherical volume will slump rapidly toward the ground after a sudden

release. The diameter increases rapidly with an associated decrease in the vertical dimension until such time as entrainment is significant. The ratio of vertical height to diameter remains quite small over most times of interest. The initial potential energy of the dense gas is converted rapidly to kinetic energy; however, this energy is also transmitted to the surrounding ambient fluid and is dissipated by turbulence at the head of the spreading plume and in its wake.

In the presence of wind shear the cloud often spreads somewhat upwind, but it eventually drifts downwind. During the initial period of movement the upwind cloud depth is somewhat thicker; however, subsequently the plume advects with the wind, and the plume depth is symmetric about a center point transported downwind at nearly background wind speeds.

Buoyancy forces tend to inhibit advection by the wind and suppress dispersion by atmospheric turbulence. The mixing of such plumes is still only partially understood despite a significant research effort of many years. The relative influence of gravity forces, viscous forces, entrainment at the plume front, entrainment at the upper surface, and modification of the background turbulent fields due to stratification effects have been active subjects of discussion.

1.2 STATUS OF RESEARCH

Several excellent review articles and workshop proceedings are now available. Britter and Griffiths (1982) edited a set of eleven articles which summarize laboratory and field experiments, numerical models; statistical approaches, and future directions for dense-gas dispersion research. The Gas Research Institute, USA, sponsored a LNG workshop in Boston, 1982. Proceedings are being prepared by Reid (1982). Battelle

Laboratories at Frankfurt, West Germany, have hosted two review meetings on dense gas behavior now available as proceedings (Hartwig 1980, 1982).

1.2.1 Field Measurement Programs

Restricting our attention to cases involving instantaneous volume source releases one finds field experiments performed with LNG released over land (AGA, 1974; Humbert - Basset and Montet, 1972) and over water (Burgess et. al., 1970, 1972; Feldbauer et. al., 1972; Boyle and Kneebone, 1972; Kneebone and Prew, 1974) and on water but drifting over land (Koopman et. al., 1979, 1981). Initial cloud specific gravities were near 1.55. The LNG experiments were complicated by release mechanisms, such as water explosions, which led to undefined premixing and enhanced initial turbulence. Each test was a single realization from the probability distribution of cases developing from a unique set of initial conditions.

In a single experiment van Ulden (1974) evaporated Freon-12 ® * quasi-instantaneously on water and tracked the resulting air-Freon-12 plume which had an estimated specific gravity of 1.25. Picknett (1981) describes 42 experiments during which 40 m^3 samples of air/Freon mixtures were released with initial specific gravities ranging from 1.03 to 4.17. The samples were released suddenly from a collapsing cubic container under various conditions of ground roughness, slope and wind speed, including calm conditions on flat ground. The adiabatic and isothermal releases noted above were not complicated by source generation mechanisms; however, concentration measurements during van Ulden's tests were very limited. Fay (1980) expressed concern about instrument

---

* Freon-12 is a trademark of duPont Company. The chemical composition is CF_2Cl_2.

placement during the Porton Down study of Picknett. He noted the majority of the plume may have passed beneath the 2 m high instruments, resulting in measurements of less than average cloud concentrations. Hall, Hollis, and Ishaq (1982) commented on the frequent disparity between mean concentration and dosage measurements.

1.2.2 Laboratory Measurement Programs

Equivalent laboratory experience includes lock exchange experiments in water (Martin and Moyce, 1952; Maxworthy, 1980; Huppert and Simpson, 1980) These experiments produce roughly equivalent cloud appearance and dispersion rates to their gaseous counterparts. Measurements are mostly visual, however, and concentration data are limited. In addition the initial depth ratio of current to intruded fluid is often significant.

Wind-tunnel measurements include finite time releases of isothermal dense gases from area sources. Concentrations are measured by aspirated hot-wire kotherometers (Hall et. al., 1974, 1977; Meroney and Neff, 1982; Neff and Meroney, 1981, 1982). In these cases the effective initial plume volume and its dimensions are somewhat ill defined. Replications for each release condition are limited. In a set of experiments preliminary to those discussed herein, Lohmeyer, Meroney, and Plate (1981) released small volumes of Freon-12 in a wind tunnel by permitting a known bubble volume of gas to rise through a liquid column and burst at the wind-tunnel ground surface. Experiments were replicated a minimum of three times to examine dispersion variability. No attempt was made to simulate the atmospheric surface layer. Initial dilution of the gas when the bubbles burst introduced variability in effective source conditions. Hall et. al. (1982) simulated six of the Porton Down Freon experiments. Replication of cloud kinematic and shape was excel-

lent, while reproduction of concentration values were "as good as could be expected" considering the uncertainties in the field measurements.

1.2.3 Numerical Model Development

Models proposed to predict the behavior of dense gas dispersion fall into five categories:

a) Modifications of classical gaussian plume formulas developed for passive gases (Burgess et. al., 1970, 1972),

b) Gravitational spread models which establish plume shape prior to a passive diffusionphase (vanUlden, 1974;Feldbauer et. al., 1972),

c) Volume integrated box models (Germeles and Drake, 1975; van Ulden, 1974; Cox and Carpenter, 1980; Eidsvik,1980; Fay, 1980; Fay and Ranck, 1981; Lohmeyer, Meroney, and Plate, 1981),

d) Depth averaged slab models (te Riele, 1977; Colenbrander, 1980; Rosenzweig, 1980; Zeman, 1982; Ermak et. al., 1981), and

e) Direct solution of the full three dimensional conservation equations by finite difference orfinite elementapproaches (England et. al., 1978; Ermak et. al., 1981).

It is evident that the number of models exceed the sets of data to evaluate them. Most models are distinguished from one another by the various ad hoc assumptions used for the mixing rates and the duration chosen for the gravity spread phase. Since various constants must be specified from experimental data the results are often dependent on the data set used to calibrate the calculation scheme. Significant differences exist among the predictions of all these models, especially for large scale LNG spills (Havens, 1980). Even models within the same

category may predict concentrations which must vary by more than an order of magnitude (Lohmeyer, Meroney, and Plate, 1981).

The latest models ought to be most reliable since they entail the fewest ad hoc assumptions, incorporate the latest understanding of plume physics, and are calibrated on the basis of more reliable experiments. Nonetheless, it is evident that further refinement awaits better and more extensive experimental data. Hartwig and Flothman (1980) specifically note the need for new time dependent, three dimensional source experiments independent of initial gas generation or release mechanisms. Further, these experiments must be repeated to determine statistics for the mean and instantaneous concentrations and plume shape.

This report considers a set of transient three dimensional experiments performed to examine the behavior of dense plumes during periods of gravity dominance. Havens (1980) discerned that these periods determine the lower flammability limit for most LNG hazard analysis. A modified box model and a depth averaged slab model are presented to provide a framework of interpretation of the experiments. The following section considers the rationale for physical modeling of dense plume motion.

2.0 PHYSICAL MODELING OF DENSE CLOUD MOTION

Two systems at different geometric scales will exhibit similar behavior if geometric, kinematic, dynamic, and thermic similarity are guaranteed by the equality of all pertinent ratios of forces, boundary conditions, and initial conditions. When it is not possible to claim a rigorous similarity in all variables it is necessary to neglect some conditions or phenomena; hence the concept of partial similarity. This is permissible when the such terms are small or their absence conservative. Scaling criteria required for partial simulation of atmospheric and plume motion are discussed in Sections 2.1 and 2.2 respectively.

2.1 SIMULATION OF THE ATMOSPHERIC SURFACE LAYER

The atmospheric boundary layer is that portion of the atmosphere extending from ground level to approximately 600 meters within which the major exchanges of mass, momentum, and heat occur. Physical modeling in wind tunnels requires consideration of the physics of the atmospheric surface layer as well as the dynamics of plume motion. The reliability of wind-tunnel shear layers for modeling atmospheric shear layers has been demonstrated by many investigators (Meroney, Neff, and Cermak, 1978; Neff and Meroney, 1982); hence only special aspects associated with dense gas dispersion need to be discussed here.

The major practical limitations of accurate wind-tunnel simulation of dense gas dispersion are operational constraints, particularly the inability to obtain a steady wind profile or to accurately simulate atmospheric turbulence at the lowest wind speeds of interest, and Reynolds number constraints (as yet somewhat ill-defined) associated with the proper scaling of near-field turbulence.

2.1.1 Mean Wind Field

The mean wind-speed profile is commonly described by either the log-linear relationship $u(z)/u_* = 2.5 \ln (z/z_o)$, where u_* is the friction velocity at the wall and z_o is the roughness length or the power-law profile relationship $u(z)/u_H = (z/H)^p$. The exponent, p, in the power-law description and the roughness length, z_o, in the log-linear description are functions of the surface roughness conditions. Rougher boundary conditions (z_o and p larger) increase the momentum deficit in the mean shear flow. Comprehensive data has been obtained in the atmosphere for a variety of different conditions. Most correlations over this data base emphasize strong winds. The flow characteristics at lower wind speeds generally display a much greater variability. Nonetheless, to obtain some basis for comparison, the high wind speed data are extrapolated to low wind speeds commonly of interest in dense plume dispersion studies. The table below shows typical variations of z_o and p with terrain type:

Terrain Type	z_o (cm)	p
Ice, mud flats	0.001	0.08
Calm open sea	0.01	
Sea, desert	0.07	
Farmland, snow cover	0.2	0.1
Short grass	0.1-0.7	0.12
Rough sea	2	0.13
Grass plains	2	0.13
Farm crops	5	0.14
Rural	20	0.16
Small towns	50	0.18
Forests	100	0.20
Large cities	150-400	0.25-0.4

Unstable stratification reduces the effective power-law exponent, whereas stable stratification increases the value. An approximate algorithm to relate z_o and p is

$$p = \frac{1 + \beta\, z_R/L_o}{\ln (z_R/z_o) + \beta\, z_R/L_o} \qquad (2\text{-}1)$$

where L_o is a Monin-Obukhov stability parameter and $\beta \sim 0(1)$*.

Most investigators use a minimum Reynolds number requirement, i.e. $Re_* = u_* z_o/\nu > 2.5$, where u_*, the friction velocity, and z_o, the roughness length, are derived from a log-linear fit to the measured mean velocity profile. The value 2.5 is an empirically determined constant. At Re_* below 2.5 it is observed that the mean velocity profiles in turbulent pipe flow lose similarity in shape and deviate from the universal curve of a rough wall turbulent boundary layer. For Re_* above 2.5 it is observed that the surface drag coefficient (and thus the normalized mean velocity profile) is invariant with respect to increasing Re_*. For Re_* between 0.11 and 2.5 the velocity profiles are characteristic of smooth wall turbulent boundary layers, and for values below 0.11 the growth of a laminar sublayer on the wall is observed to increase with decreasing Re_*.

Extrapolation of these results from pipe flow measurements to flat plate boundary layers may cause a shift in the magnitude of the minimum Re requirement, but it is generally felt that this shift is small. Precise similarity in the universal form of mean wind shear may be necessary for invariance with respect to the surface drag coefficient, but this does not necessitate that precise similarity must exist for the invariance of dispersion. It is the distribution of turbulent velocities which has the greatest effect on dispersion. It is the mean wind shear, however, which generates the turbulent velocities. It is possible that the specification of a minimum Re_* of 2.5 is overly

---

* See footnote, p. 17.

conservative. The criteria, $Re_* > 2.5$ is not applicable for flow over complex terrain or building clusters.

2.1.2 Turbulence Intensity Profiles

The turbulent intensity of a boundary layer is defined as the rms of the fluctuating component of the velocity, σ_u, divided by the local mean velocity, u. By correlating strong wind atmospheric data over a large variety of different roughness conditions ESDU (1974) concluded that the variation of turbulence intensity, σ_u, with height, z, up to 100 meters is:

$$\frac{\sigma_u}{u} = \frac{[0.867 + 0.556 \log_{10}^{z} - 0.246(\log_{10}^{z})^2] \cdot B}{\log_e(z/z_o)} \qquad (2\text{-}2)$$

where $B = 1.0$ for $z_o \leq .02$ m

$B = 0.76/z_o^{0.07}$ for $0.02 < z_o \leq 1.0$ m

$B = 0.76$ for $z_o > 1.0$ m.

Near a smooth surface this may be approximated as

$$\frac{\sigma_u}{u} = \frac{1}{\log_e(z/z_o)} \qquad (2\text{-}1)$$

Alternatively for neutral flow in the lower surface layer meteorological measurements suggest $\sigma_u/u_* = 1.5 - 3.0$, $\sigma_w/u_* = 1.2 - 1.3$, (Haugen, 1973, pp. 49, 114, 165-166) and $\sigma_w/\sigma_u = 0.3 - 0.4$ (Haugen, 1973, p. 50).* A turbulent boundary layer developing over a smooth surface may also be compared to the classical results of Klebanoff as given by Hinze (1975) who quotes values of $\sigma_u/u = 0.22$ at $z/\delta = 0.010$ ($u_* z/\nu = 30$).

---

* See Hunt and Fernholz (1975) for the quality of comparison for a number of laboratory facilities.

2.1.3 Power Spectrum Of Turbulent Velocity Fluctuations

A measure of the turbulent kinetic energy associated with the fluctuating velocity component, u' is $\overline{u'^2}$. The seemingly random variation of this energy measure, $\overline{u'^2}$ can be harmonically decomposed into the sum of cosine and sine waves of varying amplitudes and frequencies through the technique of Fourier Integral Transformations. It is convenient to present this energy measure at frequency n as the integral of power over an incrementally small frequency range, dn. Or phrasing it mathematically, $S_u(n) = d\overline{u'^2}(n)/dn$ where $S_u(n)$ is the longitudinal power spectral density and $u'^2(n)$ is the energy density at frequency n. Integrating $S_u(n)$ over all frequencies yields the total mean square velocity fluctuation, $\sigma_u^2 = \overline{u'^2}$. The characteristics of the rms velocity fluctuation, σ_u were discussed in the previous Section 2.1.2.

It is common to present spectral data in a normalized form such that equal areas on a graph represent equal fractional energies. In a presentation of $nS_u(n)/\overline{u'^2}$ versus $n/\bar{u}$ on log-log paper the magnitude of the function is the ratio of the turbulent energy at a specific wave number (or wavelength characteristic of a turbulent eddy) to the total turbulent energy of the flow. The inertial subrange will appear as a straight line with a slope of -2/3 when plotted in this manner, and the wavelength, λ_p, characteristic of the eddies of largest energy will be at the peak of the curve.

Empirical expressions have been proposed to correlate atmospheric spectral data (see Neff and Meroney, 1982). The predictions of several of these expressions for the spectral distribution of turbulent energy for a strong-wind neutrally-stable atmosphere at a ten meter height are presented in Figure 12. There is a fairly large scatter among these

correlation curves let alone the original data base. The Harris, Davenport, and Kaimal curves do not predict any variation in the spectral distribution with changing surface roughness (variable z_o), but the ESDU curves do predict a spectral variation with changing z_o. Kaimal reported that atmospheric spectra rapidly change character with the slightest onset of unstable density gradients. He proposed a neutral expression as the limit to stable distributions, and he included the shaded area presented in the Figure 12 as a highly variable range of the spectral distributions for neutral or undetectability unstable conditions. All the expressions predict the -2/3 decay characteristic of the equilibrium nature in the inertial subrange.

To use these curves as a basis for determining the approximate length scale relationship between the wind-tunnel boundary layer and the atmospheric boundary layer the peak wavelength, λ_p, representative of the energy containing eddies should be used. The peak wavelength, λ_p, ranges from 200 to 1000 meters with the majority of predictions in the neighborhood of 500 meters.

The large variability found in the peak wavelength is due to the fairly flat variation of spectral energies at peak wavelengths and the large variations in predicted atmospheric spectral behavior. The flatness of the spectral distribution is natural; thus there should be some flexibility in choosing the representative model length scale ratio. The large variations in atmospheric spectral behavior is undoubtably due to the grouping together of measurements taken at many different sites. Site specific velocity information is essential for accurate selection of a model length scale ratio.

A model Reynolds number less than that of a full scale situation changes only the higher frequency portion of an Eulerian type

description of the spectral energy distribution. As Reynolds number decreases viscous dissipation dominates at smaller wave numbers which rapidly decreases spectral energy at a given wave number. Unfortunately there is no precise idea of which portion of an Eulerian spectrum is dominant in a given dispersion application. One expects the smaller scales to be less important as the plume size increases.

2.2 SIMULATION OF HEAVY CLOUD MOTION

There exist in the literature descriptions of a variety of laboratory studies on the dispersion of neutral and buoyant gas or liquid plumes. Successful simulations exist for isolated plume behavior, as well as plume perturbations caused by buildings or obstacles, topography, and stratification (Meroney et. al., 1978). To duplicate at scale the dynamics of plume behavior, exact similitude requires the simultaneous equivalence of mass, momentum, and volume flux ratios, densimetric Froude number, Reynolds number, and specific gravity. Consideration of variable property, non-ideal gas, and thermal behavior of the plume mixture introduce additional constraints on specific heat capacity variations (Neff and Meroney, 1982; Fay and Ranck, 1981; also Fay in Reid, 1982).

An extensive discussion on the alternative advantages of different scaling parameters and the possibility of scale distortion during "partial" simulation is available in Neff and Meroney (1982). Since the present intention is to present the results of simple, isothermal, non-reacting source releases without a discussion of their implications with respect to other hypothetical more complicated circumstances these scaling arguments are not included here. Such techniques may be used to estimate conditions for situations where data are otherwise unavailable.

2.2.1 Scaling of Suddenly Released Vapor Clouds: Calm Situations

A sudden release of a volume, V_i, of dense vapor is characterized by a length scale, $L = V_i^{1/3}$. In a calm environment in the absence of any nearby obstacle, constraining fluid depth or boundaries, or unusually large roughness, this is the only characteristic length scale. Gravitational forces determine that the characteristic time scale is $T = V_i^{1/6}/(g_i')^{1/2}$, where $g_i' = g(\rho_i/\rho_a - 1)$; hence, a characteristic velocity scale would be $U = L/T = V_i^{1/6} (g_i')^{1/2}$.

Resulting dimensionless parameters might include a Reynolds number $Re = UL/\nu$, ie.:

$$Re = \frac{V_i^{1/2}(g_i')^{1/2}}{\nu} \qquad (2\text{-}4)$$

which characterizes the cloud's ability to disperse in the presence of restraining viscous effects. Large values are required to maintain prolonged periods of scale-size-independent head growth, spread rates, and entrainment. Another parameter is the Richardson number (or modified Froude number) where $Ri = g_i L/U^2$, ie.

$$Ri = \frac{g_i' V_i^{1/3}}{V_i^{1/3} g_i'} = 1.0 \qquad (2\text{-}5)$$

Since this parameter is equal to one, the cloud is expected to maintain a continual equilibrium between inertial and gravity forces. In two dimensional flow this results in a constant wave front velocity. In a radial outflow plume frontal velocities will be approximately proportional to $\sqrt{g'H}$ (until viscous forces become significant). H is dense cloud head depth.

Given a range of source release situations one expects all data to collapse together in a gravity/inertial force dominated region according to the dimensionless variables.

$$H^* = H/L = H/V_i^{1/3} \quad \text{- dimensionless depth,} \qquad (2\text{-}6)$$

$$R^* = R/L = R/V_i^{1/3} \quad \text{- dimensionless radius,}$$

$$t^* = t/T = t(g_i')^{1/2}/V_i^{1/6} \quad \text{- dimensionless time,}$$

$$u^* = u/U = u/V_i^{1/6}(g_i')^{1/2} \quad \text{- dimensionless velocity, and}$$

$$\chi = L^3/V = V_i/V \quad \text{- mole or volume fraction.}$$

Huppert and Simpson (1980) suggest the initial-slump phase sometimes seen in lock release experiments occurs when the dense gas spread rate is retarded by countercurrents required to fill the volume of space left vacant by the downward slumping fluid. Their data show this effect is no longer significant once the plume height is less than 0.075 times the vertical fluid depth. For an axisymmetric volume source the dimensionless slump time t_s^* will be:

$$t_s^* = \frac{3}{2}\pi^{1/6}\left(\frac{H_i}{D}\right)^{1/3}\left((.075\pi)^{-2/3}\left(\frac{H_i}{D}\right)^{2/3} - 1\right) \qquad (2\text{-}7)$$

where D is the total fluid depth and H_i is the original dense plume depth. In a fluid of infinite depth this phase is essentially instantaneous. Inertial/buoyancy phenomena will dominate from $t^* = t/T = 1.0$ until viscous effects are significant. A balance of the total plume inertial effects against shear effects along the wall suggests buoyancy/viscous forces are significant from $t_v = (V_i/g_i'\backslash))^{1/3}$ or

$$t_v^* = Re^{1/3} \qquad (2\text{-}8)$$

2.2.2 Scaling of Suddenly Released Vapor Clouds: Shear Flow Situations

Studies of the constant shear flow region of the atmospheric boundary layer show that it is characterized by three dimensional parameters: friction velocity, u_*, roughness height, z_o, and Monin-Obukhov length* , L_o. For neutral conditions $L_o = \infty$ and will not be regarded as a significant parameter.

In terms of all pertinent parameters the available similarity variables are now**

$$Re = \frac{(g_i')^{1/2}(V_i)^{1/2}}{\nu} \quad , \tag{2-9a}$$

$$Re_* = \frac{u_* z_o}{\nu} \quad , \text{ and} \tag{2-9b}$$

$$Ri_* = \frac{g_i' V_i^{1/3}}{u_*^2} \quad . \tag{2-9c}$$

For scale independent experiments Re must be greater than 500 (Simpson and Britter, 1979). As noted earlier in Section 2.1.1, we would like $Re_* > 2.5$. The magnitude of the initial Richardson number, Ri_*, indicates the level of shear flow dominance. For values of $Ri_* > 10^6$ calm conditions effectively exist, whereas for $Ri_* < 1$ passive dispersion may be assumed almost from the instant of release. Most field experiments performed to date have Ri_* in the range from 1,000 to 10,000. Labora-

---

* The Monin-Obukhov length is defined in terms of the momentum and heat fluxes present in the lower boundary layer, ie. $L_o = -(T/g)U_*^3/(w'T' k)$

** A relevant additional variable is the ratio of initial cloud density to ambient density. Since a single value of this parameter was used throughout these experiments it is not included here; however, initial specific gravity effects can be very significant as discussed by Neff and Meroney (1982).

tory experiments included herein range from 500 to 26,000 and infinity for calm conditions.

One discerns that there is now more than one possible set of characteristic length, time, and velocity scales since the values proposed in Section 2.2.1 are still relevant. At low or moderate velocities one expects gravity generated motions to produce velocities and entrainment rates which initially exceed any effects of a wall shear layer. In this period the earlier scales may be appropriate. Eventually density differences diminish, gravity driven movements subside, and the mixing characteristics of the shear flow and its relevant scales are expected to dominate. Many different criteria have been proposed for demarcating the early stage where the gravity currents dominate from the latter stage where the shear turbulence dominates (Fay, 1980).

The presence of a wind field influences the dispersing dense gas in the following manner. In a weak or moderate wind the cloud slumps rapidly, it spreads radially, but the portion moving upwind slows somewhat and thickens. Subsequently the entire cloud begins to drift downwind. When gravity driven velocities fall below local wind field speeds at $t^* \sim Ri_* \frac{C_f}{2}$. background turbulence and wind shear begins to enhance entrainment, and, when gravity driven velocities fall below u_* at $t^* \sim Ri_*$, the shear flow completely dominates mixing.

Since two sets of space and time scale characteristics exist, neither can be expected to correlate all data over all possible release scenarios as single curves. The choice of scale variables becomes one of taste and the expected domination of, or interest in, the mechanisms of gravity induced entrainment or shear flow enhanced mixing. Since the experiments described herein include a substantial set of calm condition data, which may be used as a reference to evaluate the respective

effects of increased shear, the starred variables introduced earlier: R^*, H^*, t^*, etc. will be used throughout most of the data comparison sections.

When shear flow effects are expected to be significant an alternative set of dimensionless variables has been recommended by Fay and Ranck (1981):

$$\tilde{H} = H\, u_*/B^{1/2} = H^*/Ri_*^{1/2} \qquad \text{dimensionless depth} \qquad (2\text{-}10)$$

$$\tilde{R} = R\, u_*/B^{1/2} = R^*/Ri_*^{1/2} \qquad \text{dimensionless radius}$$

$$\tilde{X} = x\, u_*/B^{1/2} = x^*/Ri_*^{1/2} \qquad \text{dimensionless downwind distance}$$

$$\tilde{t} = t\, u_*^2/B^{1/2} = t^*/Ri_* \qquad \text{dimensionless time}$$

$$\tilde{\chi} = \chi\ Ri_*^{3/2} \qquad \text{dimensionless concentration}$$

where $B = g_i' V_i$.

These variables may be convenient when comparing data for highly diluted gases measured during their "assymptotic" approach to passive behavior. These variables have not generally been used here, because it was desired to compare all results against a calm reference condition. The variation of the starred variables seem more physically intuitive, and their magnitudes fell over a convenient memory range. Some comparisons have been prepared of $\tilde{\chi}$ vs $\tilde{x}$ in Section 4.3.3. An extended discussion of the values of the two variable sets has been prepared by Fay in Reid (1982).

3.0 DATA ACQUISTION AND ANALYSIS

Measurements on the dispersion behavior of volumes of dense gas released in turbulent shear layers were conducted to document their statistical variability and mean behavior and to permit the development of more accurate prediction models. The laboratory equipment and methods used to make these measurements, and the techniques used to convert these measured quantities to meaningful values are discussed in this section. Attention has been drawn to the limitations of the techniques in an attempt to prevent misinterpretation or misunderstanding of the results presented in subsequent chapters. Some of the methods used are conventional and need little elaboration.

3.1 WIND-TUNNEL FACILITY

A small wind tunnel was designed to provide deep equilibrium boundary layer flows at low wind speeds. This facility, as shown in Figure 1, was an open circuit suction-type tunnel with two axial fans at the exit. The test section was 0.5 m high, 1.5 m wide, and 5 m long. At the tunnel entrance and exit were additional sections which included dense honeycombs to isolate the test section from the axial fans and entrance effects. The tunnel was driven by two 0.7 kW Ziehl-Abegg, DCDQ-501-4, axial fans. The fans were 50 cm in diameter and had seven blades each. A set of vortex spires which spanned the height of the wind tunnel were installed ten cm behind the entrance honeycomb. These spires were proportioned to match the shape of the spires used by Akins (1976). The spires were followed by a 4 cm sharp-edged fence some 10 cm further downwind. The wind-tunnel floor was a smooth dark-brown epoxy finish, and the test region was cross hatched with a 2 x 2 cm square mesh. Six 50 cm x 120 cm glass windows provided visual contact with the test section.

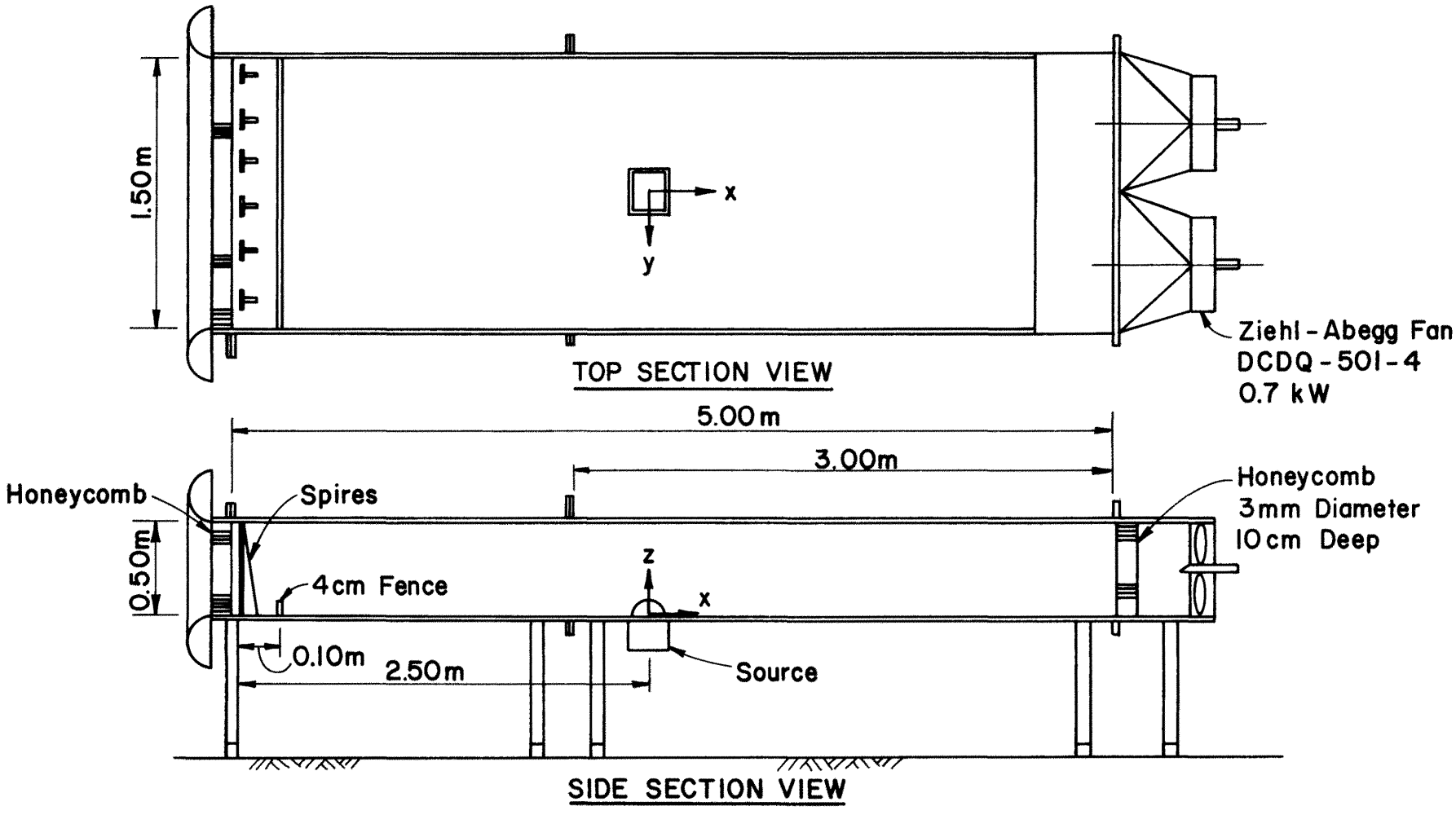

Figure 1a. Low Speed Wind Tunnel - Karlsruhe

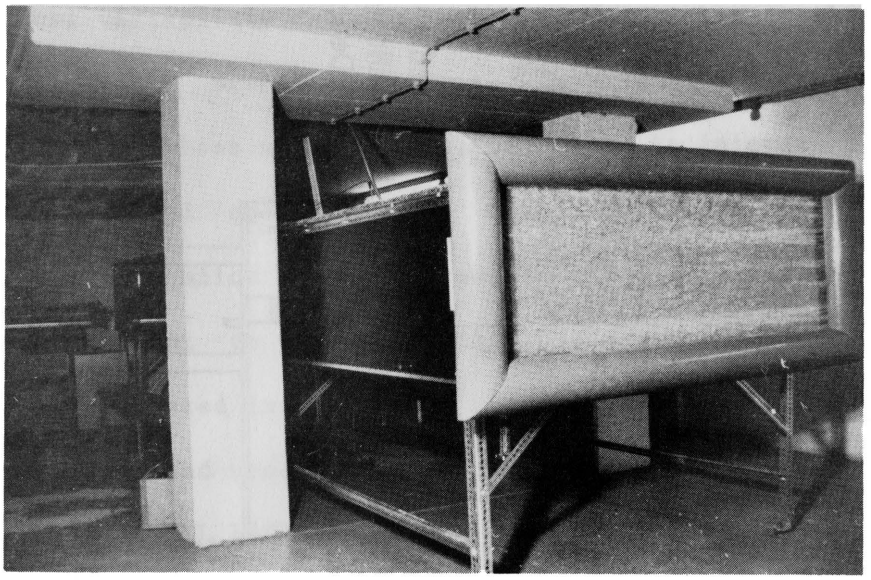

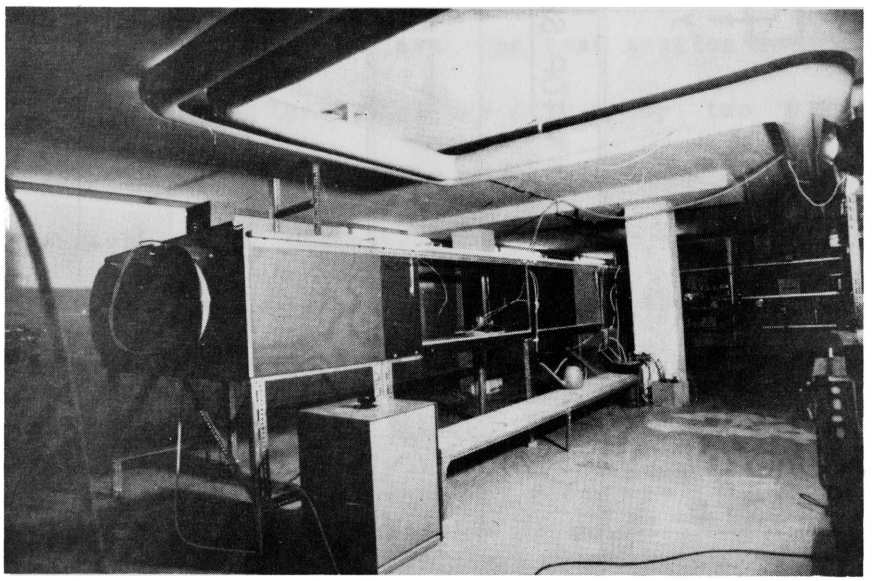

Figure 1b. Low Speed Wind Tunnel - Karlsruhe

When the two fans were adjusted to the same rotational speed the facility provided a 30 cm deep boundary layer that grew only slightly from 2 m to 4 m from the entrance. The profiles were similar within ± 5% across the test section when measured laterally every 20 cm at 2 m, 3 m, and 4 m from the entrance. Only within 15 cm of the side walls were perturbations from the side wall boundary layers apparent. No assymmetric character to the flow was observed. Detailed shear flow characteristics are described in Section 4.1.

3.2 SOURCE GAS RELEASE EQUIPMENT

Production of an instantaneous volume source at a ground surface in a shear layer without strongly intruding on the flow is extremely difficult. It is desirable to release a cloud with no self-generated initial tendency to entrain ambient fluid and with zero initial velocity components in all coordinate directions. The release apparatus must not itself induce a strong deflection of the flowfield or wake, which would make the experiments so unique as to be useless for fluid analysis.

Lohmeyer et. al. (1981) used a flush mounted water-filled bubble generator. Measurements suggested that bursting of the dense gas bubbles at the surface may have resulted in rapid initial engulfment of ambient air resulting in initial concentrations sometimes lower than one. Visualization indicated some releases occurred off the coordinate origin or with a finite initial lateral velocity in a random direction caused by the internal pressure explosion from the bubble. Picknett (1981) used a collapsing cubical tent filled with dense gas. A roof and support structure were left standing after the side walls fell. In a wind field flow perturbations must exist before the tent collapses. The presence of a roof which might slightly inhibit vertical motions is also

disconcerting. A new laboratory apparatus was created which used features of both systems, but the new system avoids their primary disadvantages.

A 14 cm x 16 cm x 12 cm deep container of water was mounted flush to the test section floor 250 cm from the entrance as noted on Figure 1. The rectangular box contained an apparatus to fill a given size half-cylinder with dense gas, to raise the filled cylinder above the water surface until it stood exposed to the wind, but isolated by a water seal, and to suddenly rotate the horizontal cylinder about its axis, leaving a volume of dense gas almost motionless above the water surface. A drawing of the apparatus is shown in Figure 2, and a sequence of sketches shows the equipment during operation in Figure 3.

Operation of the equipment for each test proceeded as follows,

Filling:

- The empty half-cylinder cup was rotated into a cup opening down position beneath the water surface.
- Dense gas was slowly released through a small port in the bottom of the box from which it rose and displaced water from the half-cylinder cup. Gas release continued until the cup was entirely full and a small quantity began to escape around the cup edges.
- During filling the cup was slowly raised until it stood above the wind-tunnel floor, but the lowest cup edges were still one or two mm beneath the water surface. The dense gas was now ready to release.

Release:

- On decision to release a restraining wire to the cup rotation mechanism was released by hand.
- A strong spring and weight system caused the downwind edge of the cylinder to drive beneath the surface and rotate the cylinder around

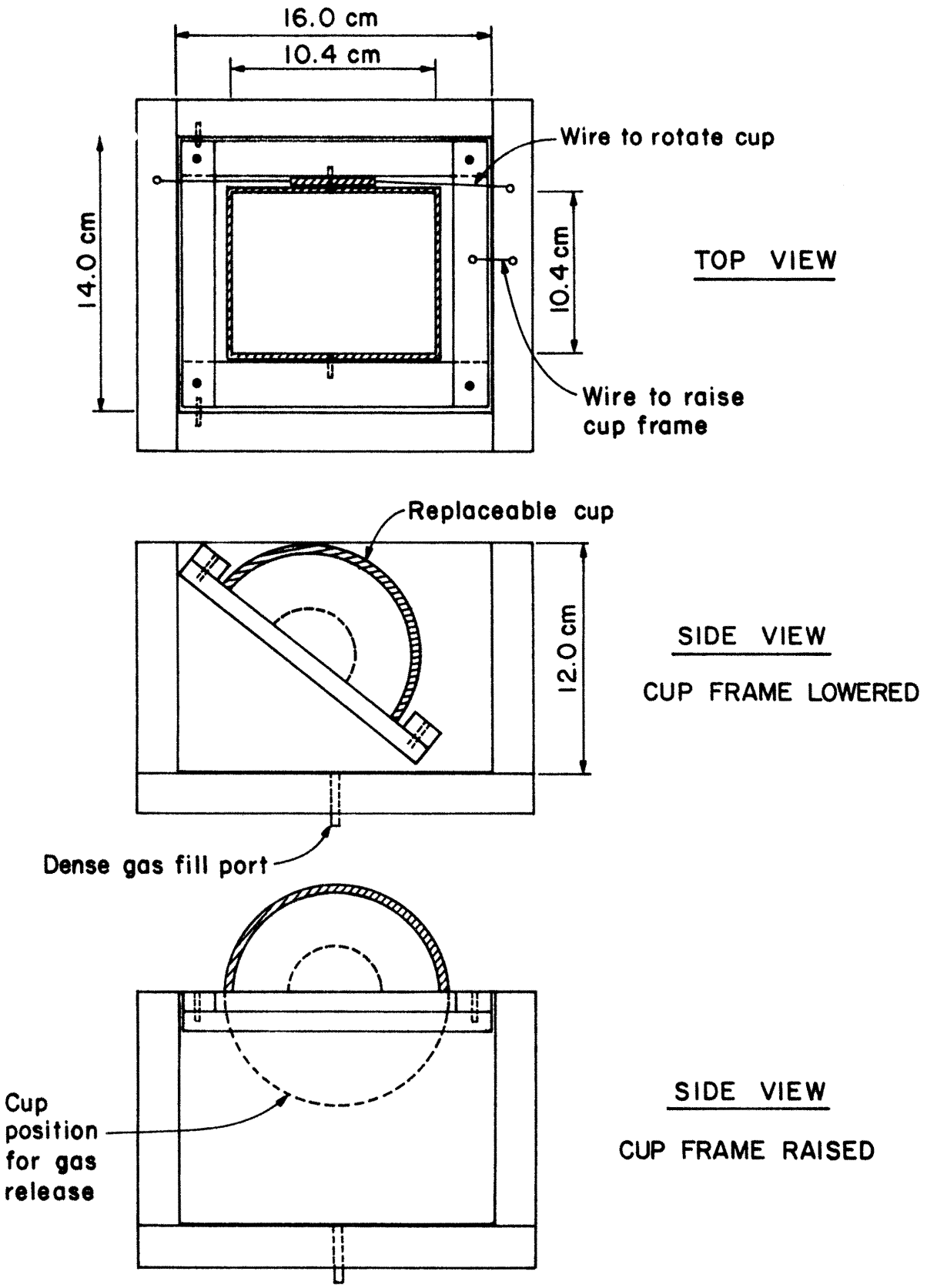

Figure 2. Source Gas Release Equipment

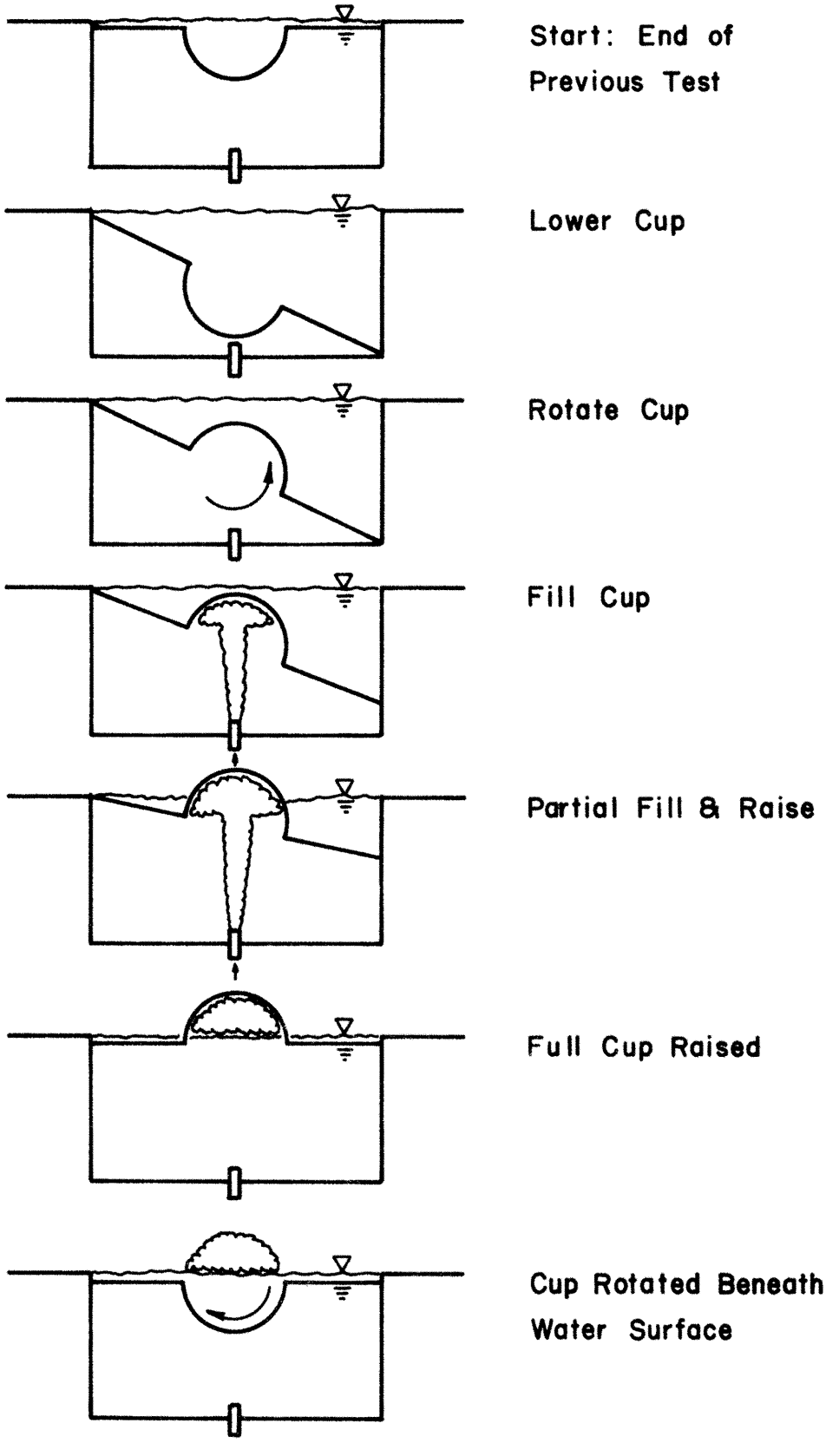

Figure 3. Sequence of Operational Steps for Source Gas Release Equipment

its horizontal axis 180 . In full rotation the water displacement of the cup was such that the water surface was normally exactly flush with the tunnel floor. No perturbations rose above the floor. The dense gas was left exposed as a nominally half-cylindrical volume.

• When the cylinder completed about 165° of its rotation a small magnet on the cylinder wall passed a glass-enclosed reed-switch sending a low voltage pulse to detectors to record the beginning of the experiment.

Tests of the apparatus were performed to detemine the effects of clockwise versus counterclockwise cylinder rotation in a wind field, the characteristic release time, the influence of rotational shear on the cloud volume, and whether the release mechanisms introduced assymetries into the dispersion patterns.

Although the effect was slight, when the upwind cup edge was arranged to dive beneath the surface, there was some tendency for low pressures in the wake of the cylinder to draw gas downwind before the cup was fully rotated. When the downwind edge was arranged to dive beneath the surface, such that the upwind face opened first, the cloud behaved satisfactorily.

Sixteen-mm and eight-mm movies were taken of the cup operation. The cup always opened in less than one frame, suggesting that the release time was less than t = 1/20 seconds. Close up shots of the gas clouds did not display any strong initial movements or entrainment effects due to rapid cup rotation. In calm situations spread patterns were uniformly circular; hence, no effects at cup corners were apparent.

Allowing the dense gas to stand some time before release did not seem to change measurements; nonetheless, cylinders were always released within 30 seconds of filling. Three cylindrical cup sizes were used.

Their dimensions and calculated volumes are shown in Table 1. To account for surface tension effects the volumes were also repeatedly measured by water displacement which led to slightly larger numbers. The volumes measured did not vary by more than 3%; therefore, source volumes are known within such variation during the actual experiments.

3.3 FLOW VISUALIZATION TECHNIQUES

Smoke was used to define cloud behavior during a visualization sequence. The smoke was produced by passing the simulation gas, Freon-12 (CF_2Cl_2), through a container of titanium tetrachloride located outside the wind tunnel. A reaction of moisture in the source gas and the titaniun tetrachloride produces a fine white suspension of titanium dioxide (typical particle diameter circa 1 μm). The plume was illuminated with arc-lamp beams. A visible record was obtained by means of pictures taken with a Nikon F2A, 35 mm camera, equipped with an electric motordrive MD-2, and pictures were taken every 0.3 sec. Ilford, HP-5, 400 ASA film was used. Additional 16 mm and 8 mm color movies were made of all release conditions. An electric digital clock with LED display permitted time resolution to the nearest .01 second. All releases were replicated at least three times. Views of each release were recorded both from above and the side, but not simultaneously.

3.4 WIND PROFILE AND TURBULENCE MEASUREMENTS

Velocity profile measurements, reference wind speed conditions, and turbulence intensity measurements were obtained with a Disa 55D01 anemometer and Disa 55A22 hot wire probes. The hot wires were calibrated several times a day in a low-speed nozzle, whose speed was set with calibrated low-volume flowrators. The zero velocity (capped) wire voltage was monitored frequently, and, if it varied significantly, the

wire was recalibrated. The wires were calibrated from 0.02 to 1.25 m/sec, and they were found to consistently fit a King's law equation with an exponent of $n = 0.818$.

Velocities were determined by direct use of calibration figures. Turbulent intensities were calculated using the expression

$$\frac{\sqrt{\overline{u'^2}}}{\bar{u}} = \frac{2}{n} \frac{\sqrt{\overline{e'^2}}}{(E^2 - E_o^2)} \frac{E}{} \qquad (3\text{-}1)$$

where $\sqrt{\overline{e'^2}}$ was the root-mean-square of the fluctuating voltage signal, E is the mean transducer voltage, and E_o is the response at zero velocity. This expression is recommended by Sandborn (1973, p. 276) when first order results are satisfactory. It is felt that velocities are reliable to $\pm$ 5% and turbulent intensity values to $\pm$ 10% based on wire drift, instrument resolution, and calibration variability experienced.

Two channel hot-wire measurements using a pair of Disa 55D01 anemometers and Disa 55M25 linearizers, were made with a Disa 55A30 crosswire probe to determine ($\overline{w'^2}$, $\overline{w^2}$, and $\overline{u'w'^2}$) profiles at a limited number of centerline locations. The cross wires were calibrated and found to be reasonably well matched. The coefficient k specified by Champagne and Sleicher (1967) to account for along-wire heat transfer effects was measured and found to be 0.07. The following equations were used to calculate the velocity characteristics from the linearized voltage signals

$$\frac{\sqrt{\overline{u'^2}}}{\bar{u}} = \sqrt{\frac{1}{4} \frac{\overline{(e_1' + e_2')^2}}{\bar{E}^2}} \qquad (3\text{-}2a)$$

$$\frac{\sqrt{\overline{w'^2}}}{\bar{u}} = \sqrt{\frac{1}{4}\left[\frac{1 + k^2}{1 - k^2}\right] \frac{\overline{(e_1' - e_2')^2}}{\bar{E}^2}} \qquad (3\text{-}2b)$$

$$\frac{\overline{u'w'}}{\bar{u}^2} = \frac{1}{4}\left[\frac{1 + k^2}{1 - k^2}\right]\left\{\left(\frac{\overline{e_1'^2}}{\bar{E}^2}\right) - \left(\frac{\overline{e_2'^2}}{\bar{E}^2}\right)\right\} \qquad (3\text{-}2c)$$

or

$$\frac{\overline{u'w'}}{\bar{u}^2} = \frac{1}{2}\left\{\frac{\overline{e_1'^2}}{\bar{E}^2} - \frac{\overline{u'^2}}{\bar{u}^2} - \frac{\overline{w'^2}}{\bar{u}^2}\right\} \qquad (3\text{-}2d)$$

Unfortunately there is some question as to whether or not the cross-wire was correctly oriented with respect to the floor, thus, values measured are probably accurate to no better than $\pm$ 20%.

The velocity sensors were mounted on a portable vertical traverse positioned over the measurement location in the wind tunnel. The traverse permitted vertical motion of 31 cm, and it could be positioned accurately within $\pm$ 0.25 mm. The traverse mechanism was raised on three pins 4 cm above the tunnel floor and was generally located at least 15 cm downwind and to the side of any measurement location. The traverse and associated probes are visible in Figure 4.

A set of records from the single wire anemometer probes were also recorded by a Bell and Howell VR3200 analog tape recorder for subsequent digitization. Digitized tapes were analyzed to produce longitudinal velocity auto-correlations. The correlations were inverted into one-dimensional energy spectra.

3.5 CONCENTRATION MEASUREMENTS

Gas concentrations were measured with an aspirated hot-wire anemometer (katherometer) constructed from a miniature Disa, 55E07, mass flow

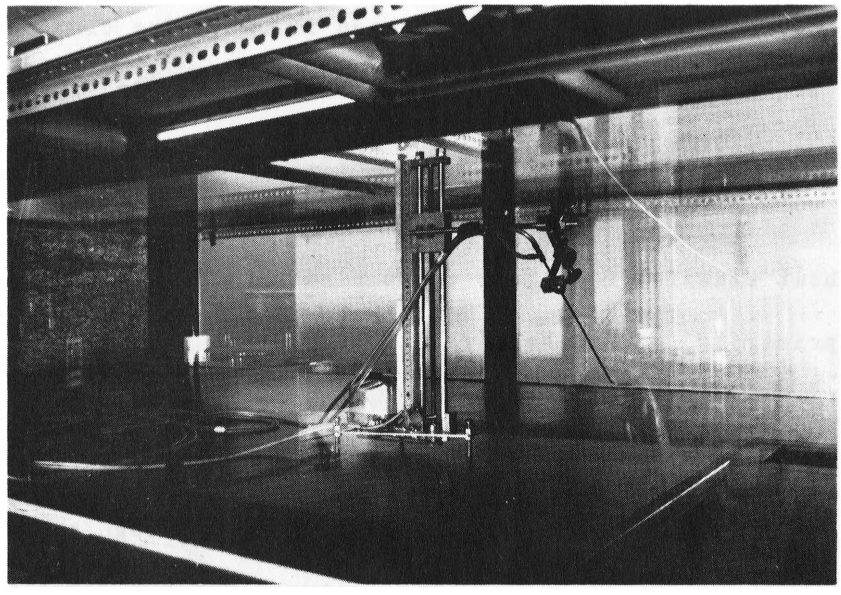

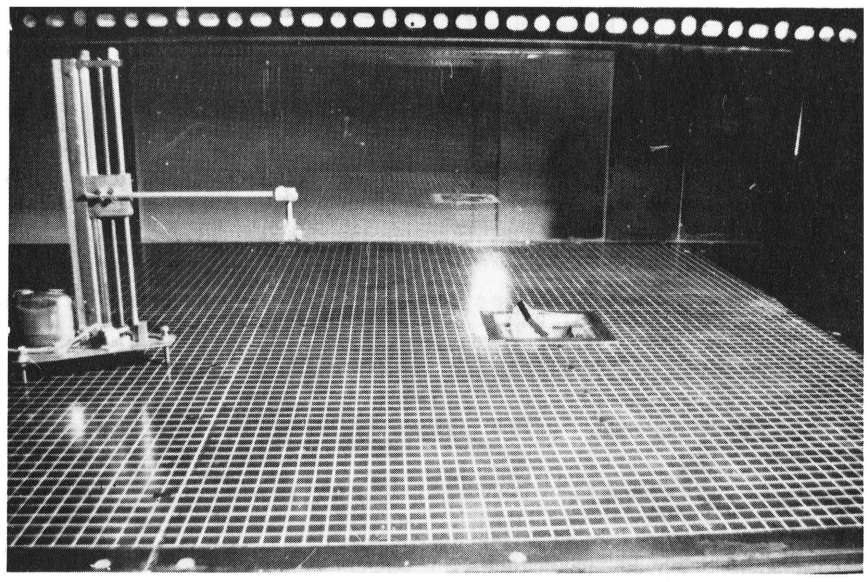

Figure 4. Traverse and Anemometer Probes

transducer. Hot-wire katherometer probes measure rapid concentration fluctuations. Such probes permit one to determine cloud arrival and departure times as well as maximum concentrations and their arrival. The basic principles governing the behavior of aspirating probes have been discussed by Wilson and Netterville (1980).

The heat transfer rate from a hot wire to a gas flowing around it depends primarily upon the wire diameter, the temperature difference between the wire and the gas, the gas velocity, and the thermal conductivity and viscosity of the gas. The latter two parameters are determined by gas composition and temperature. Hence for a fixed probe geometry, wire temperature, air temperature, and gas velocity the heat transfer rate or related voltage drop across the wire is a function of only the gas composition.

The air temperature in the wind-tunnel room was very stable, and it did not vary by more than 1/2°C over 8 hours. The wire temperature was maintained constant by a Disa 55D01 anemometer feedback circuit, as noted in Figure 5. An overheat ratio of 1.6 was used during all tests. The wire used was a platinum Wolfram wire (5 μm) installed in the 2 mm diameter throat of a miniature Disa mass flow transducer. Gas flow was maintained constant at less than 0.1 m/sec by sucking sample air through a 1 mm probe, through the detector, and, once outside the wind tunnel, through a 100 cm long 1 mm diameter capillary tube by means of a voltage regulated aquarium pump. The pressure drop across the capillary tube was monitored by a Betz micro-manometer. A portion of a fiber filter removed from a cigarette was inserted in the probe tip to reduce system sensitivity to pressure perturbations during shear flow measurements. All tests were corrected for a slight time lag required for the sample to travel through the probe to the detector wire (0.4 seconds).

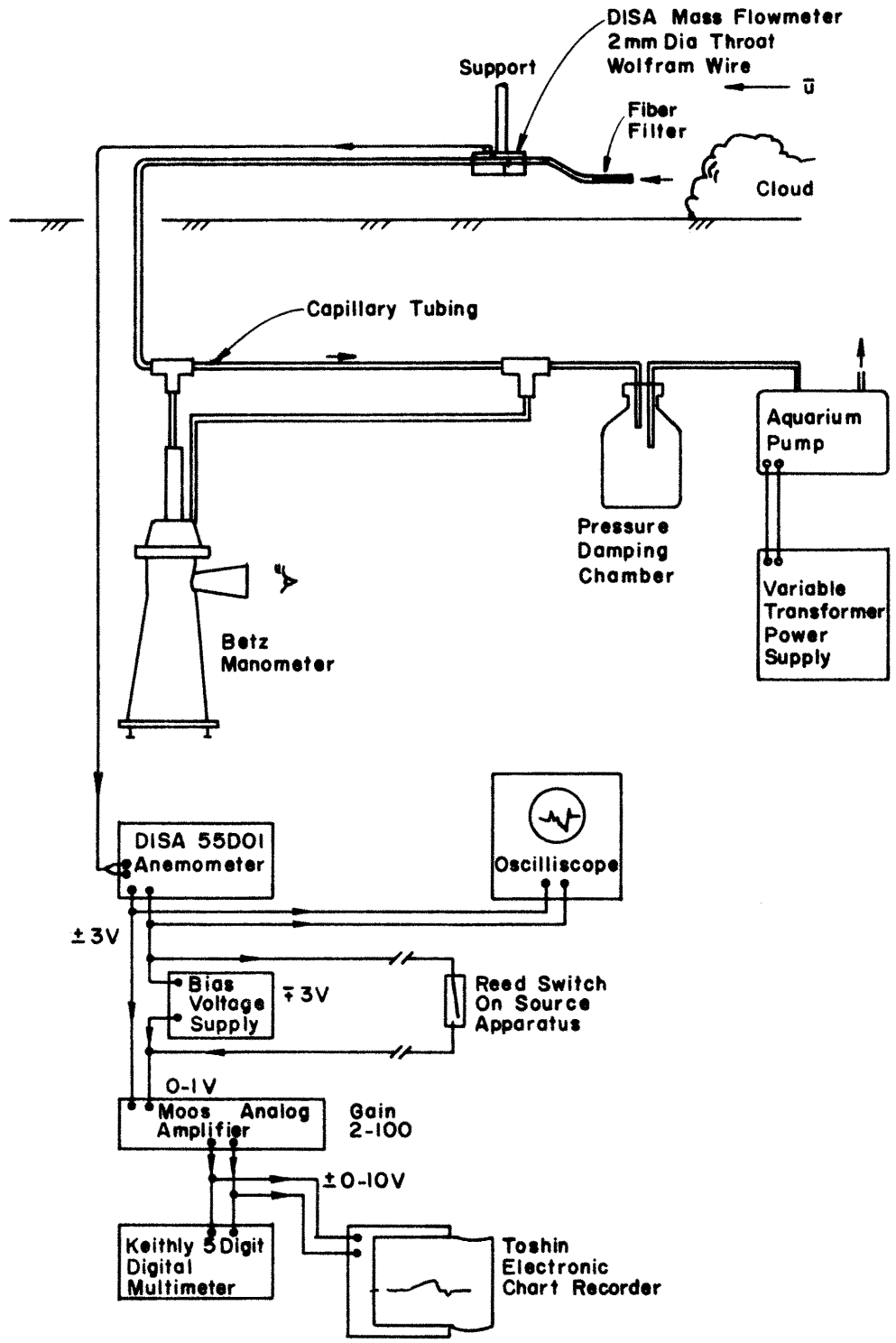

Figure 5. Concentration Equipment Block Diagram

Extensive tests by Wilson and Netterville (1980) and Neff and Meroney (1982) indicate such a probe has a flat frequency response to 150 Hertz, concentration sensitivity to 0.10 percent, and resolution to within ± 5% of measurement. The accumulative error, due to the combined effects of calibration uncertainties, nonlinear anemometer drifting, and drifting of the sample flow rate is estimated to be:

	Concentration Range (%)	Maximum Possible Errors in Measurement (%)
Freon-12	0-1	± 25
(CF_2Cl_2)	1-10	± 15
SG ≅ 4.2	10-100	± 10
80% He		
20% Freon-12	0-100	± 10
SG ≃ 1.0		

These errors represent about two to three standard deviations about the measured value.

3.5.1 Calibration

During probe calibration mixtures of 100, 50, 25, 12.5, 6.25, 3.12, 1.56, 0.78, 0.39, and 0.2 percent source gas in air were prepared by dilution. These samples were sucked into the katherometer apparatus, and the response was recorded. The signals were very reproducible and voltage response did not vary by more than 5% between all calibrations of a given wire. Response curves were nearly linear over the entire range; however, curves of the form $\chi = a\ E^{b}$ were fitted to the calibration data. b ranged from 0.95 to 1.08, when mole fractions varied from 0.001 to 1.0, and from 0.96 to 1.35, when mole fractions varied from 0.10 to 1.0.

3.5.2 Test Procedure

Each concentration measurement sequence followed the following procedure:

- The wind-tunnel wind speed was set to the required value by adjusting fan rpm.
- The concentration probe on the traverse mechanism was located at the required measurement point.
- The Betz micro-manometer and the anemometer were checked for drift.
- The cylinder cup was filled with source gas and raised into operating position.
- The gain on the amplifier was chosen, and the chart recorder was turned on and zeroed.
- The cup cylinder was released, and the cloud dispersed.
- After the chart recorder signal was completed, the recorder was stopped.
- The procedure was repeated as necessary.

4.0 TEST PROGRAM AND DATA

The dense cloud measurement program was designed to provide a basis for the analysis of plume scaling laws, and to assist in the development and verification of analytical models. All tests were performed in the wind tunnel described in Section 3.1. The clouds were released from the cup device described in Section 3.2 with zero initial momentum and minimal source generated dilution. The floor in the vicinity of the clouds was always flat and smooth with no obstacles to cause wake effects. Five nominal upwind approach wind conditions were used (0.0, 0.2, 0.4, 0.6, and 1.0 m/sec at a reference height of 10 cm). Three source volumes (35, 165, and 450 cubic centimeters) were filled with either pure Freon-12 (specific gravity = 4.17) or in a few cases a mixture of 80 percent helium and 20 percent Freon-12 (specific gravity $\simeq$ 0.97). Table 2 summarizes test conditions for the Freon-12 runs and indicates the resultant values of various parameters of interest. Notice that gravity forces always should generate velocities larger than imposed wind speeds at some time. Initial values of the parameters, Re, always exceed the critical value of 500, but maximum values of the surface Reynolds number, Re_*, never exceed 2.5. The shear flow must thus have smooth surface turbulent boundary layer characteristics.

Section 4.1 reviews the approach wind flow conditions for all tests, Section 4.2 discusses the visual plume results, and Section 4.3 examines the transient plume concentration results. This section also reports the results of the 100 replication test series and the behavior of the neutrally buoyant cloud tests.

The zero position of the coordinate system is located over the center of the source apparatus 250 cm from the entrance. The positive x coordinate will be downwind, and the positive z coordinate is upward.

4.1 VELOCITY AND TURBULENCE RESULTS

Velocity and turbulence profiles were measured upwind and downwind of the source release location in the wind tunnel. Representative measurements along tunnel centerline are provided in Figures 6, 7, and 8 at a location 0.5 m downwind of the source apparatus. Figure 6 also depicts the initial cloud sizes with respect to the profile gradients. The boundary layer thickness in all cases extended beyond 20 cm; however, since variations were small and wind-tunnel ceiling effects eventually became apparent, a nominal boundary layer height of 20 cm during all runs was used.

4.1.1 Mean Velocity Profiles

The mean wind speed profile is commonly described by a logarithmic relationship $u(z)/u_* = 2.5 \ln (z/z_o)$ where u_* is the friction velocity at the wall and z_o is the roughness length. As noted in Figure 7 a logarithmic description fits all profiles well between heights of 1 to 10 cm. Volumes were calculated for the friction velocity by three different means. The value was determined from the slope of the data on a semilogarithmic plot, $(u_*/u_\delta)_s$; the value was judged by comparing the entire curve to a universal Clauser-law plot, $(u_*/u_\delta)_c$; or the value was calculated from the empirical Ludwig-Tillmann equation, $(u_*/u_\delta)_{LT}$. The Ludwig-Tillmann equation is

$$\left(\frac{u_*}{u_\delta}\right)^2_{LT} = 0.123 \times 10^{-0.678H} \left(\frac{u_\delta \theta}{\nu}\right)^{-0.268} \qquad (4\text{-}1)$$

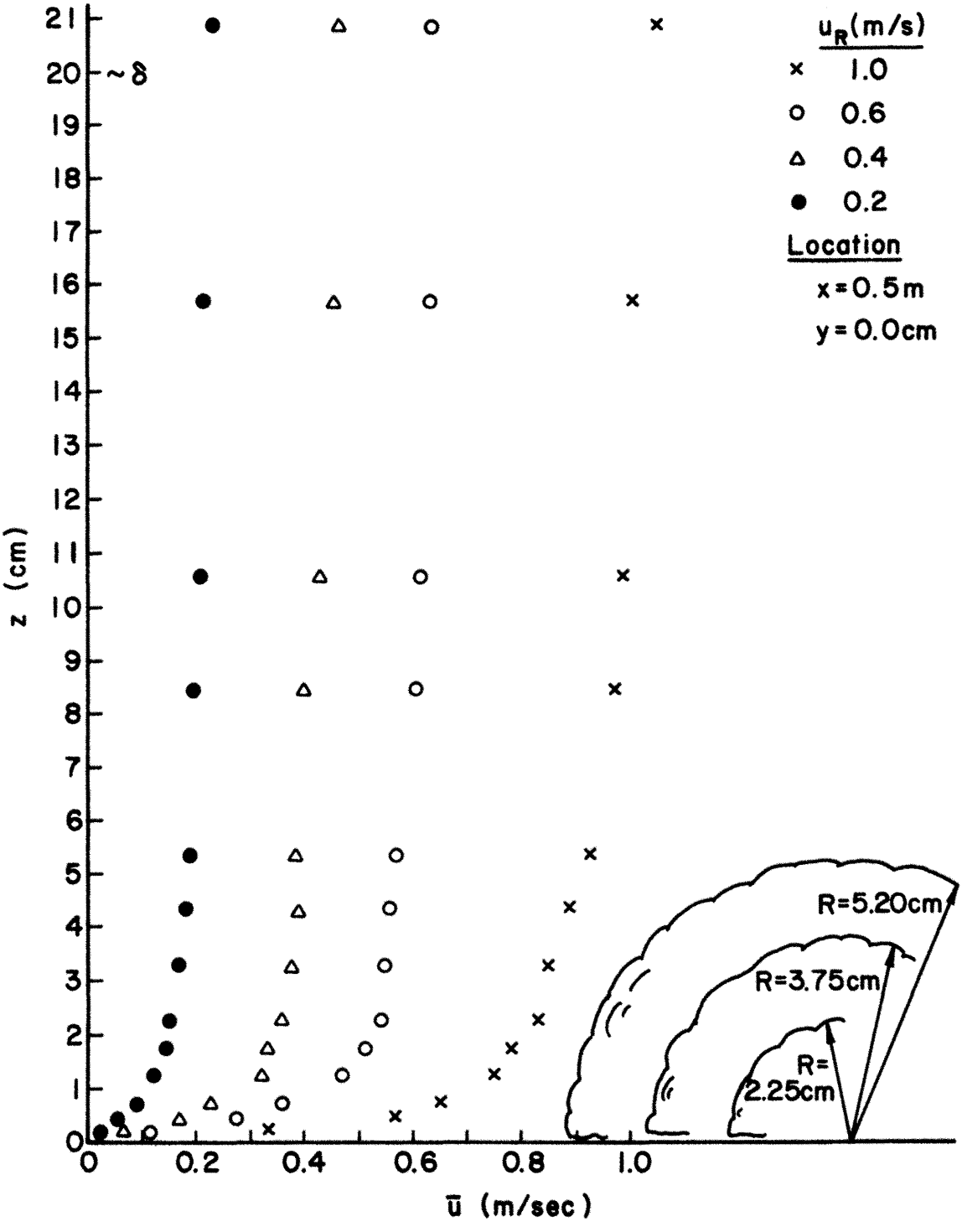

Figure 6. Velocity Profiles for Model Boundary Layer

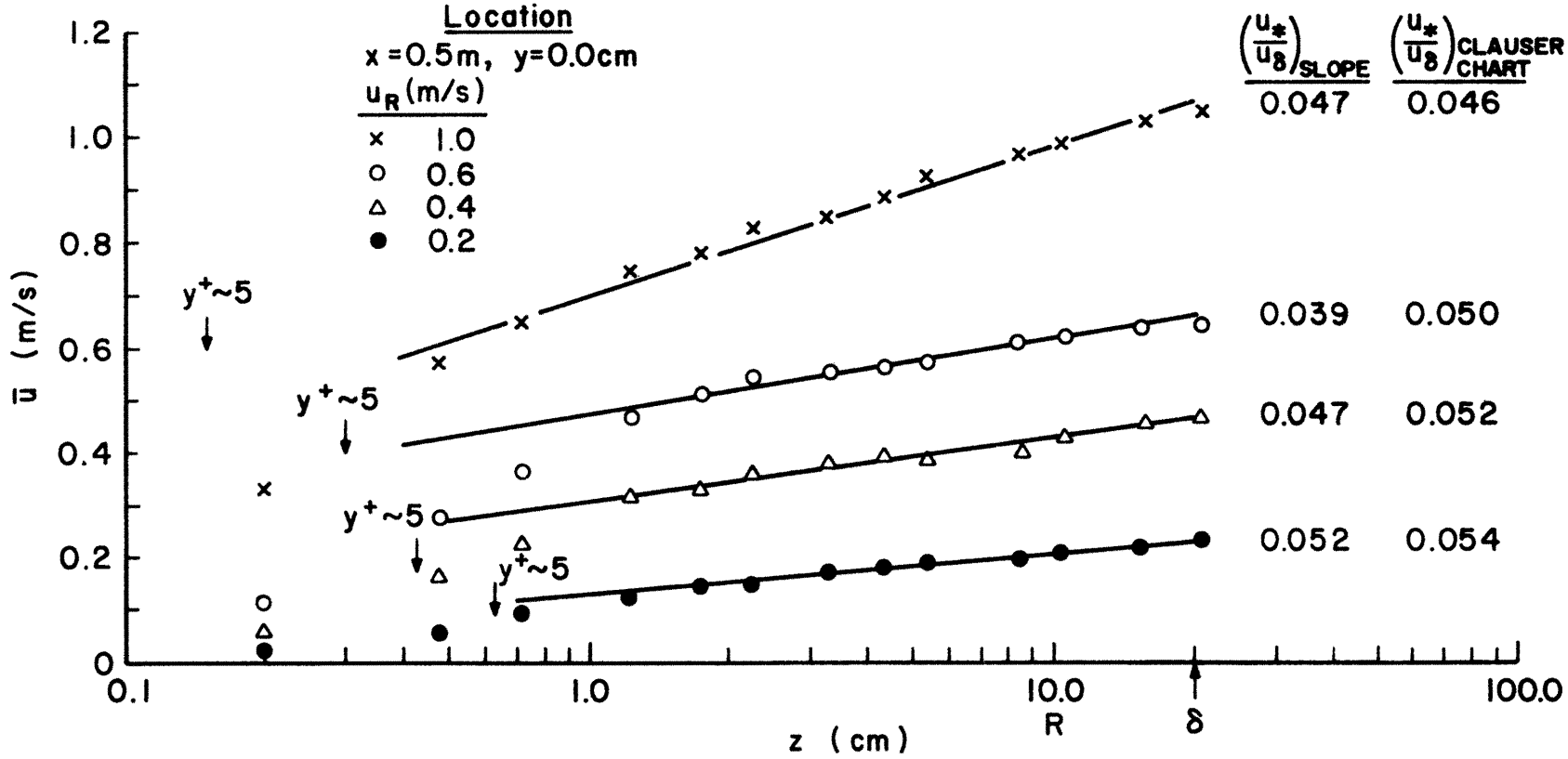

Figure 7. Velocity Profiles - Semilogarithmic

where

$$\theta/\delta = \int_0^1 \frac{u}{u_\delta}\left(1 - \frac{u}{u_\delta}\right) d\xi, \quad \text{momentum thickness}$$

$$\delta_*/\delta = \int_0^1 \left(1 - \frac{u}{u_\delta}\right) d\xi, \quad \text{displacement thickness, and}$$

$$H = \delta_*/\theta \quad \text{shape factor}$$

Centerline values calculated at x = −0.5, +0.5, and +1.5 m for all wind speeds are included as Columns 1, 2, and 3 on the summary Table 3. The associated value of the roughness length was also estimated for each profile and is included as Columns 11 and 12 on Table 3. An overall value of friction velocity and roughness length are intepreted to be

$$(u_*/u_\delta) \simeq 0.048 \quad \text{and} \quad (4\text{-}2)$$

$$z_o \simeq 2.4 \times 10^{-5} \text{m}.$$

If length scaling were based on roughness alone an atmospheric model scale of 1:1000 would be representative of grass plains or a rough sea. Scales of 1:2000 to 1:3000 would be representative of farm crops or rural regions.

Figure 8 displays the overall power law correlation of the mean velocity profiles. A value of the power-law index, p, equal to 0.13 fits most of the data for heights above 2 cm as noted in Column 13 of Table 3. From Equation (2-1) a value of p = 0.13 and $z_o = 2.4 \times 10^{-5}$ m correspond to a reference height of 5.25 cm. At smaller reference heights the power law index, p, would become larger. A power-law index of p = 0.13 is generally expected to correspond to flow over grassy plains, which again suggests a model boundary layer scale of 1:1000.

Most of the cloud dispersion occurs below 1 to 2 cm; hence a power law profile approximation is not representative of the advective wind field. Logarithmic-law formulas will be somewhat better, but they will

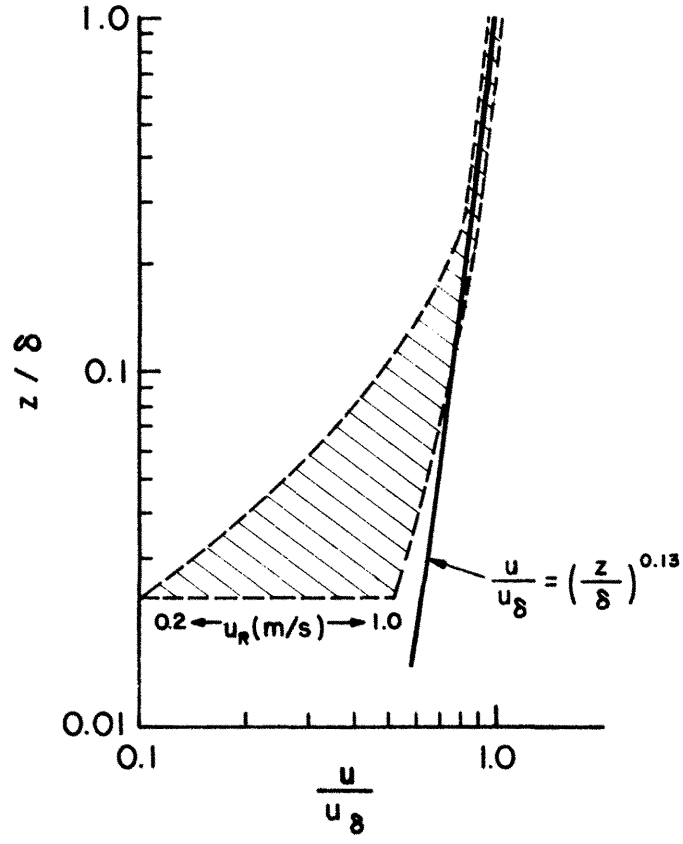

Figure 8. Power Law Description of Mean Velocity Variation for Model Boundary Layers

overestimate wind speeds at 0.5 cm by as much as 50%. Formulas which include sublayer corrections may be more suitable.*

4.1.2 Turbulent Intensity Profiles

The turbulent intensity of a turbulent velocity is defined as the rms of the velocity fluctuations divided by the local mean velocity. Figure 9 shows the variation of the turbulent intensity of the longitudinal velocity component. Magnitudes fall off at upper levels faster than equivalent atmospheric profiles. Nonetheless at the z = 1 to 2 cm level values will be comparable to ESDU Equation (2-2) for scale ratios between 1:1000 to 1:2000. As noted in Column 8 of Table 3 magnitudes of (u'/u_*) at z = 1 cm are near 1.55 which is at the lower end of typical atmospheric value. (Note, however, there is no possibility of undetected thermal instabilities, as are sometimes present in atmospheric measurements.)

Figure 10 displays almost no vertical variation in turbulent intensity of vertical fluctuations. Values listed in Column 9, Table 3 for w'/u_* at z = 1 cm are also very low with values near 0.55. These low values suggest strong wall effects or cross-wire misalignment. Turbulent shear profiles included in Figure 11 also display anomalous magnitudes. Nonetheless one might infer a constant stress region exists for the velocities tested at least 5 cm thick.

4.1.3 Turbulent Spectra and Integral Scales

The characteristics of the power spectrum of turbulent intensity in the atmosphere were discussed in Section 2.1.3. It is pertinent to recall the variability of measurements indicated by the range seen on

---

* See for example: Spalding D. B. Tran. ASME, J. Appl. Mech., 28E, pp. 455f (1961).

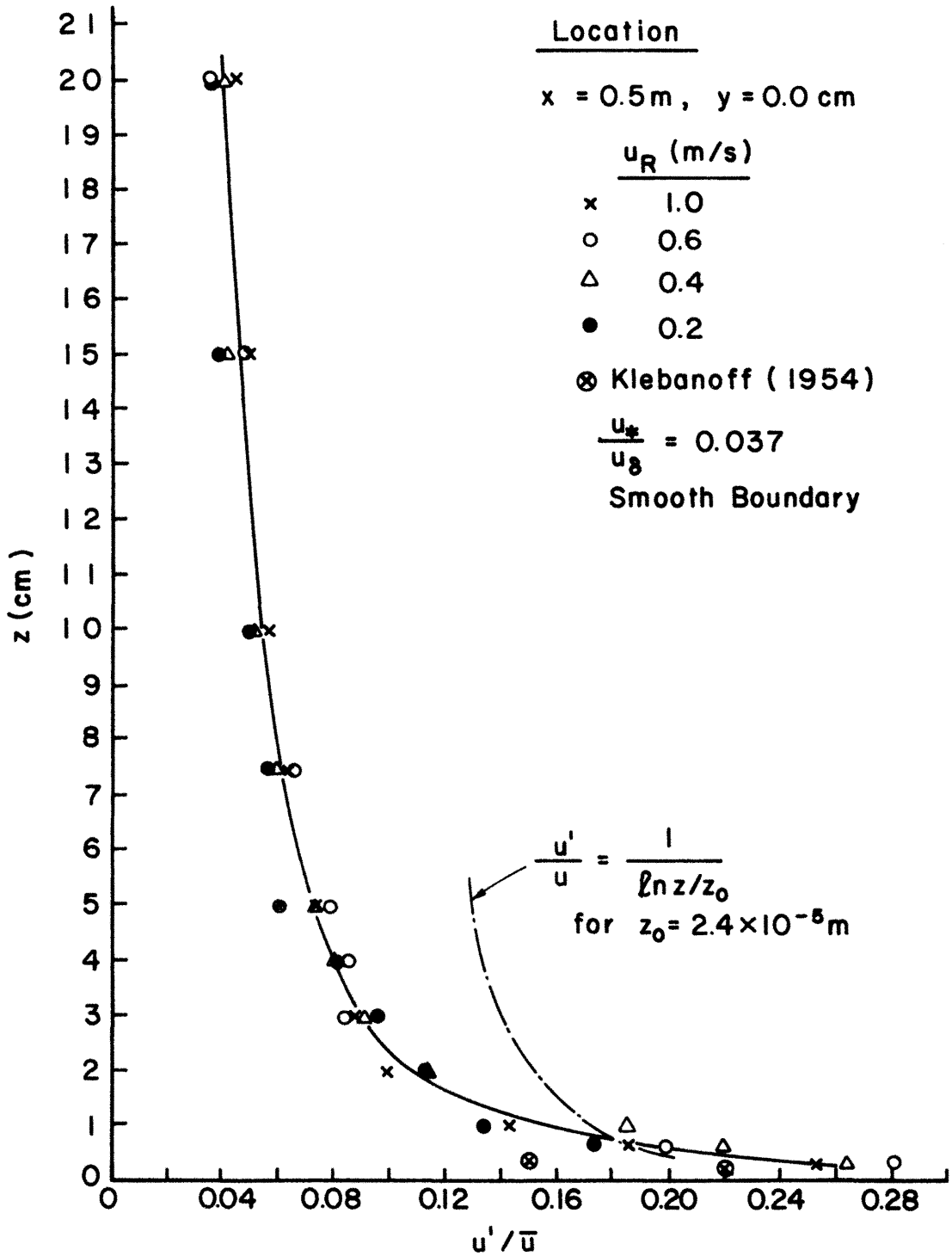

Figure 9. Longitudinal Turbulent Intensity Profiles

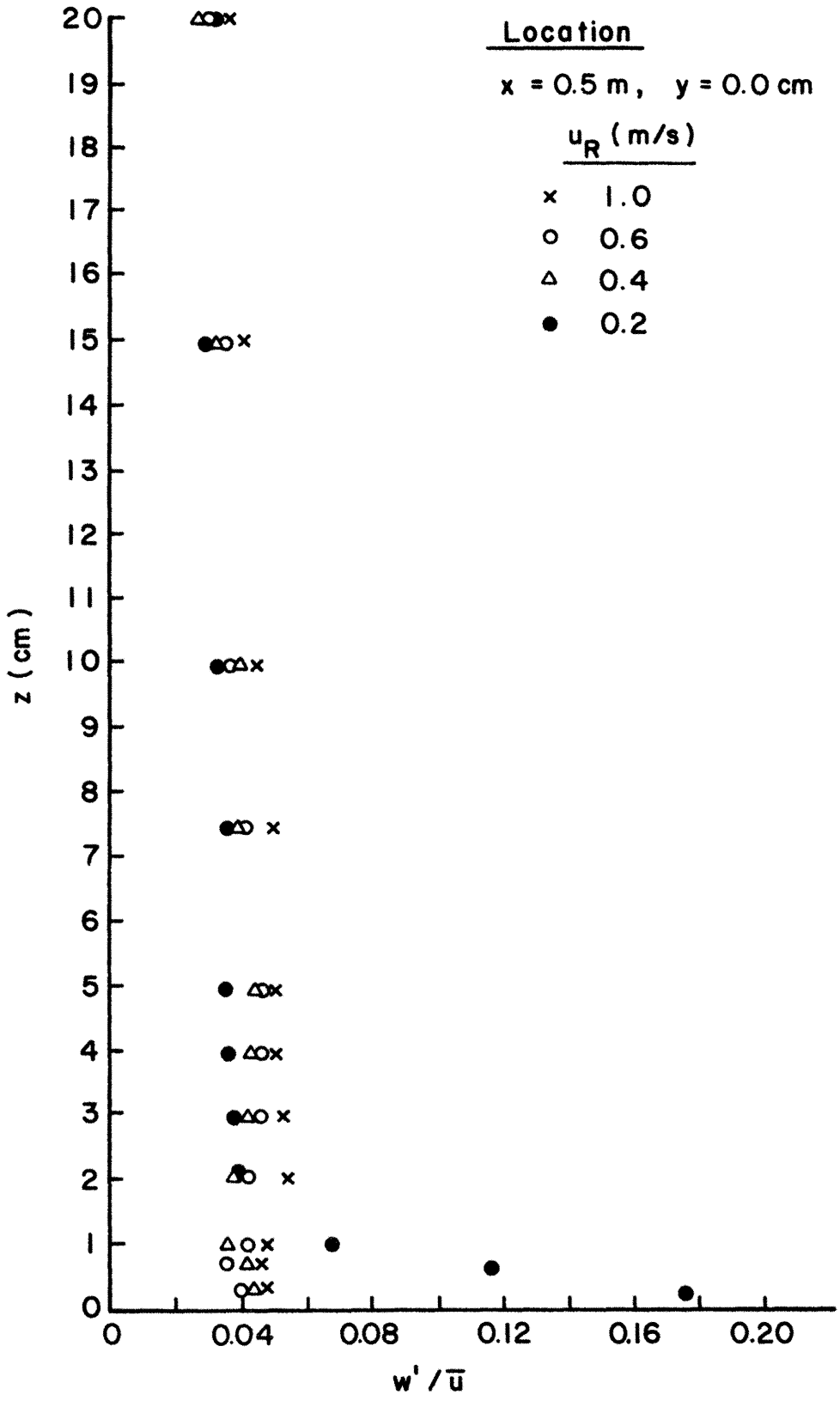

Figure 10. Vertical Turbulent Intensity Profiles

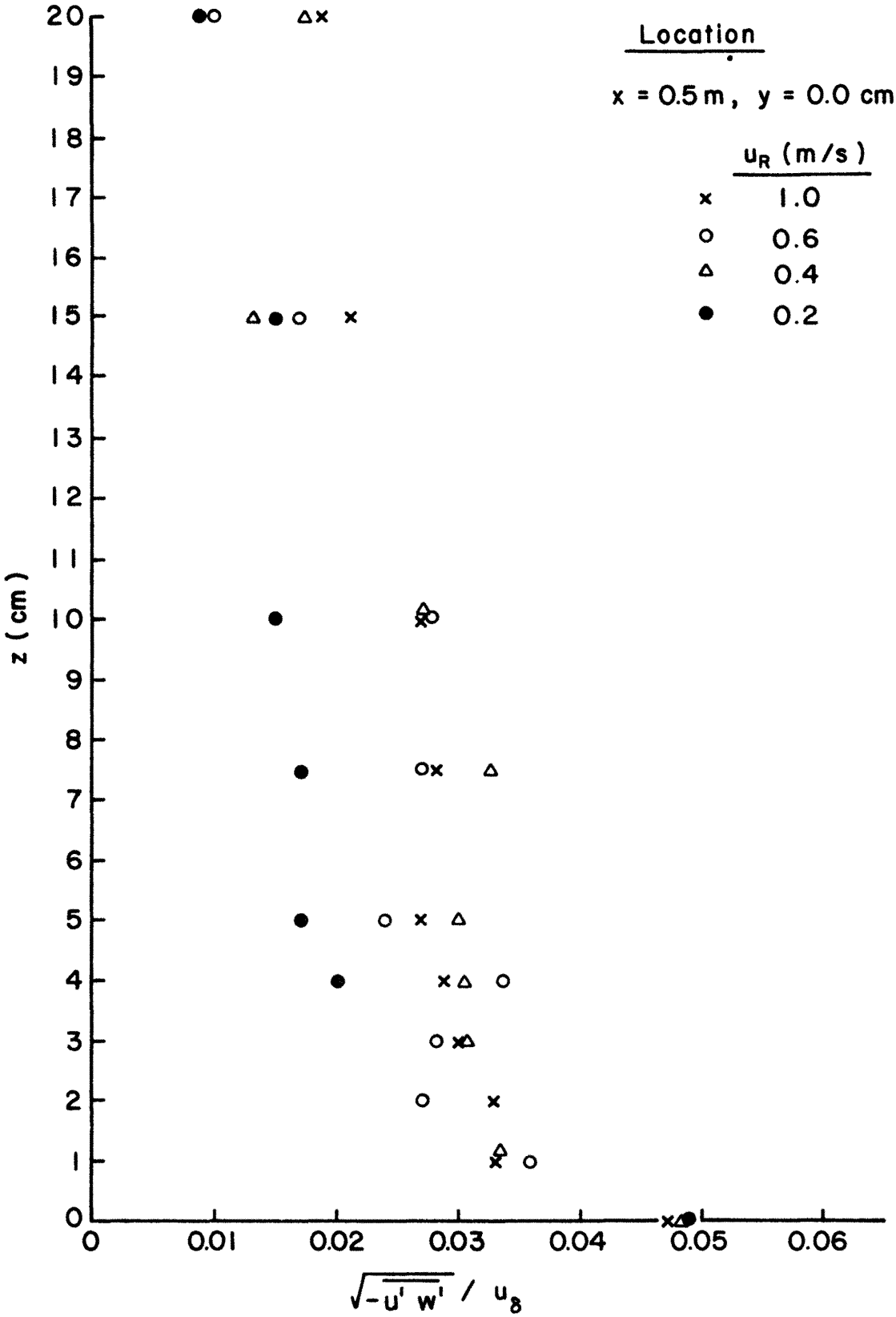

Figure 11. Turbulent Shear Stress Profiles

Figure 12. Figure 13 compares the Harris spectra scaled down by three different length scale ratios to the wind tunnel spectral energy distribution at z = 1 cm and for u_R = 1.0 m/sec. The data scatters, but supports the conclusion that the wind-tunnel boundary layer has a scale of the order of 1:2000. Selecting an exact peak value from the flat distribution is not reasonable.

Autocorrelation curves were also prepared from data at z = 1 cm for each wind speed. The u_R = 1 m/sec values are shown in Figure 14. Integral time scales were estimated from these figures by two methods. First a value $T_{1/e}$ was specified by noting the time at which the autocorrelation decreased to 1/e. Second the correlation was graphically integrated to the first zero crossing. The integral found was set to $T_{\int Rdt}$. Integral scales were estimated under Taylor's hypothesis by multiplying time scales with local wind speed. Values of estimated T and Λ are recorded as Columns 14 to 19 of Table 3. A scale ratio of 1:1000 would indicate field values of integral scale ranging from 50 to 100 m at a height of 10 meters, whereas a scale ratio of 1:2000 indicates a range between 100 to 200 meters. Counihan (1975) suggests the integral scale ranges from 100 to 150 m for neutral flow at a height of 10 meters over roughness heights, $z_o \simeq 0.01$ to 0.1 m.

4.2 VISUAL APPEARANCE OF DISPERSING CLOUDS

The techniques used to obtain the visual plume data are discussed in Section 3.3. Visual measurements of maximum upwind cloud extent, L_u, and maximum lateral cloud extent at x = 0.0, L_{H_o}, were determined from photographs for the wind shear cases. The appearance of clouds released during calm situations is discussed in Section 4.2.1, whereas wind shear cases are discussed in Section 4.2.2.

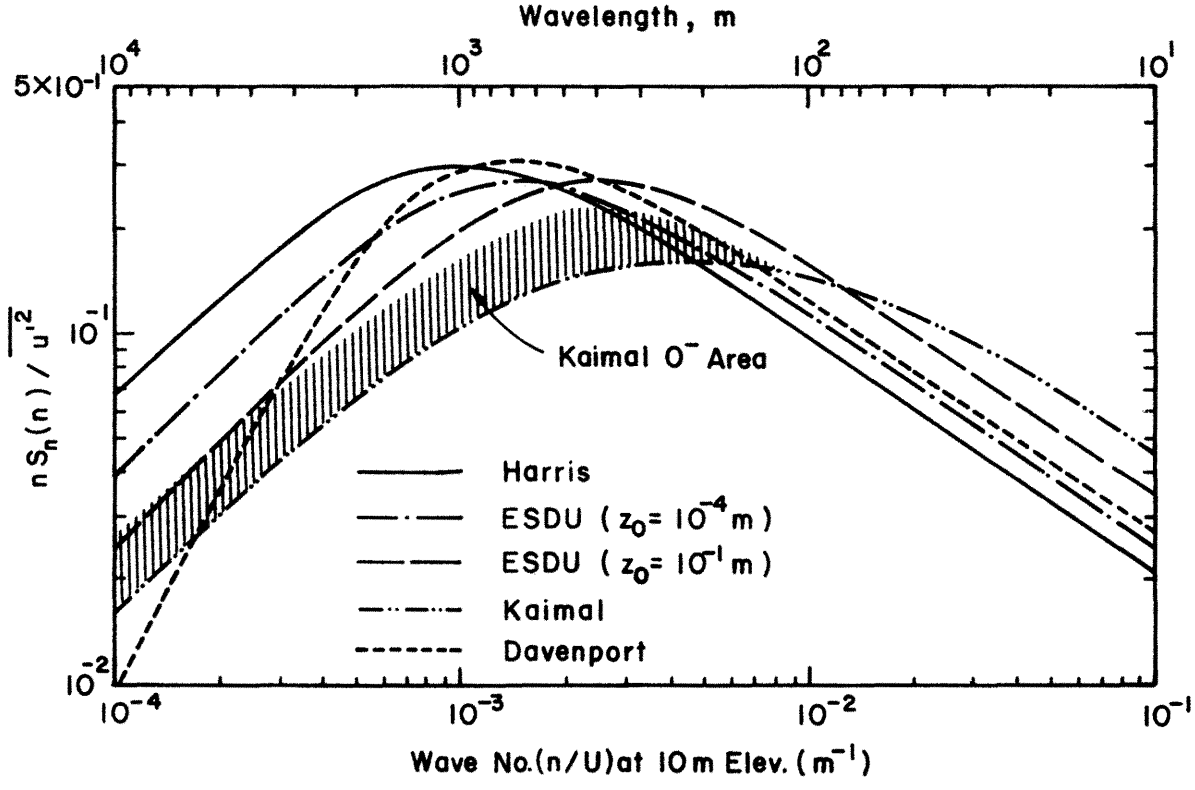

Figure 12. Different Descriptions of the Power Spectrum of Turbulent Velocity Fluctuations for the Longitudinal Velocity Component in the Atmospheric Boundary Layer

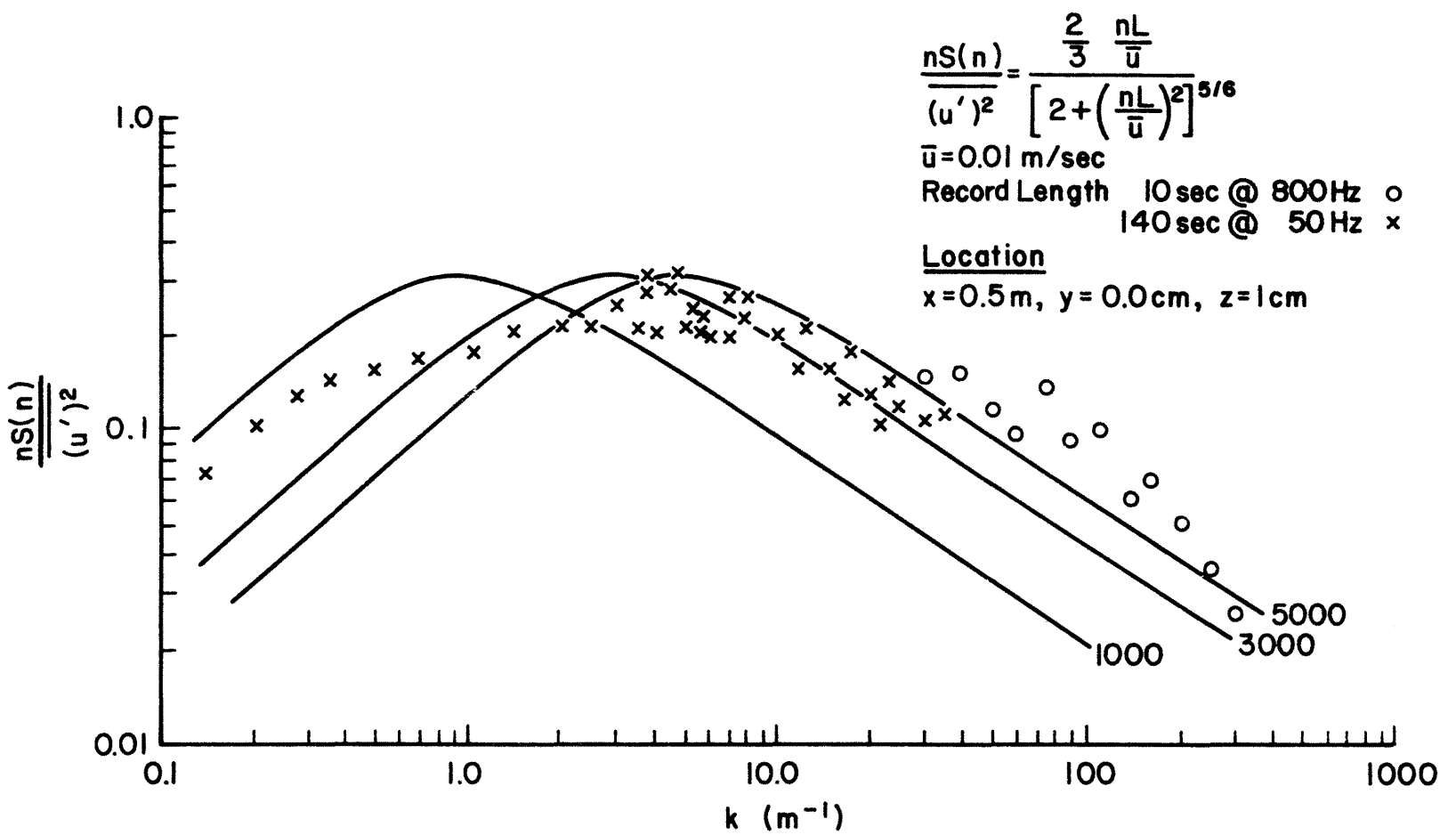

Figure 13. Turbulent Spectra, x = 1 m, z = 1 cm, u_R = 1 m/s, $\bar{u}$ = 0.71 m/s

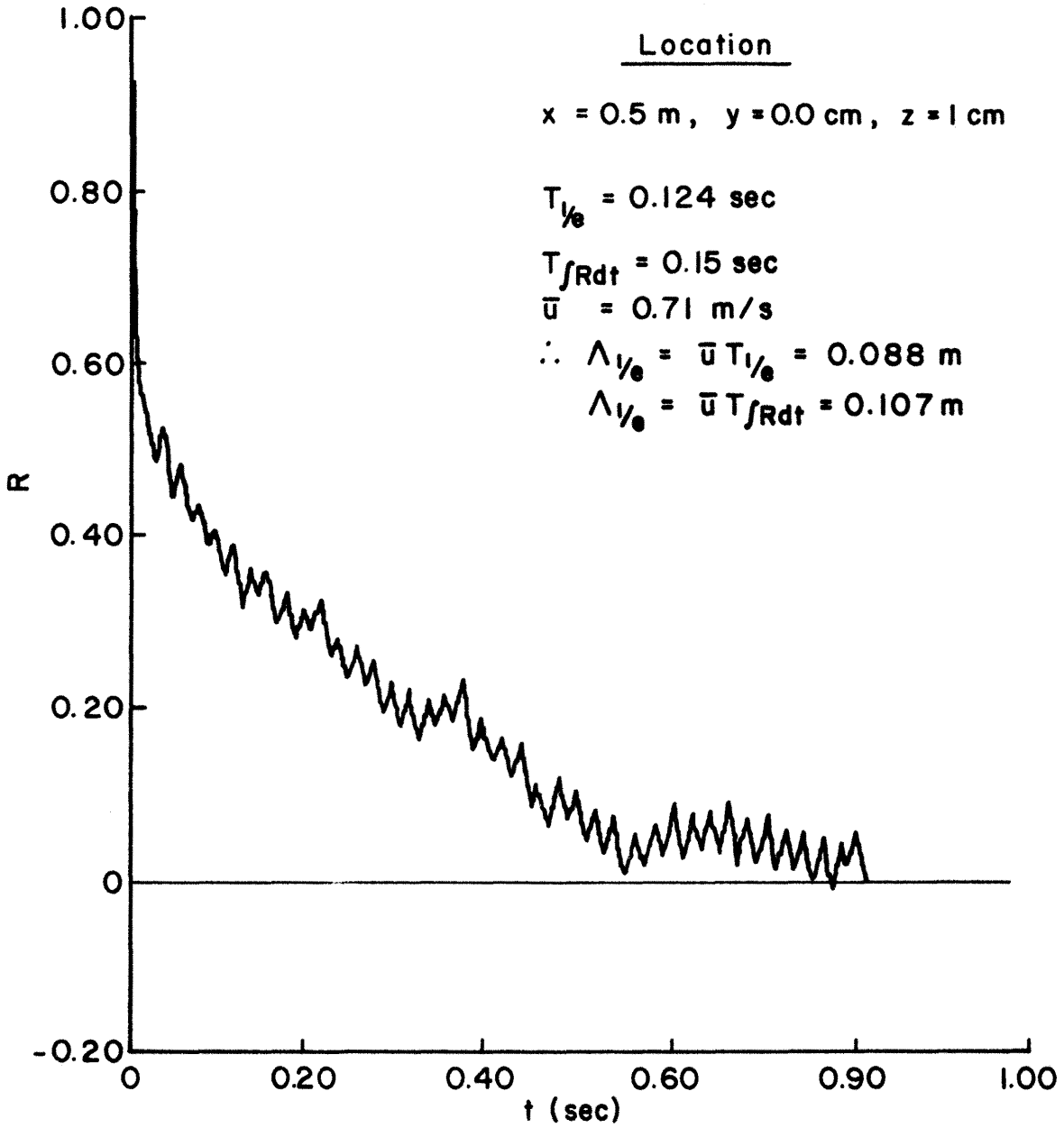

Figure 14. Longitudinal Turbulent Velocity Autocorrelation, x = 1 m, z = 1 cm, u_R = 1 m/s, $\bar{u}$ = 0.71 m/s

4.2.1 Visual Appearance of Clouds Released in Calm Situations

As suggested by Martin and Moyce (1952) the collapse of a dense column of fluid is similar to the appearance of the base surge noticed in photographs of atomic bomb explosions over the sea. They performed experiments with salt water in a stilling tank, which look very similar to present results. Momentarily after the rotation of the cup the cloud is seen to keep roughly to its original shape, but gravity acts to cause an accelerating movement towards the ground, followed by an outward movement in the form of a billowing torus. Martin and Moyce describe the shape of the surge as being "like that of a half anchor ring expanding out over the bottom of tank." Picknett (1981) saw his field experiments behave like an expanding horizontal disc, which flattens toward the ground except for a raised annular rim. The wind-tunnel experiments might be described in the same manner. Of course as the cloud spreads radially it begins to decelerate, and after a long time the cloud sits as a quiescent slowly undulating thin disk. The authors have examined photographs of field releases by van Ulden (1974), Picknett (1981), and the AGA (1974). The appearance of the wind-tunnel model results were all similar with no significant differences in appearance.

Movements caused by the larger cup sizes were quicker to develop; however, when scaled by the recommended time, T, and length scales, L, listed in Table 2, all kinematics appeared similar. A sequence of camera frames shown in Figure 15 display the typical appearance of a dense cloud.

4.2.2 Visual Appearance of Clouds Released in Wind Shear Situations

The main actions of wind shear are to superimpose normal turbulent dispersion on the dense cloud motions and to advect the cloud downwind.

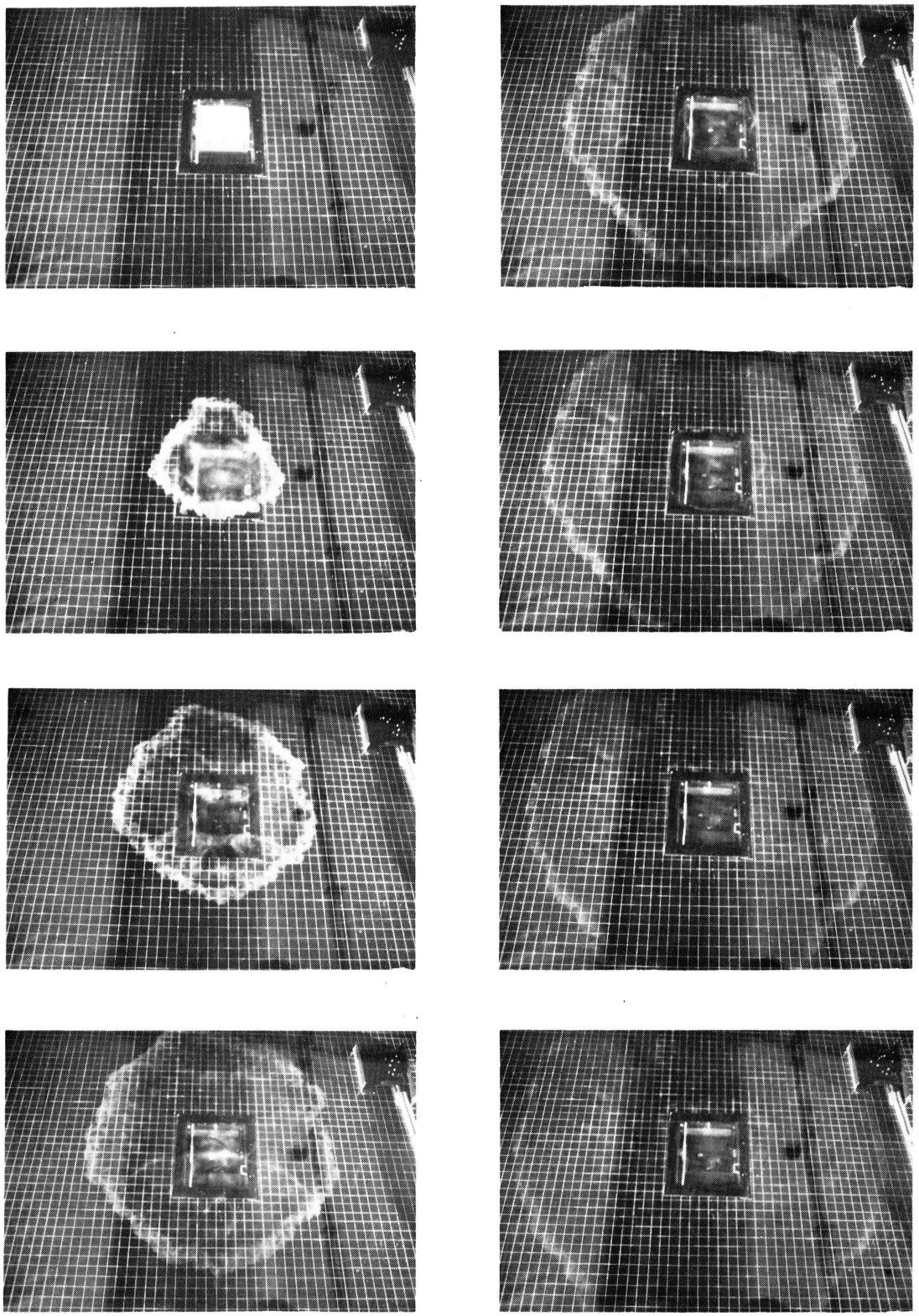

Figure 15. Sequence of Cloud Locations During Release in a Calm Situation, V_i = 450 cm^3 (Successive plates are taken ~0.3 sec apart)

Initially the cloud behaves as in a calm situation; that is the cloud collapses toward the ground and moves outward as a radial torus. The cloud motion in the upwind direction initially persists; however, the cloud eventually is brought to a halt by the opposing flow, and this portion of the cloud thickens with respect to the rest of the cloud. At this moment the cloud is wider than it is long; subsequently the cloud begins to drift downwind in a "horse-shoe" shape, much as was depicted by Neff and Meroney (1982) for steady area releases shown in Figure 16. Subsequently the profile viewed crosswind becomes "wedge shaped" with the sharp end upwind, and the downwind end is blunt with a raised nose. In later stages the cloud becomes longer than it is wide. The upwind end of the cloud becomes whispy, patchy, and shows long elongated patches of floor surface like the head of a man going bald. Finally the wind sweeps all traces of the cloud downwind.

Larger volume cups produced greater upwind movement than smaller cups for a given wind speed. Similarly larger wind speeds reduced upwind movement for a given cup size. Figure 17 displays the typical appearance of a cloud developing in a wind field. Such photographs were used to determine maximum upwind movement, L_u, and maximum source position lateral movement, L_{H_o}. These values are plotted as L_u/L and L_{H_o}/L versus dimensionless buoyancy length $L/\ell_b = (Ri_*)$ in Figures 18 and 19. Britter (1980) and Neff and Meroney (1982) examined similar parameters for continuous release sources of dense fluids. Such information is helpful to predict areas contaminated by toxic releases, to determine detonation zones for flammable gases, and to bound the fluid kinetics of analytic or numerical models.

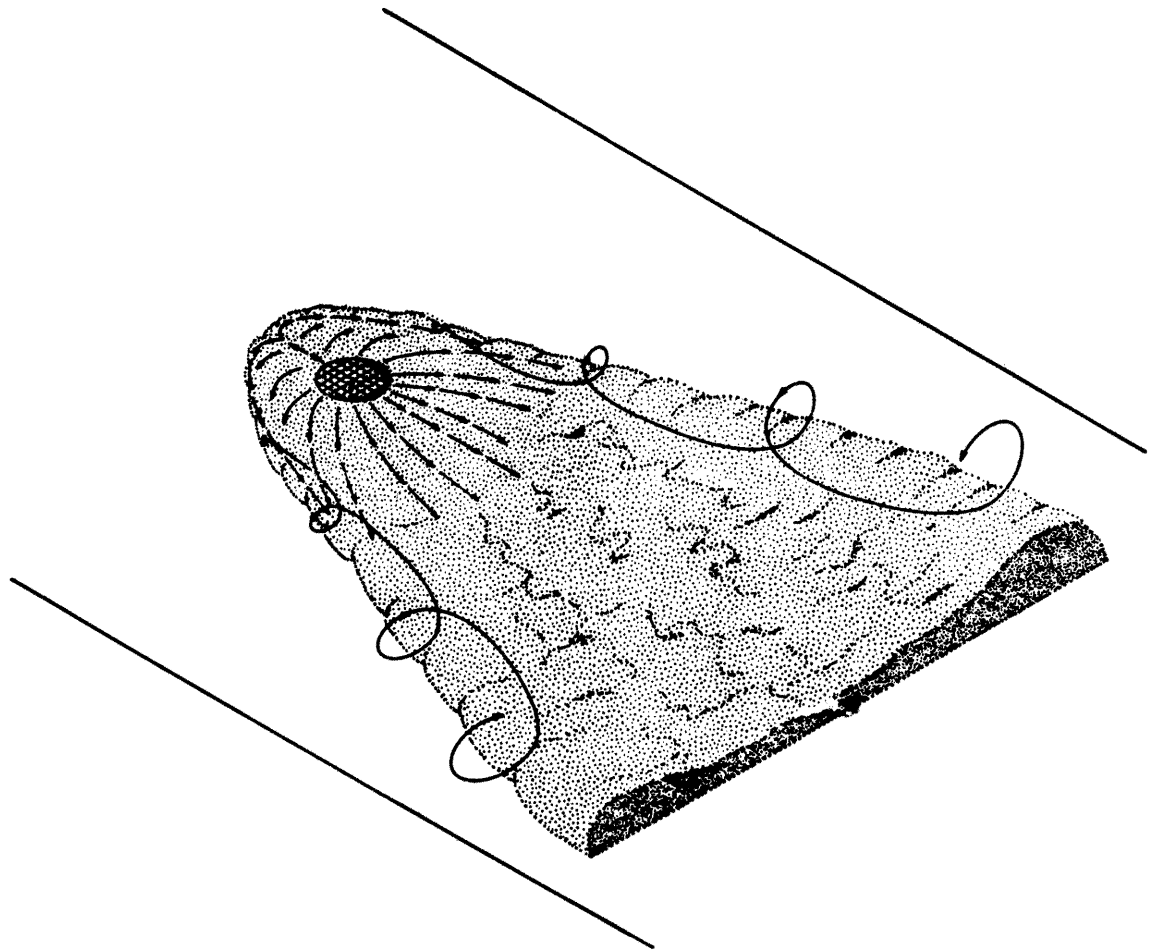

Figure 16. Qualitative Appearance of a Continuous Area Source of Dense Gas in a Velocity Field From Neff and Meroney (1982)

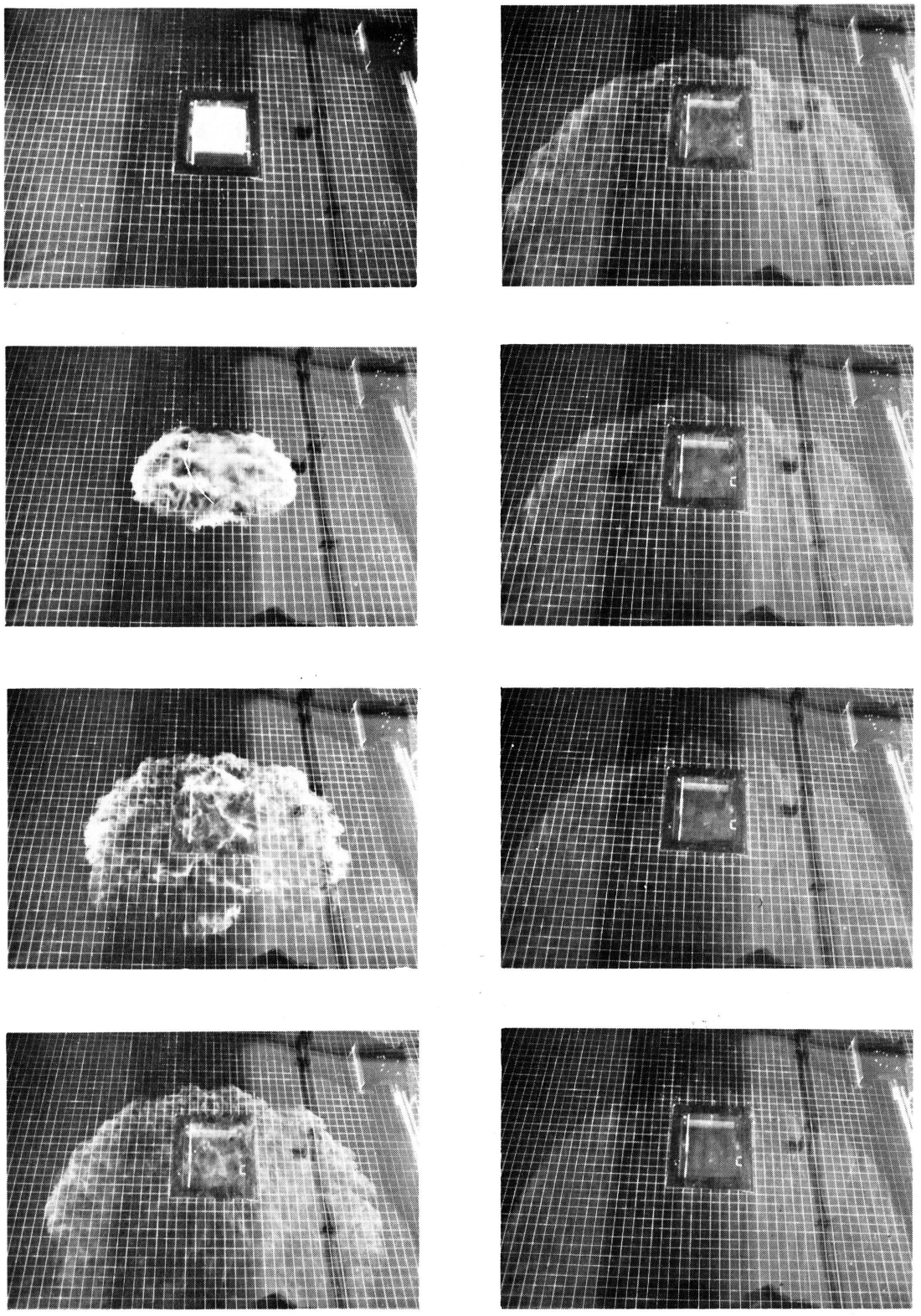

Figure 17. Sequence of Cloud Locations During Release in a Wind Shear Situation, V_i = 450 cm^3, u_R = 0.6 m/s
(Succesive plates are taken ~0.3 sec apart)

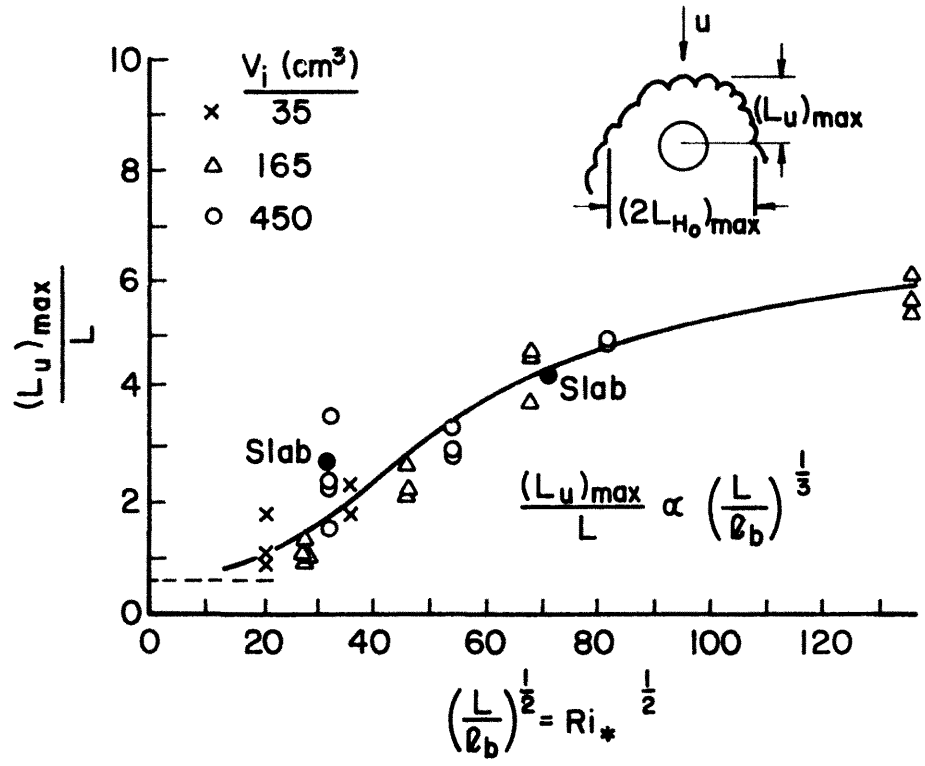

Figure 18. $(L_u/L)_{max}$ versus L/ℓ_b

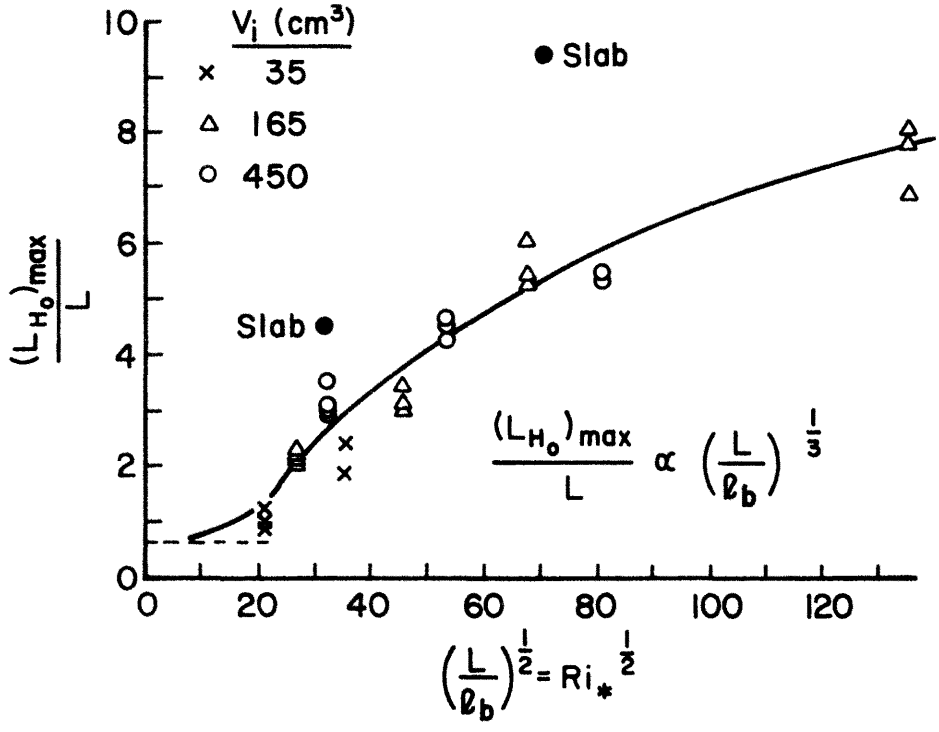

Figure 19. $(L_{H_o}/L)_{max}$ versus L/ℓ_b

For passive plumes, ie. L/ℓ_b small, the values of L_u/L and L_{H_o}/L should approach source volume dimensions. As L/ℓ_b increases the scaled quantities increase more or less as L_u/L or $L_{H_o}/L \sim (L/\ell_b)^{+1/3}$.

4.3 TRANSIENT PLUME CONCENTRATION RESULTS

In this section the general appearance and statistics of the sensor response are discussed in Section 4.3.1. Subsequently data for calm and windy situations are presented in Sections 4.3.2 and 4.3.3 respectively. Measurements of neutral density volume sources released in wind shear are reviewed in Section 4.3.4.

4.3.1 Statistics of Dense Cloud Dispersion Behavior

The time response of the aspirated hot-wire probe during a typical sequence of measurements is shown in Figure 20. Replications of the same release scatter as noted. Data recorded from such response curves are shown on Figure 21 and include the arrival time, t_a, the arrival time of the concentration maximum, t_m, and the departure time of the cloud, t_d. The maximum concentration, χ_m, was also recorded. Each scenario was repeated about 5 times and the average values of $\overline{t_a}$, $\overline{t_m}$, and $\overline{t_d}$ scaled by T to produce $\overline{t_a^*}$, $\overline{t_m^*}$, $\overline{t_d^*}$ are recorded in Tables 4 through 8. The standard deviation of each average is provided to indicate the degree of statistical variation.

A single release scenario of a large cup, u_R = 0.4 m/sec, and a location of x = 40 cm, y = 0 cm, z =2 mm was repeated about 100 times. The measured arrival time was found to have an average value, $\overline{t_a^*}$ = 205, and a standard deviation, $\sigma_{t_a^*}$ = 2.79. A plot of the probability distribution indicated that t_a^* was normally distributed about its mean.

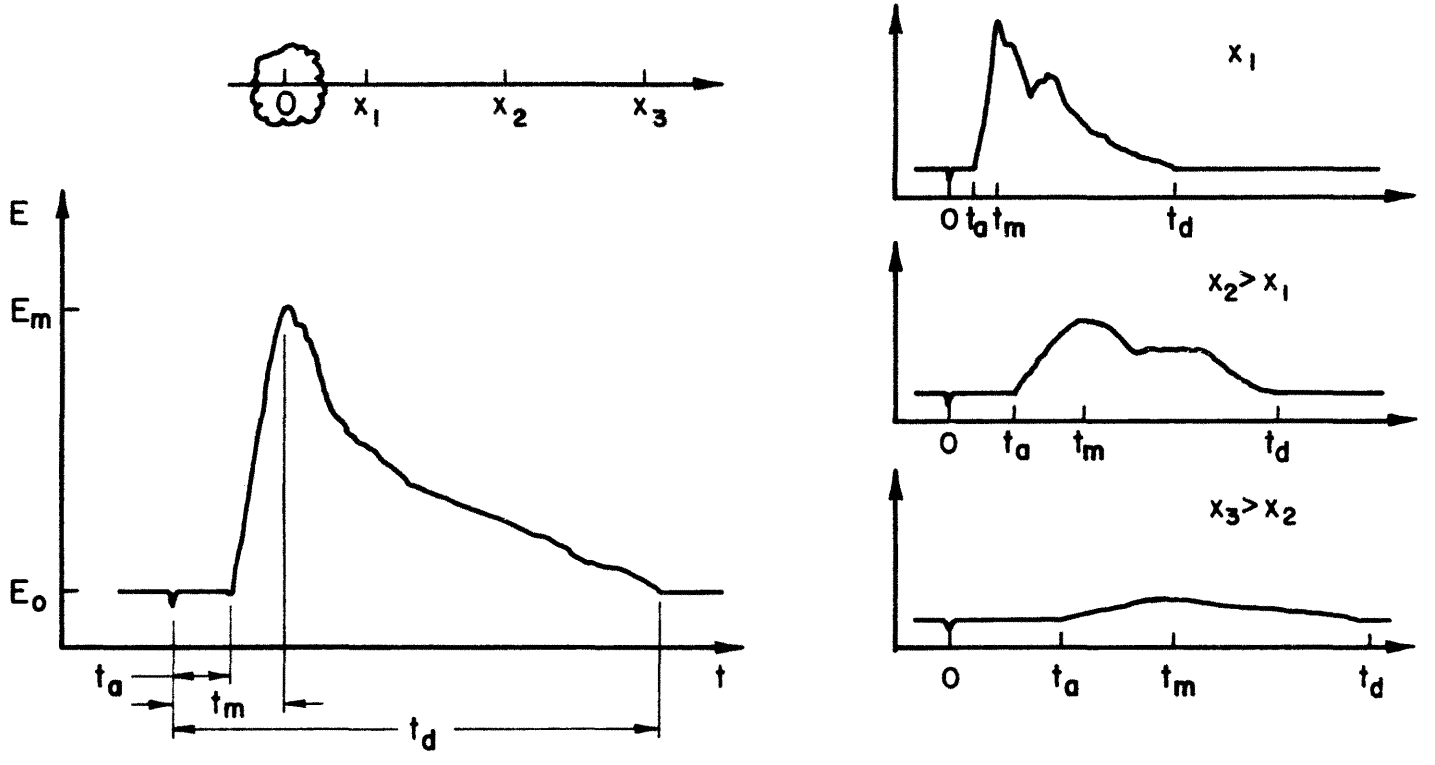

Figure 20. Typical Time Response Characteristics of Katherometer Located at Various Positions Downwind of Source

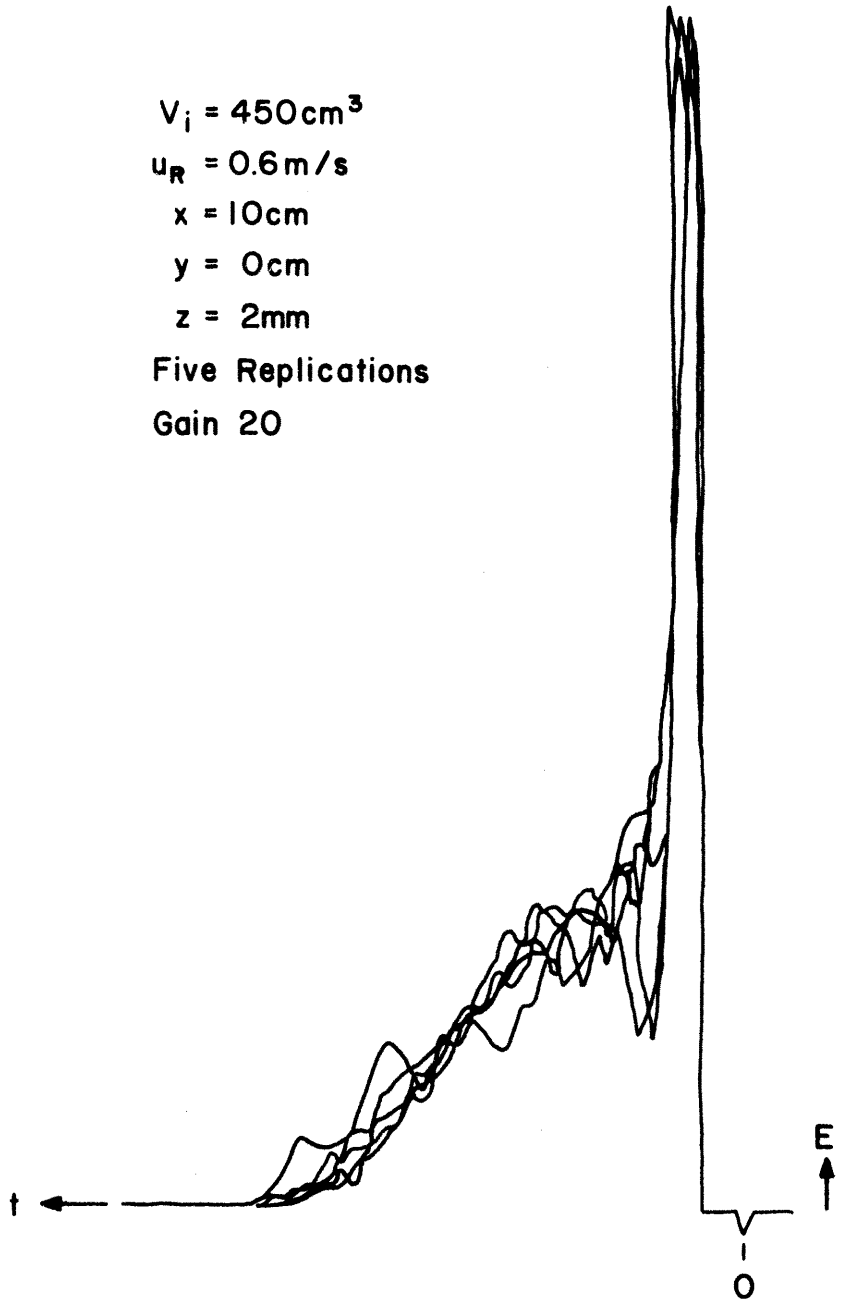

Figure 21a. Replications of Katherometer Response at Various Downwind Locations, V_i = 450 cm^3, u_R = 0.6 m/s

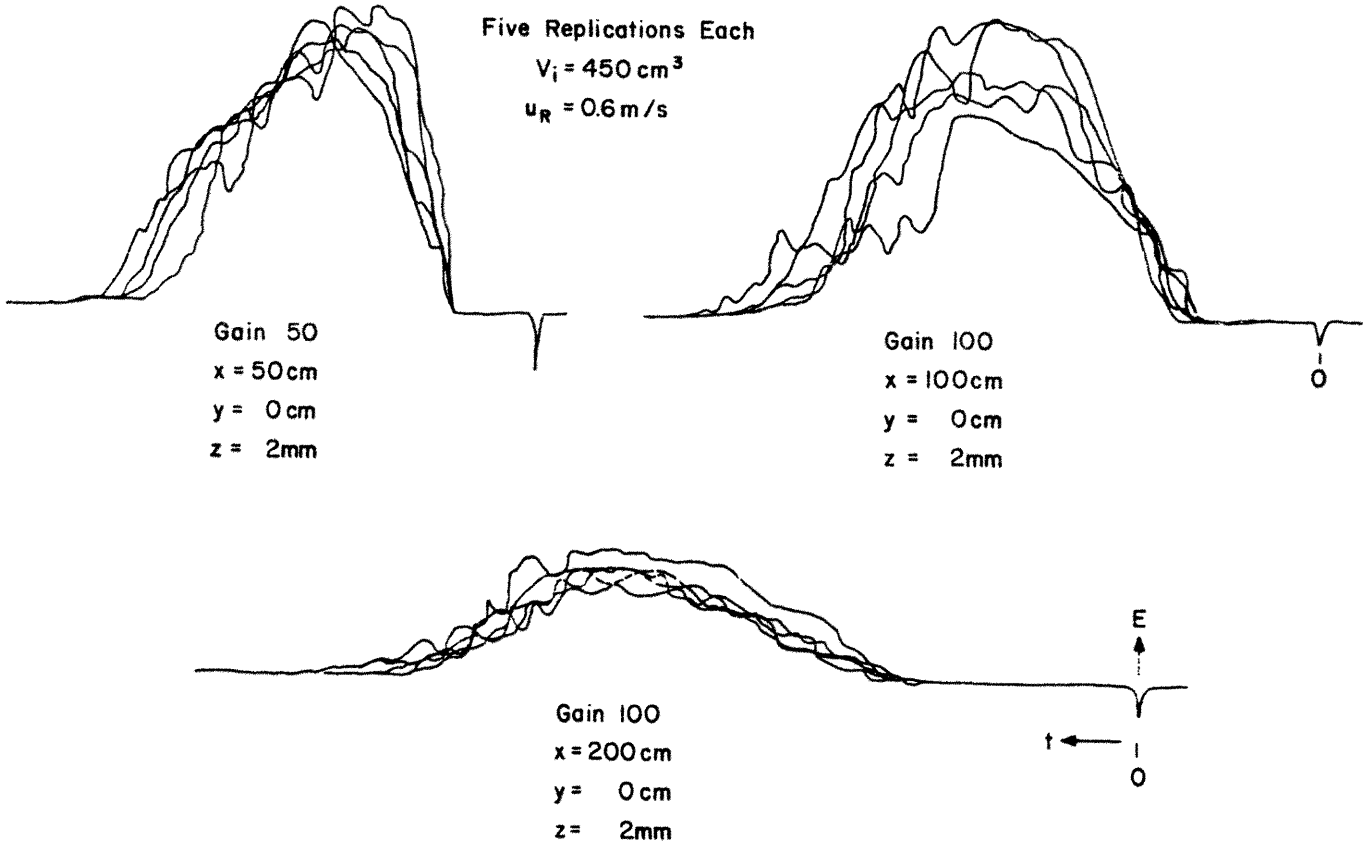

Figure 21b. Replications of Katherometer Response at Various Downwind Locations, V_i = 450 cm^3, u_R = 0.6 m/s

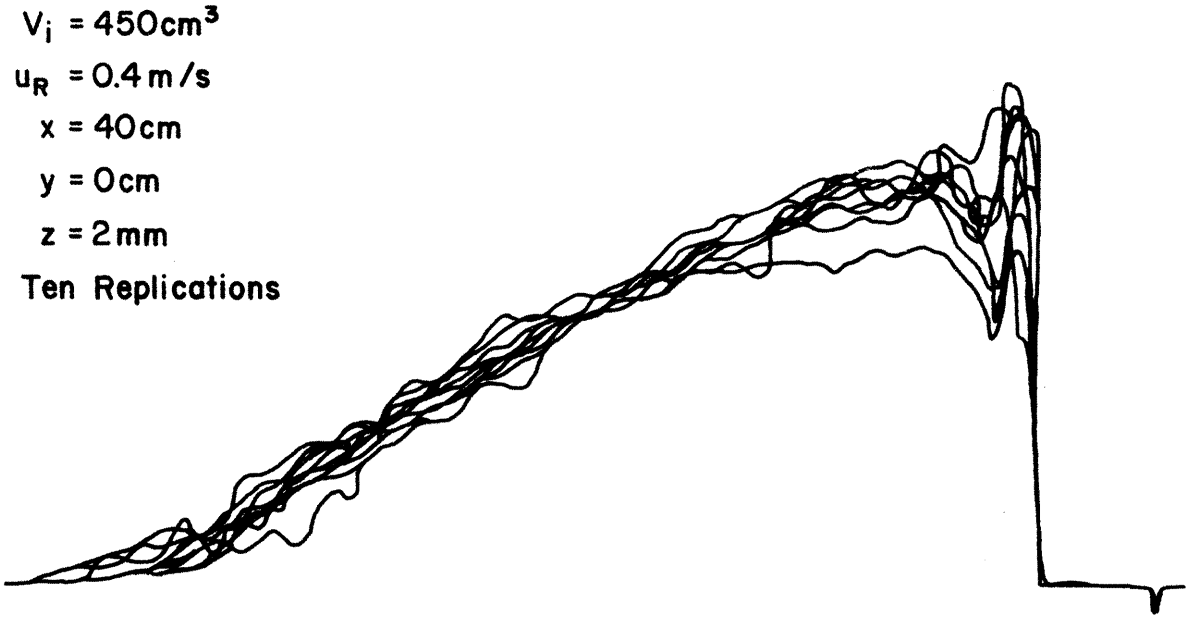

Figure 21c. Replications of Katherometer Response at Various Downwind Locations, V_i = 450 cm^3, u_R = 0.6 m/s

The mean value of the arrival time for the maximum concentration was $\overline{t_m^*} = 30.5$, and its standard deviation was $\sigma_{tm^*} = 8.00$. A plot of the probability distribution indicated that t_m^* is not normally distributed. This is reasonable since $t_m^* > t_a^*$. Rather a log-normal probability plot indicates

$$f(t_m^*) = \frac{1}{\sqrt{2\pi}} \frac{1}{\beta} \frac{1}{(t_m^* - 20.5)} \exp - \frac{(\ln(t_m^* - 20.5) - \alpha)^2}{2\beta^2} \qquad (4\text{-}3)$$

where $\alpha = 2.218$ and $\beta = 0.544$ and a lower bound for $t_m^* = 20.5$ was assumed. One might expect t_a^* to follow a normal distribution more closely as x^* increases and t_a^* and t_m^* differ from one another significantly.

The concentration maximum measure, χ_m, was normally distributed with an average value $\overline{\chi_m} = 6.805$ and a standard deviation $\sigma_{\chi_m} = 1.442$. For values of χ_m very near to 1.0 or 0.0 one may find an assymmetric distribution occurs.

The standard deviations measured were significant. Single measurements could deviate markedly for this highly transient instantaneous source situation from the means. Indeed it appears possible to interpret entrainment rate parameters which vary by an order of magnitude if one calibrates analytic or numerical models based on outlying values.

4.3.2 Concentration Results for Calm Situations*

Radial growth of the dense cloud is plotted versus dimensionless arrival time, t_a^*, in Figure 22. After an initial acceleration period

---

* Hereafter the bar superscript will be eliminated from all symbols since all values and figures contain only mean values.

all data follow a $(t_a^*)^{1/2}$ growth rate from $t_a^* \simeq 10$ to $t_a^* \simeq 240$. Radial growth appears to be similar over all cup sizes tested. Viscous effects may cause late arrival times at the larger R^* values; however, scatter of data precludes any definite conclusion.

A second plot of radial growth versus dimensionless arrival of the maximum concentration time, t_m^*, is shown in Figure 23. Growth rate seems to go from a linear variation with t_m^* to a third or fourth power, ie. $(t_m^*)^{1/4}$.

Cloud dilution, χ_m, is plotted versus t_a^*, t_m^*, and R^* in Figures 24, 25, and 26 respectively. Again the chosen scale variables appear to collapse data from all cup sizes. Maximum concentrations appear on the average to decay as $(t_a^*)^{-2/3}$ in the range $10 < t_a^* < 300$, or as $(t_m^*)^{-2/3}$ over the range $10 < t_m^* < 400$. Concentration decays versus position as $(R^*)^{-1/2}$ in the range $2 < R^* < 7$ and as $(R^*)^{-1/3}$ or faster thereafter.

Earlier measurements for a source bubble volume, $V_i = 50\ cm^3$, performed in a different wind tunnel with different measuring instrumentation all fall within the error bounds of the present measurements. (Lohmeyer, Meroney, and Plate, 1981). As noted before these experiments reproduced plume behavior seen in field experiments at scales 350 times greater.

4.3.3 Concentration Results for Wind Shear Situations

Mean and standard deviations of all cases are provided in Tables 4 to 8. In addition concentration at various vertical locations are provided in Tables 9 to 12. These data have been cross-plotted as x^* vs t_a^*, x^* vs t_m^*, χ_m vs t_a^*, χ_m vs t_m^*, and χ_m vs x^*.

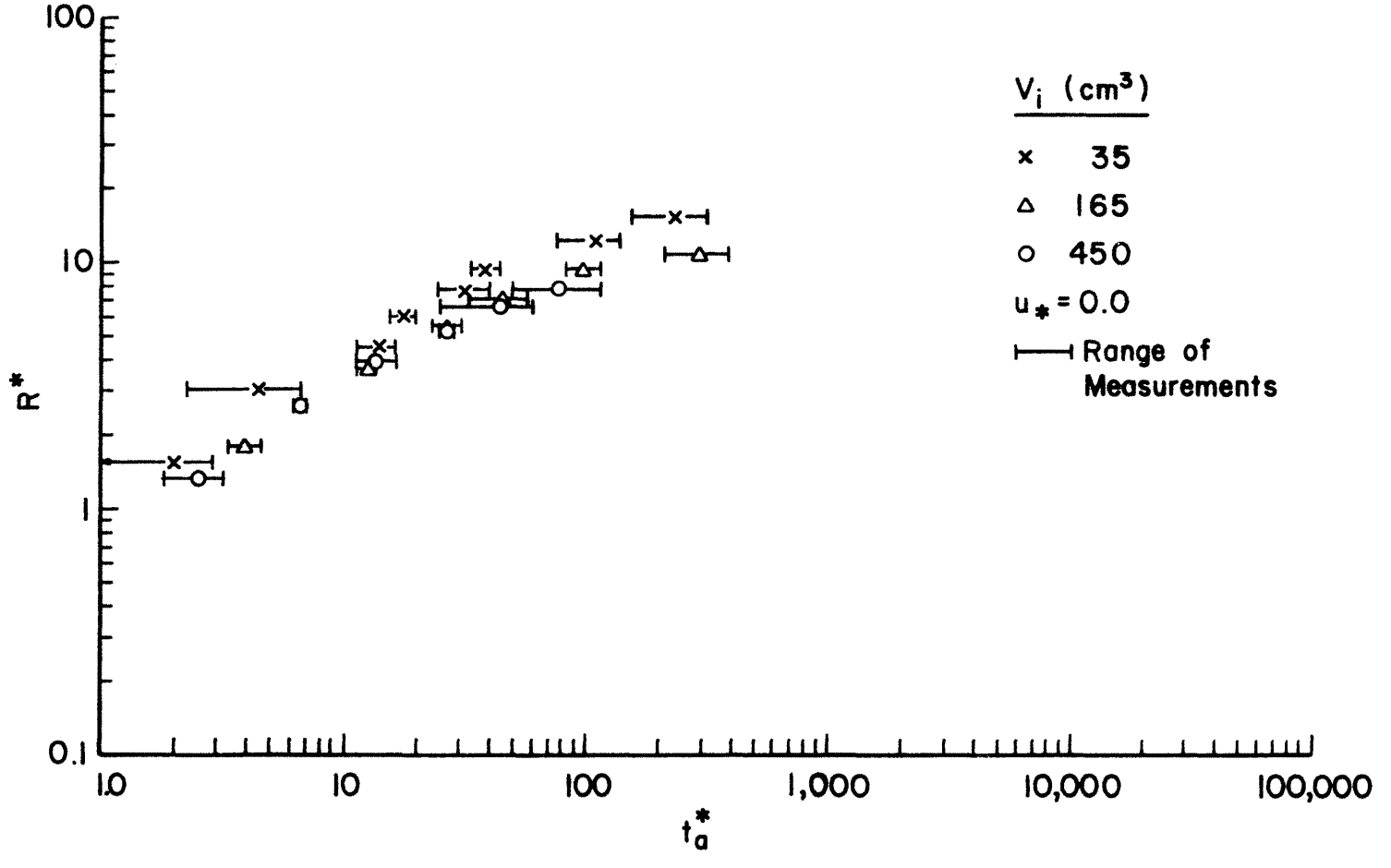

Figure 22. Radial Growth of Dense Cloud: R^* vs t_a^*, $u_R = 0$

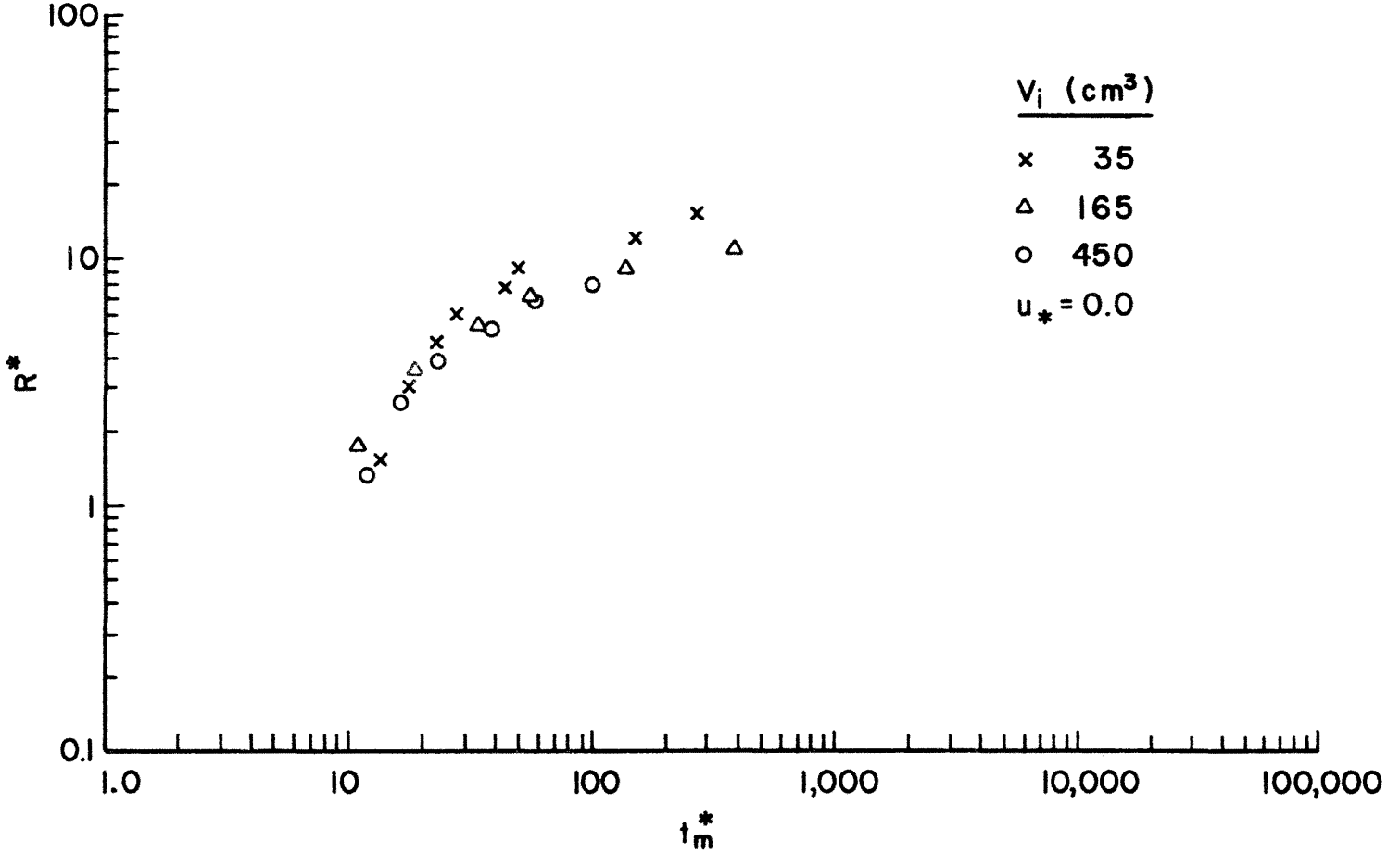

Figure 23. Radial Growth of Dense Cloud: R^* vs t_m^*, $u_R = 0$

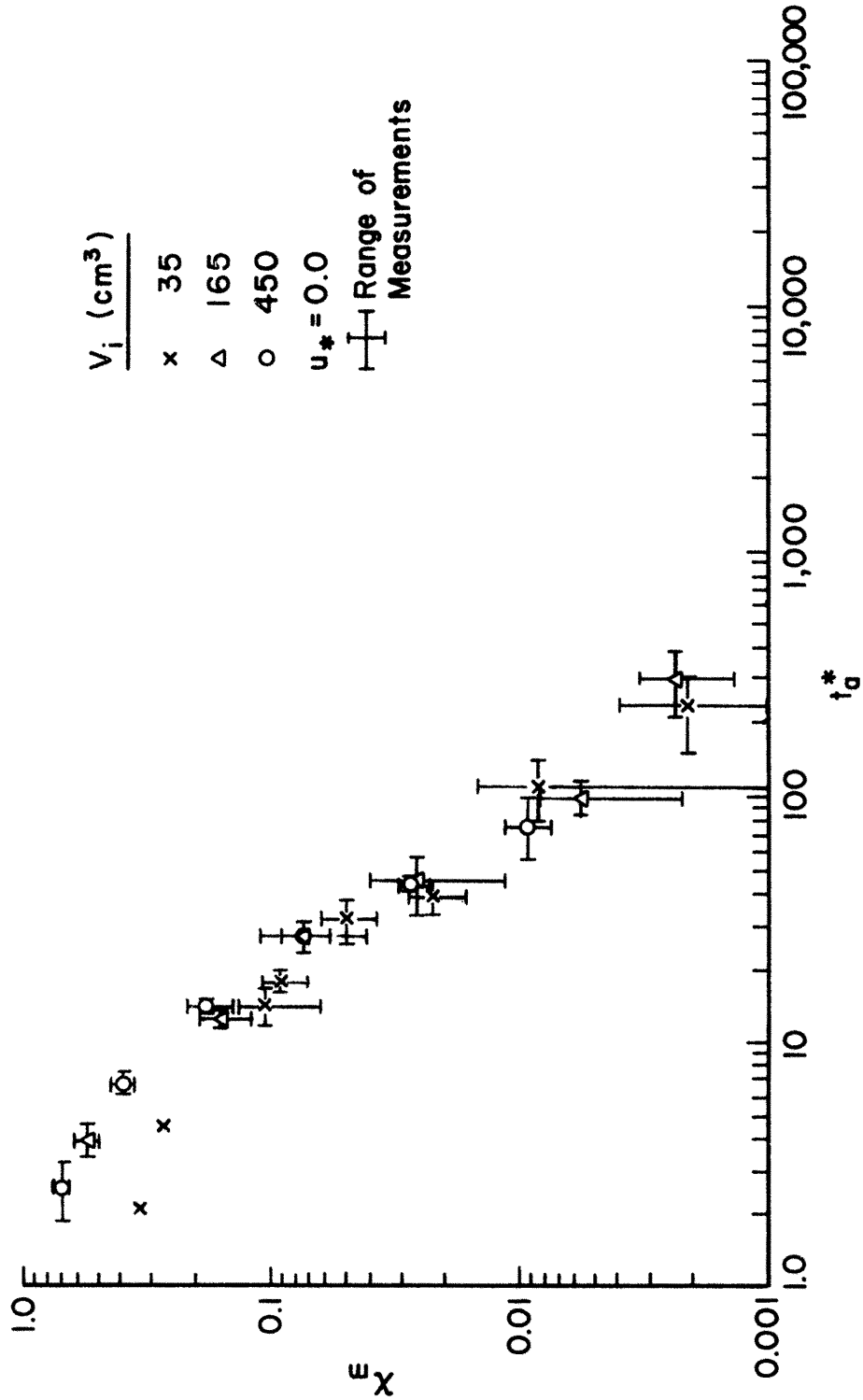

Figure 24. Plume Dilution: χ_m vs t_a^*, u_R = 0 m/s

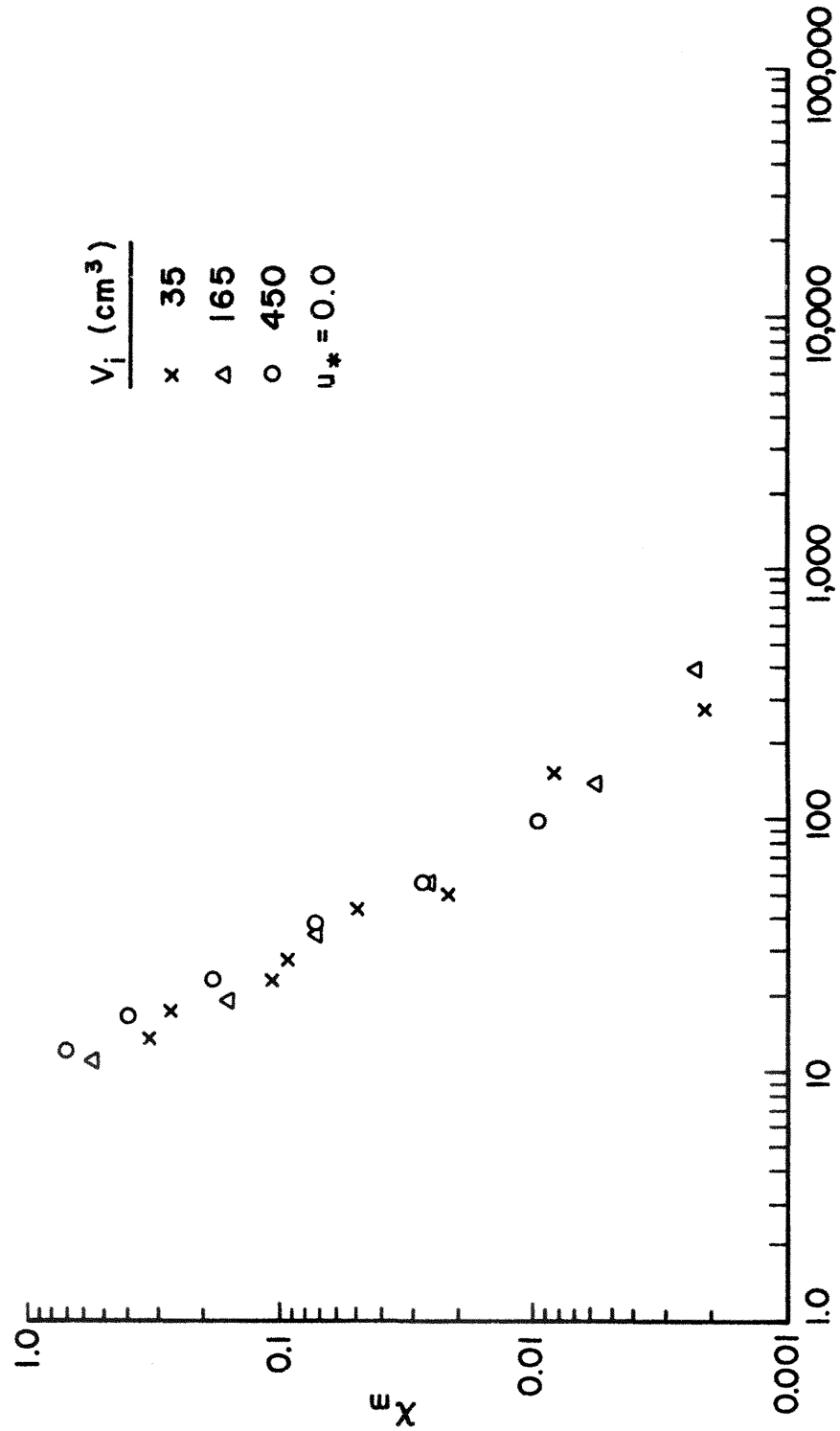

Figure 25. Plume Dilution: χ_m vs t_m^*, u_R = 0 m/s

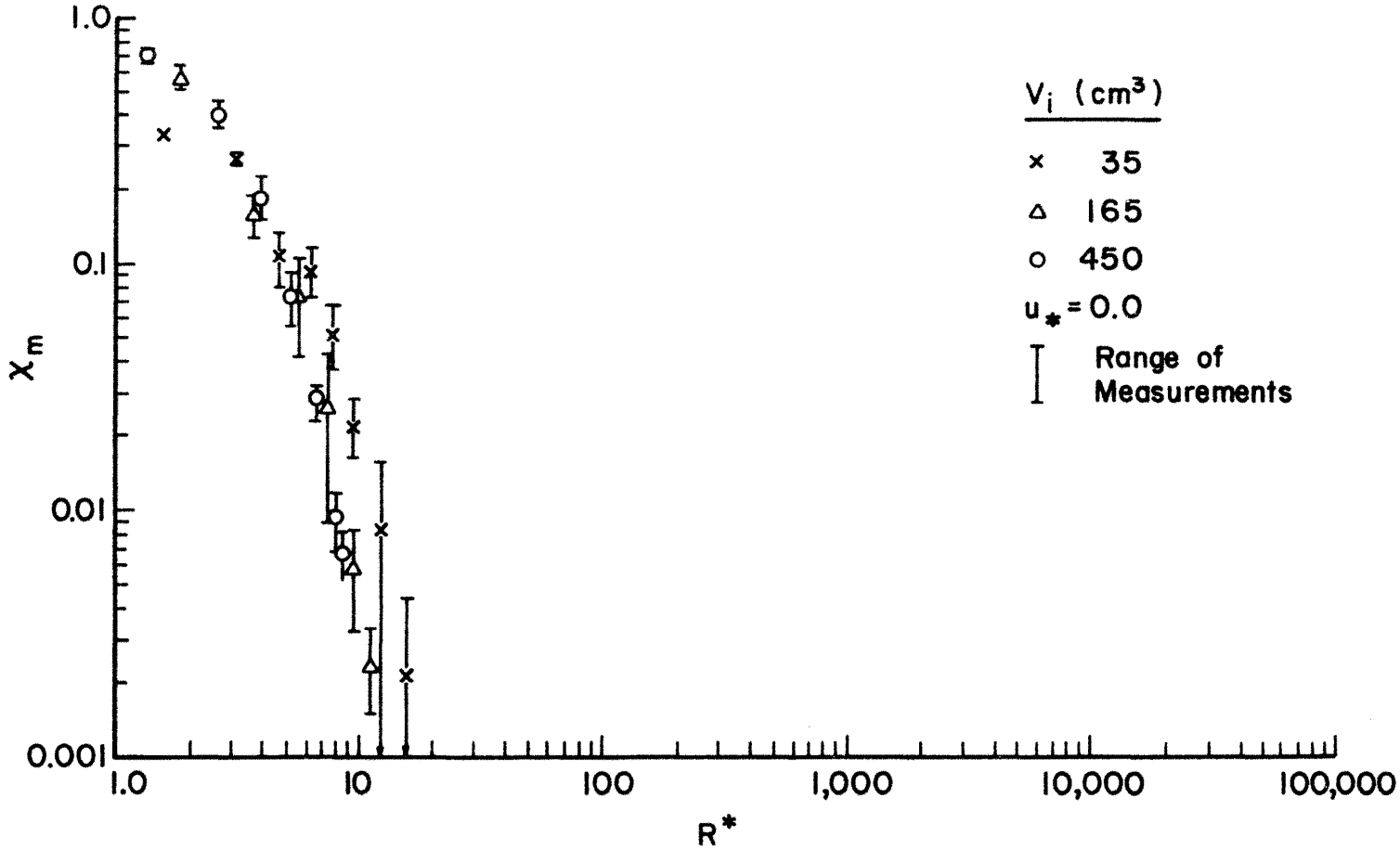

Figure 26. Plume Dilution: χ_m vs R^*, u_R = 0 m/s

Ground Level Behavior

Figures 27 through 31 summarize the effects of wind shear. Calm situation data are also included as a reference condition.

Wind shear results in earlier arrival times of the dense cloud at downwind locations. Figure 27 suggests that the combination of cup sizes and wind speeds studied arrange themselves in a regular perturbation about the calm situation as u_R^* increases (or as Ri_* decreases). x_* varies as $t_a^{*1/2}$ during calm situations, but the slope increases with wind velocity until x^* varies as t_a^* (or even faster) as u_R^* approaches one. Figure 28 suggests x^* varies with t_m^* in a similar manner as velocity increases.

Concentration variation with arrival time, t_a^*, (Figure 29) behaves in a rather irregular manner depending on initial cloud size. For the smallest cup size increasing wind speed results in progressively faster concentration decay rates. For the medium and large cup sizes initially small wind velocities result in apparently lower concentration decay rates, as the clouds are convected downwind without a proportionally higher rate of dilution. Under such conditions it may be assumed that background turbulence or wind shear has not yet significantly increased the entrainment of ambient air above that self generated by the dense plume motions.

At higher wind speeds the cloud dilutes faster, the decay rate increases, and the shape of the χ_m vs t_a^* curves steepens again. Thus, for the medium and large cloud sources, gas concentrations at a given time, t_a^*, are sequentially higher than, equal to, and then less than zero wind speed conditions as u_R^* increase. Figure 30 displays the same

features of decay response to wind shear for χ_m vs t_m^*. In this case even the smallest cup size displays this coy "dance like" forward and then backward tendency with increased wind speed.

As shown on Figure 31 concentrations universally increase downwind with wind speed compared to the calm wind speed situaion; however, the data suggest for each cloud size and downwind location a wind speed exists which results in maximum concentrations measured. At higher speeds one expects the added diluting capacity of the atmosphere to cause concentrations to vary inversely with wind speed for a fixed source rate. Havens (1979) and Raj (1981) predict numerically that the downwind distance to LFL continuously increases with wind speed for LNG spills of 25,000 and 30,000 m^3 liquid. Raj remarks calculations increased as 2/3 power of wind speed. Havens attributes the behavior to the finite time duration of the LNG vaporization from the water surface and the relative importance of vertical diffusion and x-direction advection. These experiments suggest shorter duration spills are more likely to produce a maximum LFL at some unique windspeed.

Figure 32 emphasizes again the influence of wind shear by examining the variation of t_a^* and χ_m when x^* is held constant and the variation of χ_m when t_a^* is held constant. No source size perturbation is apparent in the distribution of arrival times; however, source size obviously influences concentrations at low wind speeds. As u_R^* becomes large χ_m appears to approach similar values for all source sizes studied at a given t_a^*.

Elevated Behavior

Close to the source location, i.e. $x^* < 4$, maximum concentrations vary with height in a similar manner. One can conclude that in this

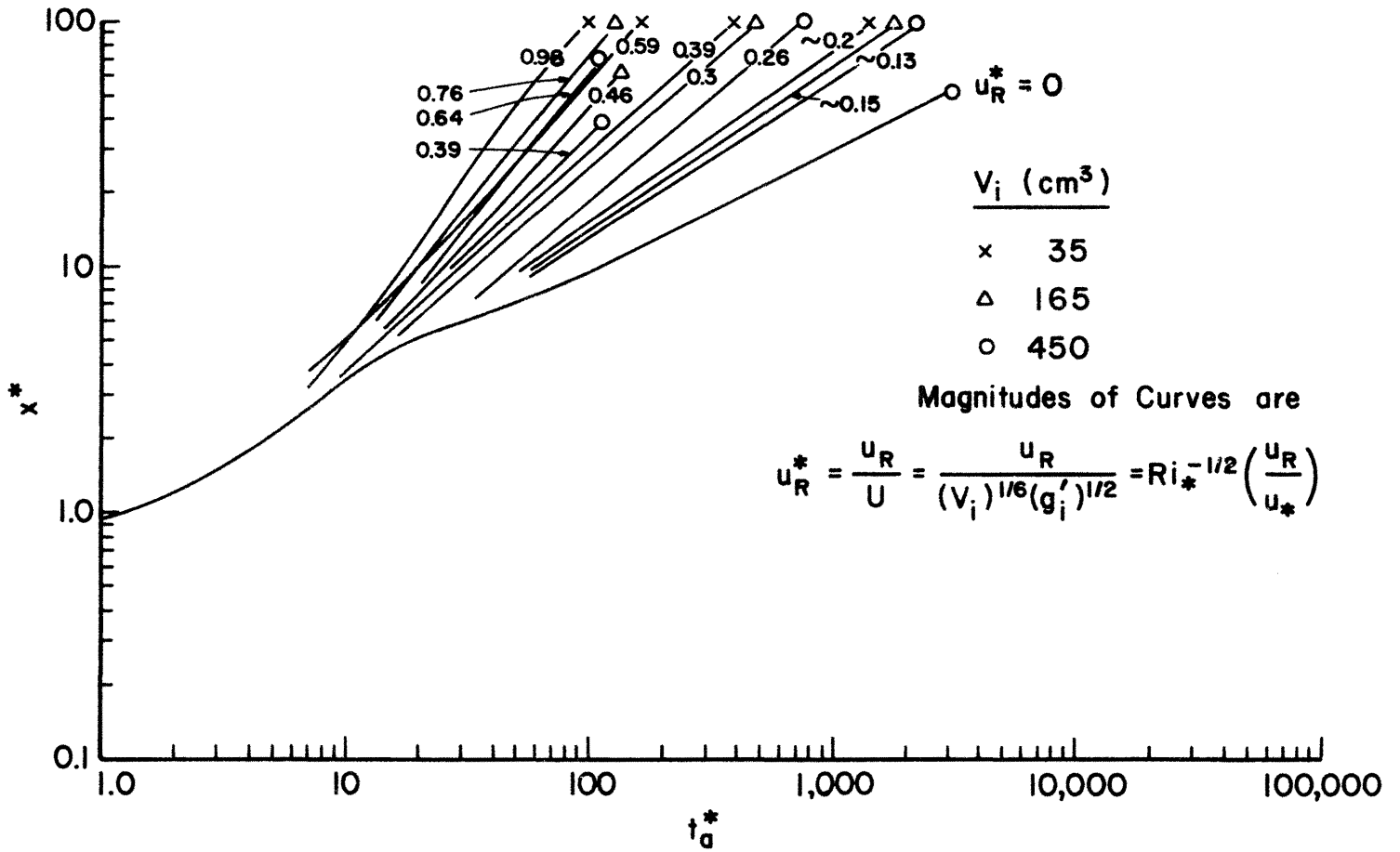

Figure 27. Distance, x^*, versus Arrival Time, t_a^*, $u_R \geq 0$

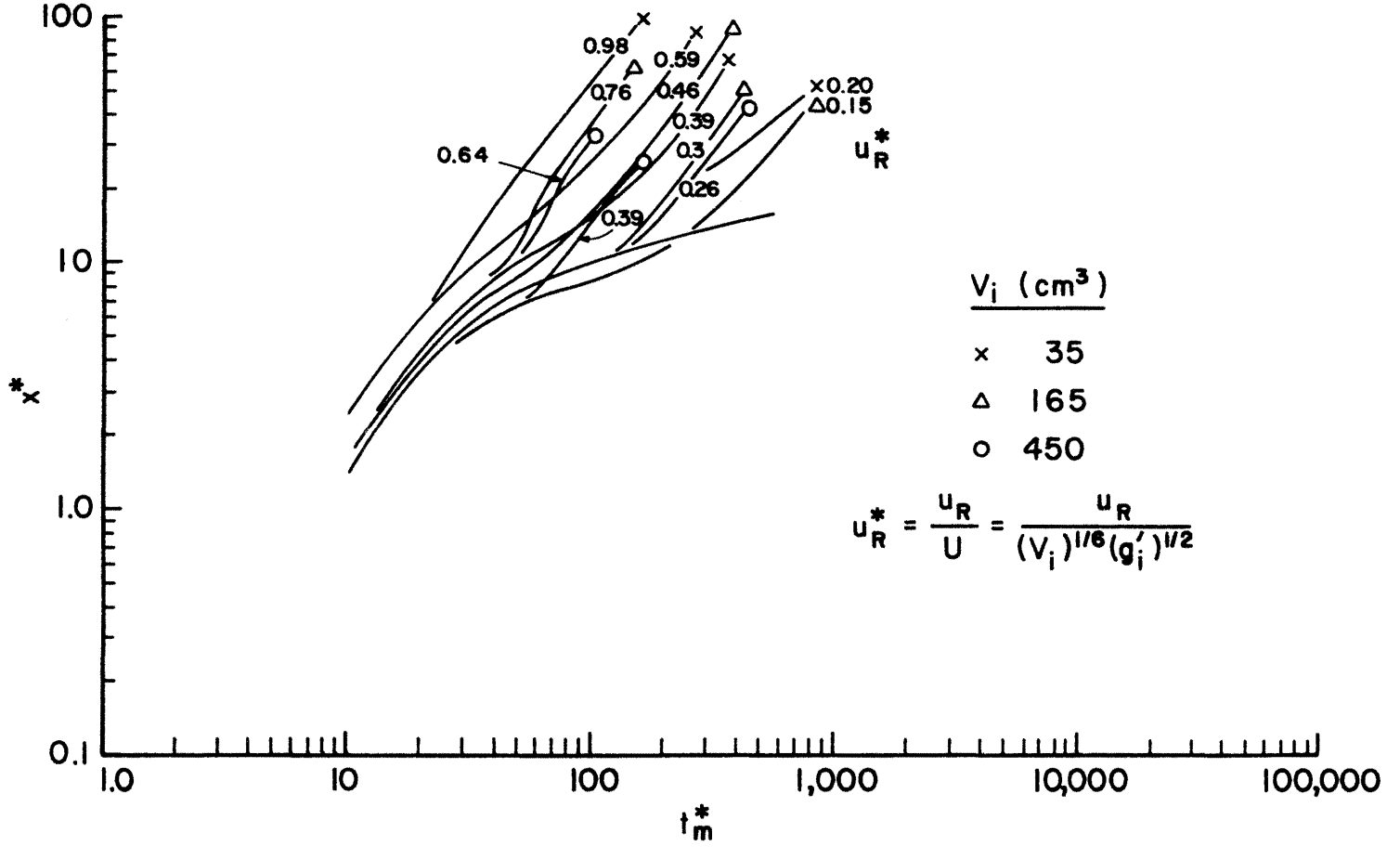

Figure 28. Distance, x^*, versus Maximum Concentration Arrival Time, t_m^*, $u_R \geq 0$ m/s

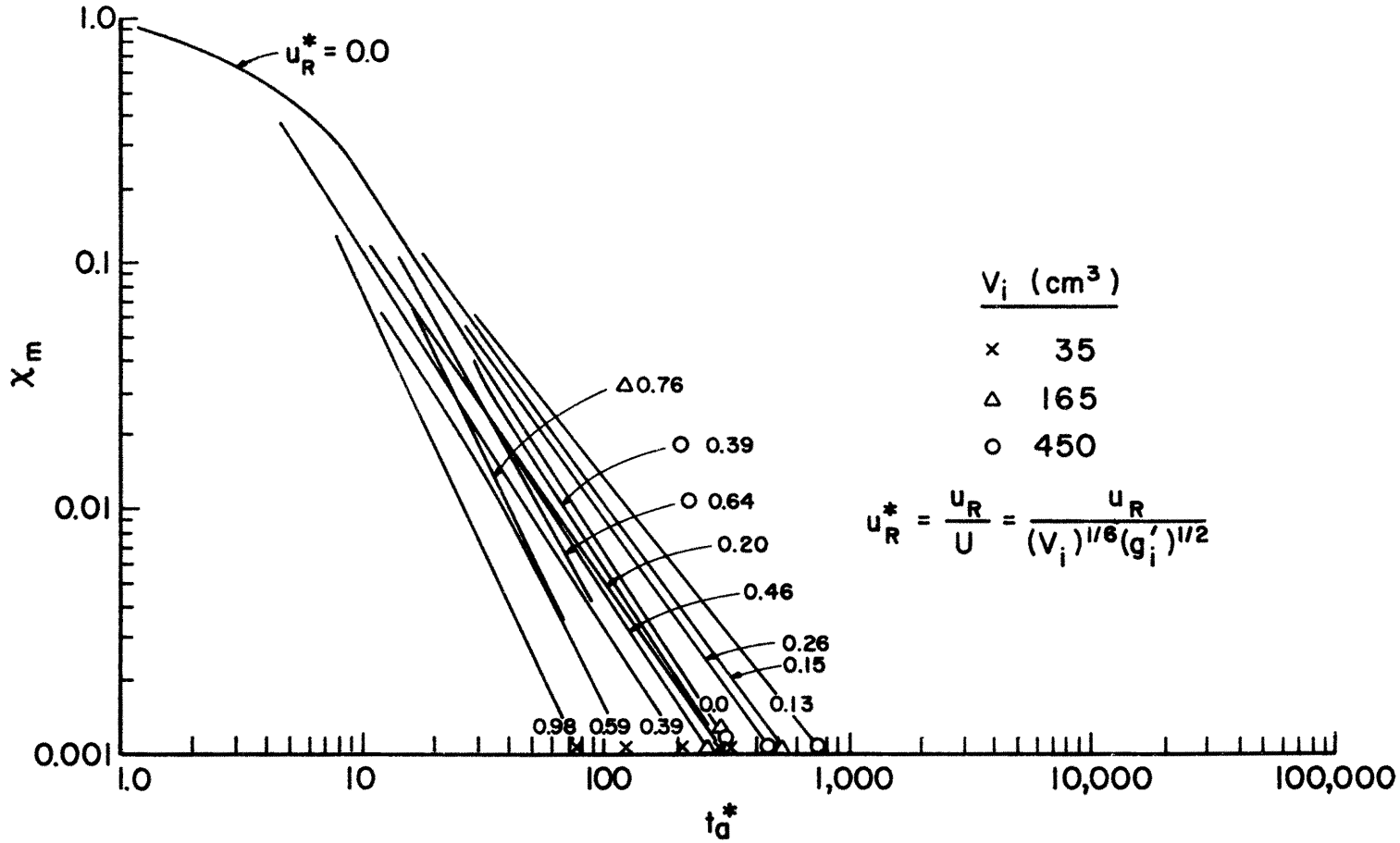

Figure 29. Cloud Dilution: χ_m vs t_a^*, $u_R \geq 0$ m/s

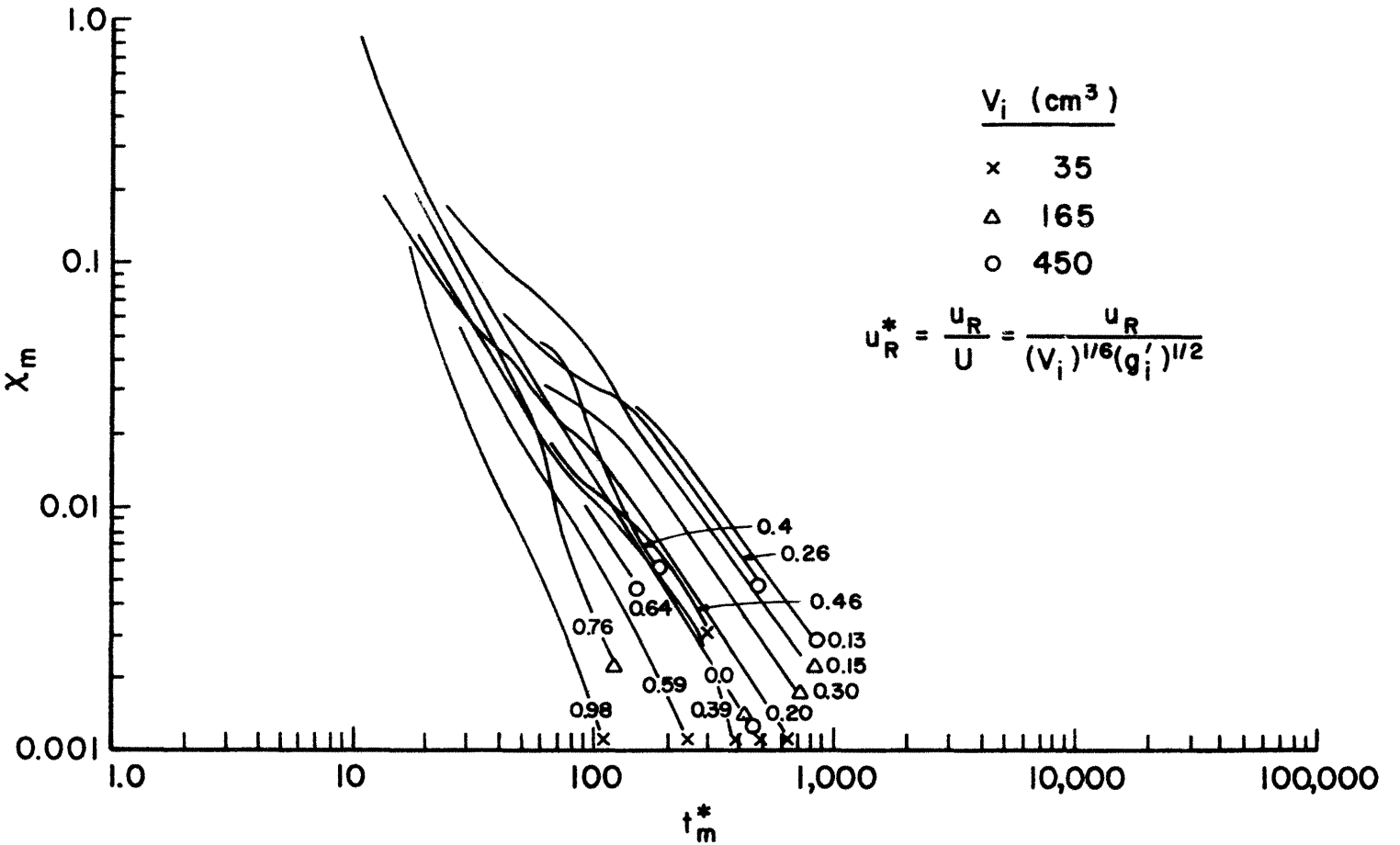

Figure 30. Cloud Dilution: χ_m vs t_m^*, $u_R \geq 0$ m/s

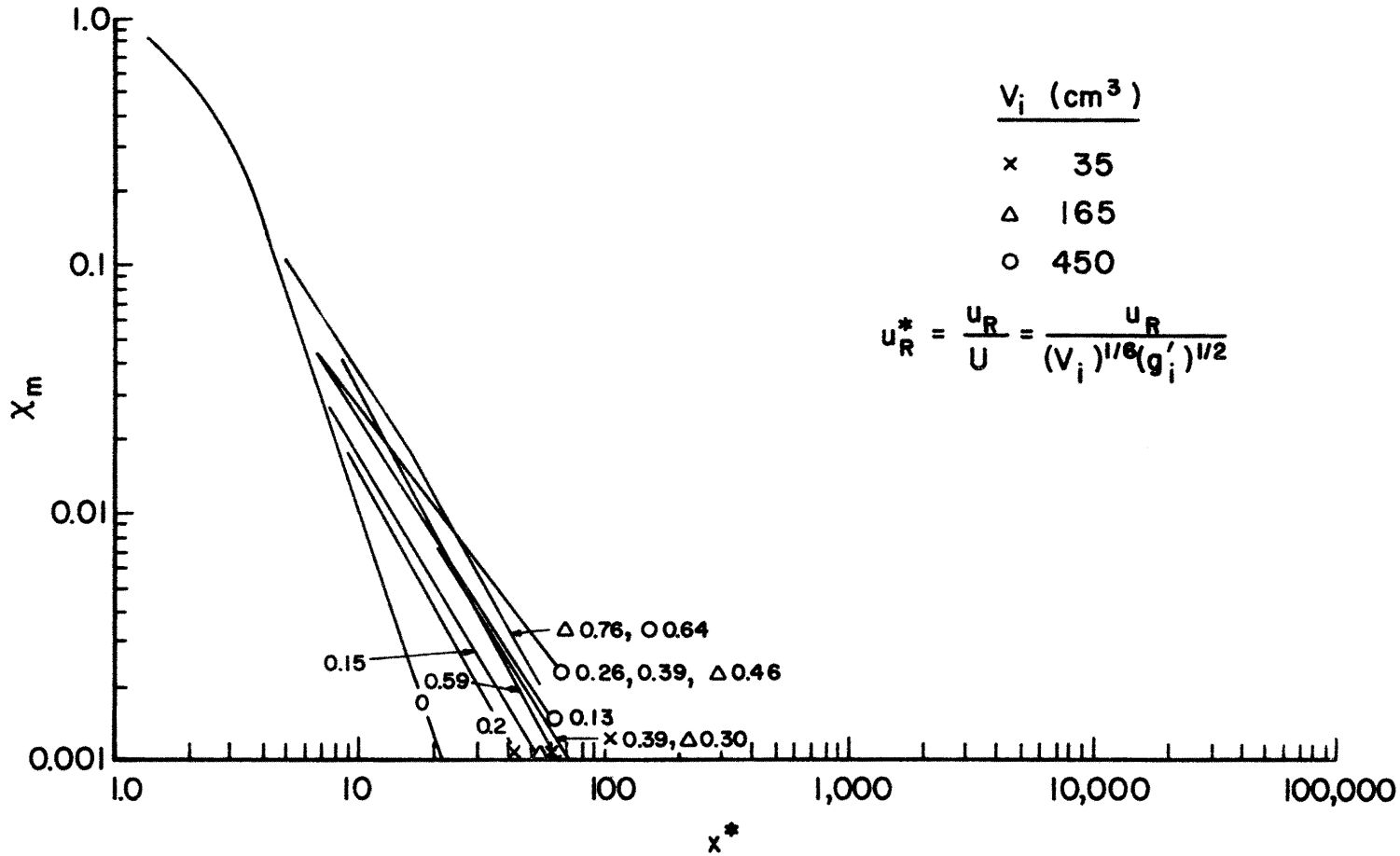

Figure 31. Cloud Dilution: χ_m vs x^*, $u_R \geq 0$ m/s

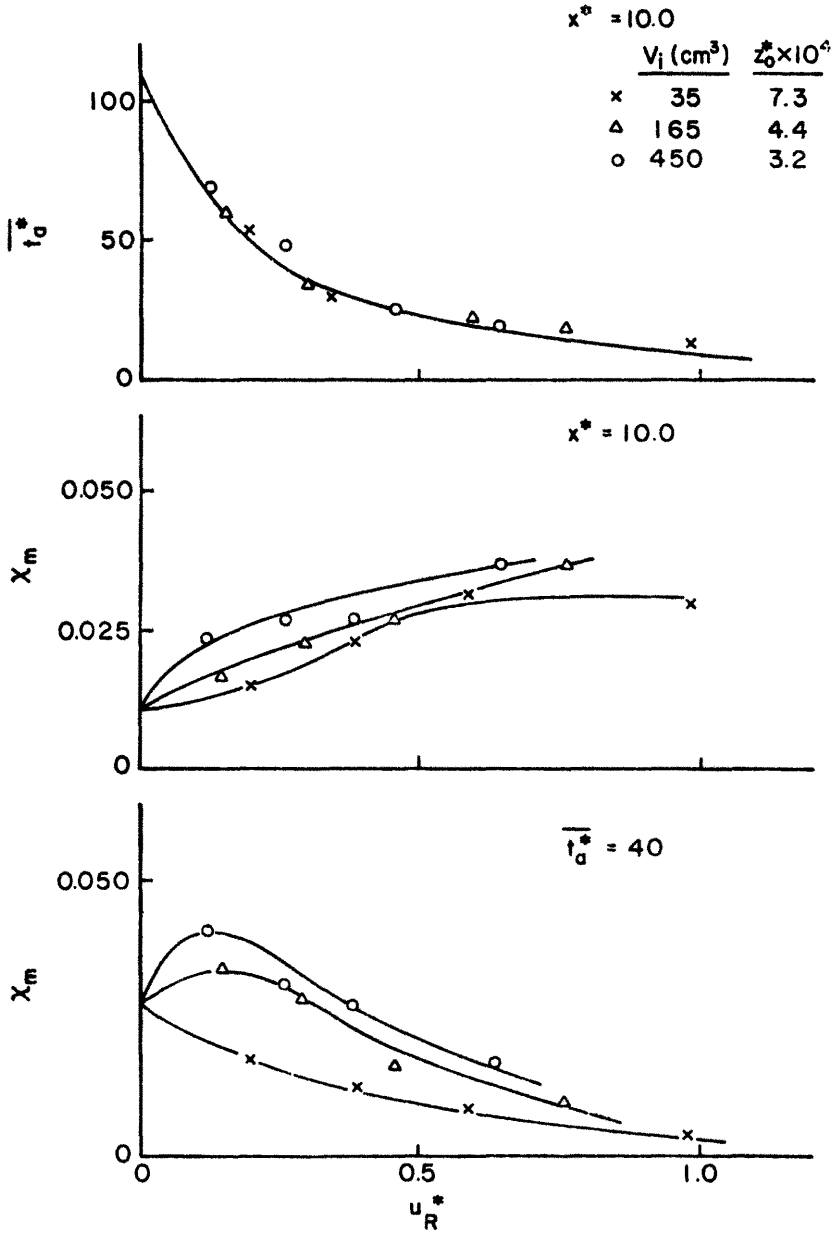

Figure 32. Variation of Arrival Time, t_a^*, and Concentration, χ_m, With Velocity, u_R^*

region the cloud is still governed by gravitational dynamics alone. Figure 33, 34, and 35 display vertical profiles taken at locations between $x^* = 2.5$ to 20. Beyond $x^* = 5$ the effects of source size and wind speed are noticeable. Higher wind speeds generally result in higher concentrations, but even higher speeds reduce concentrations. As wind shear increases there is also a tendency for the associated background turbulence to mix gases to distances further from the wall. Vertical profile shape varies; however, there is a noticeable tendency to pass from exponential, to Gaussian, and then to an elevated nose profile as velocity increases.

Ground Level Trajectories

Ground level cloud trajectory plots are presented in Figures 36 through 39. x^* is plotted versus t_a^*, t_m^*, and t_d^*. In Figures 36a, 37a, 38a, and 39a concentration profiles are overlayed on the trajectory plot at three locations. This figure indicates how the cloud eventually becomes symmetric about cloud location. The gravity driven acceleration phase is apparent in Figures 36, 37, and 38; however, the characteristic sin curve is absent at $u_R = 1.0$ m/sec in Figure 39.

Rosenzweig (1980) predicted such characteristic trajectory shapes for dense gas clouds based on an one-dimensional unsteady vapor cloud model assuming no friction or entrainment. The vapor cloud starting from rest passes through two stages of flow development. Initially it quickly accelerates to the free stream velocity; subsequently, it drifts with the free stream velocity and spreads laterally with respect to the center. Rosenzweig found his analytical solutions in the assymptatic limit of large times approached each other regardless of whether the initial cloud is stationary or drifting.

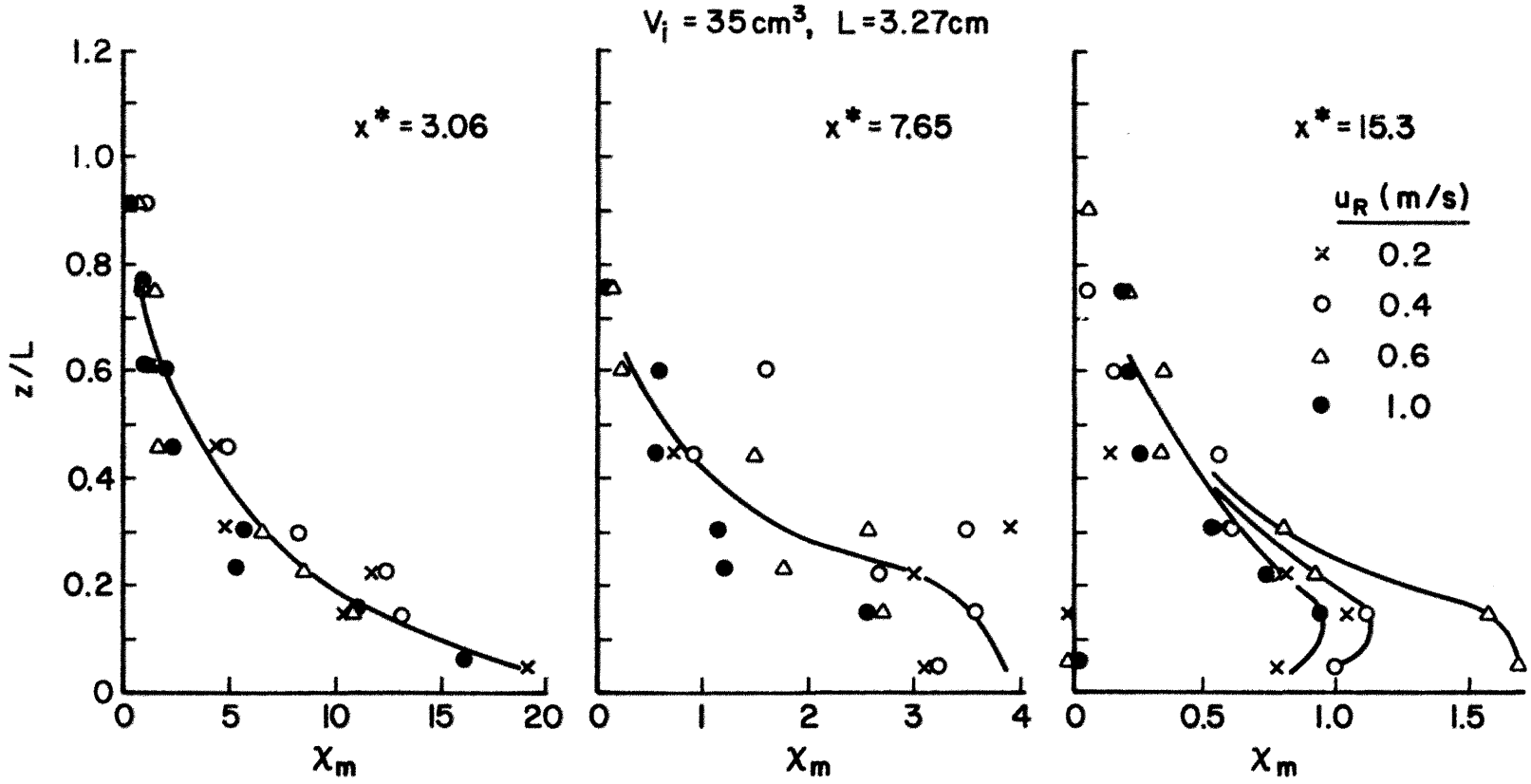

Figure 33. Vertical Concentration Profiles: V_i = 35 cm^3

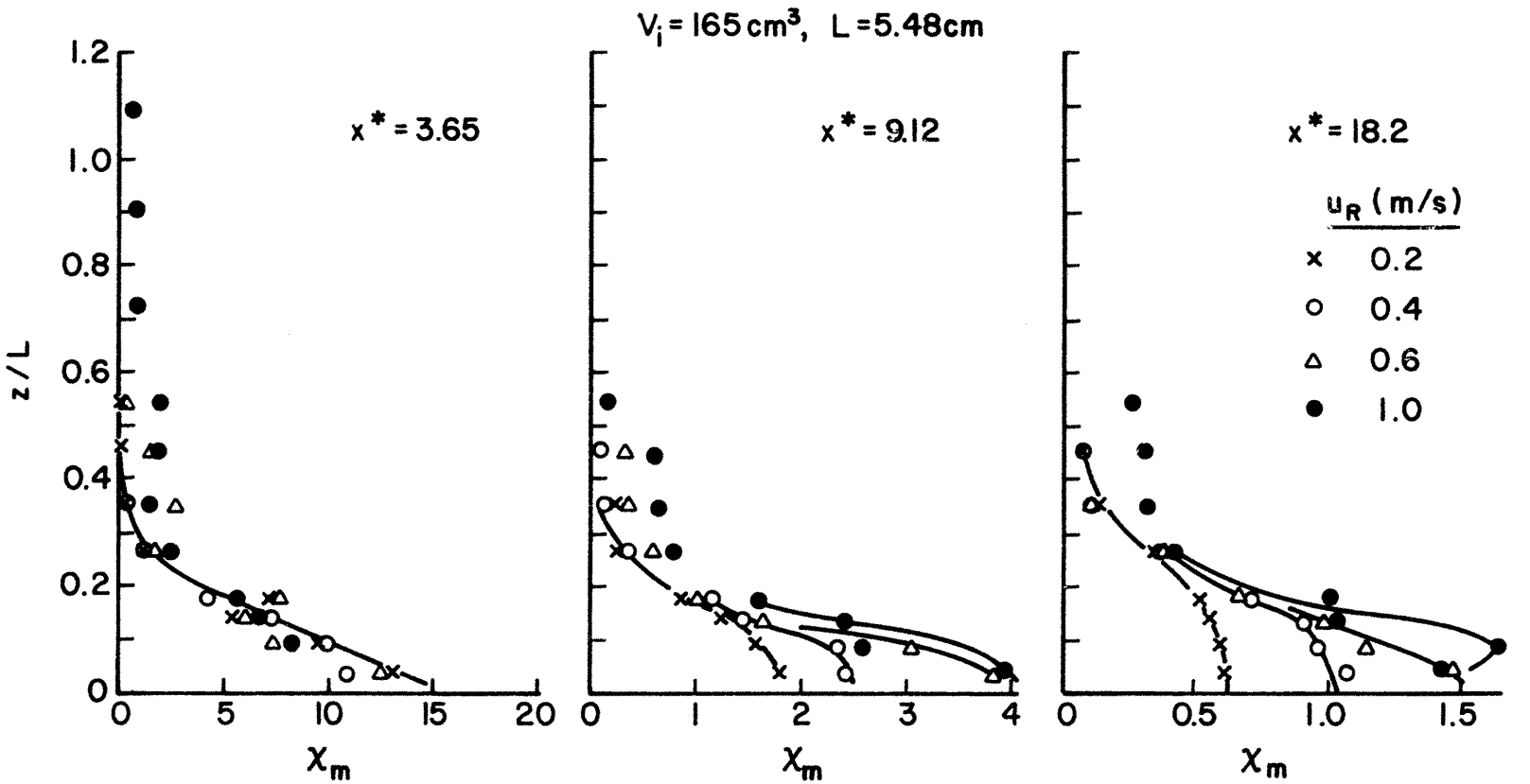

Figure 34. Vertical Concentration Profiles: V_i = 165 cm^3

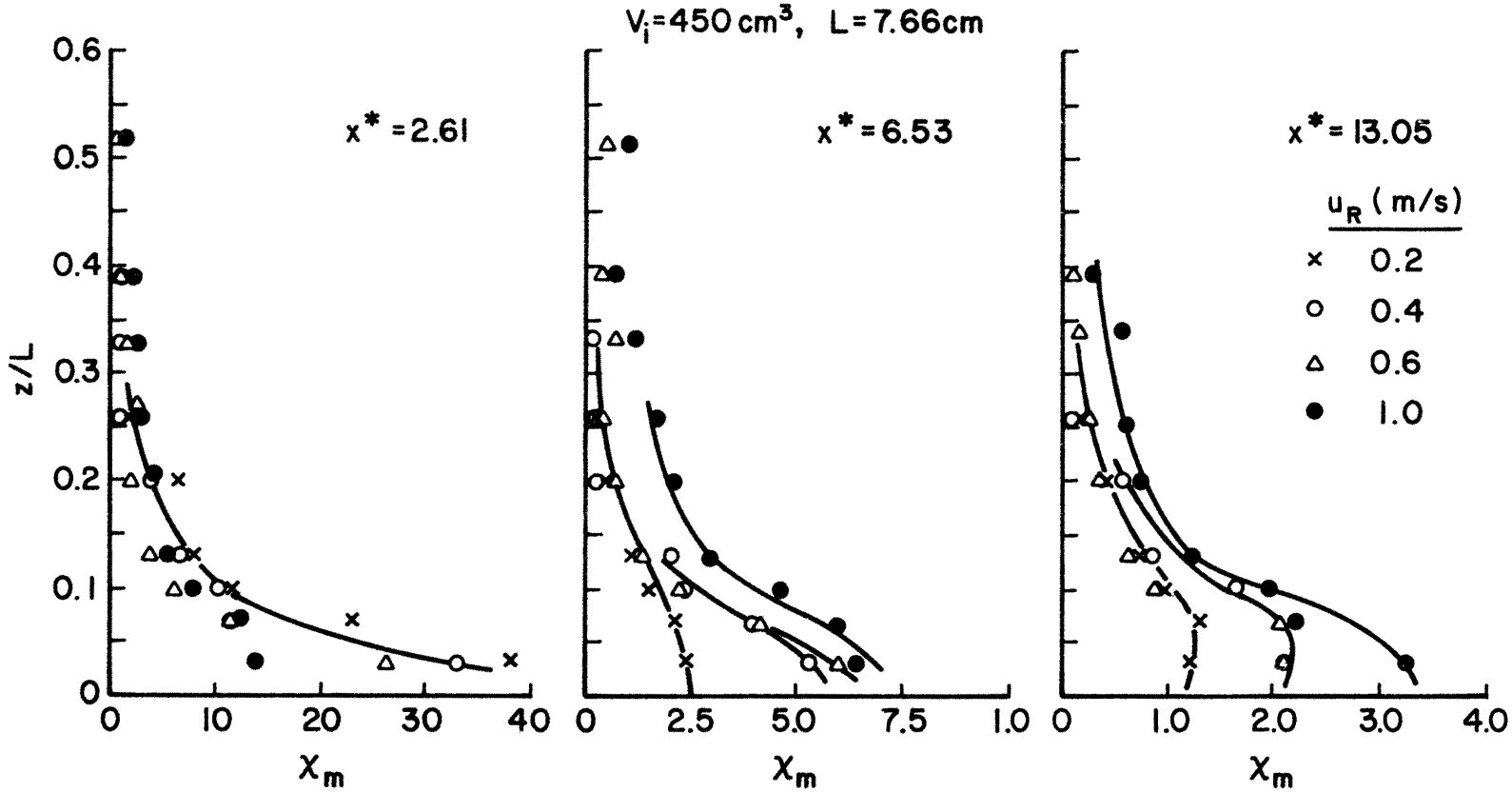

Figure 35. Vertical Concentration Profiles: V_i = 450 cm^3

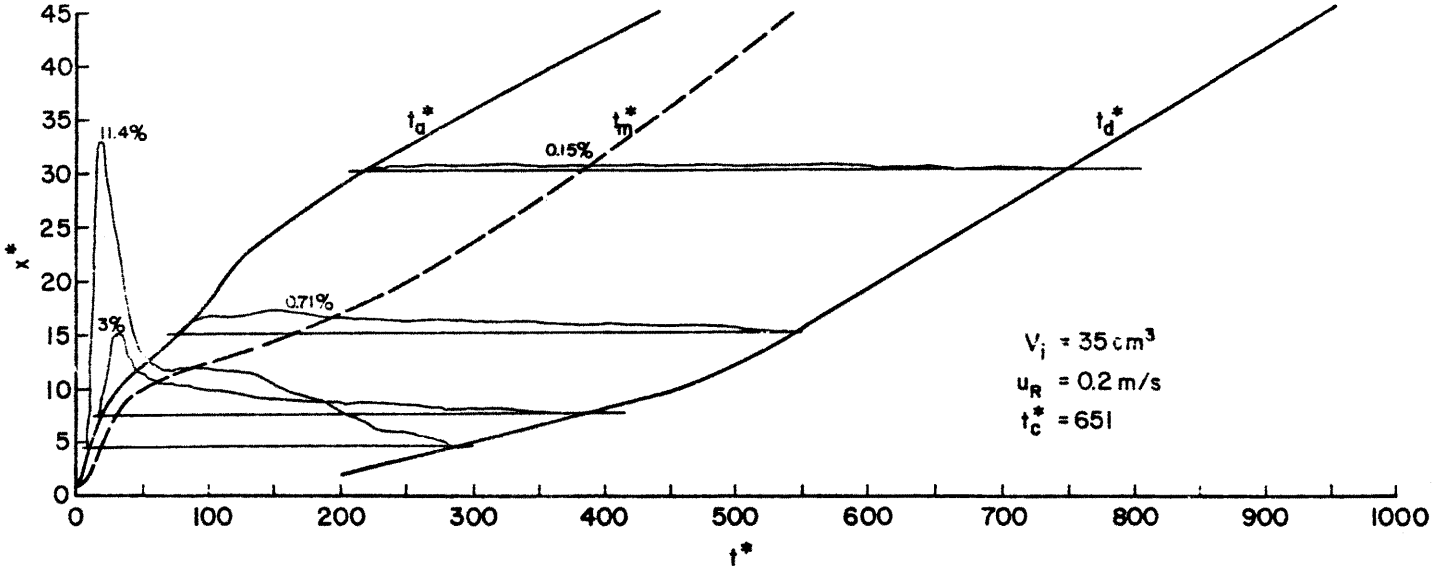

Figure 36a. Longitudinal Cloud Growth versus t^*, u_R = 0.2 m/s

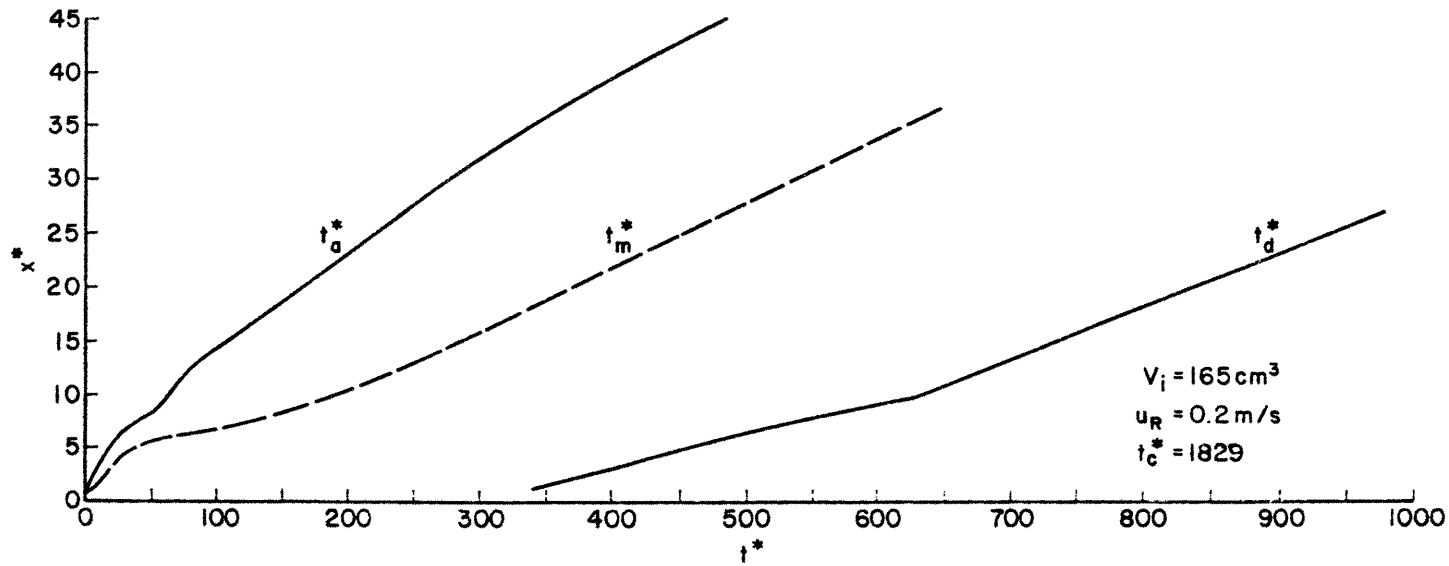

Figure 36b. Longitudinal Cloud Growth versus t^*, u_R = 0.2 m/s

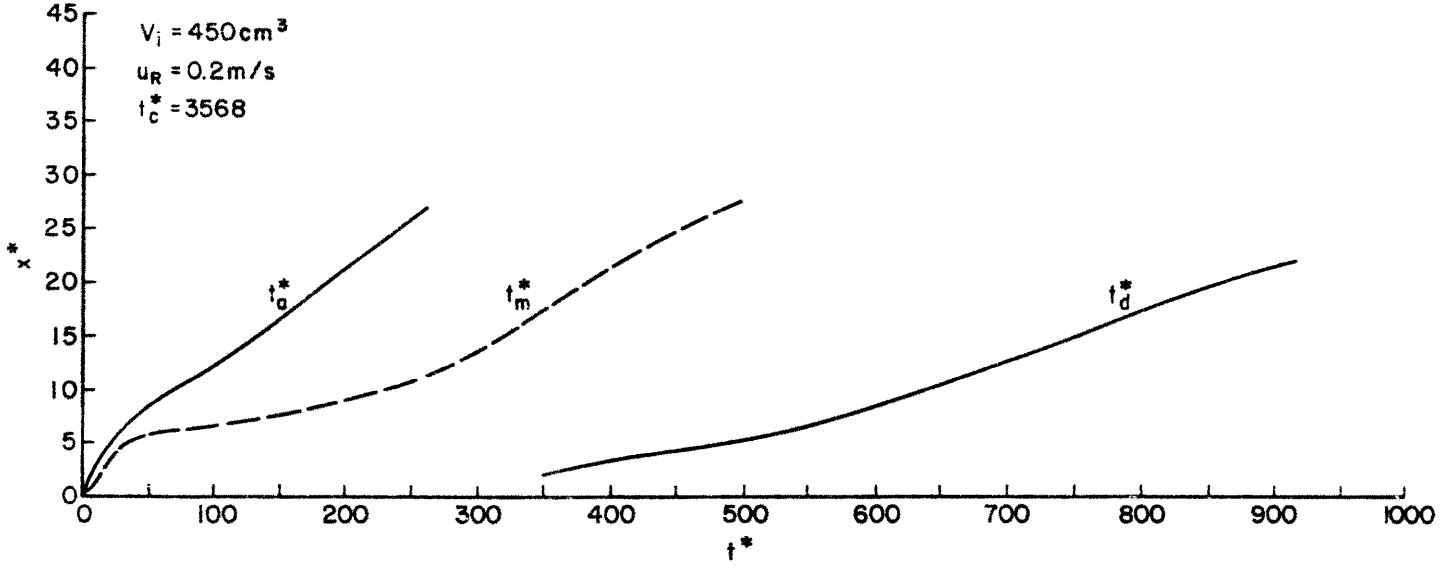

Figure 36c. Longitudinal Cloud Growth versus t^*, u_R = 0.2 m/s

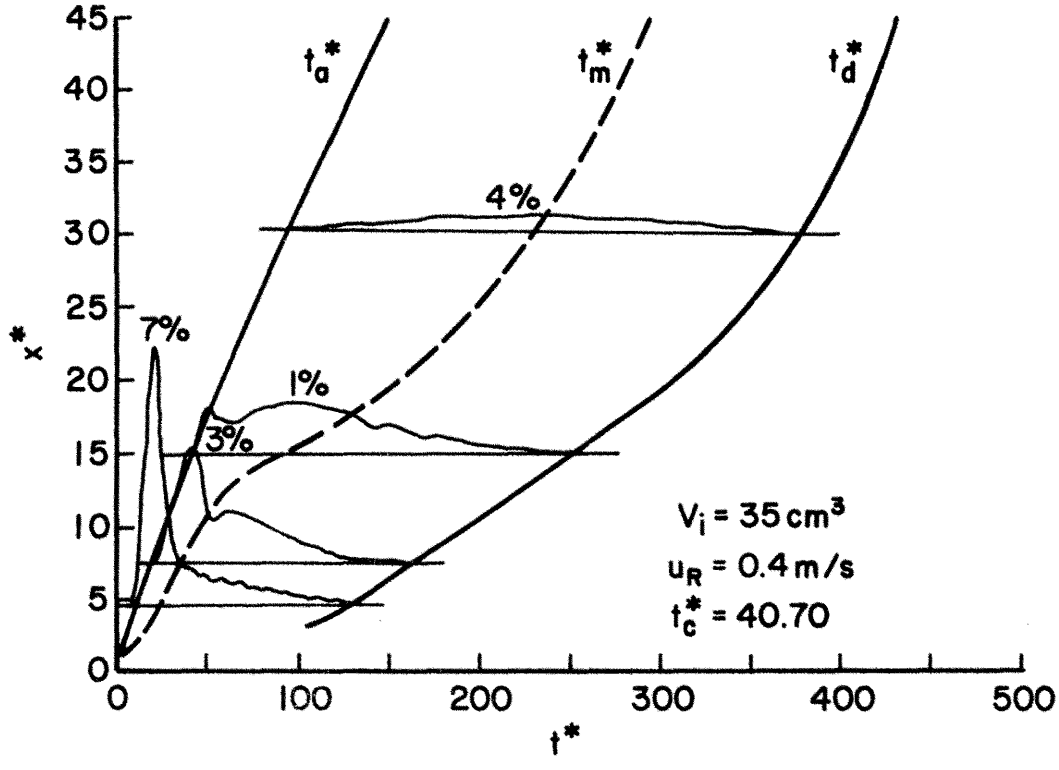

Figure 37a. Longitudinal Cloud Growth versus t^*, u_R = 0.4 m/s

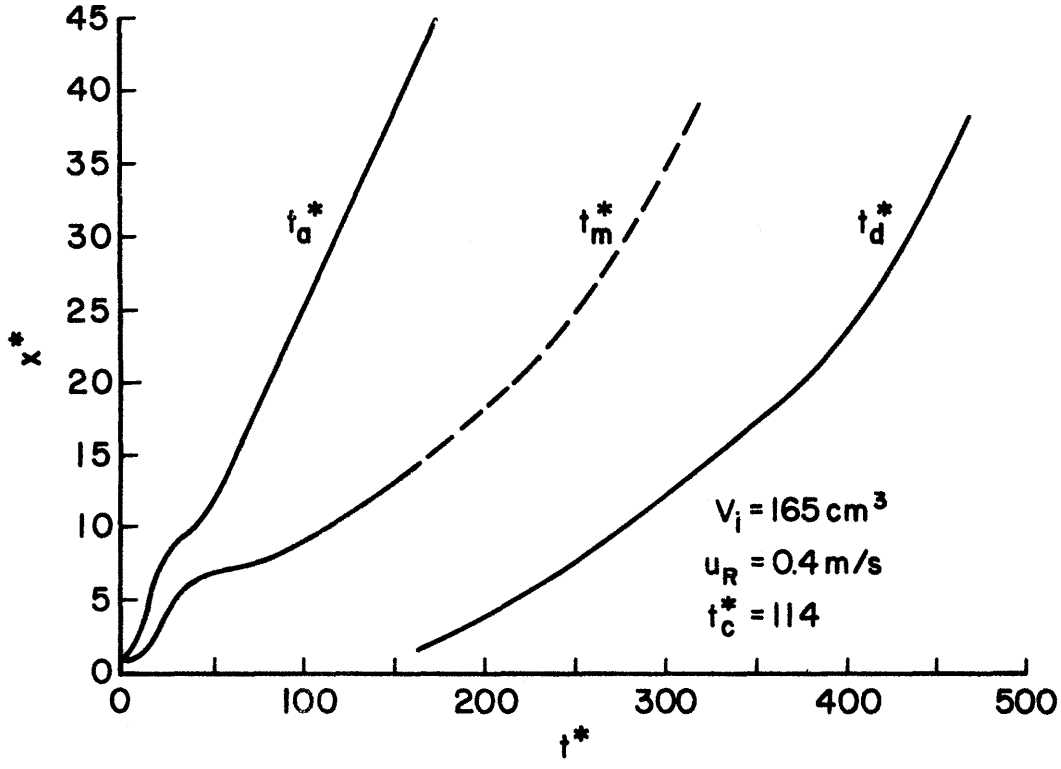

Figure 37b. Longitudinal Cloud Growth versus t^*, u_R = 0.4 m/s

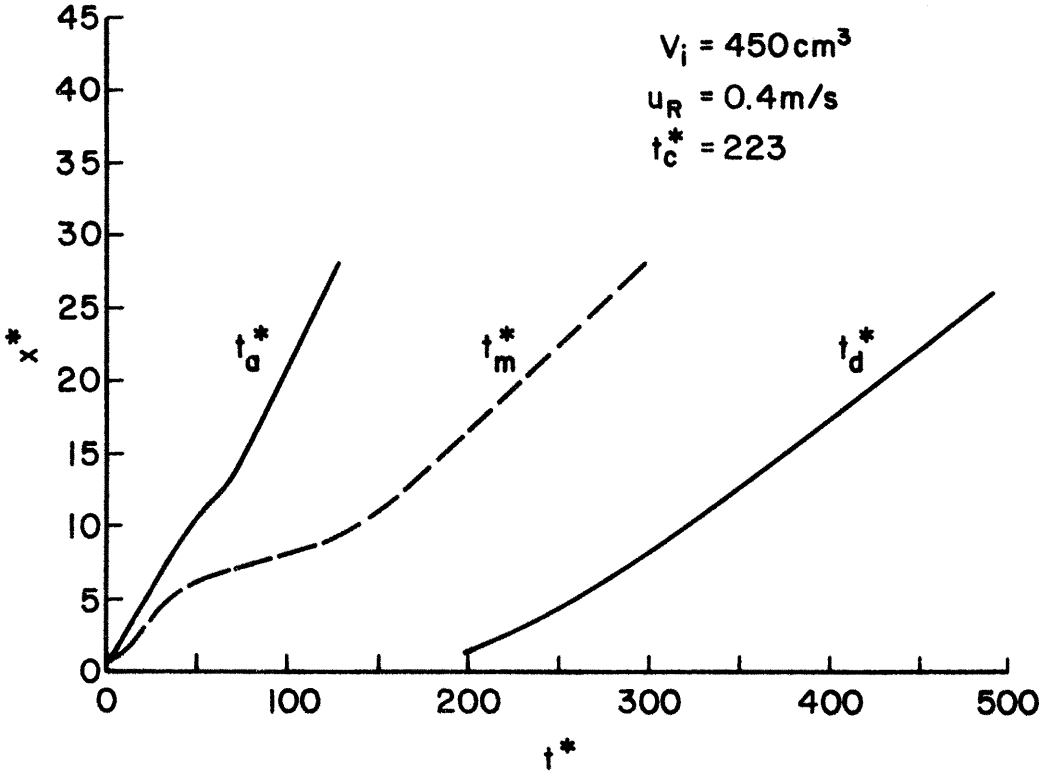

Figure 37c. Longitudinal Cloud Growth versus t^*, u_R = 0.4 m/s

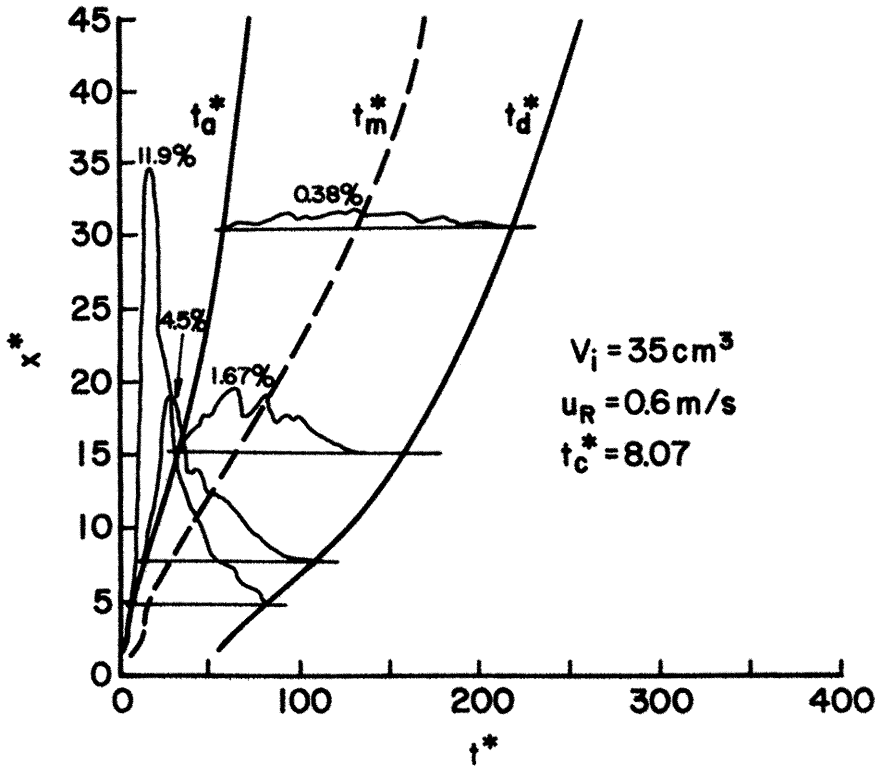

Figure 38a. Longitudinal Cloud Growth versus t^*, u_R = 0.6 m/s

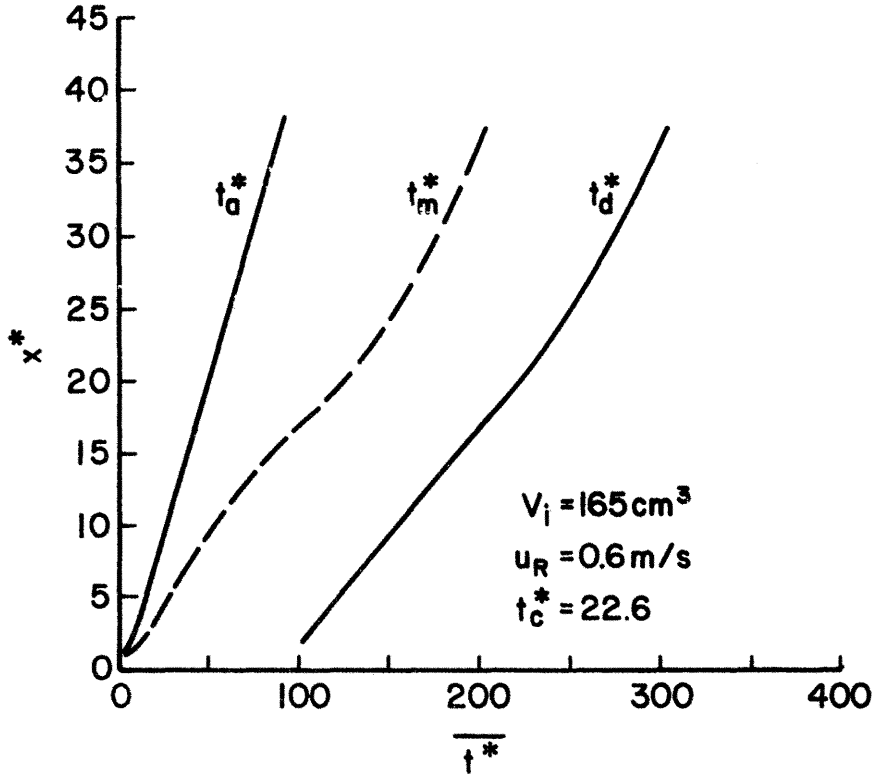

Figure 38b. Longitudinal Cloud Growth versus t^*, u_R = 0.6 m/s

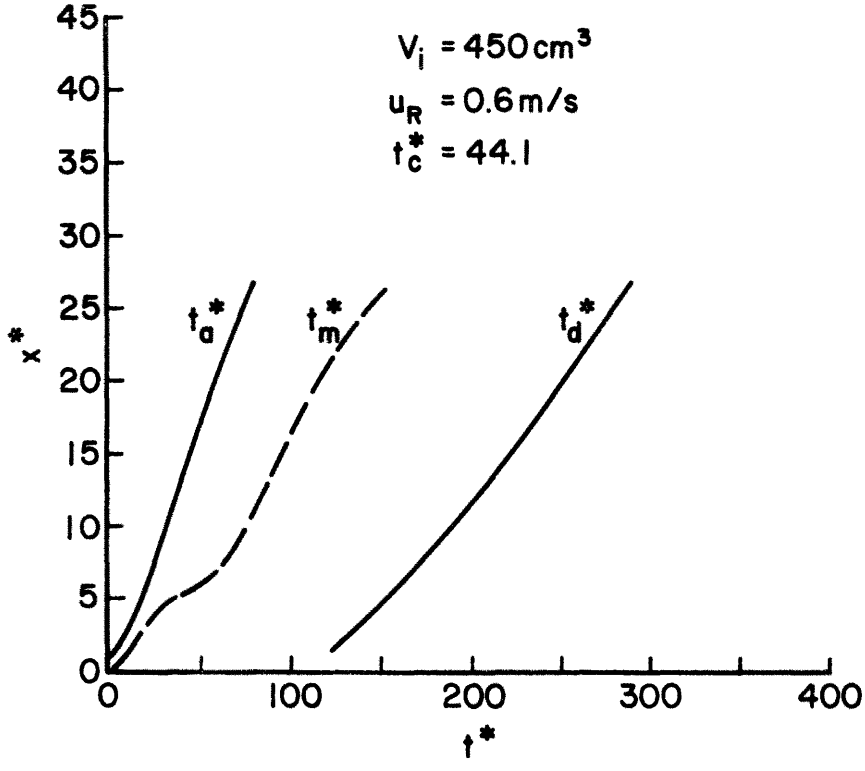

Figure 38c. Longitudinal Cloud Growth versus t^*, u_R = 0.6 m/s

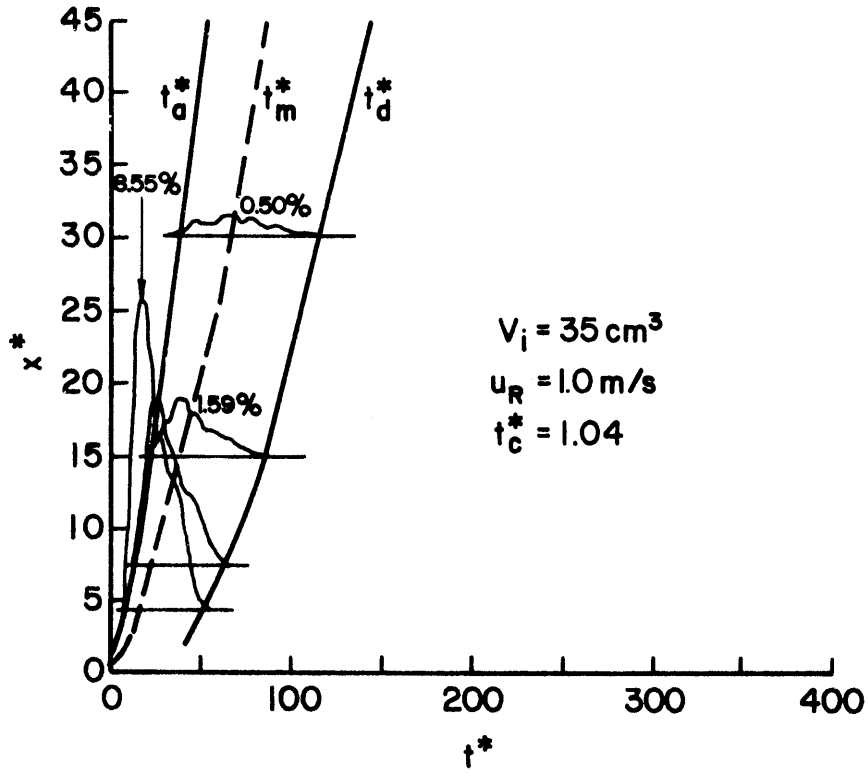

Figure 39a. Longitudinal Cloud Growth versus t^*, u_R = 1.0 m/s

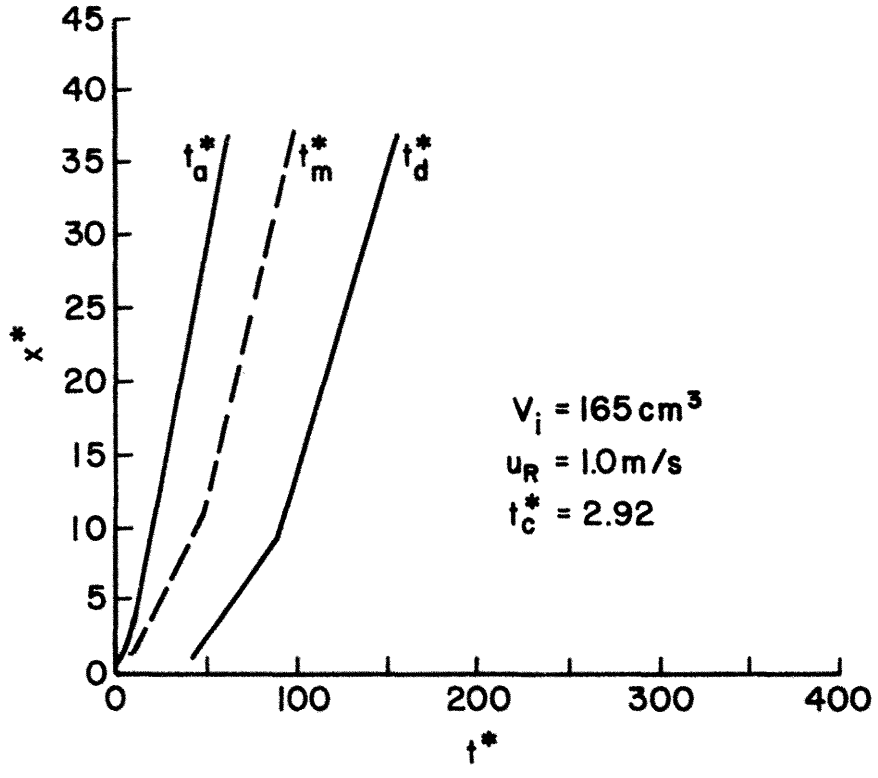

Figure 39b. Longitudinal Cloud Growth versus t^*, u_R = 1.0 m/s

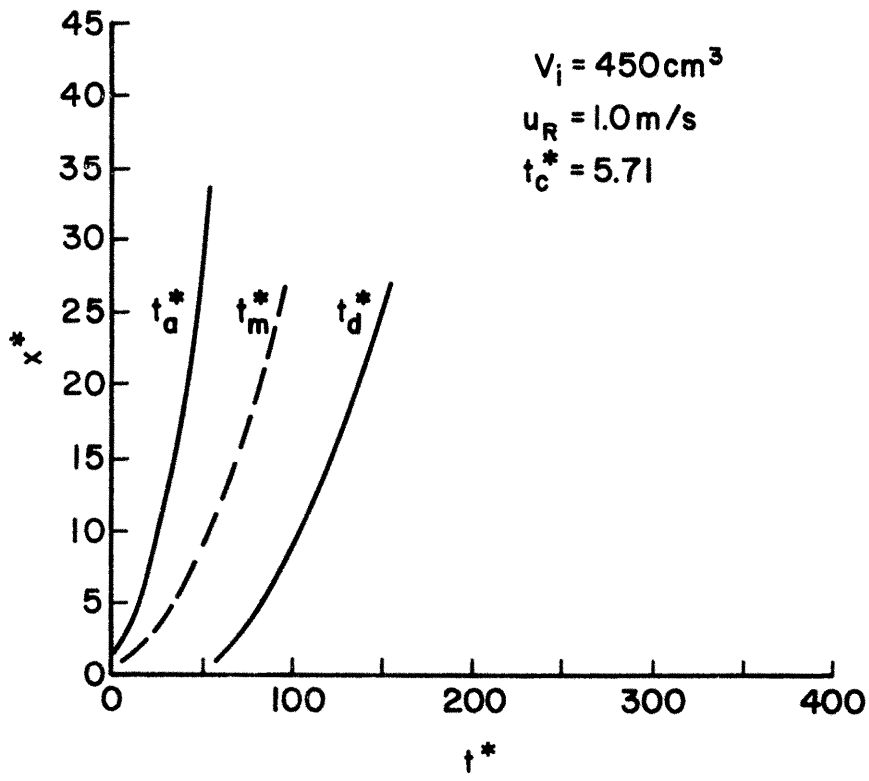

Figure 39c. Longitudinal Cloud Growth versus t^*, u_R = 1.0 m/s

He also suggested a characteristic acceleration time would be

$$t_c \sim \left\{\frac{g' A^{1/2}}{U_\infty^2}\right\}^{3/2} \left\{\frac{A^{1/2}}{U_\infty}\right\} \qquad (4\text{-}4)$$

where A is the initial area of cloud in the alongwind direction. In terms of dimensionless starred variables this would be

$$t_c^* \sim Ri^2 \qquad (4\text{-}5)$$

At the lowest wind speed, u_R = 0.2 m/sec, this expression results in characteristic acceleration times which are much too long; however, for all other cases the scale seemed to correlate with the end of the sin shaped displacement on the x^* vs t_m^* curves.

Assymptotic Scaling

In Section 2.2.2 an alternative set of scaling length and time scales were discussed. These scales may be suitable for describing plume behavior after long times, when the plume behaves in an assymptotic limit independent of initial release conditions. The variables modified concentration, $\tilde{\chi}_m$, and dimensionless distance, $\tilde{x}$, as defined in Equation (2-10) are used in Figure 40a to display all ground level data. Figure 40b plots $\tilde{\chi}_m$ versus $\tilde{t}_m$.

The concentration, $\tilde{\chi}_m$, varies both with distance, $\tilde{x}$, and Richardson number, Ri_*, for $\tilde{x} < 1.0$. Larger Ri_* values result in higher concentrations at a given distance. Overall, however, $\tilde{\chi}$ varies as $\tilde{x}^{1/2}$ for $\tilde{x} < 1.0$ and as $\tilde{x}^{1/3}$ for $\tilde{x} > 1.0$. There is some evidence for an assymptotic data collapse at distances greater than $\tilde{x} = 1.0$; however, data is limited, and actual concentrations measured are less than 0.5%. Plots of $\tilde{\chi}$ versus $\tilde{x}/(-\ln \tilde{z}_o)$ were also prepared, however there was no

significant improvement in correlation even though $\tilde{z}_o$ varies by an order of magnitude.

Comparison calculations made using the model of Fay and Ranck (1981)* produced concentrations about four times higher than measured, but similar decay rates and Ri_* variation. Using an entrainment constant, $C_2 \simeq 2.5$, rather than the author's value of 0.5 improves the comparison. The value 2.5 corresponds to magnitudes used in Section 5.1 of this report when comparing data against a simple box model analysis.

4.3.4 Behavior of Transient Neutral Density Volume Source Releases

A near-neutral volume source of traceable gas was created by mixing 80% Helium and 20 % Freon-12. This mixture was released from the $V_i = 35\ cm^3$ cup at two wind speeds, $u_R = 0.2$ and 0.6 m/s. The resultant behavior of these clouds are included in Table 14. There is no initial acceleration period due to cloud density; however, there is a lag in cloud movement as the background flow accelerates the cloud to its own velocity field.

Summarizing one finds that assymmptotically

$$x \sim t_a^{3/2},$$

$$x \sim t_m^{3/2},$$

$$\chi \sim t_a^{-4/3},$$

$$\chi \sim t_m^{-2}, \text{ (or for large } t_m \text{) } \sim t_m^{-3}, \text{ and}$$

$$\chi \sim x^{-4/3}.$$

Since $g' = 0$, these clouds cannot be scaled in the same manner as previously.

---

* Equations used were Fay and Ranck (1981) equations (2.37) and (2.39) with $C_2 = 0.5$, $\gamma = 2\pi^{1/2}$, $\beta = 0.4$, and $\tilde{z}_o = 10^{-5}$ for $500 < Ri_* < 25{,}000$.

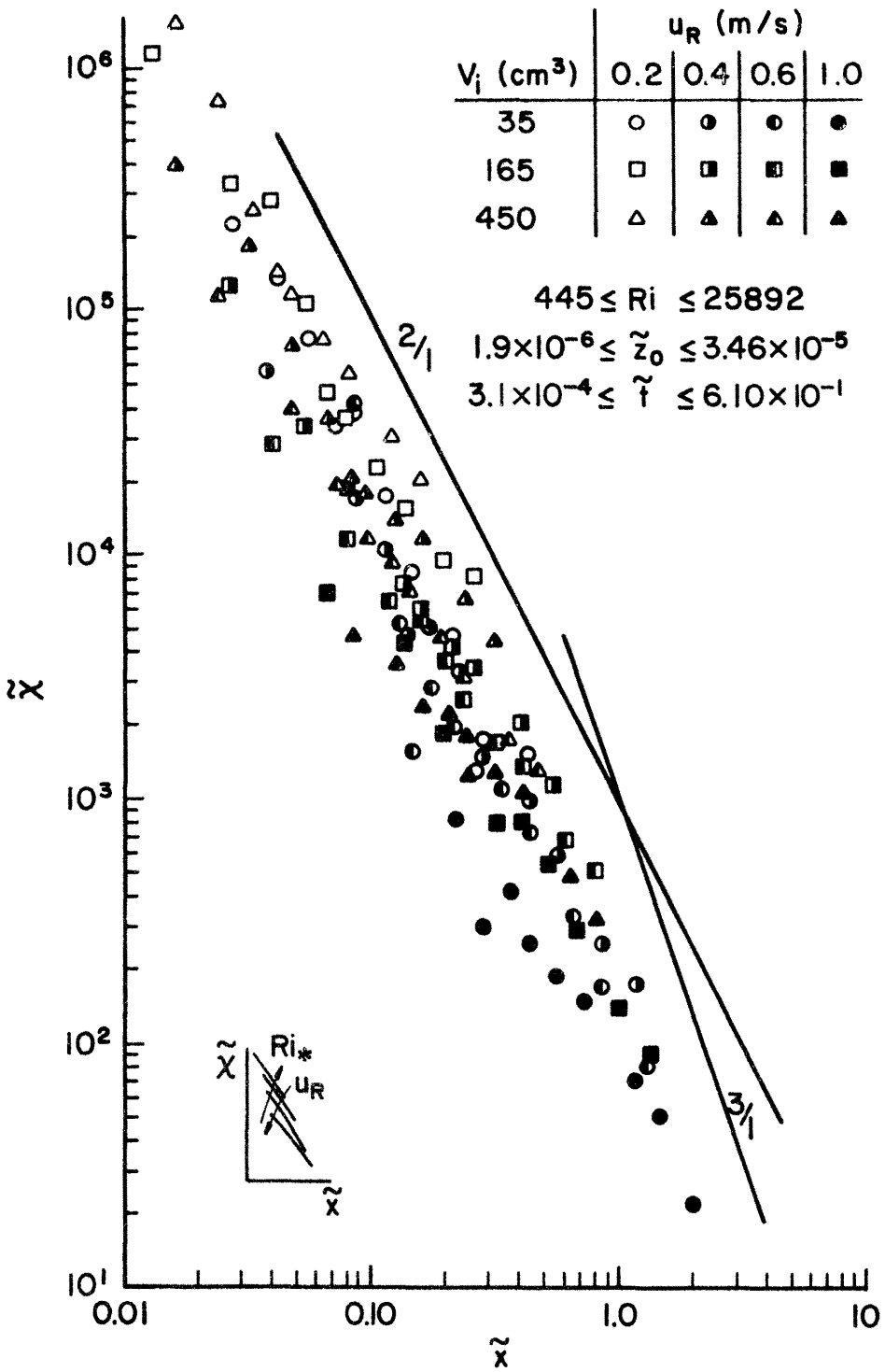

Figure 40a. Modified Concentration, $\tilde{\chi}$, versus Dimensionless Distance, $\tilde{x}$

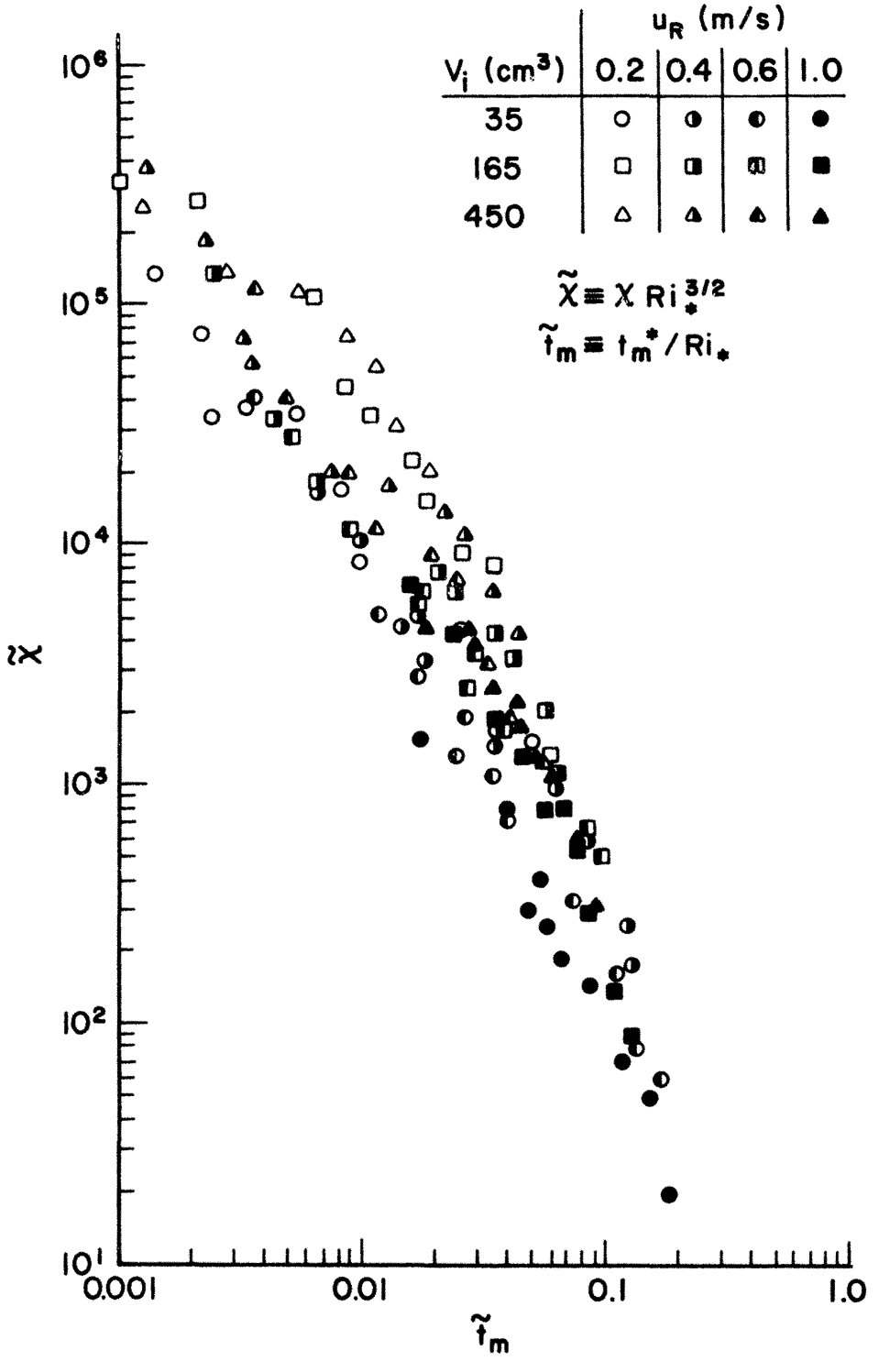

Figure 40b. Modified Concentration, $\tilde{\chi}$, versus Dimensionless Time to Maximum Concentration, $\tilde{t}_m$

Yang and Meroney (1972) also studied instantaneous volume releases of neutral gases in boundary layers. They presented a set of relations based on Lagrangian similarity theory for plume behavior. The theory suggests the appropriate time scale is $T = V_i^{1/3}/u_*$ and $L = V_i^{1/3}$. A dimensionless time will be defined as $\tilde{t} = t/T = t^*/Ri_*^{1/2}$. Relevant expressions are

$$\chi = 0.2979/\tilde{t}^3 \qquad \text{Point Source} \tag{4-6}$$

$$\chi = 0.5469 \text{ erf } (.4828/\tilde{t})/\tilde{t}^2 \tag{4-7}$$

Finite width line source where $w^* = 0.683$

$$x_a^* = \frac{1}{k}\tilde{t} \ln\left[1+\frac{k\tilde{t}}{\tilde{z}_o e^{\gamma+1}}\right] + 2a\tilde{t} + 1 \tag{4-8}$$

$$x_m^* = \frac{1}{k}\tilde{t} \ln\left[1+\frac{k\tilde{t}}{\tilde{z}_o e^{\gamma+1}}\right] - \frac{a}{2}\tilde{t} + 1 \tag{4-9}$$

$$x_d^* = \frac{1}{k}\tilde{t} \ln\left[1+\frac{k\tilde{t}}{\tilde{z}_o Re^{\gamma+1}}\right] - 6a\tilde{t} - 1 \tag{4-10}$$

where $a = 1.5$ and $\gamma = 0.577$.

The data for both reference velocity conditions collapse together very well in terms of χ, x^*, and $\tilde{t}$. Figure 41 indicates cloud trajectories are accurately predicted by relations (4-8, -9, and-10). Relations (4-6) and (4-7) overpredict concentrations as noted in Figure 42. The theory does seem to predict the assymptotic behavior for $\tilde{t} > 1.0$. Since the analysis was for sources released over infinitisimally small volumes it would not be expected to correlate except in the limit as $\tilde{t}$ becomes large.

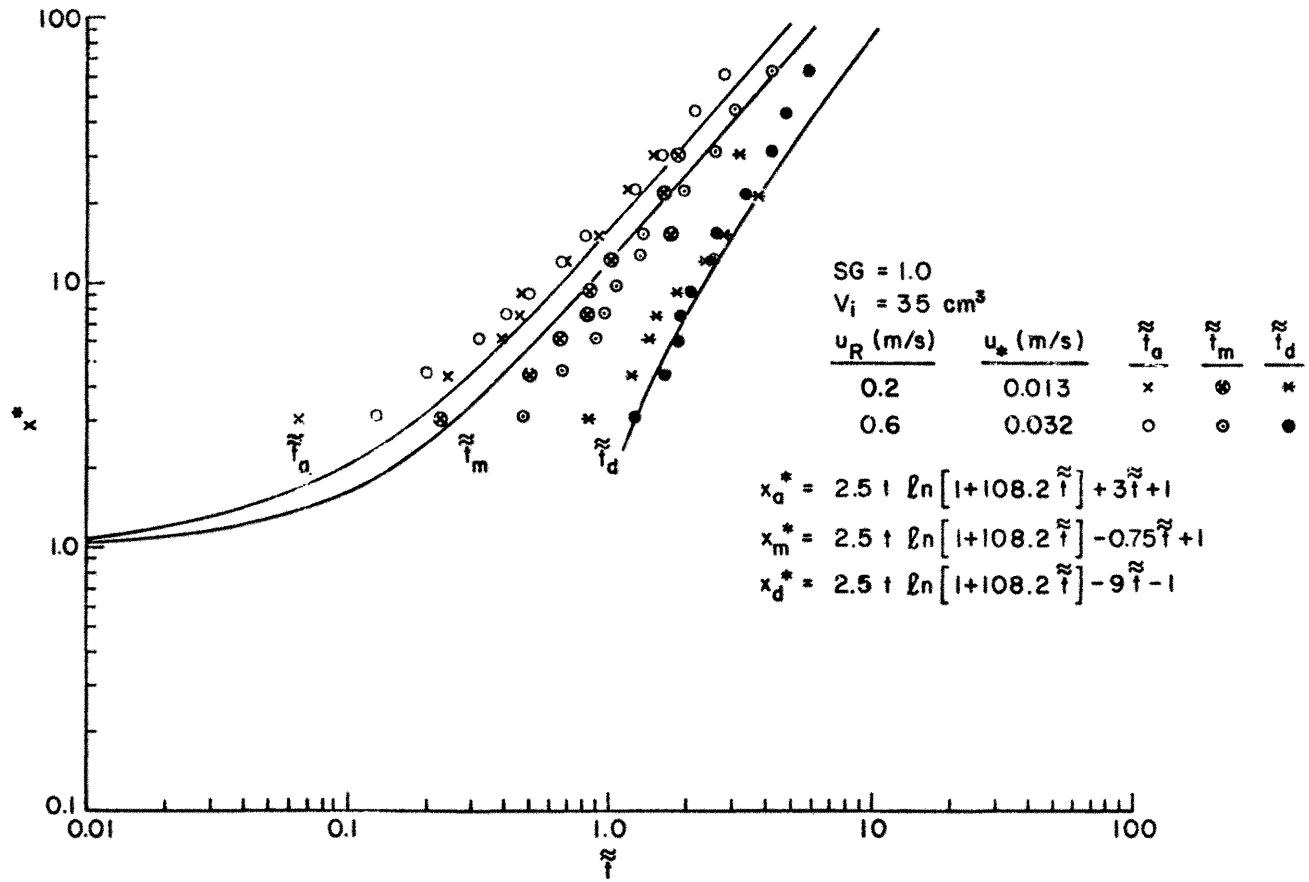

Figure 41. Longitudinal Cloud Growth versus Dimensionless Time Neutral Density Gas, $\tilde{t}$

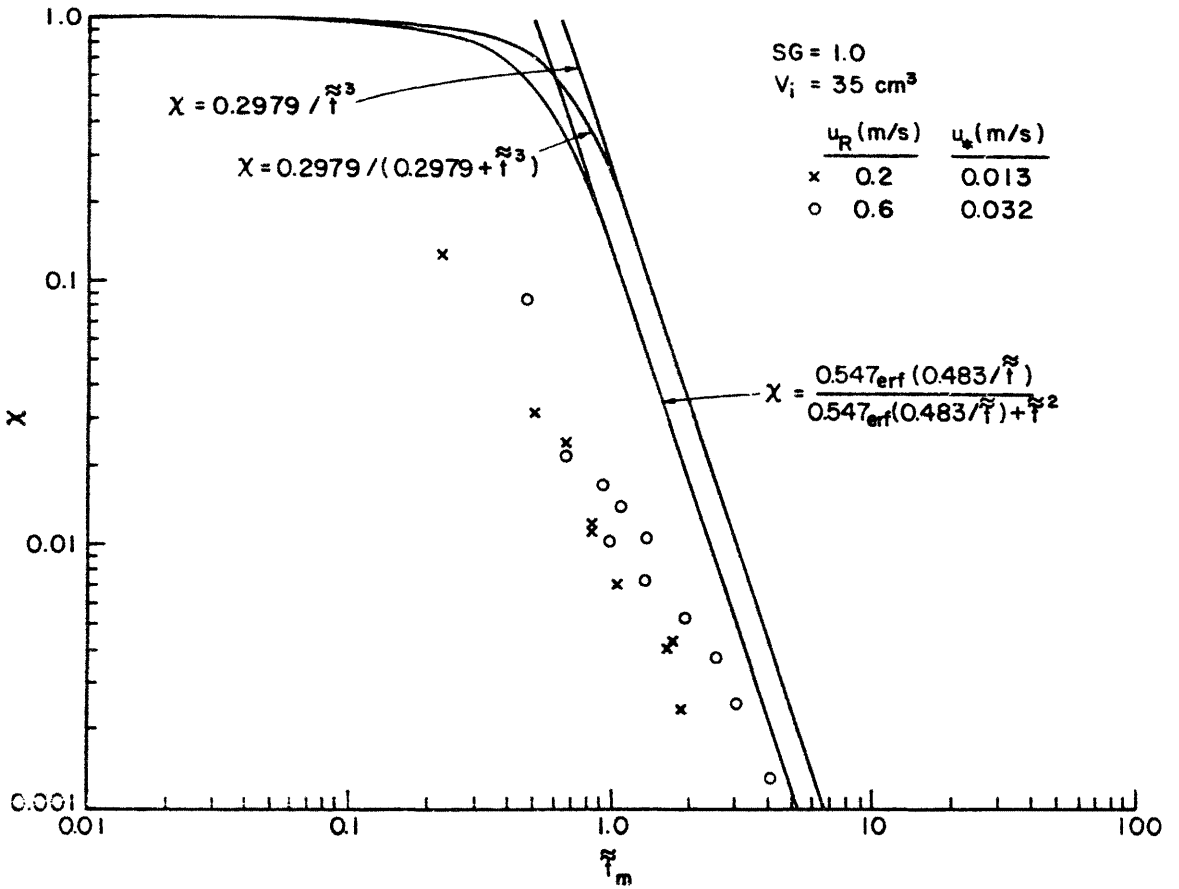

Figure 42. Cloud Dilution versus Dimensionless Time, $\approx t$, Neutral Density Gas

5.0 DISCUSSION OF DENSE GAS DISPERSION RESULTS

As noted in Section 1.2.3 the number of analytic and numerical models seems to exceed the sets of data to evaluate them. Most of these models do contain a common physical foundation, but differ on the entrainment mechanisms or constants chosen. A generalized box model will be used in Section 5.1 to specify preferred entrainment mechanisms based on comparison with the new data. Since the box model does not predict spatial variations within the cloud, a depth averaged slab model is presented in Section 5.2.

5.1 COMPARISON OF DENSE GAS DATA WITH NUMERICAL BOX MODEL

The box model described in Appendix A uses an energy equation to solve for cloud spread rate and an entrainment hypothesis to solve for cloud dilution. Advection of the cloud by the wind field is considered by integrating for transport by a fraction of the background wind speed. The model considers initial inertial effects by retaining the cloud density in advection terms. Model constants are tuned to fit the present data; however, examination of the following Table 15 suggests these values are consistent with other investigators.

5.1.1 Comparison Between Box Model and Near Dense Gas Cloud Results

Calculations with the box model were performed over the source volume, wind speed, and roughness conditions examined experimentally. The equivalent ranges of dimensionless parameters are (See Table 2): SG = 4.17, $450 < Ri_* < 26{,}000$ (also $Ri_* = \infty$), and $3.2 \times 10^{-4} < z_o^* < 7.3 \times 10^{-4}$. Alternatively the range of roughness is $2 \times 10^{-6} < \tilde{z}_o < 35 \times 10^{-6}$.

Cloud transport distance, x^*, is plotted versus arrival time, t_a^*, in Figure 43. The behavior is quite similar to the summarized experimental results found on Figure 27. In order to produce an initial period where spread is dominated by gravity effects no advection by the

Table 15

Box Model Constants Specified by Various Investigators

Author (Date)	α_1	C_r	C_Z	α_4	α_6	α_7	β_2
van Ulden (1974)	1.00	0.05	0.00	0.00	0.00	0.0	–
Germeles and Drake (1975)	$\sqrt{2}$	0.00	0.10	0.00	0.00	0.0	–
Picknett (1978)	0.94	0.82	0.00	0.00	0.15	–	–
van Ulden (1979)	1.40^{Δ}	0.00	0.00	0.00	0.00	0.0	–
Cox and Carpenter (1980)	1.00	0.60	0.00	2.00	0.36	0.0	–
Eidsvik (1980)	1.30	$\frac{0.5\ u_F^*}{u_F^*(0)}$	$\sim 0.00^{+}$	4.55	0.39	0.0	–
Lohmeyer et. al. (1981)	1.00	0.05	0.05	–	–	–	–
Fay and Ranck (1981)	1.00	0.00	0.00	0.50	2.50	0.0	0.40
Zeman (1982)	–	–	–	12.50	0.64	–	–
Present Results	$1.00^{\Delta\Delta}$	0.10	0.10	2.60	0.30	3.5	0.1–0.15

$\Delta_{\beta_1} = 1.0$

$\Delta\Delta_{\beta_1} = 0.9$

+ Uses α_4 and α_6 relation

wind was permitted before $t^* = 10$. This suggests there is a finite acceleration time required before the cloud drifts at background wind speeds. The variable t_c^* suggested by Rosenzweig (1980) discussed in Section 4.3.3 was not used because it consistently overpredicted acceleration times.

Cloud dilution, χ_m, is plotted versus arrival time, t_a^*, in Figure 44. The curves should be compared to experimental results found on Figure 29. Here the limitations of the box model become apparent. Due to the well mixed cloud (uniform internal properties) assumption the box model cannot reproduce the lower decay rates at low wind speeds and large cup sizes shown on Figure 29. The box model does produce the set of curves representative of higher mixing rates at the higher velocities. No effect of z_o^* is seen during the calculations. At the highest wind speeds dilution proceeds at long times as $\chi \sim t_a^{*-1/3}$.

Cloud dilution, χ_m is plotted versus dimensionless distance, x^*, on Figure 45. These curves may be compared with experimental data found on Figure 31. Only the results for $z_o^* = 7.3 \times 10^{-4}$ are shown. The other cup sizes overlap these results in a similar manner to that displayed during the experimental measurements. The box model does reproduce the occurrence of higher concentrations at a given dimensionless distance with increased wind speed. The box model results appear to approach a limiting decay rate of $\chi_m \sim x^{*-1/3}$ at very large times. This would be consistent with a final dispersion phase as expected for neutral gases where $x \sim u_R t$ and $\chi_m \sim t^{-1/3}$.

To illuminate the independent effects of Ri_* and z_o^* the box model results were plotted as shown on Figure 46. The comparable data is found on Figure 32. Note that the box model results are generally simi-

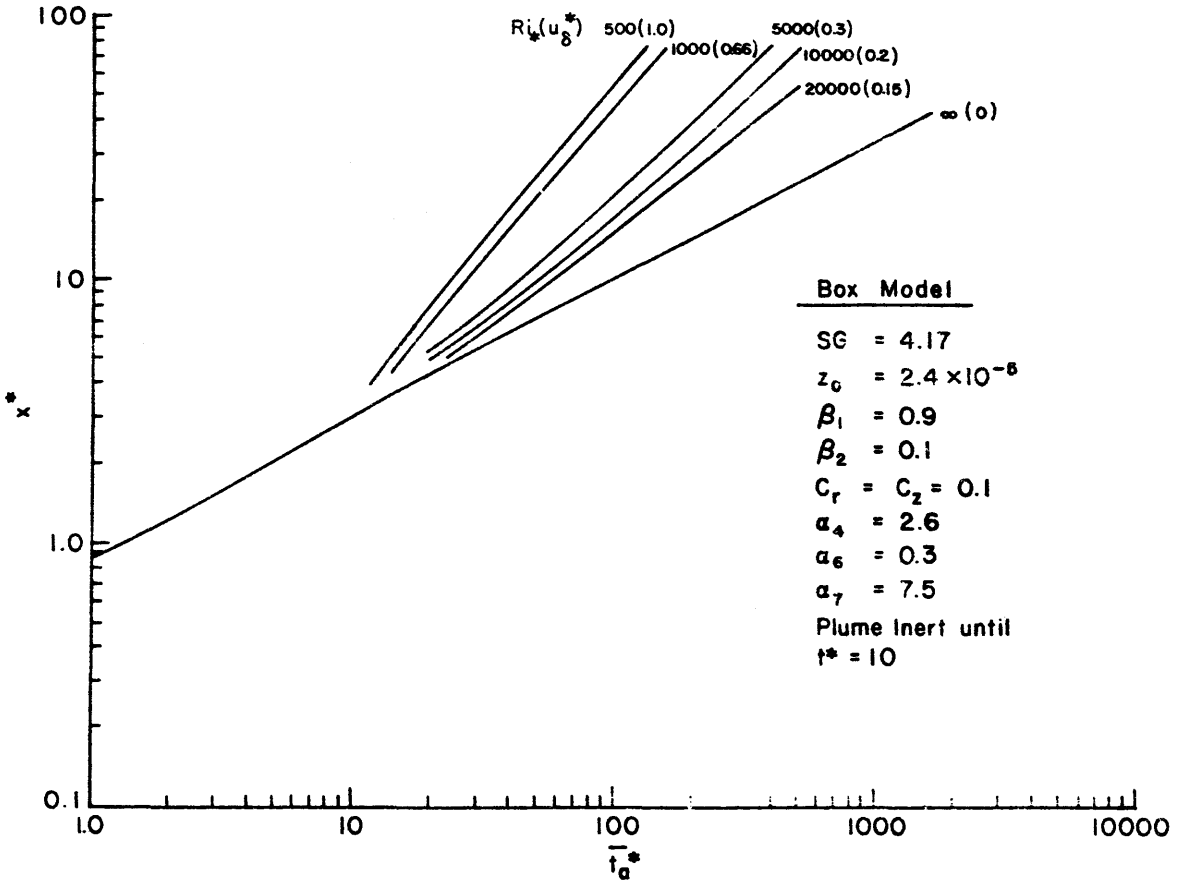

Figure 43. Distance, x^*, versus Arrival Time, t_a^*, $u_R \geq 0$, Box Model Results

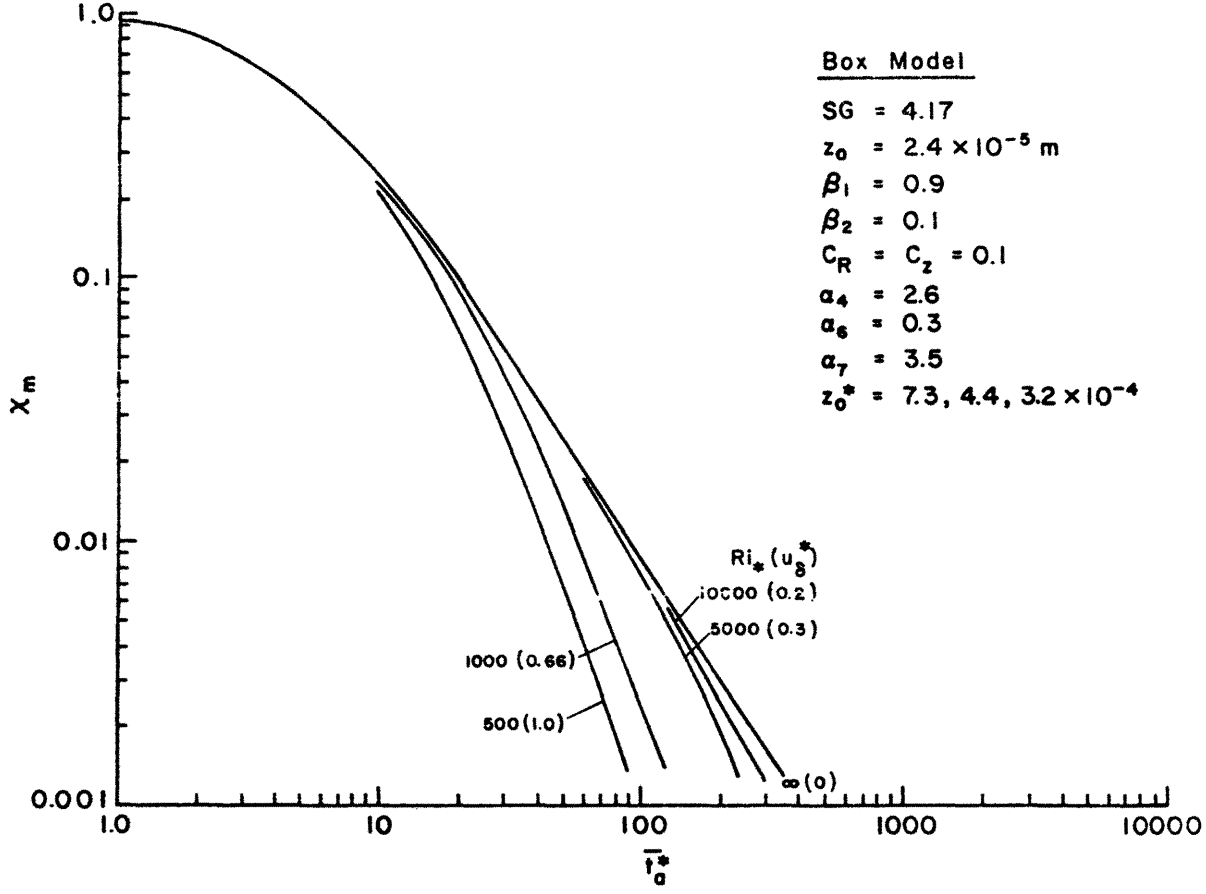

Figure 44. Cloud Dilution, χ_m, versus Arrival Time, t_a^*, $u_R \geq 0$, Box Model Results

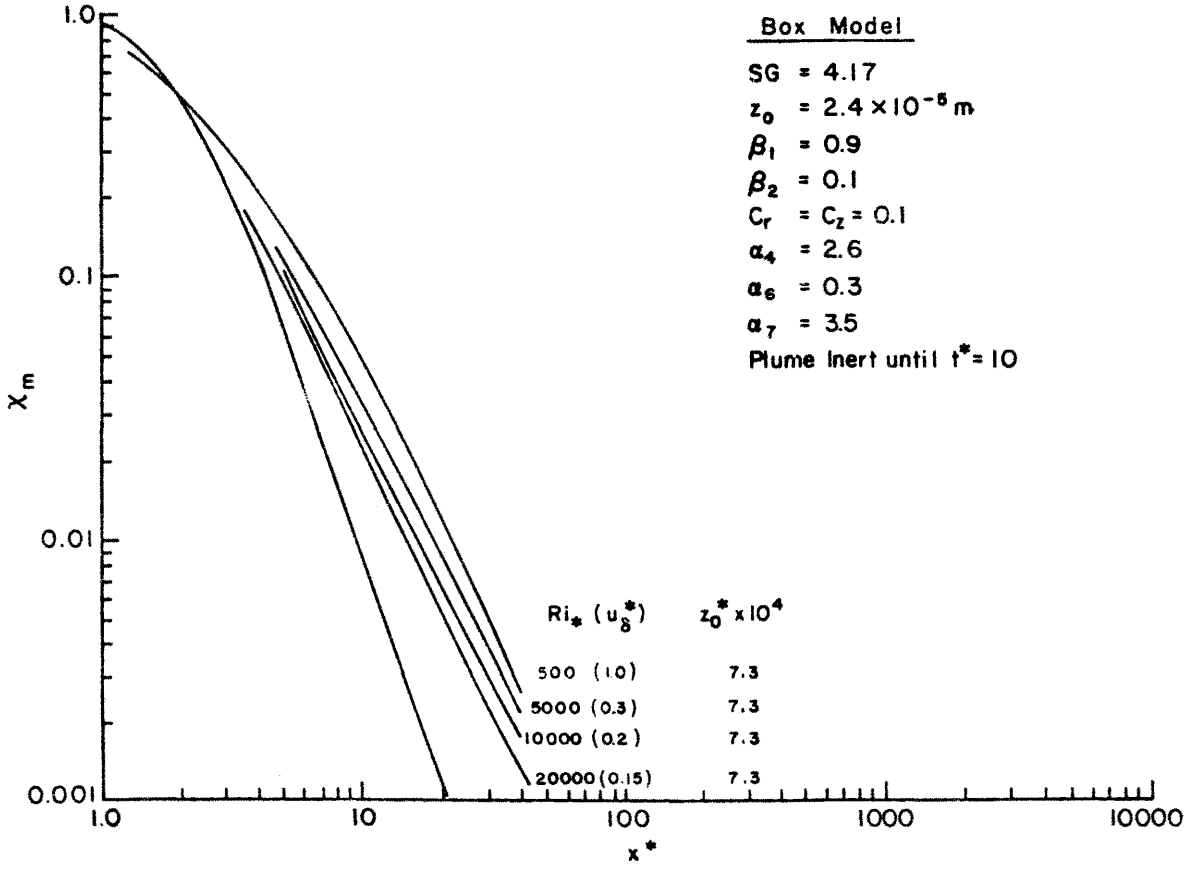

Figure 45. Distance, χ_m, versus Distance, x^*, $u_R \geq 0$, Box Model Results

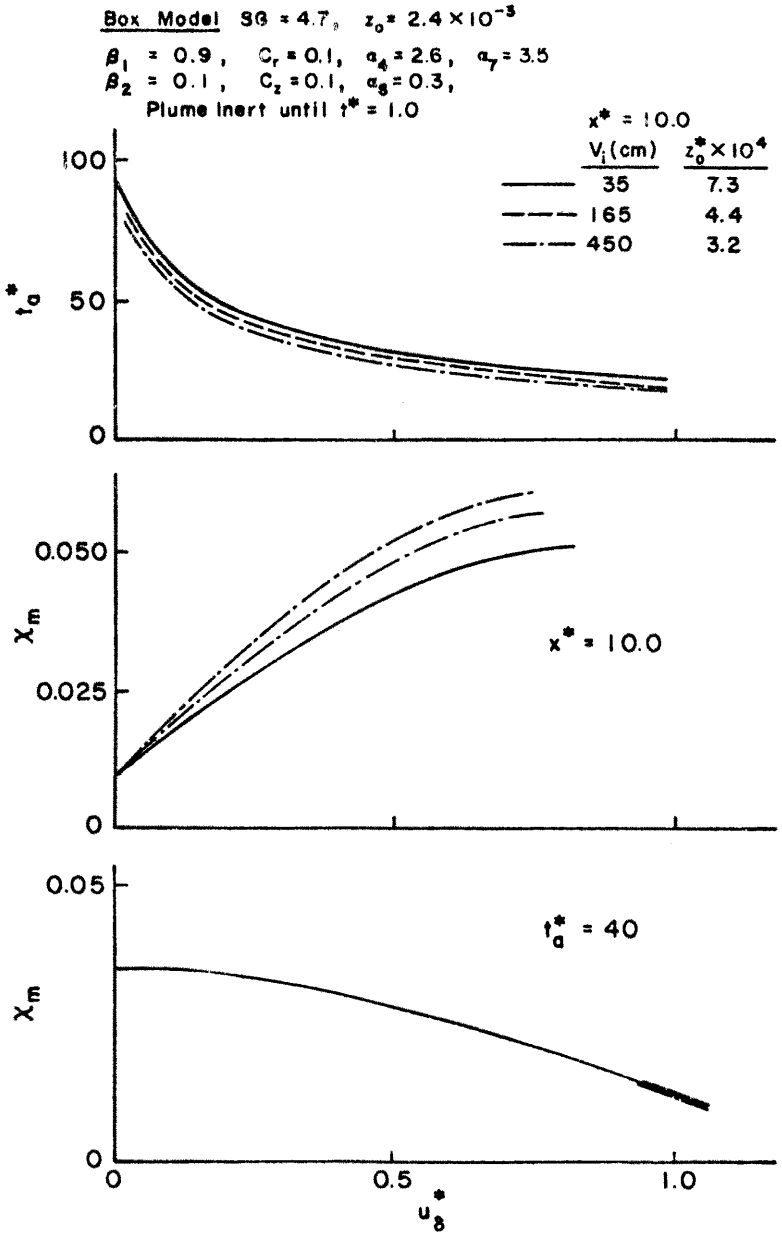

Figure 46. Variation of Arrival Time, t_a^*, and Concentrations, $_m$, with Velocity, u_R^*, Box Model Results

lar, but they do not reproduce the nuances of roughness effect found in the plots of dilution versus wind speed. Nonetheless for such a simple model the predictions are respectable.

The box model only predicts mean quantities. Actual measurements are expected to vary around the mean results by at least the order of standard deviations recorded in Tables 4 through 8. The model does not predict vertical distributions; however, vertical predictions might be made by assuming a set of similarity profiles as suggested by Ermak et. al. (1981).

5.1.2 Comparison Between Box Model and Hall (1979)

When Fay and Ranck (1981) examined Hall's (1979) data they deduced rather low values for entrainment constants. When the current box model is compared to this data lower initial entrainment coefficients are also required (See Figure 47). The data in Figures 47 and 48 are taken from Figures 19 and 20 in Hall (1979, LR312(AP)). The smoothed lines provided by the author rather than the data points were used since no data appears in Figure 20. Values were read from the figures for every 0.1 m from 0.1 to 1.5 m. Excellent agreement between data and prediction of χ vs t_a^* is obtained for $C_r = 0.05$ and $C_z = 0.01$. Such a large variation in C_z seems unusual at first glance.

The explanation becomes clear if one considers the manner in which the experiments were performed. Hall used a source made from a hemisphere of porous plastic foam. Gases were emitted at a constant rate from this source over a finite length of time. The dimensionless release time, t_r^*, for each set of data examined are marked near the bottom of Figure 47. It immediately becomes apparent that over these time periods one may not treat the data as suddenly released. When one

examines a plot of distance versus arrival time, Figure 48 one notes that the gravity dominated spread region is nearly absent.

Since the cloud is emitted over finite time it never develops the potential energy state required to drive a strong gravity spread period. In addition typical minimum heights reached by the cloud, $H^* \sim .05$, are of the same order as the measured roughness height ($z_o^* \sim .03$). The experimental configuration results in low initial transport and dilution rates which require modified entrainment coefficients (lower) to permit box model comparisons.

5.1.3 Comparison Between Box Model and Picknett (1981) Data

Runs number 28 and 36 were chosen from Picknett's (1981) paper describing the Porton experiments to compare with the present box model. Both are releases under equivalent wind speed conditions, but for Run number 28 the SG = 2.1 and z_o = 0.002 m whereas for Run number 36 the SG = 1.5 and z_o = 0.01 m. The plume width, downwind travel, and height are considered, but only total cloud volume is reported not local maximum concentrations. These data are based on visual examination of photographic records.

Figure 49 compares the box model to Run number 36. This release has a Richardson number, $Ri_* = 244$, and a roughness, $z_o = 29 \times 10^{-4}$; hence the plume behaves passively after a short time. After only ten seconds the box model predicts the cloud will grow laterally like a passive plume. The plume width is produced by gravity forces until at least 8 seconds, as shown on the figure. The box model significantly underpredicts plume height which seems surprising. The model is expected to overpredict plume volume since it is calibrated on local concentration maximum rather than average dilution. Perhaps the large experimental depths reflect an exponential variation of concentration

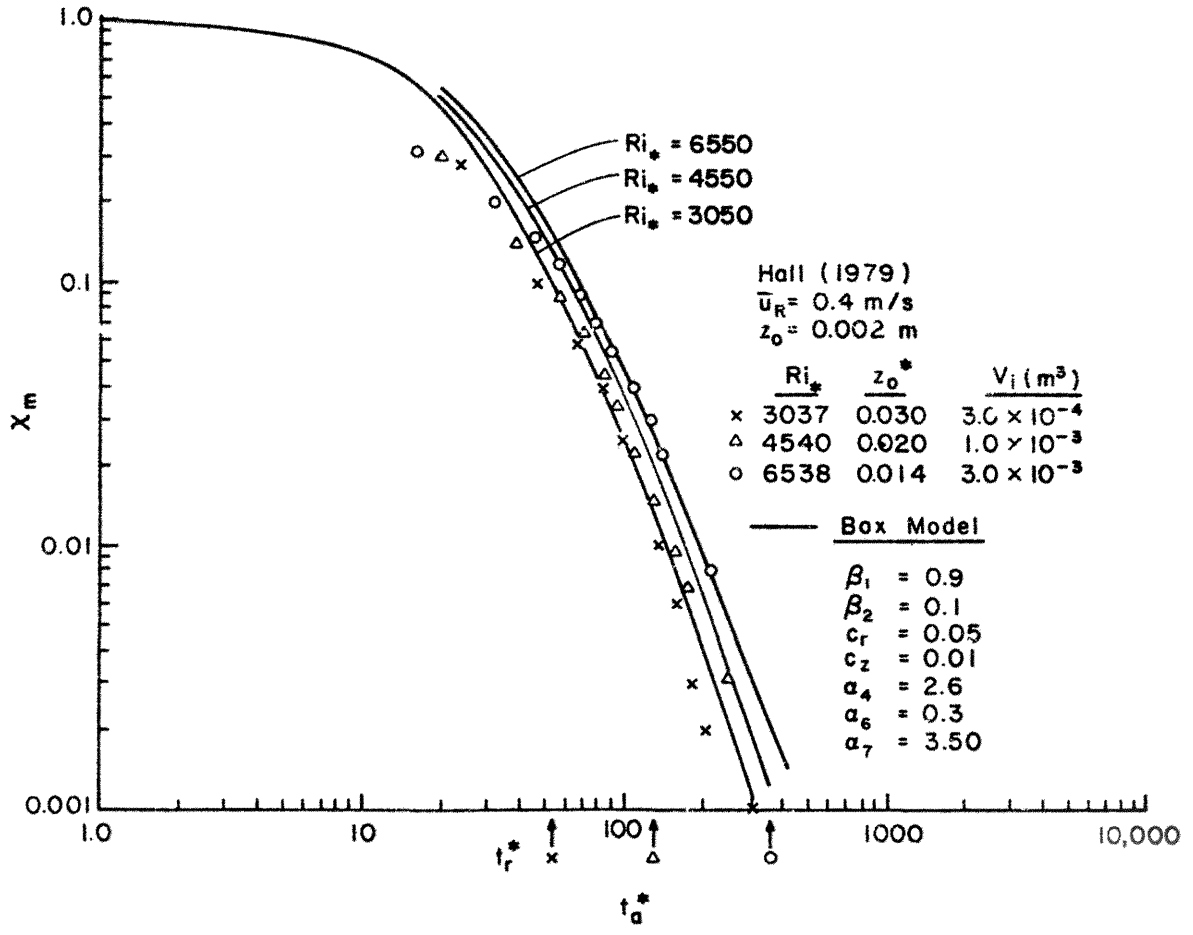

Figure 47. Comparison of Box Model to Hall (1978) Data, Cloud Dilution, χ_m, versus Arrival Time, t_a^*

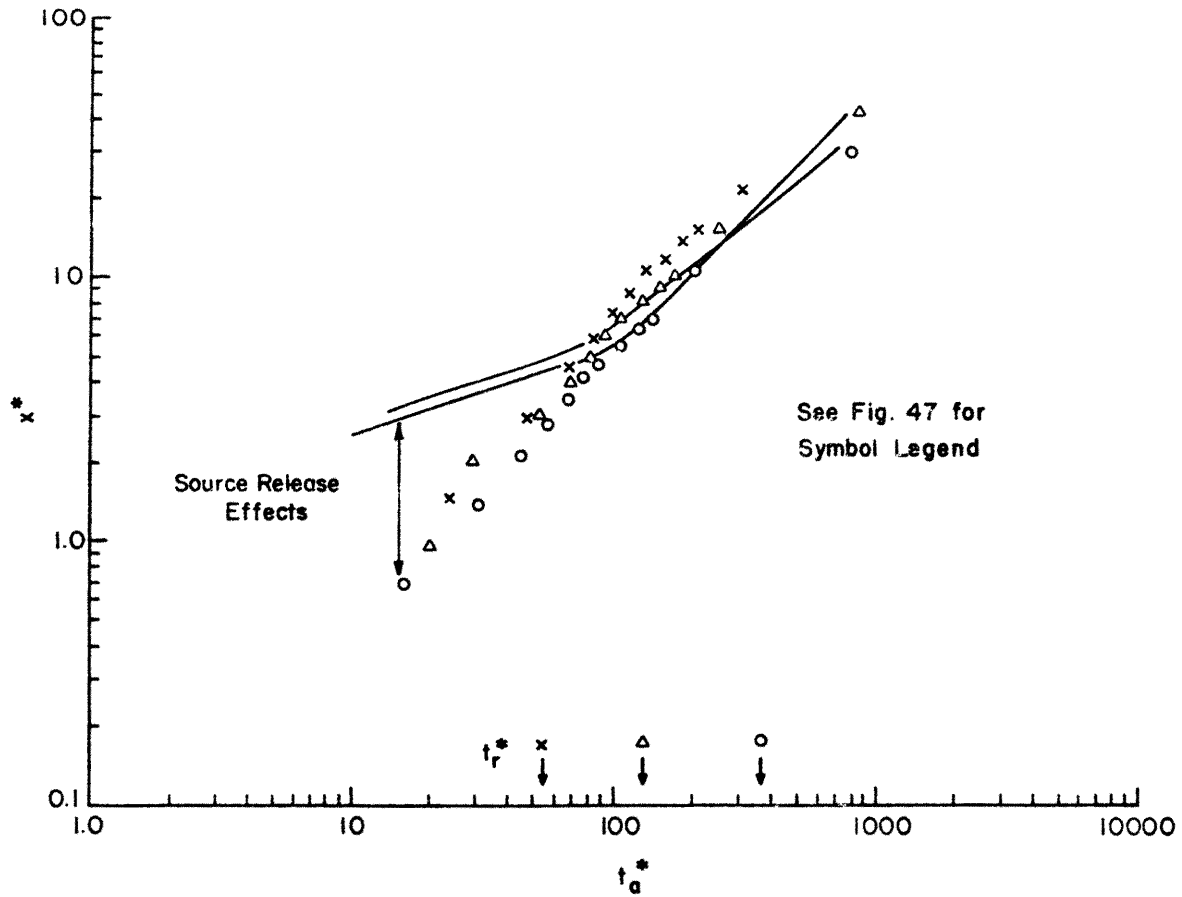

Figure 48. Comparison of Box Model to Hall (1978) Data, Distance, x^*, versus Arrival Time, t_a^*

with height as suggested by Figures 33 to 35. Alternatively one can redistribute gas from the intensive vortex ring observed by Picknett into a disk as suggested by Eidsvik (1980). Redistribution of the mass from a circumferential ring of radius $H_p/2$ evenly over a cylindrical cloud of radius R gives a disk height of $\pi H_p^2/2R$. The "corrected height" is noted on Figures 49 and 50. Although this argument improves agreement it is more likely that mass is not concentrated in the ring - see Section 5.2.1 and Figures 57 to 60.

Figure 50 compares the box model to Run number 28. In this case $Ri_* = 620$ and $z_o^* = 5.8 \times 10^{-4}$. Again, based on the visual observations, plume growth seems much larger than predicted by the box model. The linear growth of plume width for times less than 10 seconds is unexpected, especially since Run number 38 produces close agreement with a classical $R \sim t^{1/2}$ behavior. Since constants recommended by Eidsvik (1980) and Picknett (1978) are based on the Porton data it is not surprising they conclude $c_r \sim 0$ (1).

Fay and Ranck (1981) quote a measured local concentration value of $\sim 1 \times 10^{-4}$ at $t \sim 125$ seconds at $\chi = 500$ meters for Run number 28. The box model predicts a value of $\sim 3 \times 10^{-4}$ at this time and location. A prediction by a box model within a factor of three compared to a single realization measurement must be considered reasonable.

Hall, Hollis, and Ishaq (1982) reproduced the behavior of Runs 3, 8, 21, 29, 33, and 37 from the Porton trials in a set of wind-tunnel experiments. In all cases they reproduced the time variation of plume width, plume shape, plume arrival and plume departure very well. There were very strong visual similarities between the field and model plumes. Comparisons were also made between field concentration measurements and the model measurements. Some of the comparisons showed very good

agreement, but others were poor. Differences were attributed to the naturally occurring high levels of repeat variability and anomalies in the field measurements. (In some cases integrated continuous monitors and dosage monitors from the field experiments varied by more than an order of magnitude.)

These same data were calculated by the box model. In each case the model replicated the Hall et. al. behavior quite well and differed from the field data in the same manner that their tests did. Porton Trial 8 results are shown in Figures 50a, b, c. The field tests were performed at wind speeds below the threshhold values of the instruments available; hence the trial experiments were effectively in still air. Figure 50a displays peak gas concentrations measured at different downwind locations. Hall's model tests and the box model agree very well, but the field measurements do not seem to vary at all with distance. Figure 50b compares model, full scale, and box model cloud widths at various times from release. Agreement is excellent. Figure 50c displays concentration versus time traces at various radial locations. The box model predicts model test peak concentrations and arrival times very well.

5.1.4 Specific Gravity Influences on Dense Gas Behavior

Neff and Meroney (1982) found significant perturbations in trajectory and concentration for continuous source plumes when specific gravity varied from 1.2 to 4.17 while Densimetric Froude number, $Fr \equiv u^2/g'L$, and the Volume Flux Ratio, $V = Q\,L^2$, remained constant. It is important to examine suddenly released plumes for similar effects.

Lohmeyer and Meroney performed a few argon and carbon dioxide releases during their 1981 experiments. These included only a few exploratory measurements. Compared to the Freon-12 releases the argon

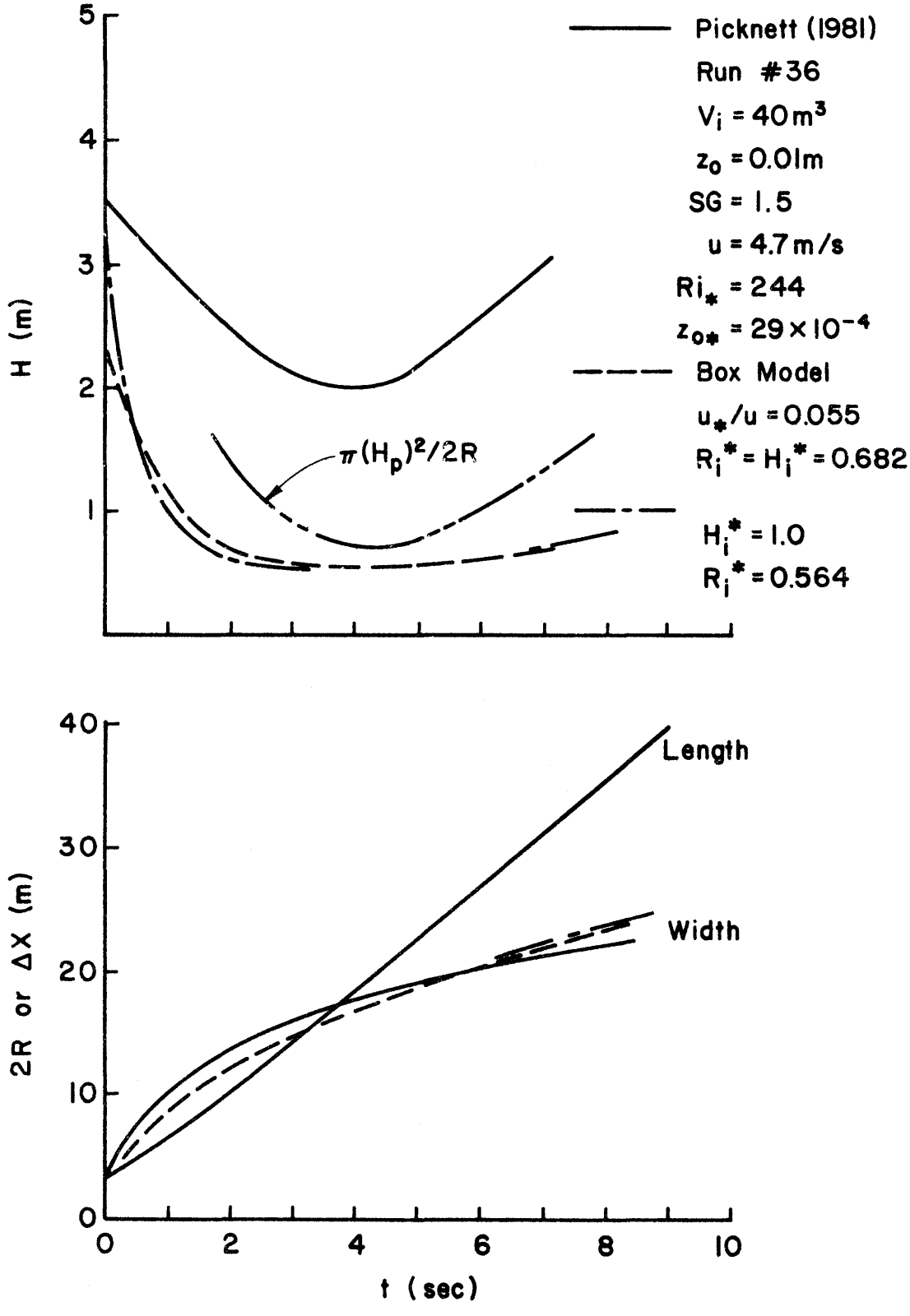

Figure 49a. Comparison of Box Model to Run # 36 of Picknett (1981)

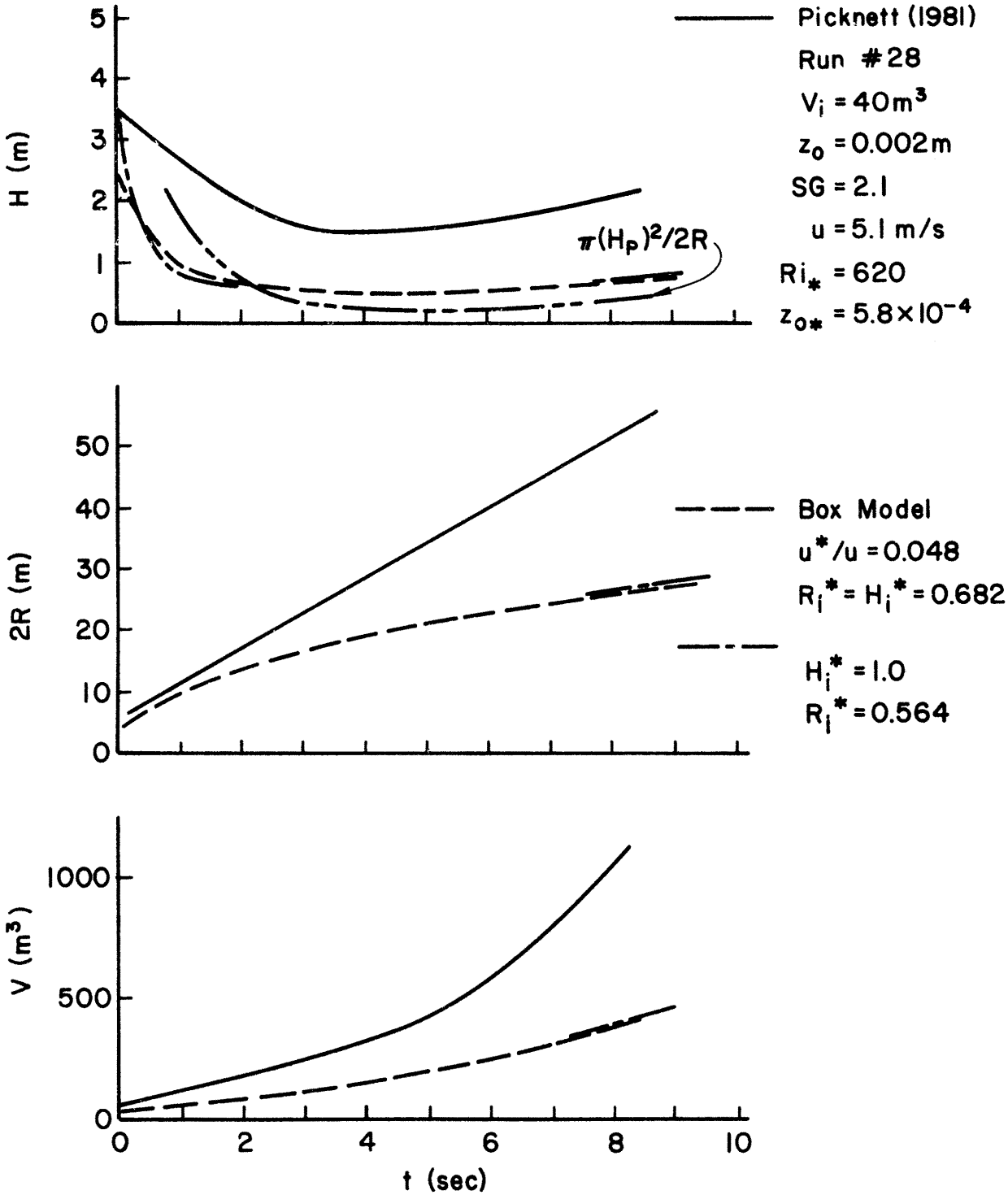

Figure 49b. Comparison of Box Model to Run # 28 of Picknett (1981)

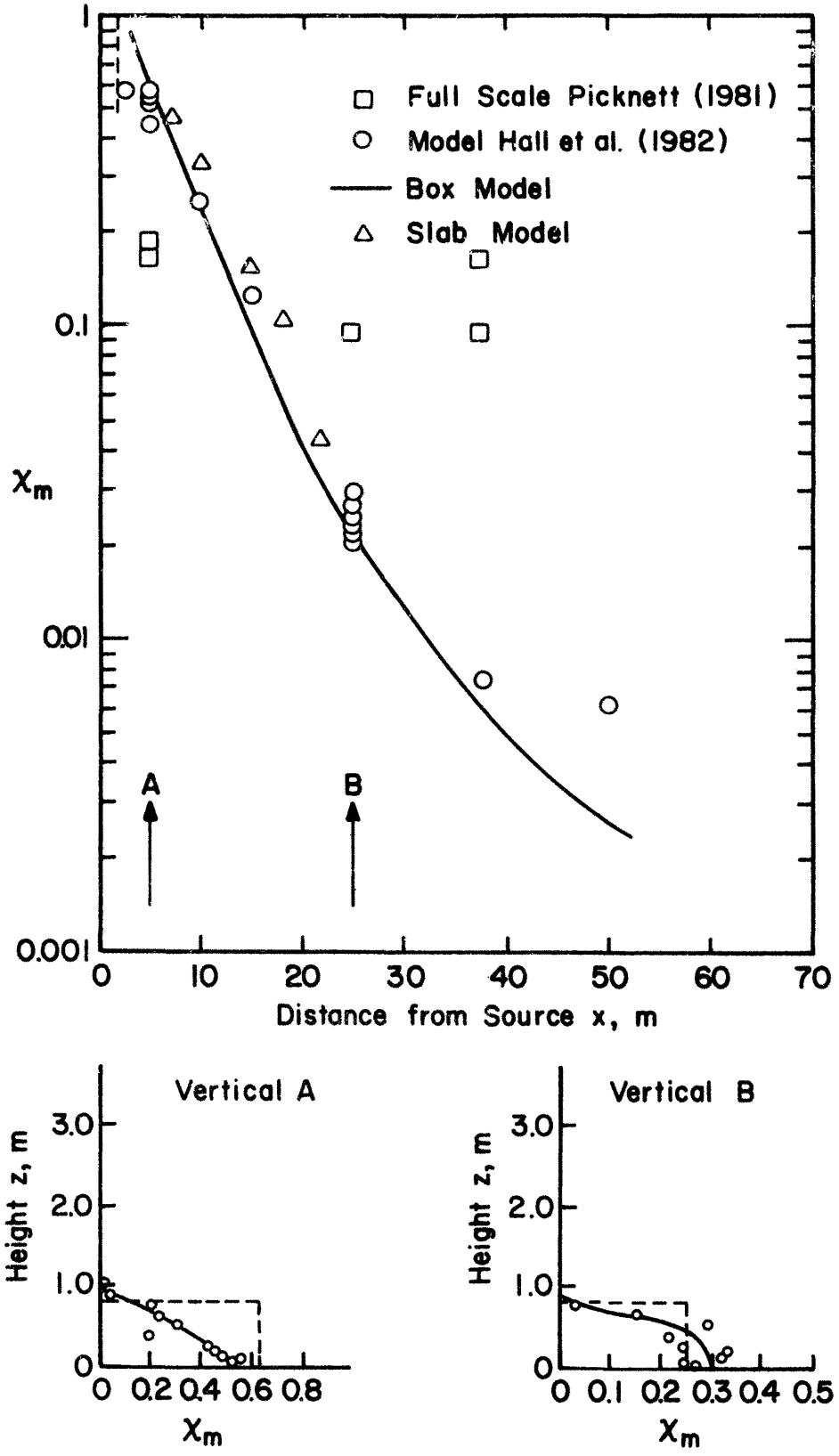

Figure 50a. Porton Trial No. 8 - Peak Concentrations in Cloud

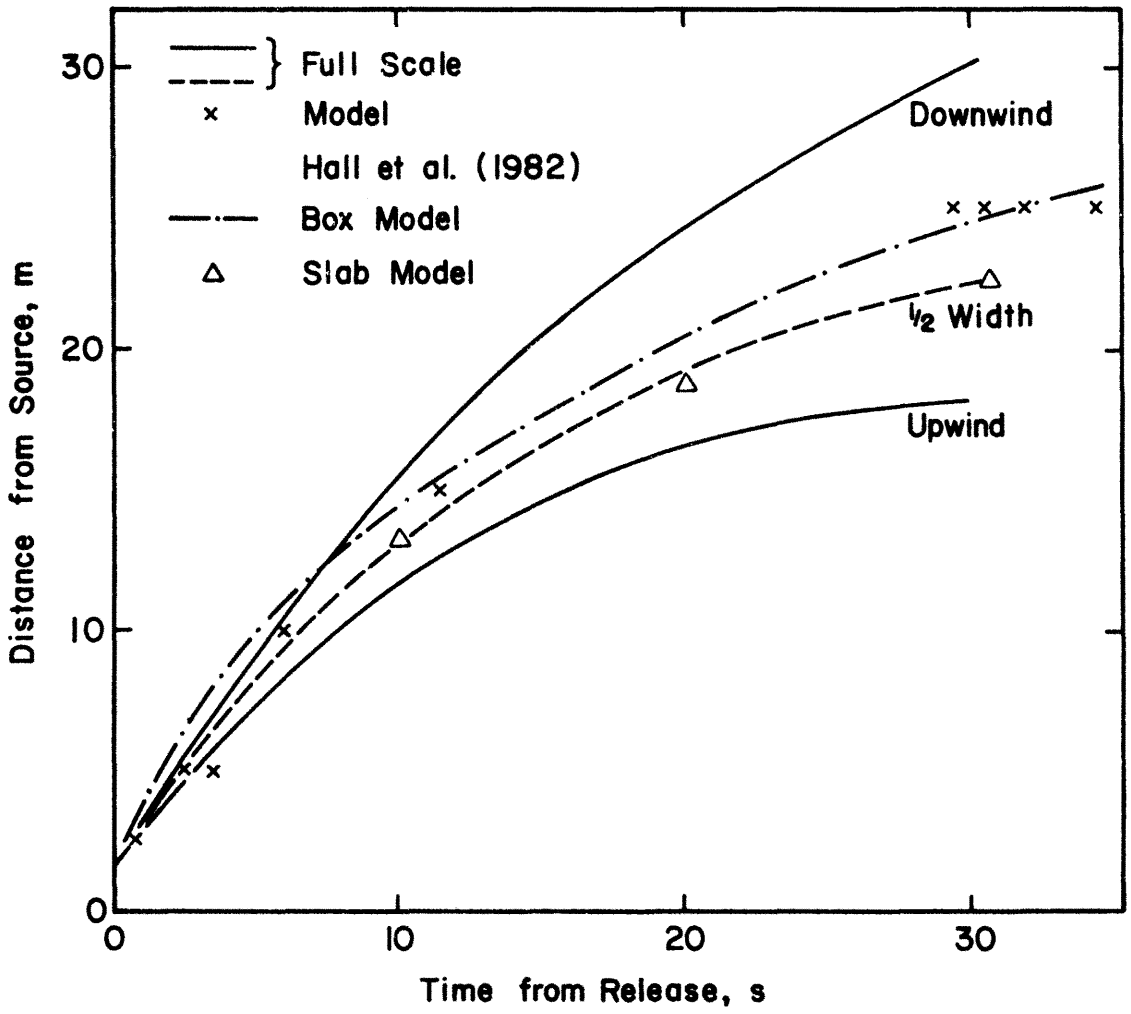

Figure 50b. Porton Trial No. 8 - Cloud Size Variation

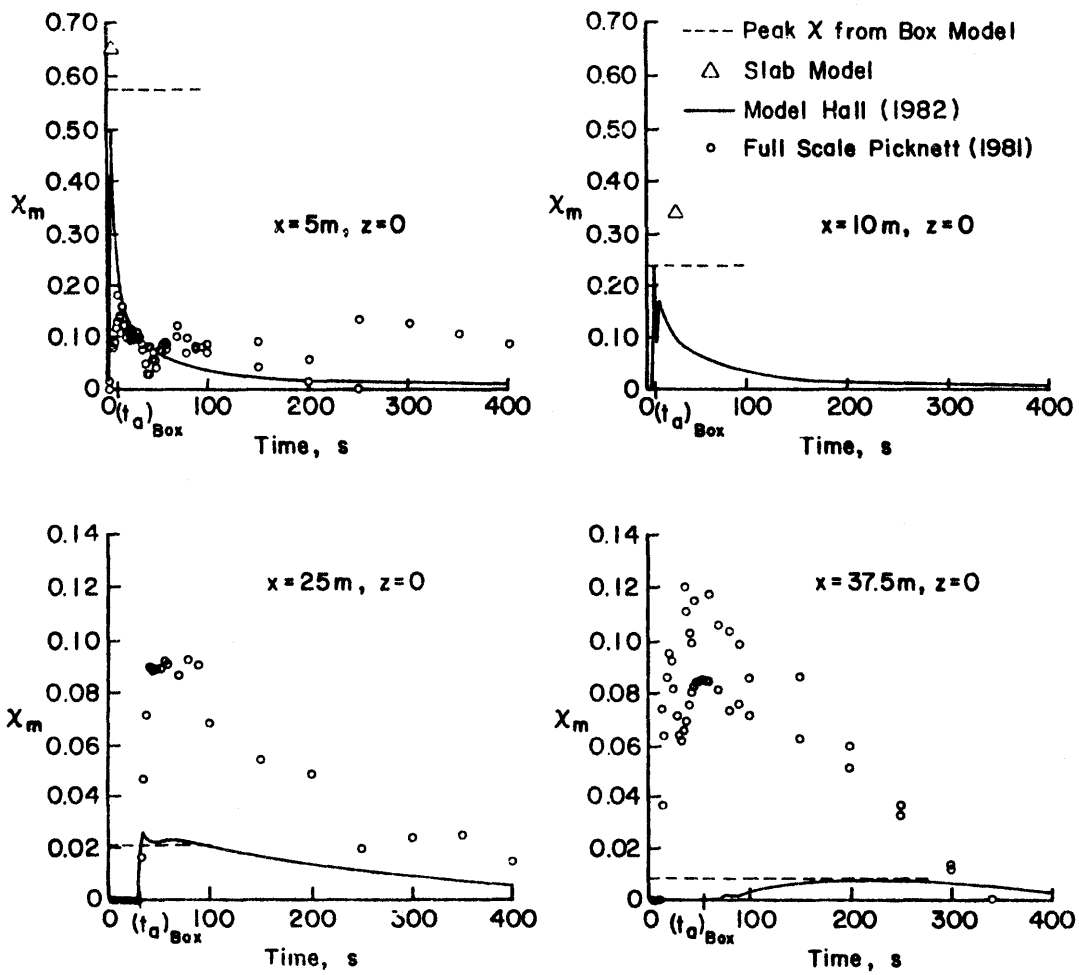

Figure 50c. Porton Trial No. 8 - Continuous Monitor Measurements

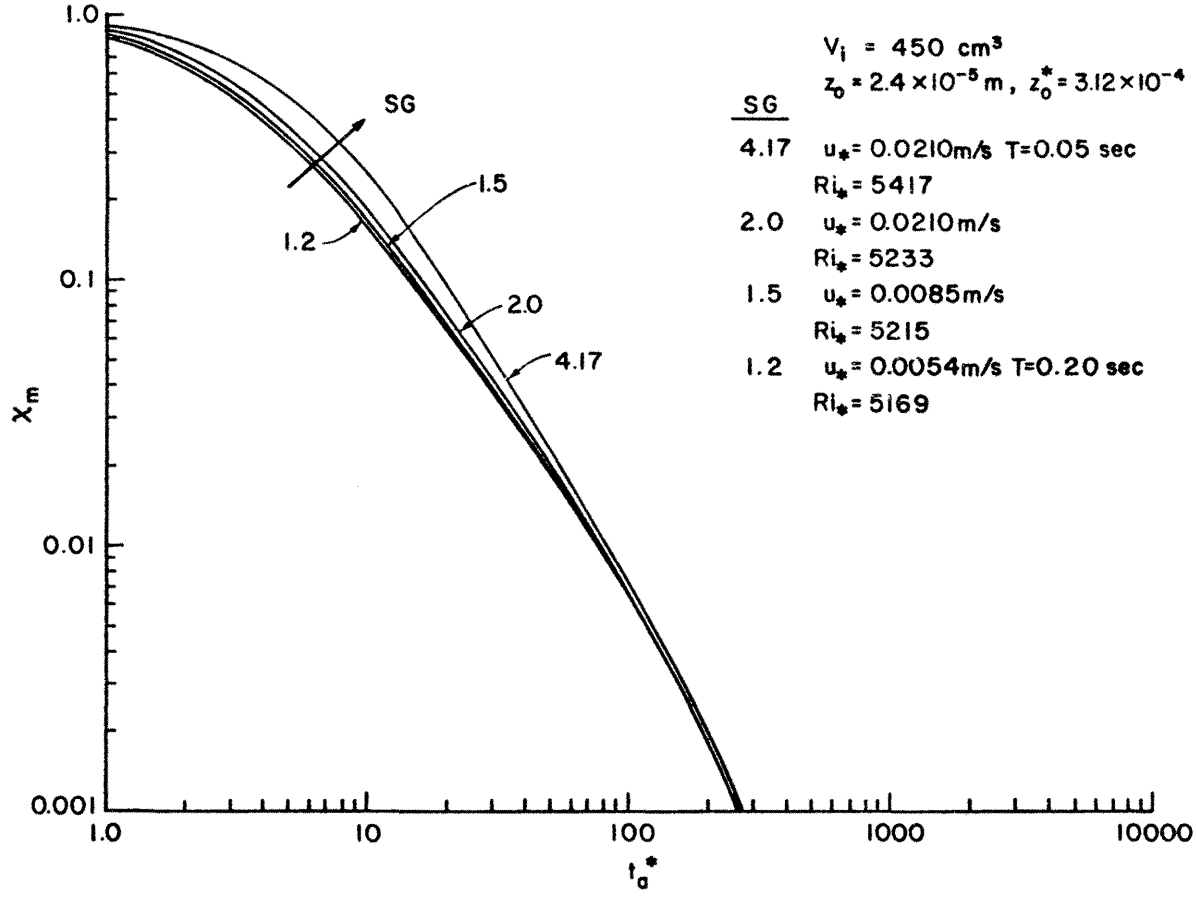

Figure 51a. Influence in Variation in Specific Gravity on Box Model Prediction for $Ri_* = 6000$, $z_o^* = 3.13 \times 10^{-4}$

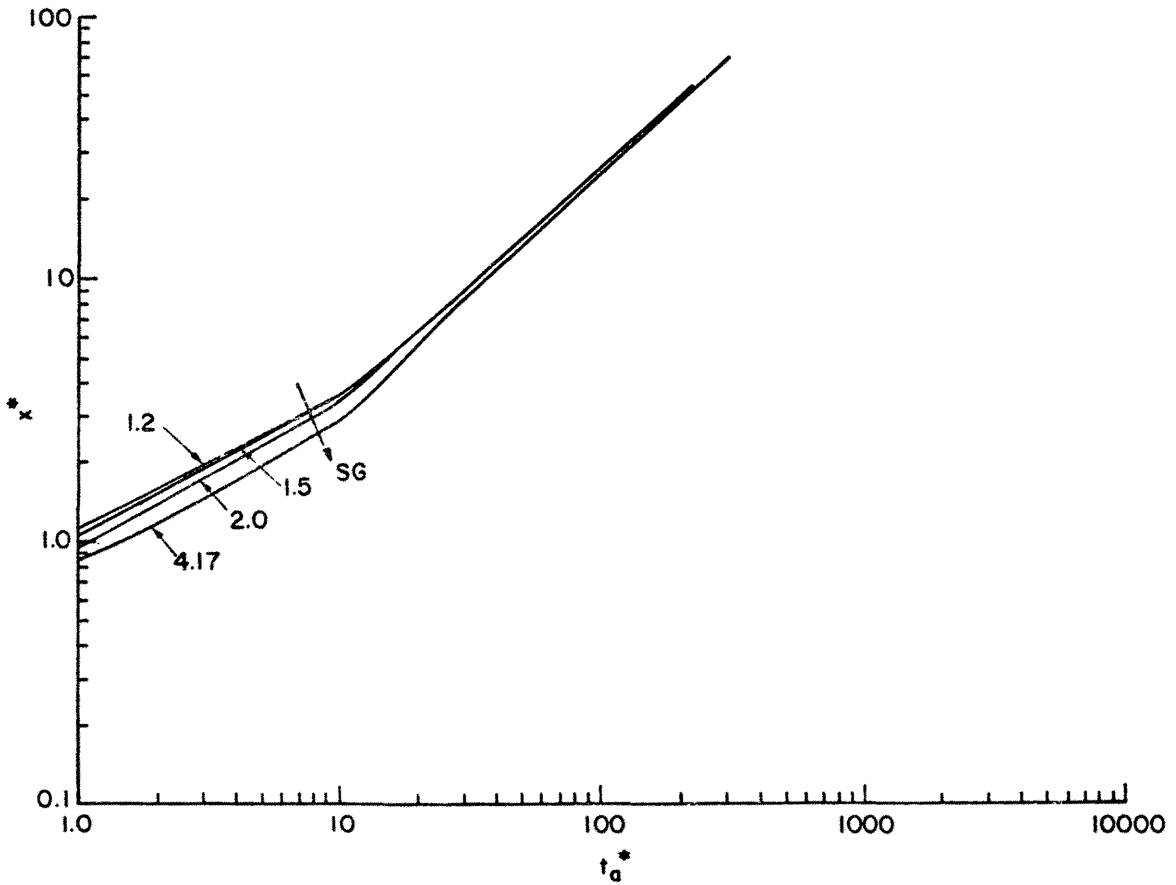

Figure 51b. Influence in Variation in Specific Gravity on Box Model Prediction for $Ri_* = 6000$, $z_o^* = 3.13 \times 10^{-4}$

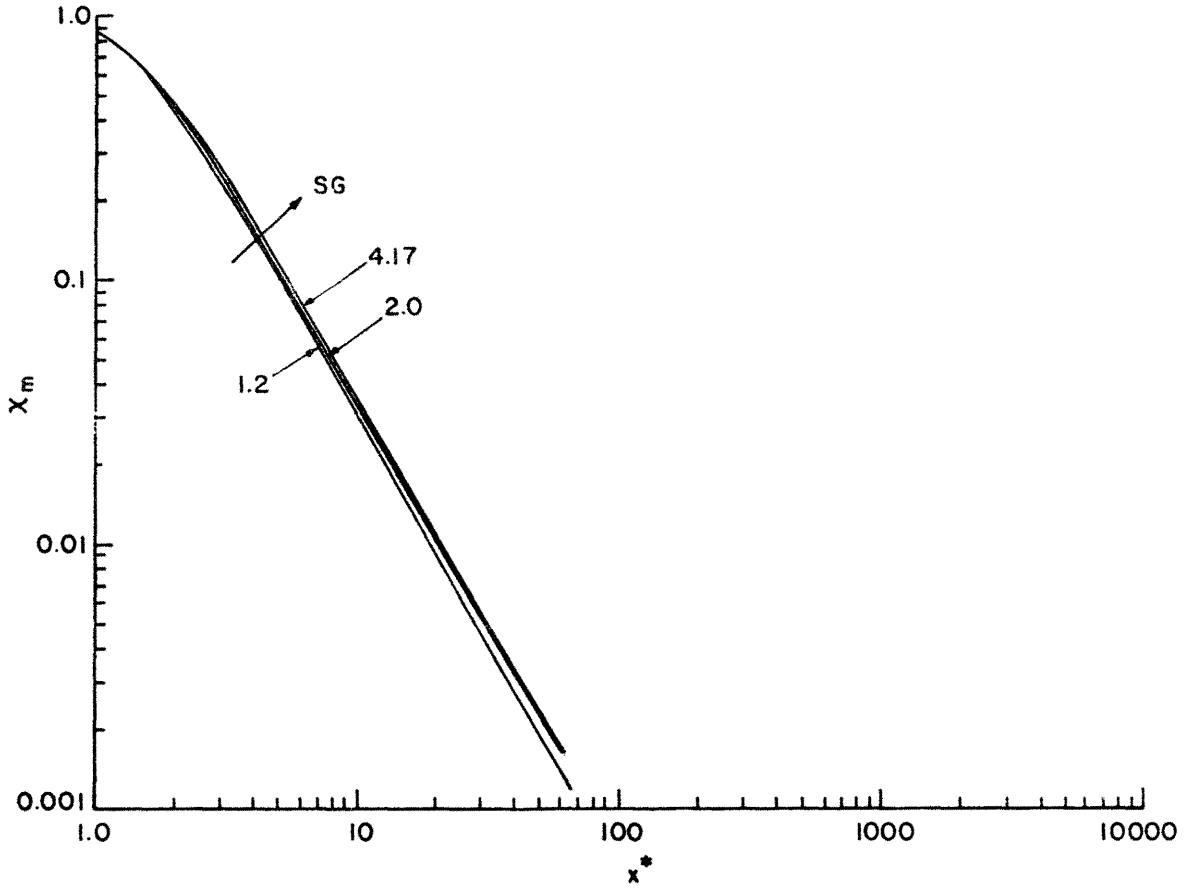

Figure 51c. Influence in Variation in Specific Gravity on Box Model Prediction for $Ri_* = 6000$, $z_o^* = 3.13 \times 10^{-4}$

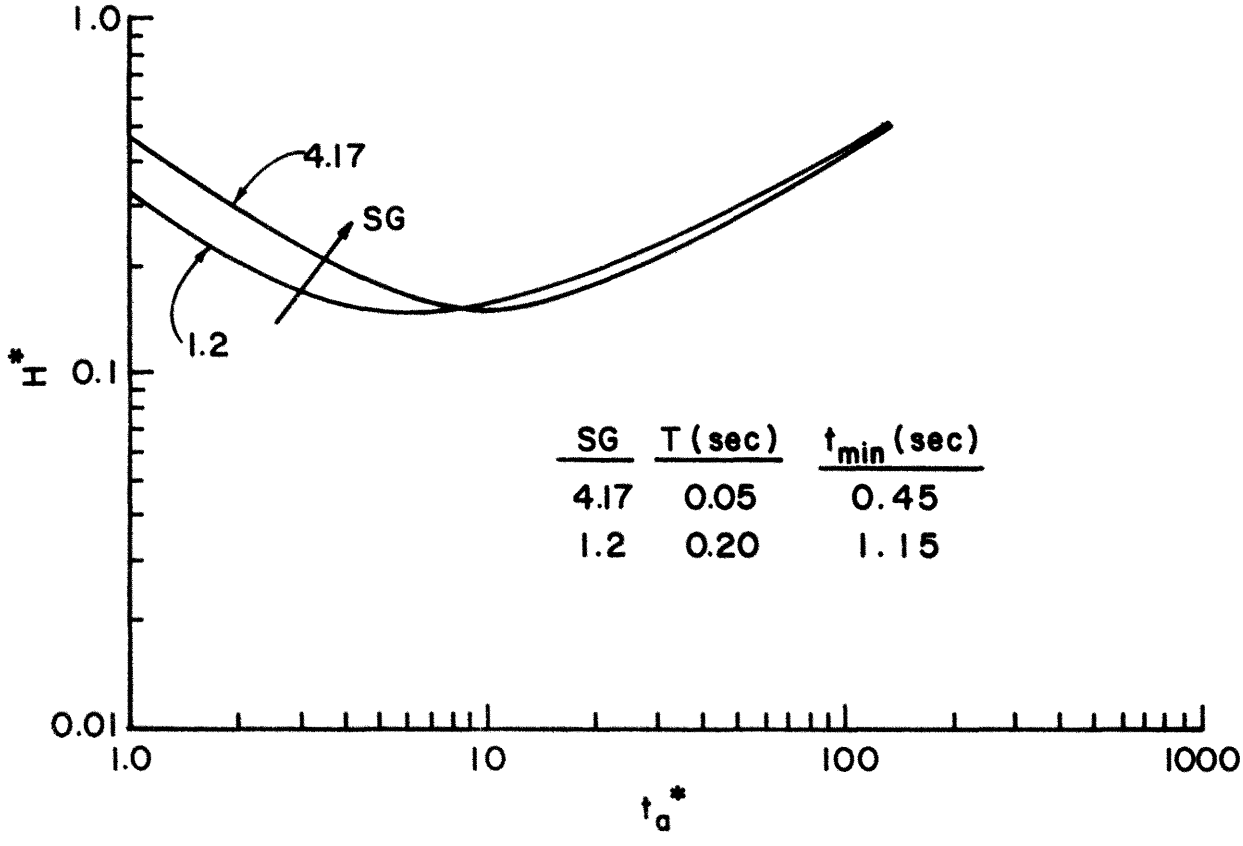

Figure 51d. Influence in Variation in Specific Gravity on Box Model Prediction for $Ri_* = 6000$, $z_o^* = 3.13 \times 10^{-4}$

concentrations decayed faster with t_a^* and x^*, and the clouds spread a little faster. The carbon dioxide also spread faster than the Freon-12 in K^* vs t_a^* coordinates. At the time the variations were attributed to instrument errors and calibration variability. Picknett (1981) reported greater initial density led to higher concentrations, smaller minimum cloud height, and the minimum cloud height was reached earlier. He noted that effects seen were small, but conclusive.

The box model has been run for a cloud volume of 450 cm^3, $Ri_* \simeq 5000$, and $z_o^* = 3.2 \times 10^{-4}$ but SG = 4.17, 2.0, 1.5, and 1.2. The results shown on Figure 51 clearly bear out the influence of initial cloud specific gravity. The influences are in the directions discussed, but they are generally small in dimensionless coordinates. The effect in real time will be even less apparent, and in some cases will invert.

5.2 COMPARISON OF DENSE GAS DATA WITH NUMERICAL DEPTH AVERAGED MODEL

The depth averaged (slab) model described in Appendix B solves the depth averaged mass continuity, momentum, and concentration equations for radially varying depth, and depth averaged densities, velocities, and concentrations. Advection of the cloud is included by integrating for transport of the cloud center by a fraction of the background wind speed. The model does not make the Boussinesq assumption, but it implicitly makes the hydrostatic pressure assumption (ie. vertical velocities are assumed to be small). Model constants are tuned to fit the present data; however, examination of the following table reveals these values are consistent with other investigators.

Table 16

Slab Model Constants Specified by Various Investigators

Author (date)	C_F	α_1	α_2	γ	β_1	β_2
Rosenzweig (1980)	$\sim 0.1/\lvert\bar{u}_g\rvert$	-	0.08	0.1	1.0^{Δ}	-
Zeman (1982)	0.08	-	0-0.051	0.64	0.667^{*}	-
Present Results	0.25	- 0.1	0.05 0.05	0.40	0.333^{+}	0.10

$^{\Delta}$ Assumes a uniform distribution in $\Delta\rho$

* Assumes a linear distribution in $\Delta\rho$

$^{+}$ Assumes a power law in $\Delta\rho \sim (1-z/H)^2$

5.2.1 Comparison Between Slab Model and New Dense Gas Cloud Results

Calculations with the slab model were also performed over the source volume, wind speed, and roughness conditions examined experimentally. The ranges of dimensionless parameters studied are mentioned in Section 5.1.1.

Again the entrainment relation was found to be critical in defining concentration behavior. The entrainment relation used initially was that chosen by Rosenzweig (1980)

$$w_e = \alpha_2 \lvert u_g \rvert + \gamma u_* . \qquad (5\text{-}1)$$

The constants were chosen to fit mean behavior for $t^* = 0$ to 100 ($\alpha_2 = 0.05$, $\gamma = 0.4$). Nonetheless it results in slightly too low initial entrainment rates and too high a rate of entrainment at later times. An ad hoc revision of the type used by Eidsvik (1980) was introduced as

$$w_e = [\alpha_1 |u_g| + \alpha_2] |u_g| + \gamma u_* \qquad (5\text{-}2)$$

where $\alpha_1 = 0.1$, $\alpha_2 = 0.05$ and $\gamma = 0.4$. As shown in Figure 52 this improved computed behavior slightly hence, all subsequent calculations were performed using Equation (5-2).

Cloud transport distance, x^*, in plotted versus arrival time, t_a^*, in Figure 53. The behavior is very close to the summarized experimental results plotted in Figure 27. No advection of the cloud center was permitted before $t^* = 10$ in the model. As one might expect from the fact that the box model and the slab model treat the effects of cloud advection in the same manner, their predictions of cloud displacement are nearly identical (note that $(\beta_2)_{\text{box model}} = 0.1$ and $(\beta_2)_{\text{slab model}} = 0.10$).

Cloud dilution, χ_m is plotted versus arrival time, t_a^*, in Figure 54. The curves should be compared to experimental results found on Figure 29. The program tabulates χ_m versus radial location R^*; hence to obtain this graph one must first construct χ_m versus x^* and x^* versus t_a^*. Figure 54 results from a transpose via the other graphs; thus, some error may be introduced during construction of Figure 54. Nonetheless, the depth averaged model does reproduce the lower decay rates at low wind speeds seen in the experimental data. One can also now detect variability between different source sizes released at the same Ri_*. The slab model also permits one to calculate t_m^*. Since the calculated results are referenced to a moving cloud center, the semi-Lagrangian results must be corrected to Eulerian values at a point. The resulting plots permit construction of the other curves.

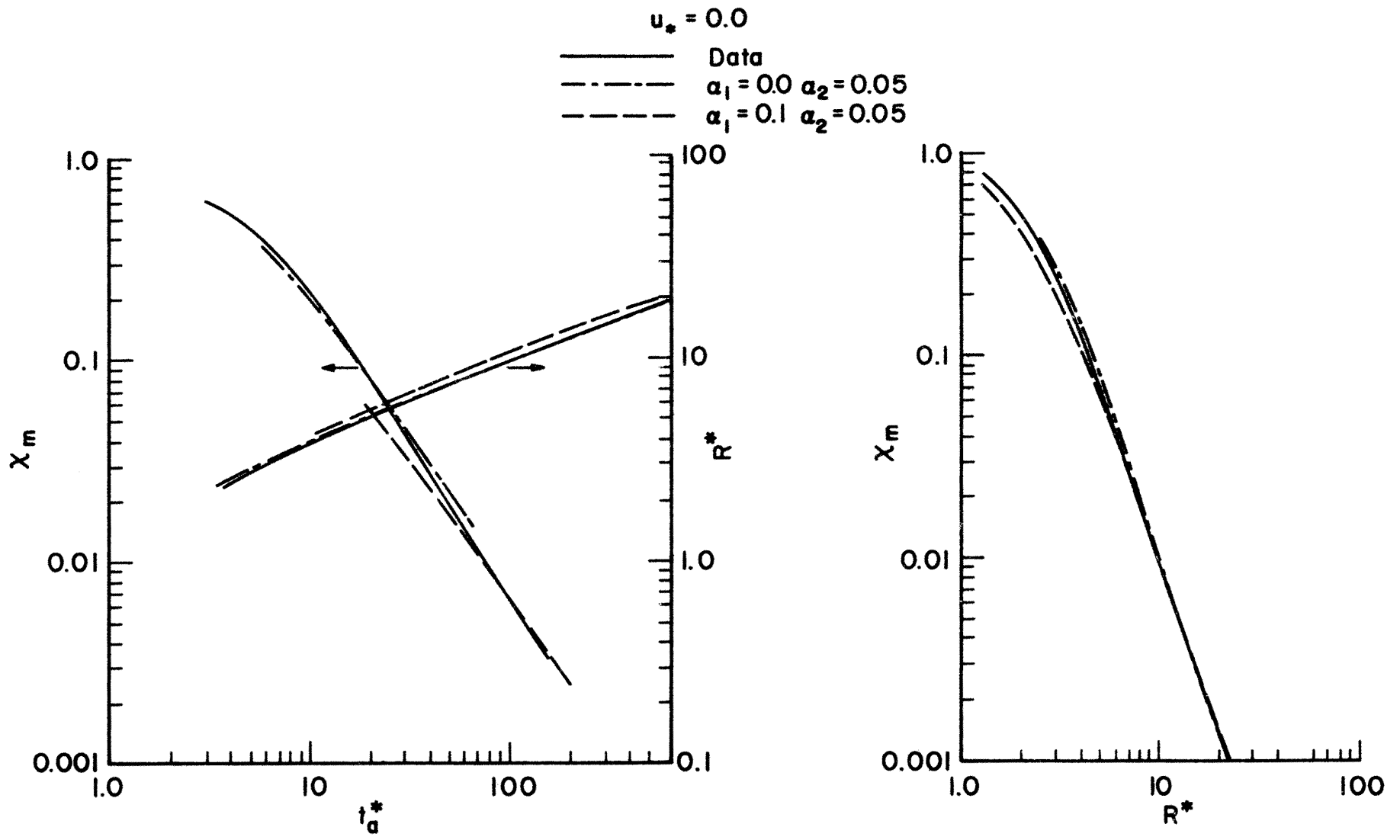

Figure 52. Influence of Entrainment Model on Depth-Averaged Model Performance

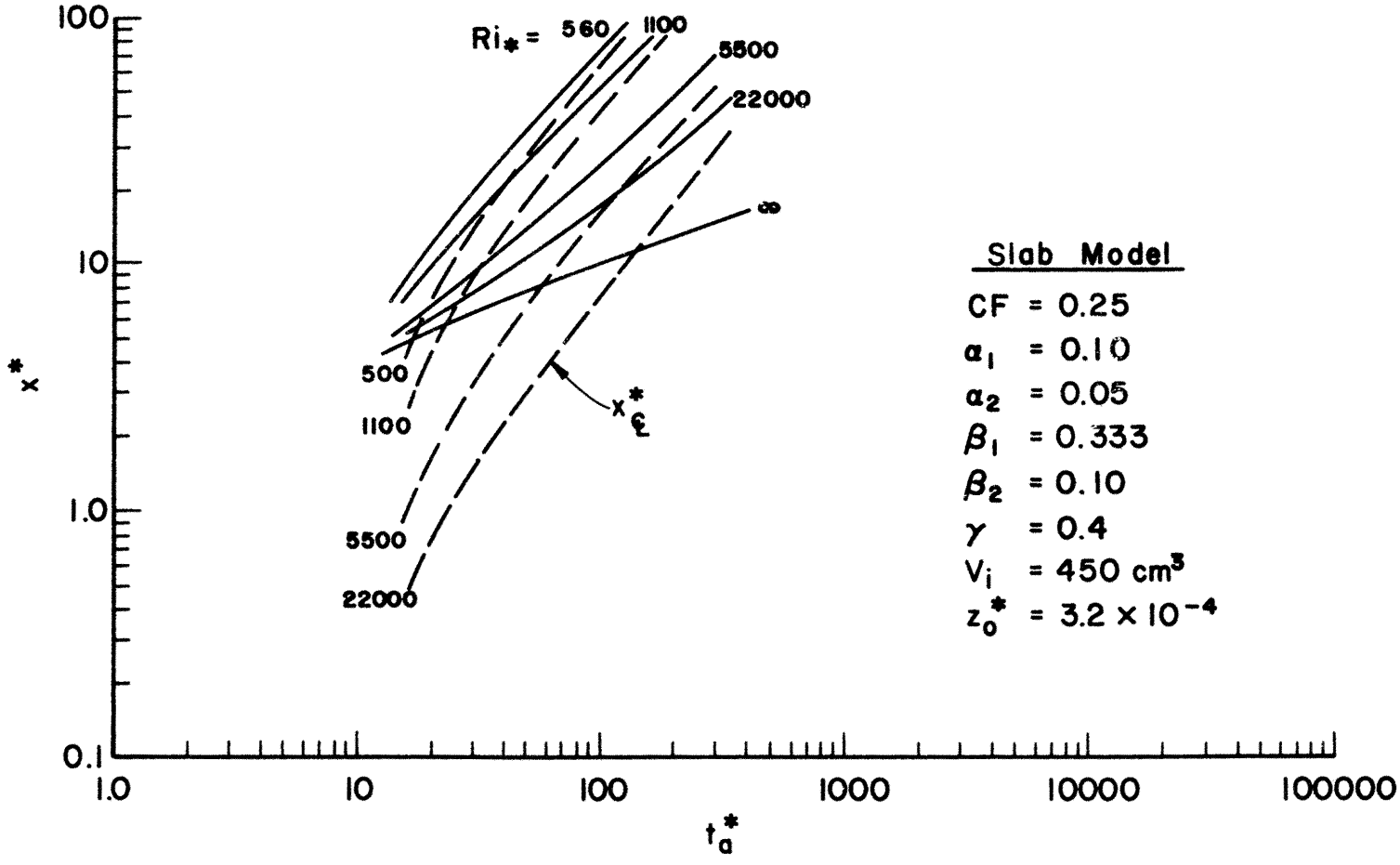

Figure 53a. Distance, x^*, versus Arrival Time, t_a^*, $u_R \geq 0$, V_i = 450 cm^3, Slab Model Results

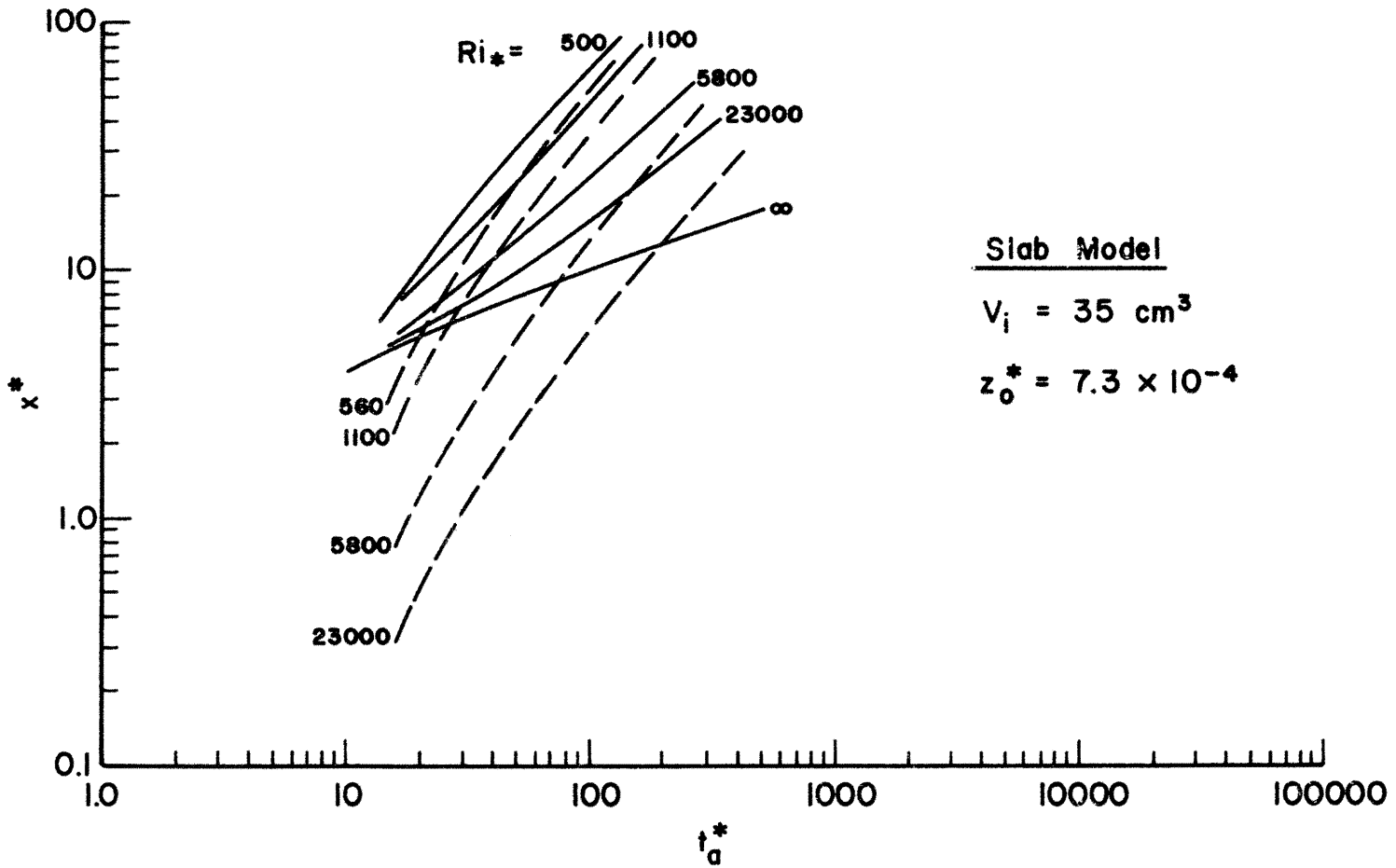

Figure 53b. Distance, x^*, versus Arrival Time, t_a^*, $u_R \geq 0$, $V_i = 35$ cm^3, Slab Model Results

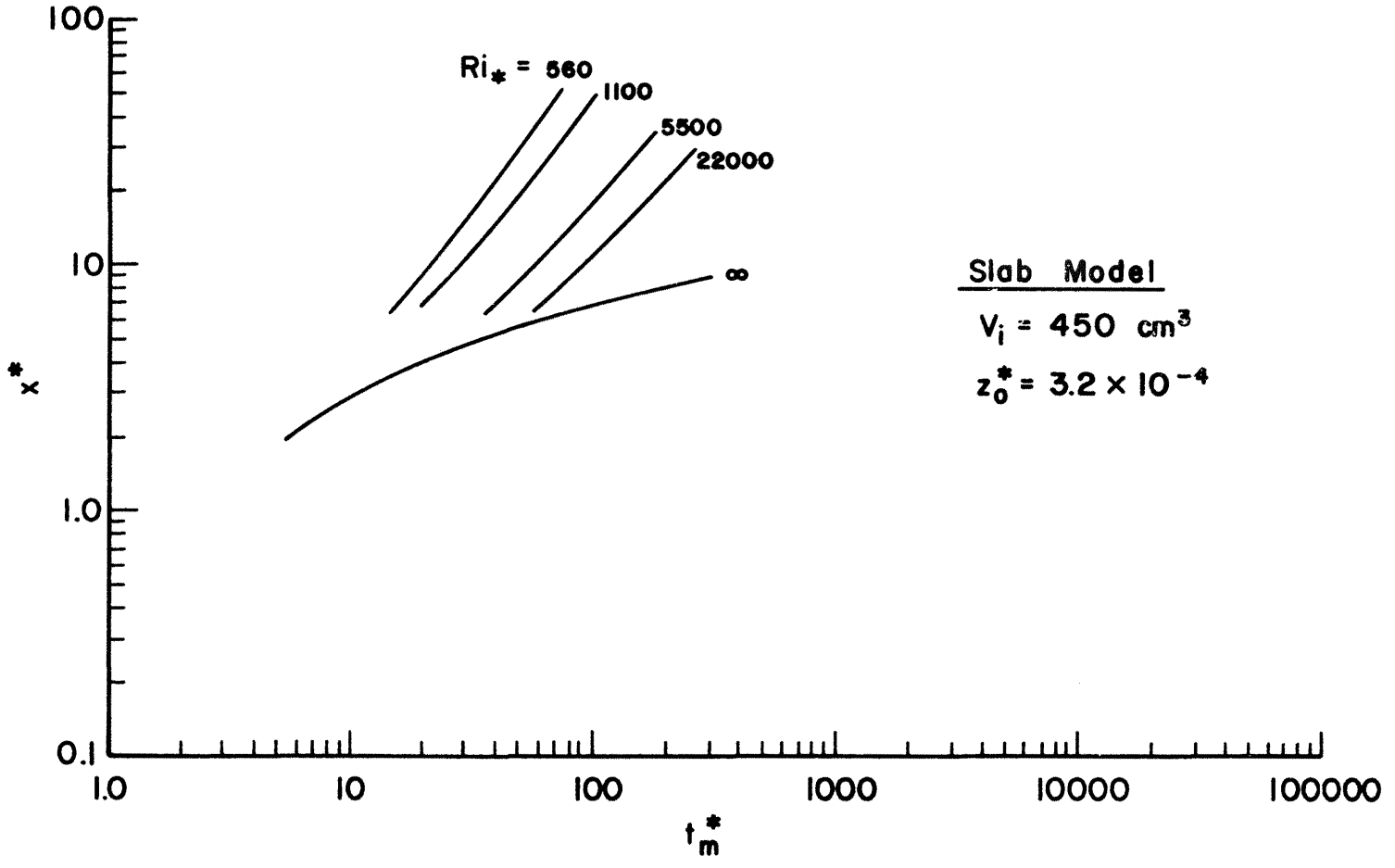

Figure 53c. Distance, x^*, versus Arrival Time of Maximum Concentration, t_m^*, $u_R \geq 0$, $V_i = 450\ cm^3$, Slab Model Results

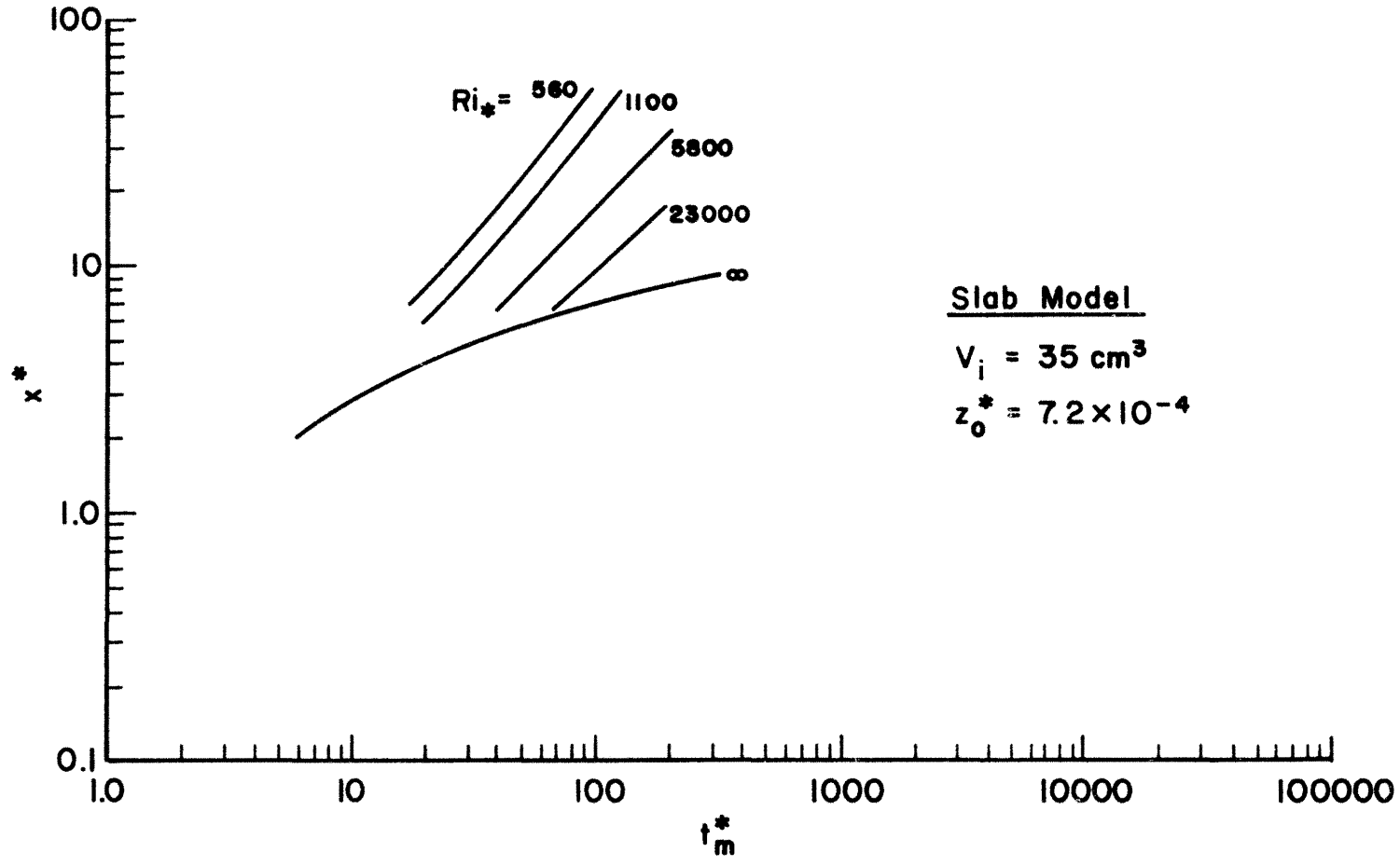

Figure 53d. Distance, x^*, versus Arrival Time of Maximum Concentration, t^*_m, $u_R \geq 0$, $V_i = 35$ cm^3, Slab Model Results

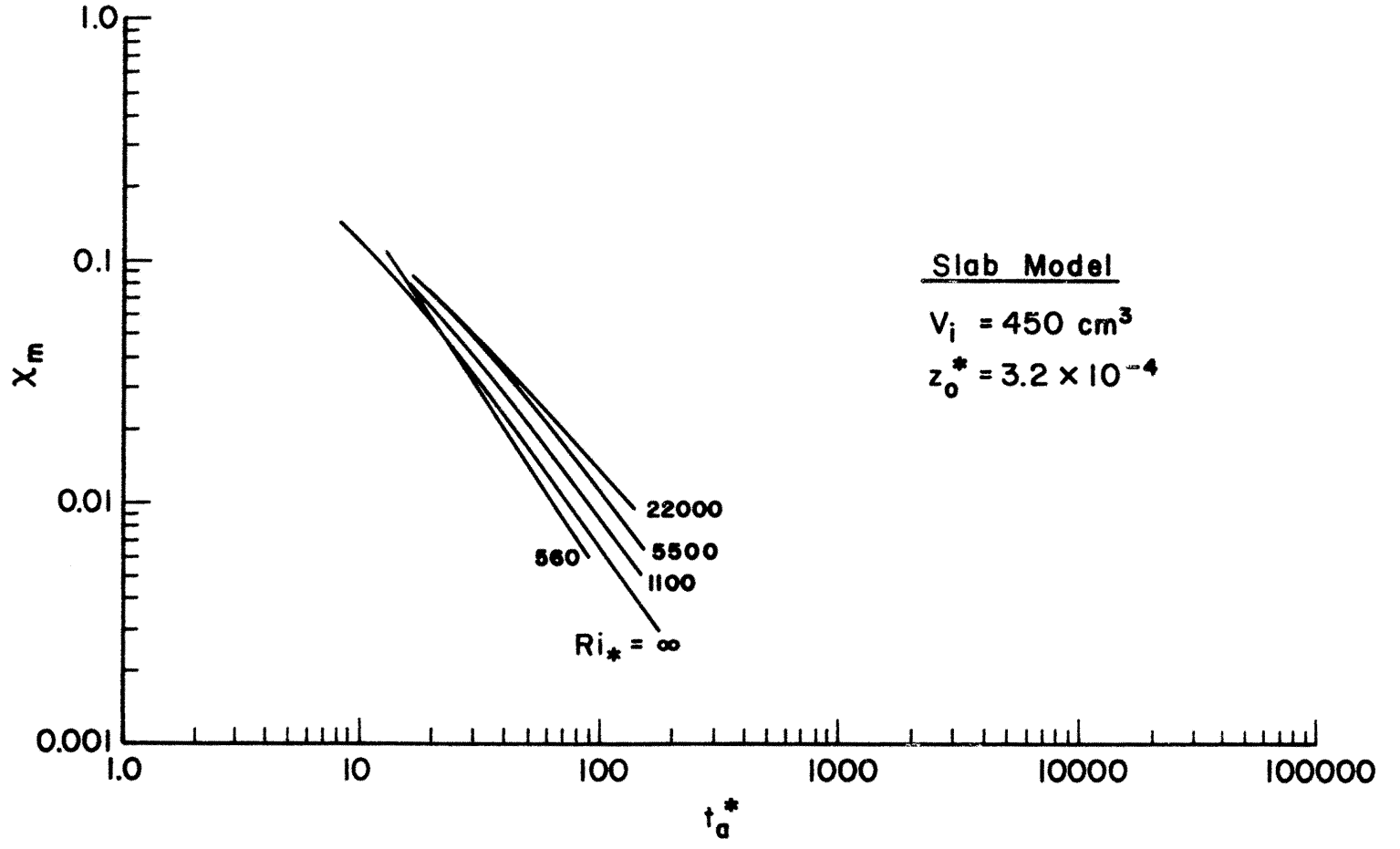

Figure 54a. Cloud Dilution, χ_m, versus Arrival Time, t_a^*, $u_R \geq 0$, V_i = 450 cm^3, Slab Model Results

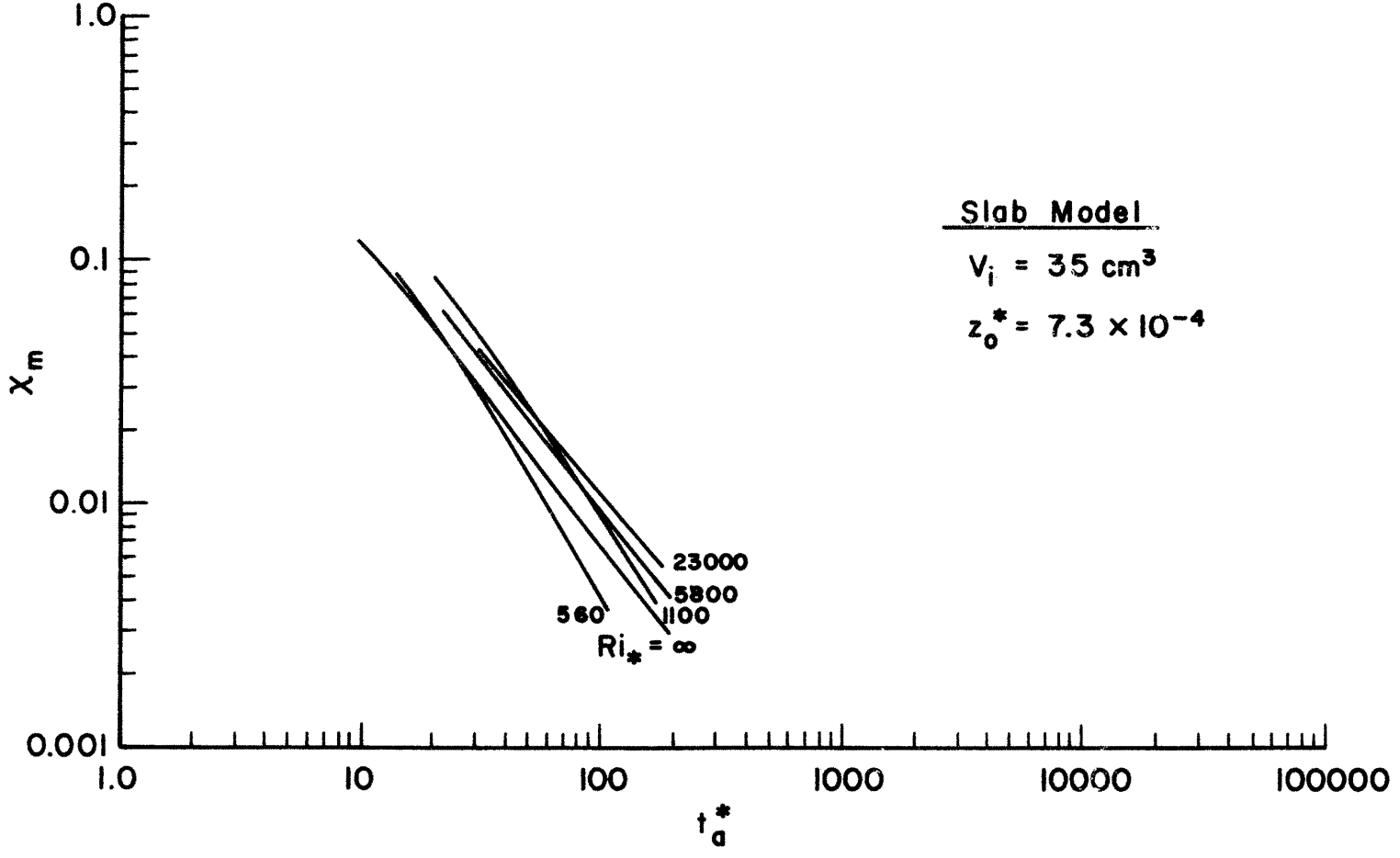

Figure 54b. Cloud Dilution, χ_m, versus Arrival Time, t_a^*, $u_R \geq 0$, V_i = 35 cm^3, Slab Model Results

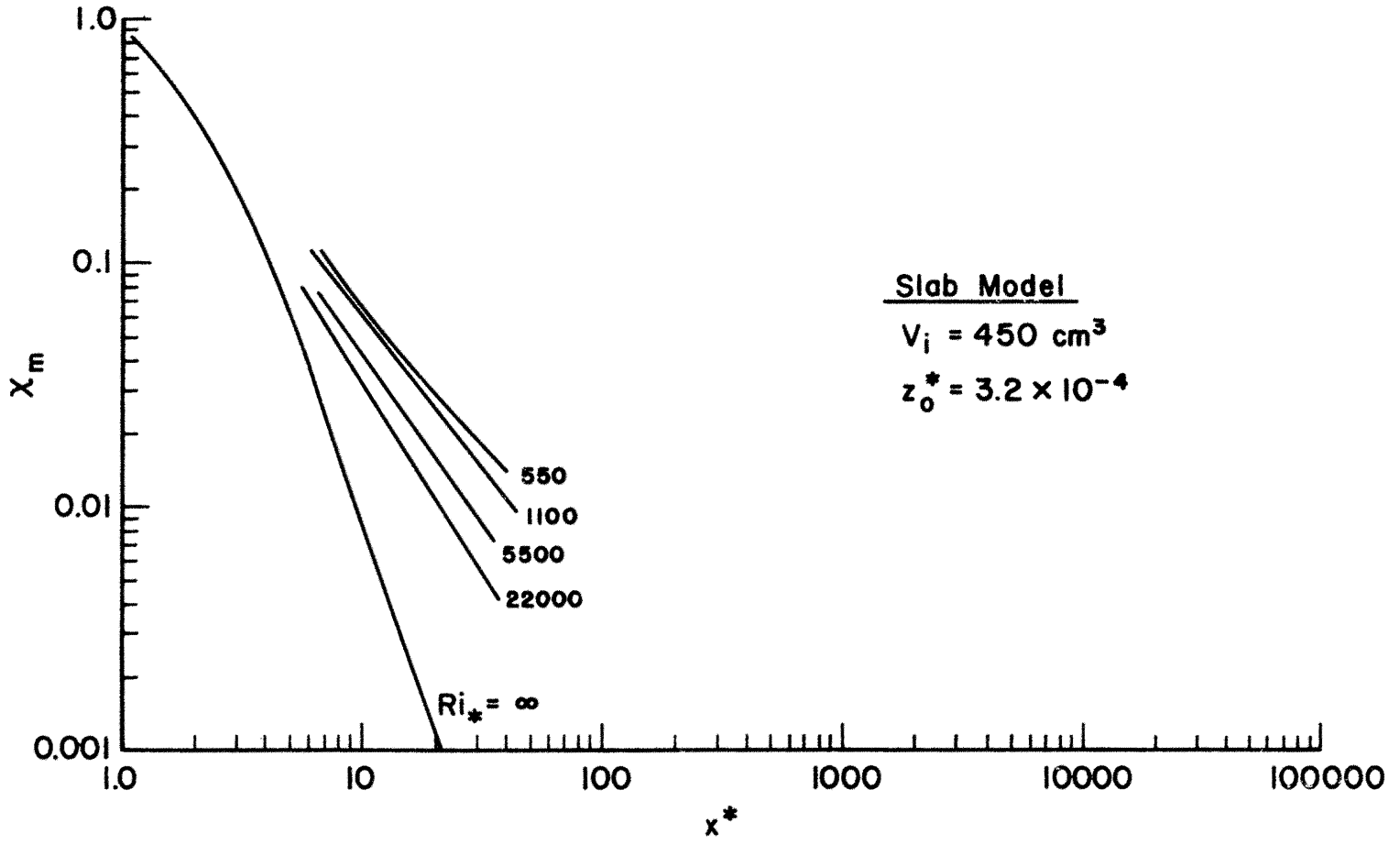

Figure 55a. Cloud Dilution, χ_m, versus Dimensionless Distance, x^*, $u_R \geq 0$, Slab Model Results

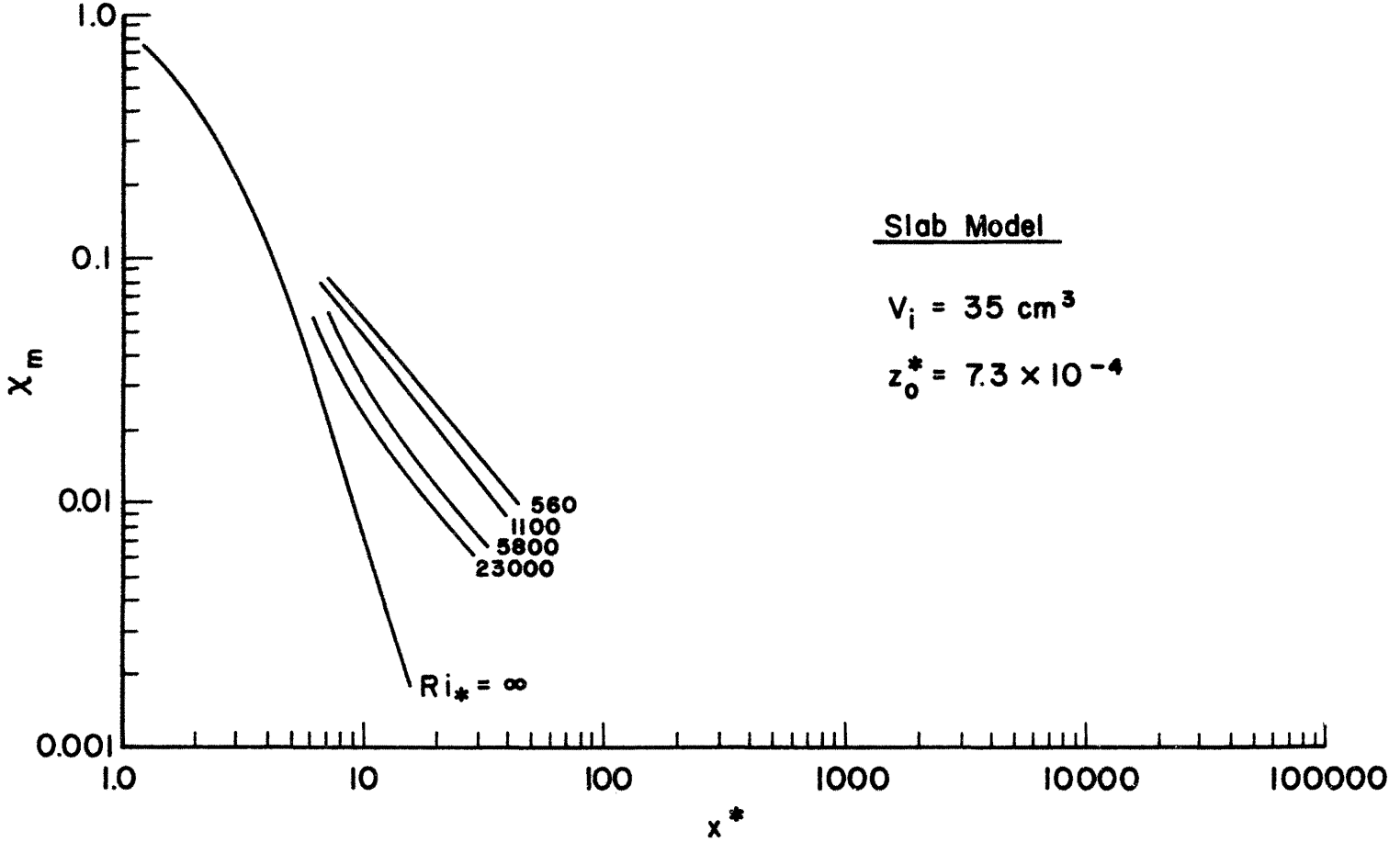

Figure 55b. Cloud Dilution, χ_m, versus Dimensionless Distance, x^*, $u_R \geq 0$, Slab Model Results

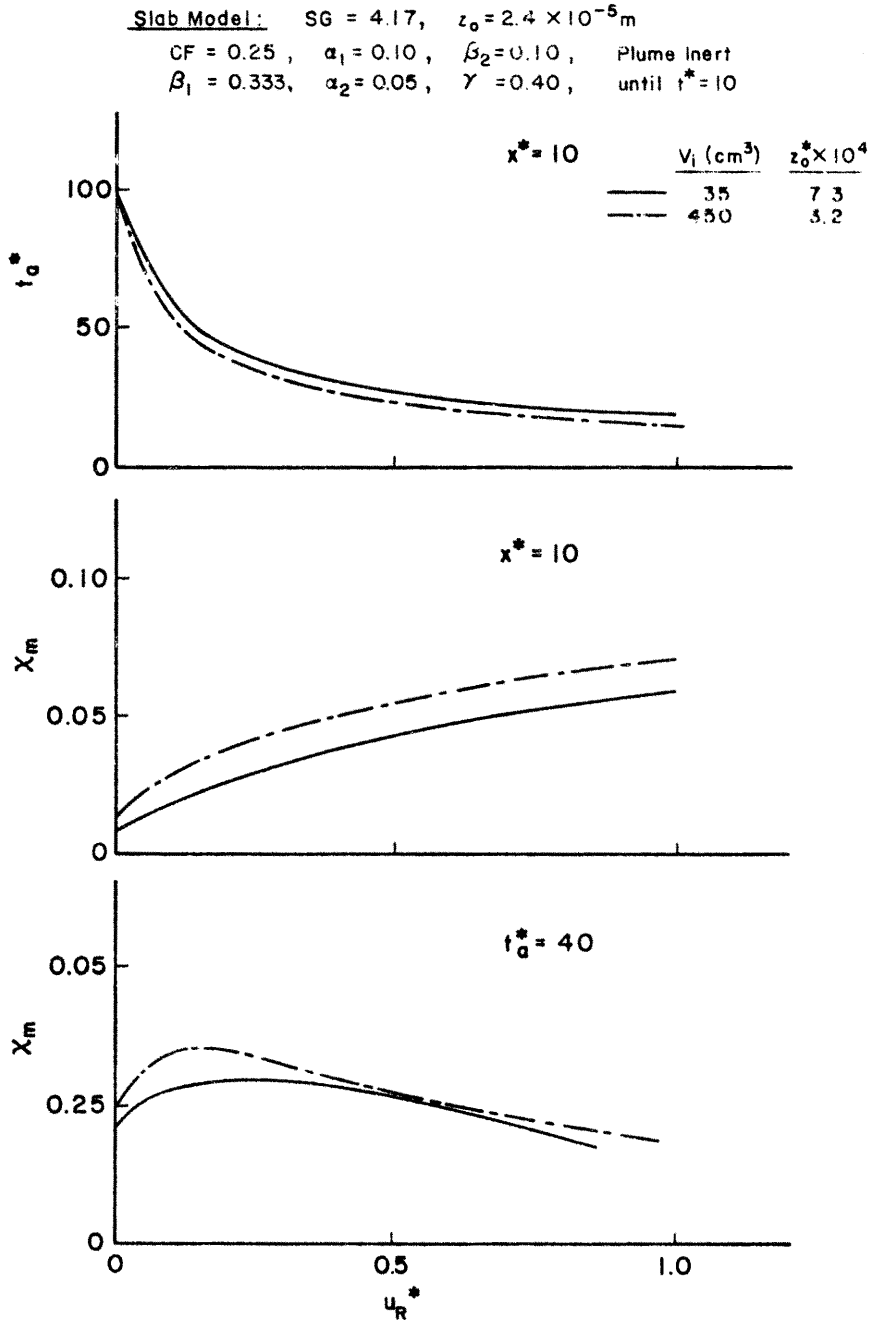

Figure 56. Variation of Arrival Time, t_a^*, and Concentration, χ_m, With Velocity, u_R^*, Slab Model Results

Cloud dilution, χ_m, is plotted versus dimensionless distance, x^*, in Figure 55. These curves may be compared with experimental data found in Figure 31. The values for a given source volume still arrange themselves in the orderly fashion seen during the box model calculations (See Figure 45). There is no overlapping and crossing of curves as noted on the data in Figure 31. Higher concentrations exist at a given dimensionless distance as wind speed increases. There is an indication that such behavior may peak.

Figure 56 displays the independent effects of Ri_* and z_o^* for the slab model results. This figure may be compared to similar distributions shown on Figures 32 and 46. One now sees that the slab model reproduces the nuances of roughness effect found in the data, Figure 32, but missing during box model calculations, Figure 46. Small deviations in calculated magnitudes for t_a^* and χ_m still exist from the measurements; however, the agreement is acceptable for the simple entrainment equations used.

5.2.2 Calculated Evidence for Gravity Waves on the Cloud Surface*

Plots of plume dilution, χ, and height, H/HI, versus radial location R/RI, reveal an interesting cloud surface phenomenon. At first, Figures 57 and 59 display progressive cloud profiles for calm and 0.2 m/sec wind speed conditions. The depth averaged equations produce the appearance of a gravity head at early times; however, an elevated cloud nose cannot be produced by a depth-averaged approach. Notice that the long time cloud height is nearly constant with radius and time for low

---

* Figures 57 through 65 were run with slightly different constants α_1, α_2, and γ. Subsequent analysis suggested values listed in Table 16 were to be preferred; hence these figures will not give results which transpose exactly to Figures 52 through 56.

wind speeds. The cloud grows more rapidly for finite wind speed conditions, because shear layer turbulence permits growth at a rate $u_F \sim u_*$, rather than $u_F \sim 1/R$.

Surface waves develop on the cloud top after about $t^* = 30$. One's first reaction might be that these waves are evidence of numerical instability; however, they are actually a real phenomenon. Sketched on Figure 61 are typical plots of local radial density, ρ , and the cloud height, H , at some time greater than $t^* = 30$. Also displayed is the product $\Delta\rho H^2$ which is the hydrostatic pressure. The product term has a maximum, which means fluid to the left of the maximum will be accelerated toward cloud center, while fluid to the right of the center will be accelerated outward. The result is fluid moving toward cloud center as shown in the second sketch. Such behavior exists during the depth averaged model calculations. As fluid piles up at the cloud center it produces local wave speed conditions which exceed the average fluid velocities and a series of waves move outward. These waves grow in time as they induce additional pressure perturbations, high local velocities, and greater entrainment rates. The typical progression cloud shapes calculated are shown at the bottom of Figure 61.

Picknett (1981) reported the presence of gravity waves during the Parton experiments. He notes:

> "Of special interest is the consistency in cloud height after the initial violent motion has subsided. ...In this slow expansion phase the surface of the disc of cloud is sometimes disturbed by regular undulations, 100-200 mm in amplitude, several meters in wavelength and traveling at perhaps 200 mms^{-1}, which may, perhaps, be gravity waves."

Picknett also commented on the "surprising" rate of cloud dilution after initial cloud collapse. He attributes this mixing to persistent cloud turbulence possibly aided by the gravity waves.

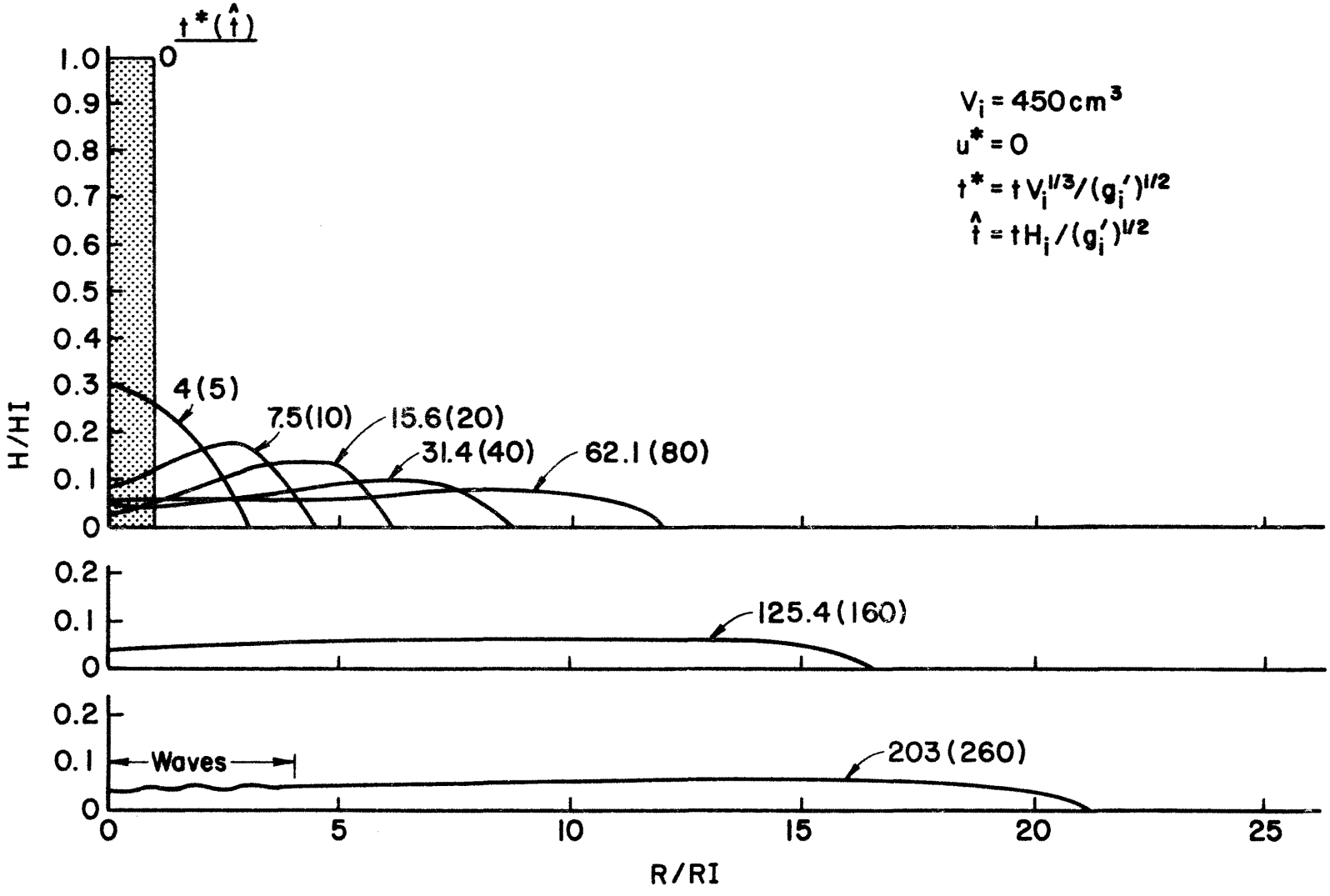

Figure 57. Cloud Height, H/HI, versus Radius, R/RI, Slab Model Result, $Ri_* = \infty$

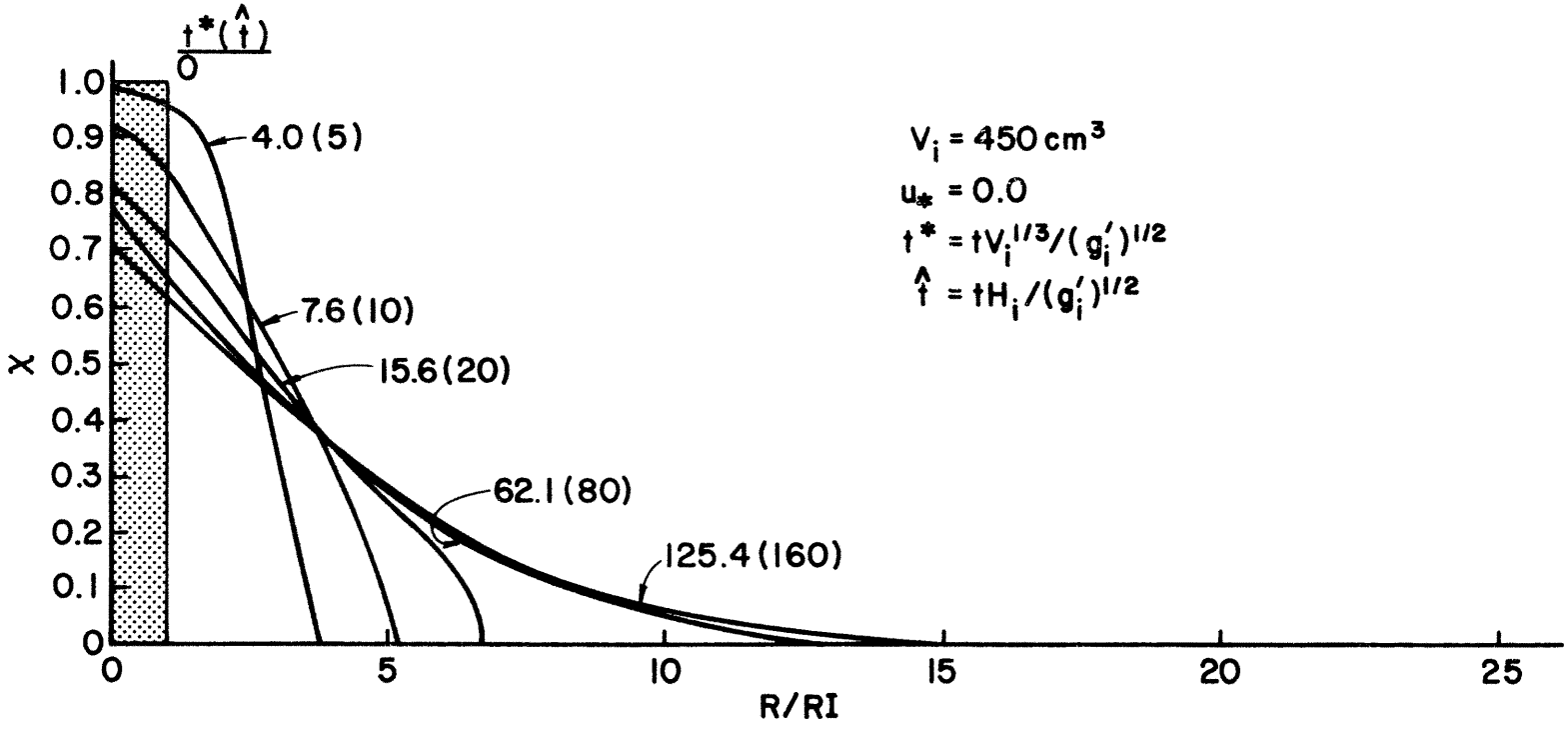

Figure 58. Cloud Dilution, χ_m, versus Radius, R/RI, Slab Model Result, $Ri_* = \infty$

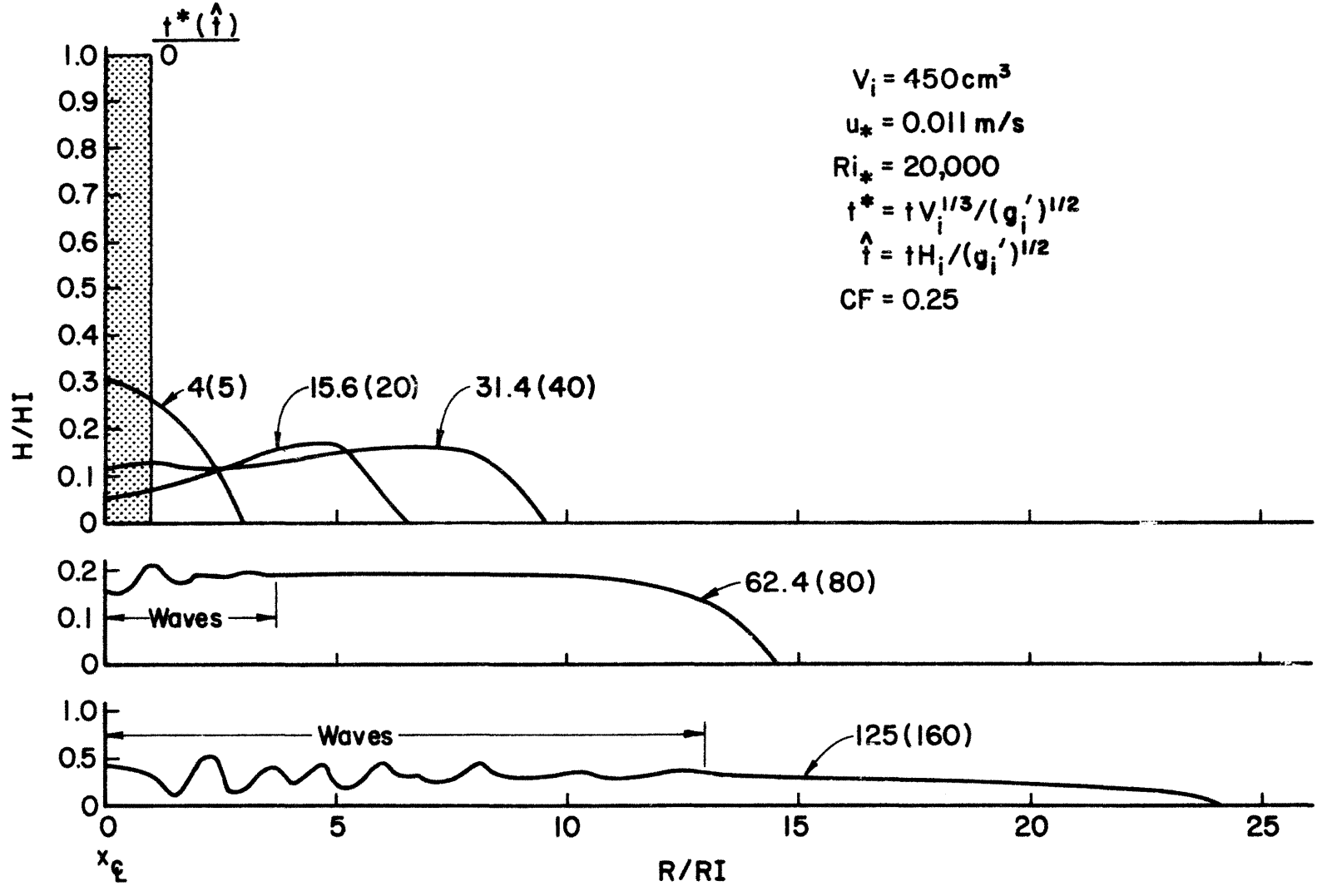

Figure 59. Cloud Height H/HI, versus Radius, R/RI, Slab Model Result, Ri_* = 20000

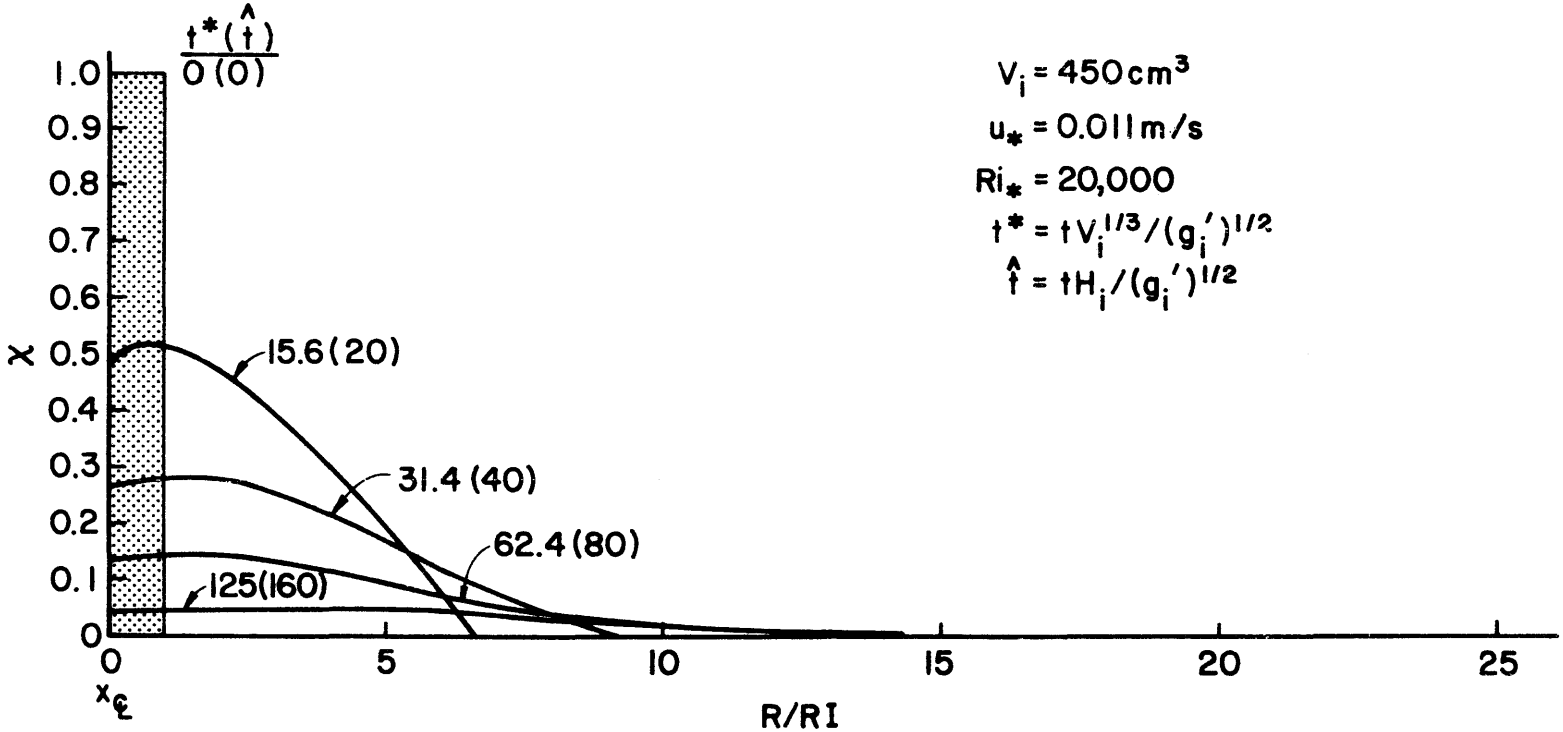

Figure 60. Cloud Dilution, X_m, versus Radius, R/RI, Slab Model Result, Ri_* = 20000

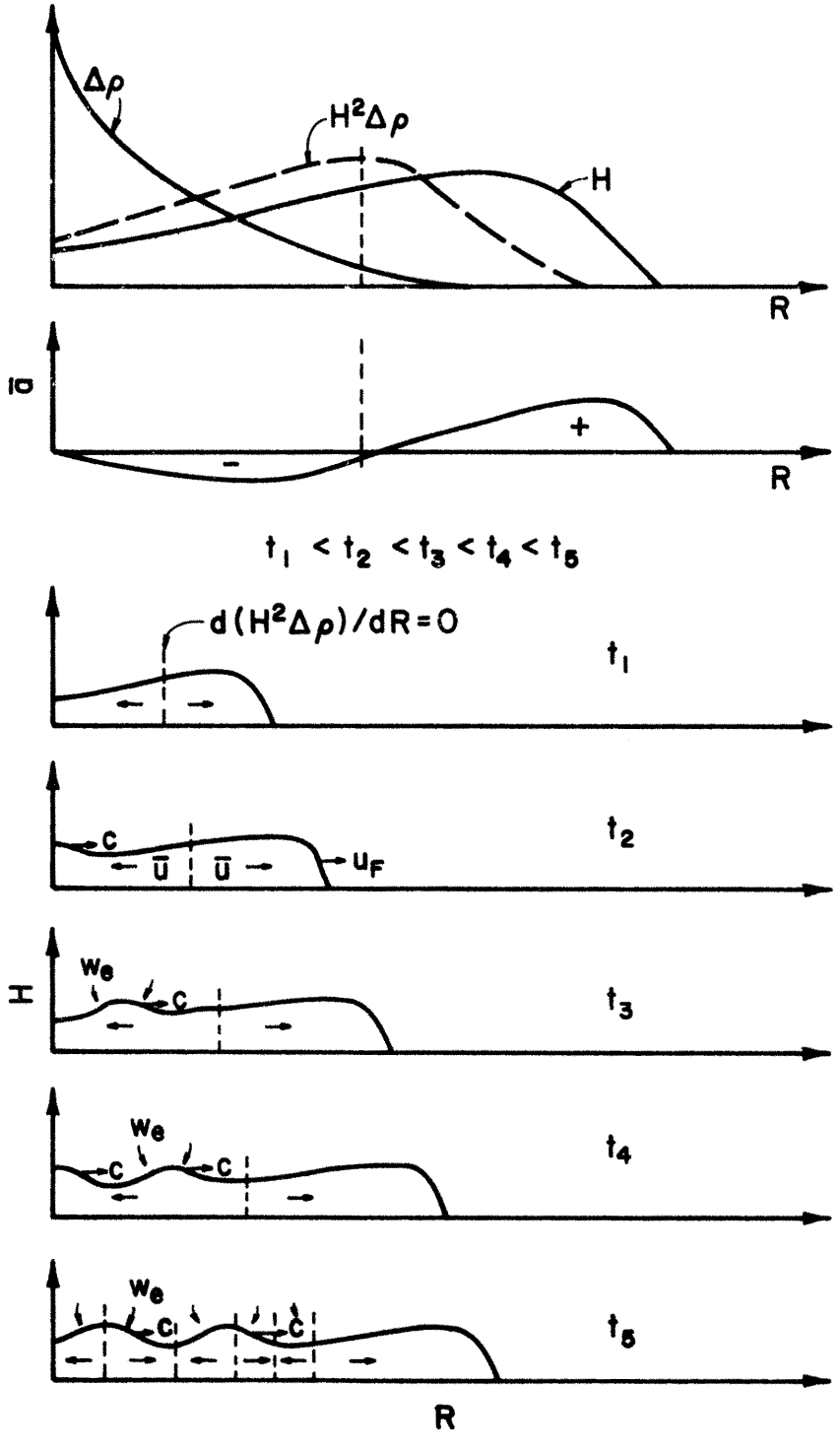

Figure 61. Physics of Surface Waves on Dense Clouds

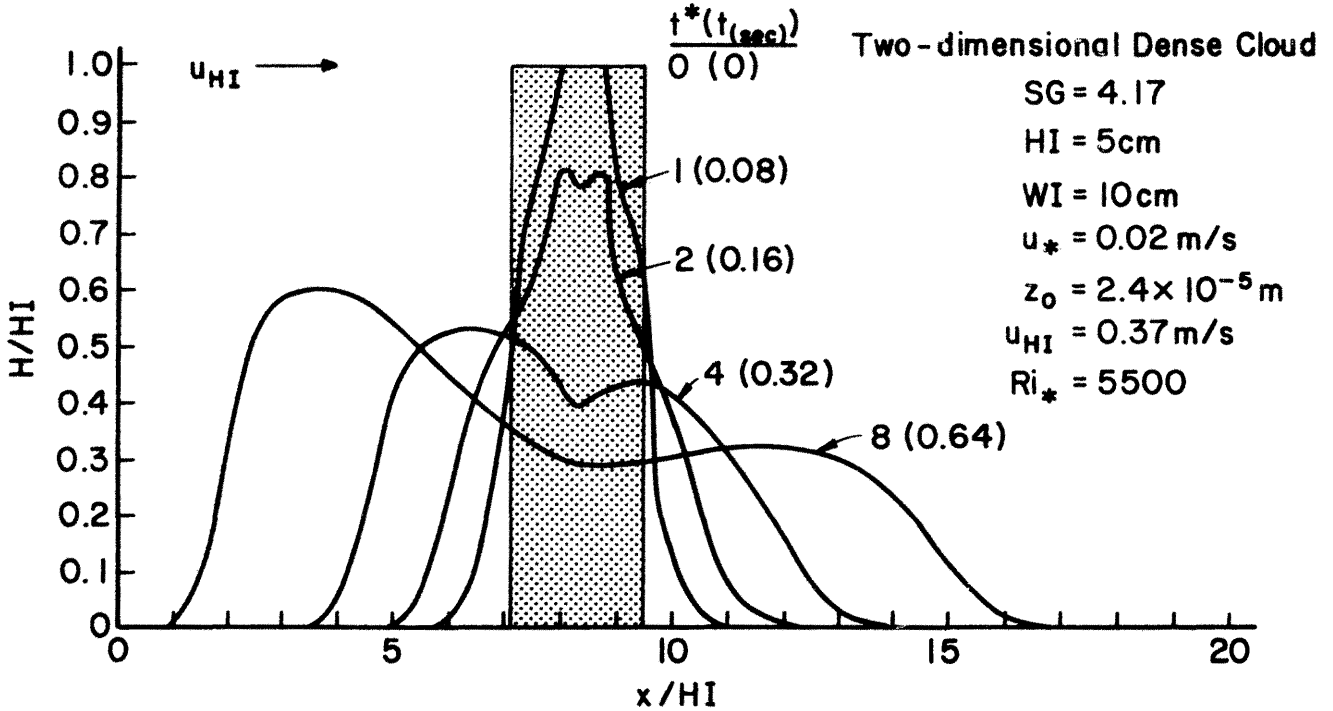

Figure 62. Transient Cloud Growth and Concentration Decay for a Two-Dimensional Dense Cloud, SG = 4.17

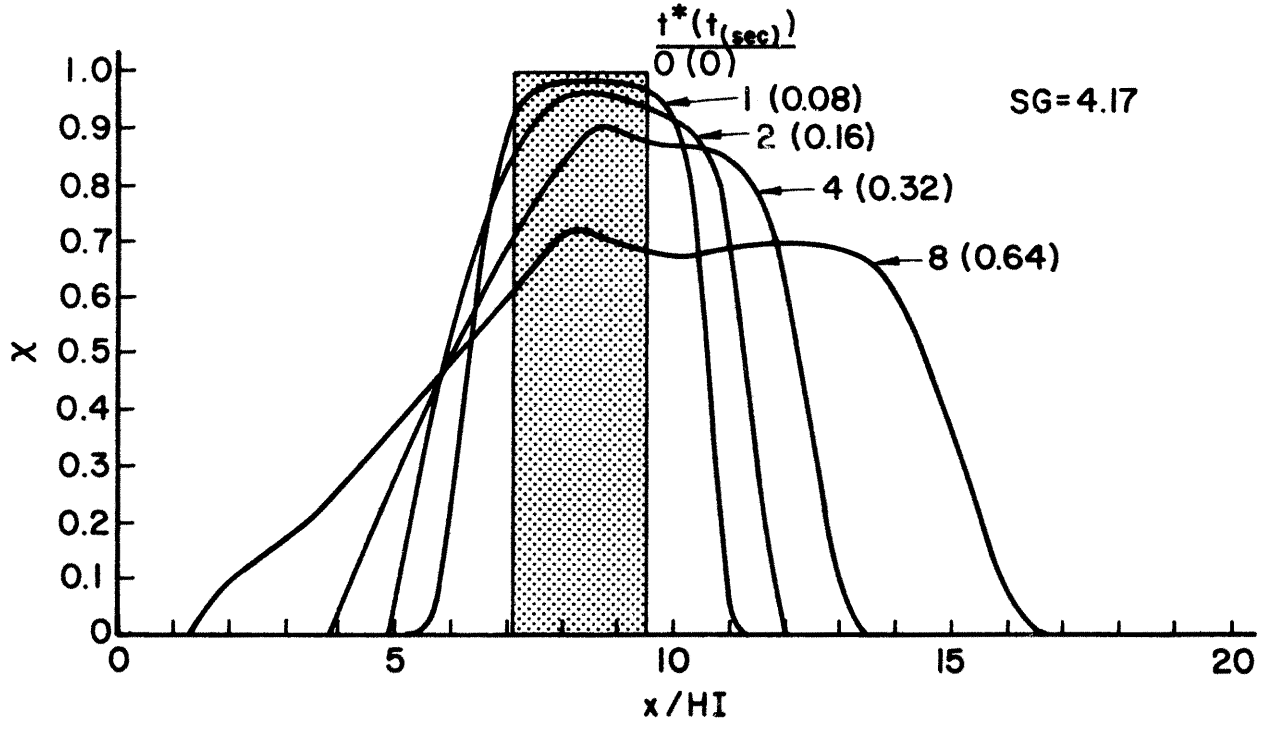

Figure 63. Transient Cloud Growth and Concentration Decay for a Two-Dimensional Dense Cloud, SG = 4.17

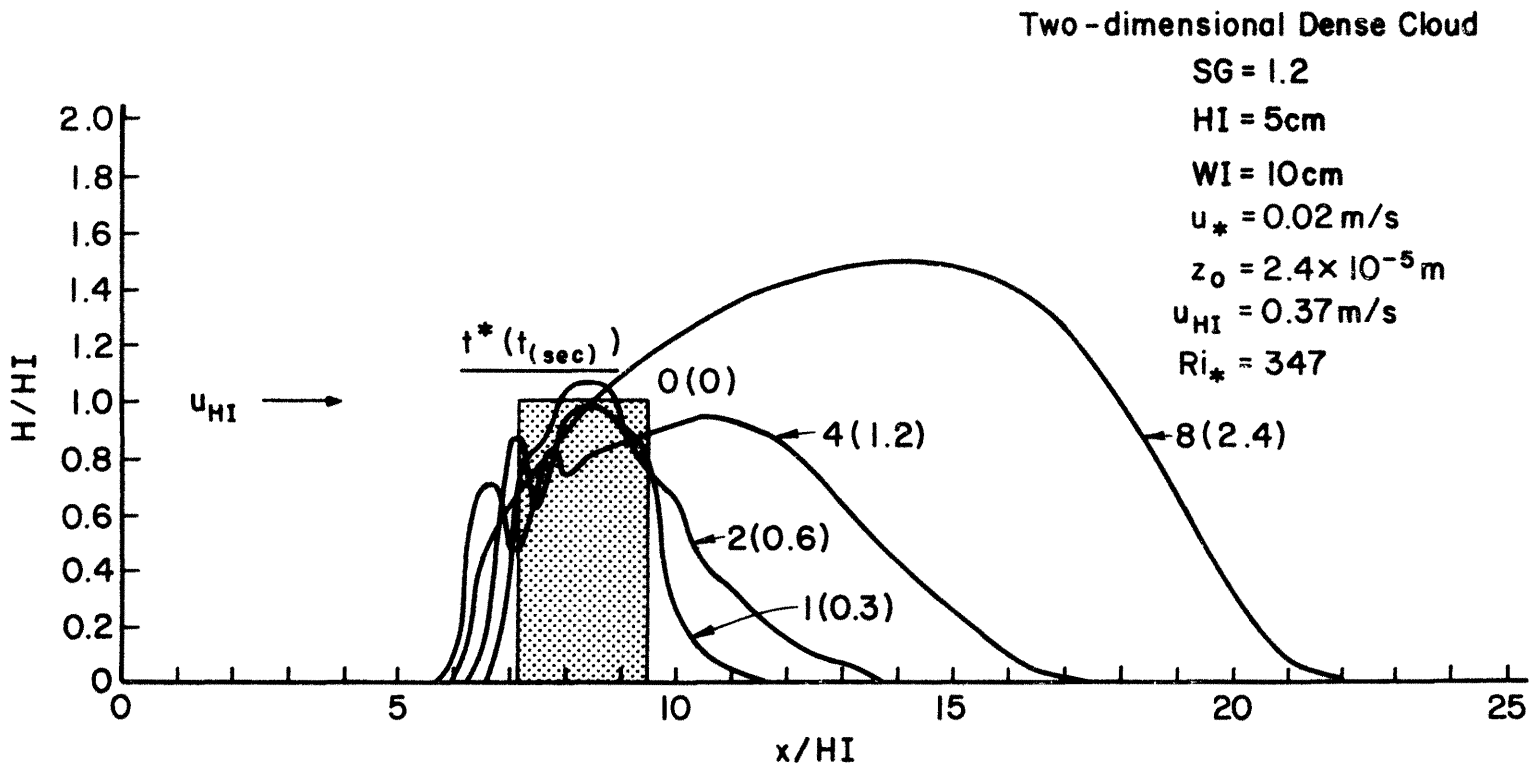

Figure 64. Transient Cloud Growth and Concentration Decay for a Two-Dimensional Dense Cloud, SG = 1.2

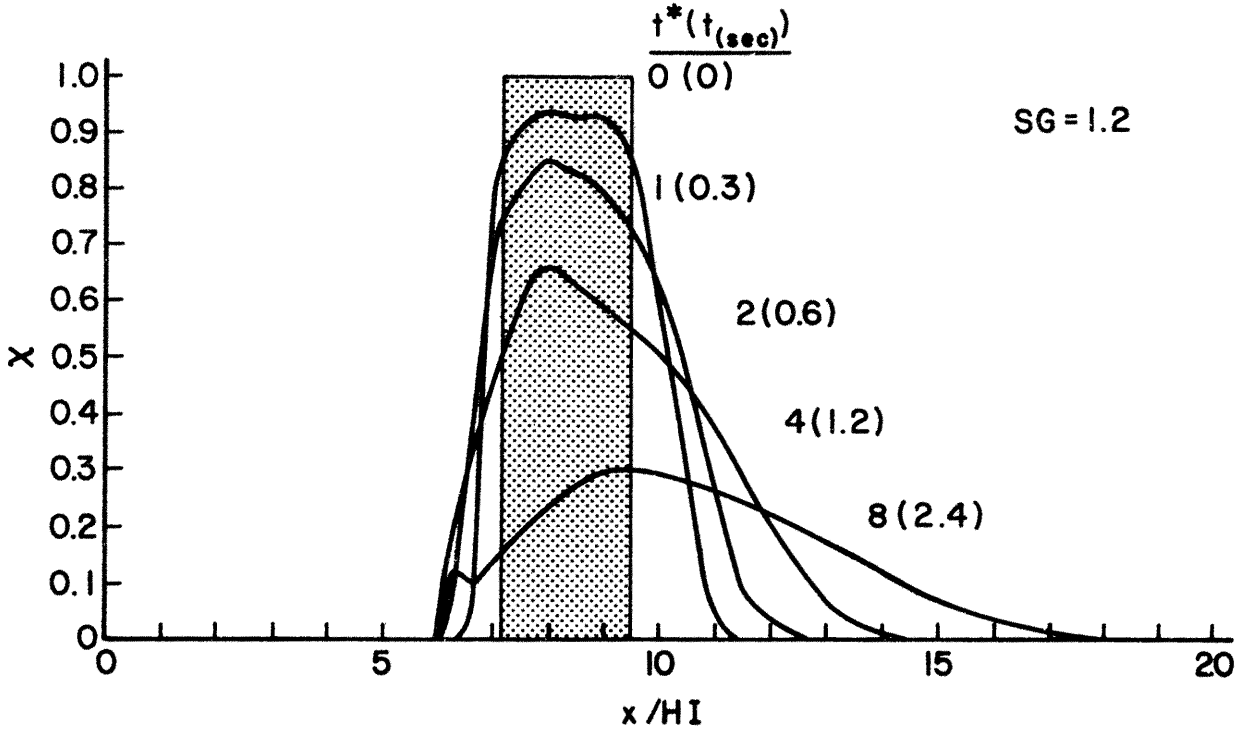

Figure 65. Transient Cloud Growth and Concentration Decay for a Two-Dimensional Dense Cloud, SG = 1.2

5.2.3 Specific Gravity Influence on Dense Gas Behavior

In section 5.1.4 the box model was run to examine specific gravity effects on dense gas cloud behavior. The slab model was also run to examine the influence of specific gravity variations for a cloud volume of 450 cm^3, $Ri_* = 5000$, and $z_o^* = 3.2 \times 10^{-4}$, but SG = 4.17 and 1.2.

As for the box model the deviations due to specific gravity variation were small, less than 5-10% variation in x^* versus t_a^*, less than 30% variation in χ_m versus x^*, and perhaps a maximum of 20% variation in χ_m versus t_a^*.

In the box model the specific gravity enters directly through the frontal velocity equation (See Equation A-4). As initial specific gravity increases the term du^*/dt^* decreases. In the slab model the specific gravity enters the equations indirectly through a relation which relates mass fraction and density (See Equation B-12) and through the initial conditions. The implications of varying specific gravity on $\bar{u}$ are not immediately apparent.

5.2.4 Two-Dimensional Version of Depth Averaged Model*

One disadvantage of advecting the dense cloud center in the cylindrically-symmetric slab model is that the effects of an opposing wind on the upwind cloud front are not reproduced. The slab model was modified to run as a two-dimensional approximation while retaining all the same constants and solution methods. The equations solved are now

$$\frac{\partial(\bar{\rho}^* h^*)}{\partial t^*} + \frac{\partial(\bar{\rho}^* h^* \bar{u}^*)}{\partial x^*} = w_e^* \qquad (5\text{-}3)$$

---

* See Footnote, Section 5.2.2.

$$\left.\begin{aligned} &\frac{\partial(\bar{\rho}^{*}\bar{h}^{*}\bar{u}^{*})}{\partial t^{*}} + \frac{\partial(\bar{\rho}^{*}\bar{h}^{*}\bar{u}^{*2})}{\partial x^{*}} = \tau_{o}^{*} \\ &-\frac{\beta_1}{2}\frac{\partial(h^{*2}(\rho^{*}-1))}{\partial x^{*}} + w_{e}^{*}\left(u_{e}^{*}(H)-\bar{u}^{*}\right) \end{aligned}\right\} \quad (5\text{-}4)$$

$$\frac{\partial(\bar{\rho}^{*}\bar{C}h^{*})}{\partial t^{*}} + \frac{\partial(\bar{\rho}^{*}\bar{h}^{*}\bar{C})}{\partial x^{*}} = 0 \quad (5\text{-}5)$$

where $w_e^* = \alpha_2 |u_e^*(H) - \bar{u}^*| + \gamma u_x^*$, and the initial situation is a square container filled with dense gas. Two cases are examined one for SG = 4.17 and one for SG = 1.2.

Figure 62 displays the variation of the denser gas cloud height H/HI versus longitudinal location X/HI, with time, t^*. The cloud initially surges upwind, deepens at the upwind front as a result of the opposing fluid field, and then shifts downwind. At long times the height distribution becomes symmetric about cloud center again.

Figure 63 shows the spatial variation of concentration in space and time as the cloud slumps. More dilution takes place at the upwind edge where the relative velocity of the wind to the cloud is greater.

Figures 64 and 65 display similar plots for the less dense cloud. In this case very little upwind movement occurs. The cloud moves only one cloud height upwind and then retreats downwind. The cloud attempts to send another gravity head upwind, but this again fails, finally the cloud moves downwind as a semicircular cloud. The concentration curves suggest that although larger relative velocities exist on the upwind side there is relatively less surface over which to entrain. The greater cloud surface downwind presents an opportunity for more dilution even though it occurs at a smaller rate per unit area. Thus the concentration curves in Figure 63 and 65 slump in opposite directions.

6.0 CONCLUSIONS

The primary goal of this laboratory program was to obtain an extensive set of reliable data on the behavior of suddenly released dense gas clouds emitted into various simulated atmospheric boundary layers. Once the data were acquired they were interpreted in terms of appropriate phenomena time and space scales. Finally the data were used to calibrate and evaluate the behavior of two numerical prediction models - a box model and a depth averaged slab model.

6.1 DENSE GAS CLOUD DATA BASE

Concentration and visualization measurements were made for three source sizes and five wind speeds in a low-speed meteorological wind tunnel. The boundary layers developed over the test section appeared to simulate most characteristics of a neutral atmospheric boundary layer to a scale of 1:1000. The combination of experiments performed covered parameter ranges as follows:

$$450 \leq Ri_* \leq 26{,}000 \text{ and } \infty,$$

$$3.2 \times 10^{-4} \leq z_o \leq 7.3 \times 10^{-4},$$

$$0 \leq Re_R \leq 5100,$$

$$0 \leq Re_* \leq 0.08,$$

$$2000 < Re < 8000, \text{ and}$$

$$0 \text{ and } 2 \times 10^{-6} < \tilde{z}_o < 35 \times 10^{-6}.$$

To place these values in context previous authors report data ranging from

$$620 < Ri_* < 3130 \text{ and}$$

$$1 \times 10^{-7} < \tilde{z}_o < 3 \times 10^{-4}.$$

The low value range of Re_* reflects the presence of laminar sublayer over a smooth ground surface. The range of Re studied assures the reader that the initial gravity head behavior should be Reynolds number independent. All terms are defined on Table 2.

All experiments were replicated several times. The statistical behavior of the data suggests that the arrival time, t_a, and cloud dilution, χ_m, are distributed in a normal manner, whereas the arrival time of the maximum concentration, t_m, varies in a log-normal manner. Standard deviations of all variables were significantly large with respect to the measured means. This suggests due caution must be taken when predicting concentrations from formulas designed to predict mean values.

Mean values and standard deviations for all cases are included in Tables 4 through 12. Values are dimensionless; however, the original dimensional quantities can be retrieved by use of the time and space scales included in Table 2.

6.2 SCALED BEHAVIOR OF DENSE GAS CLOUD DATA

All data were interpreted in a dimensionless manner appropriate to permit interpretation over a wide prototype range. The results of the discussions found in Sections 4.2 and 4.3 are summarized as follows:

- In calm situations the defined length and time scales, $L = V_i^{1/3}$ and $T = V_i^{1/3}/(g_i')^{1/2}$, were sufficient to collapse the results for source sizes studied to a single set of curves. Variation in specific gravity produces small perturbations from these curves.

- Sources released in shear flows were advected downwind. The arrival time, t_a^*, measured at a given position, x^*, varied almost entirely with Richardson number, Ri_*; although there was a small roughness length, z_o^*, influence perceived. As Ri_* increased then the arrival time, t_a^*, decreased.

- Increased shear flow velocities for a given source size resulted in initially a lower rate of dilution; however, subsequent velocity increases produced faster dilution rates. The net effect was an initial

increase in maximum concentration measured at a given measurement location with increasing wind speed followed by a decrease.

• Vertical concentration profiles measured very near the source location (ie. $R^* = 2$ to 4) were all similar in magnitude and varied in an exponential or power law manner with height. At greater distances during wind shear situations concentrations appeared normally distributed in the vertical.

• In a wind field the cloud center seems to initially hesitate and then accelerate to near the local advection speeds. Cloud trajectories at the lower wind speeds display a characteristic sin-shaped signature at early times when the gravity driven cloud frontal speed dominates spreading rates. Subsequent cloud growth is linear as the cloud spreads about its center proportional to u_* or the background turbulence rate.

• Plotting the data in the coordinates, $\tilde{X}$ versus $\tilde{x}$, recommended by Fay and Ranck (1981) reveals that decay at a -3 power-law rate similar to a passive plume is not likely to occur before $\tilde{x} = 1.0$ or $x^* = Ri_*^{1/2}$. Only a small fraction of the current data lies in this range, since the minimum Ri_* condition equalled 445, and all measurements were for $x^* < 60$.

• Neutral gas density cloud release studied correlated well against time and length scales suggested by Yang and Meroney (1972), ie. $T = V_i^{1/3}/u_*$ and $L = V_i^{1/3}$. Dilution correlates well versus dimensionless time, $\approx{t} = t/T$; however, spatial locations should also be a function of $\approx{z}_o = z_o/L$. Equations (4-8) to (4-10) predicted the arrival time, arrival of the maximum concentration time, and departure times very well. The dilution rates assymptotically approached the Equations (4-5) and (4-7) for instantaneous point and line sources. These correlations are reassuring, since the relations are known to correlate with full

scale atmospheric transport behavior. Agreement of the data with these relations suggests the laboratory boundary layers did simulate larger scale phenomena.

6.3 CHARACTERISTICS OF DATA COMPARISON TO BOX MODEL

The simple box model performed surprisingly well. Indeed, within the expected variability of the phenomena, it is hard to justify using a more complex model to predict hazards for isolated releases of toxic or flammable gases, where heat transfer, humidity, and building or topographical effects are not significant. The results from the discussions in Section 5.1 are summarized as follows:

- The box model reproduced the mean behavior of χ_m, x^*, and t_a^* for calm conditions within the error bounds of the measurements.

- The box model reproduced the general character of cloud advection by a wind field. The cloud location, x^*, is a function of arrival time, t_a^*, Richardson number, Ri_*, and roughness length, z_o^*. The constants selected are a compromise, and the resultant equations slightly overpredict cloud transport at the higher wind speeds.

- The box model predicts increased dilution rates for χ_m versus t_a^* for all wind speeds. The model cannot reproduce the smaller decay rates shown by the data at low wind speeds. Yet the model also underpredicts cloud dilution rates at higher wind speeds.

- The box model does not predict a specific velocity for which concentrations at a measurement location are maximum. Concentrations continued to increase for all velocity conditions surveyed.

- The box model was used to critique the experimental data of Hall (1979) and Picknett (1981). Comparisons suggest that the Hall release time persisted too long for the data to be treated as an instantaneous source. The model reproduced the cloud growth data for several Picknett

runs examined; however, model results suggest that visual plume depths quoted are at the edges of a cloud where concentrations vary in an exponential manner with height.

- The box model predicts higher concentrations at a measurement location as specific gravity increases. Variation in dimensionless parameters is rather small over the range $1.2 \leq SG \leq 4.17$.

This report has primarily dealt with the generalized implications of the effect of negative plume density on the dispersion of gas clouds. Appendix C discusses the implications of density effects with respect to a specific hazardous gas - Propane. Calculations with the calibrated numerical box model suggest that existing hazard predictions using previous recommendations are significantly in error.

6.4 CHARACTERISTICS OF DATA COMPARISON TO DEPTH-AVERAGED MODEL

The depth averaged model permitted prediction of the radial variations of cloud properties about its center. Such a feature permitted the model to predict special features of the Eulerian measurements noted in Section 4.3.3. The model was used to reproduce the behavior of x^* vs t_a^*, χ_m vs t_a^*, and χ_m vs x^* as the Richardson number, Ri_*, changed in steps of wind speed. The comments found in Section 5.2 suggest that:

- The slab model reproduces the behavior of a dense gas suddenly released in a calm situation within the error bounds of the measurements. This agreement required the use of an ad hoc entrainment relation where $w_e = \alpha_1 |\bar{u}_g|^2 + \alpha_2 |\bar{u}_g| + \gamma u_*$.

- The depth averaged equations with the associated entrainment relation produced variations in t_a^* and χ_m noted in the data as wind speed, u_R^*, varied. The quantitative magnitudes of these parameters were not exactly predicted; however, the tentative nature of the entrainment model did not justify further tuning of constants.

• At $t^* > 30$ gravity waves appeared on the cloud surface. These waves grew and moved as time progressed. It is probable that these waves play a key role in cloud dilution.

• Although results were similar to the box model, the depth averaged model produced somewhat larger variations with specific gravity. Nonetheless the dimensionless variations are generally small; hence it may be difficult to resolve this difference in behavior with experimental data.

6.5 RECOMMENDATIONS

Improvements are possible in both source production and measurement procedures. Versions of numerical models may continue to appear faster than data; nonetheless the following ideas might improve the science.

• Measurements of the velocity fields within dense clouds should be considered. Advection models generally attempt to correct for changes in cloud kinematics in an ad hoc manner without any actual wind field measurements.

• The statistics of a single cloud release situation should be measured in the laboratory in detail. Even including measurements of this report such information is scarce.

• Fast response laboratory measurement techniques should be developed which are operational in temperature fields and sensitive to lower concentrations (ie. 1 - 100 ppm).

• Numerical models should only be calibrated against mean values from sets of measurements. Tuning constants against individual and unique releases is futile since the standard deviations measured are normally large.

• Box models can produce general plume behavior, but they are not likely to replicate behavior over a wide range of cloud release

situations. It may be necessary to specify different constants for ranges of the parameters Ri_* and z_o^* if the models are to be routinely used for hazard predictions. Otherwise the tendency to over or under-predict certain quantities should be acknowledged.

- The version of the depth averaged model used advected the cloud center independently. Although convenient, this approach is not required. A model which solved the depth averaged equations over a horizontal cartesian coordinate system would include assymmetric plume entrainment at the upwind cloud edge.

- The experimental data showed a regular increase of maximum concentration with wind speed at moderate distances and a peaking of concentration with increase of wind speed at greater distances. Numerical models (Havens, 1979; Raj, 1981) predict a regular increase of LFL distance with wind speed for LNG spills. Such models should be run for an instantaneous release case to determine if they also predict concentration peaks with wind speed.

- Raj (1982) recommends that models which assume no specific heat capacity effects, humidity effects, or heat transfer are adequate to predict real cold gas behavior since such perturbations are minimal. On the other hand Zeman (1982) argues thermally driven mixing is dominant. Careful laboratory experiments should be performed to examine heat transfer effects on cold gas dispersion.

- All the experiments discussed in this report were performed for neutral atmospheric stratification. It would be worthwhile to examine the effects of stable stratification on cloud transport and dispersion.

References

1. Akins, R. E. (1976), Wind Pressures on Buildings, Ph. D. Thesis, Civil Engineering Department, Colorado State University, Fort Collins, Colorado, 295 pp.

2. American Gas Association (1974), LNG Safety Program, Interim Report on phase II work, AGA Project IS-3-1, Battelle - Columbus Laboratories, 493 pp.

3. Book, D. L., Boris, J. P. and Hain K. (1976), Flux Corrected Transport III: Minimal-error FCT Algorithms, J. Comp. Phys., Volume 20, pp. 397-431.

4. Boyle, G. J. and Kneebone, A. (1972), Laboratory Investigations Into the Characteristics on LNG Spills on Water, Evaporation, Spreading and Vapor Dispersion, Shell Research, Ltd. Report to API, 80 pp.

5. Brandeis, J. and Kansa, E. J. (1982), Numerical Simulation of Liquefied Fuel Spills: I. Instantaneous Release into a Confined Area, Lawrence Livermore National Laboratory Paper UCRL-87205-1, 225 pp.

6. Brandeis, J. and Ermak, D. L. (1982), Numerical Simulation of Liquefied Fuel Spills: II. Instantaneous and Continuous LNG Spills on an Unconfined Water Surface, Lawrence Livermore National Laboratory Paper UCRL 87205-2, Livermore, Calif., 31 pp.

7. Britter, R. E. and Griffiths, R. F. ed. (1982), Dense Gas Dispersion, Elsevier Scientific Publications Company, Amsterdam, Netherlands.

8. Britter, R. E. (1980), The Ground Level Extent of a Negatively Buoyant Plume in a Turbulent Boundary Layer, Atmospheric Environment, Volume 14, pp. 779-785.

9. Burgess, D. S., Biordi, J. and Murphy, J. (1972), Hazards of Spillage of LNG into Water, U.S. Department of Interior, Bureau of Mines, Pittsburgh, Report of Investigations, Z-70099-9-12395.

10. Burgess, D. S., Murphy, J. N., Zabetakis, M. G. (1970), Hazards Associated With the Spillage of Liquefied Natural Gas on Water, Report of Investigations 7448, U. S. Department of Interior, Bureau of Mines, Washington D. C., 35 pp.

11. Champagne, F. H. and Sleicher, C. A. (1967), Turbulence Measurements with Inclined Hot-Wires, Part 2, Journal of Fluid Mechanics, Volume 28, pp. 177-182.

12. Colenbrander, G. W. (1980), A Mathematical Model for the Transient Behavior of Dense Vapour Clouds, Kininblijke/Shell Laboratories, Amsterdam, Netherlands, 29 pp.

13. Counihan, J. (1975), Adiabatic Atmospheric Boundary Layers: A Review and Analysis of Data From the Period 1880-1972, Atmospheric Environment, Volume 9, No. 10, pp. 971-905.

14. Cox, R. A. and Carpenter, R. J. (1980), Further Development of a Dense Vapor Cloud Dispersion Model for Hazard Analysis, Heavy Gas and Risk Assessment, D. Reidel Publishing Company, pp. 55-87.

15. Doo, Y. C. (1979), A Two-dimensional Model of Negatively Buoyant Vapor and Dispersion, Master of Science Dissertation, Department of Mechanical Engineering, Mass. Inst. of Technology, 94 pp.

16. ESDU (1974), Characteristics of Atmospheric Turbulence Near the ground, Engineering Science Data Item Numbers 74030 and 74031, 251 Regent St., London, U.K., October, 55 pp.

17. Eidsvik, K. J. (1980), A Model for Heavy Gas Dispersion in the Atmosphere, Atmospheric Environment, Volume 14, pp. 764-777.

18. England, W. G., Teuscher, L. H., Hauser, L. E., and Freeman, B. E. (1978), Atmospheric dispersion of Liquefied Natural Gas Vapor Clouds Using SIGMET, a Three-dimensional Time-dependent Hydrodynamic Computer Model. Proc. 1978 Heat Transfer and Fluid Mechanics Institute (Ed. C. T. Crave and W. L. Grasshandler), Stanford University Press, pp. 4-20.

19. Ermak, D. L., Chan, S. T., Morgan, D. L. and Morris, L. K. (1981), A Comparison of Dense Gas Dispersion Model Simulations with Burro Series LNG Spill Test Results, UCRL Preprint 86713 Lawrence Livermore Laboratory, Livermore, Calif., 46 pp.

20. Fay, J. A. (1982), Some Unresolved Problems of LNG Vapor Dispersion, MIT/Gas Research Institute LNG Workshop, Cambridge, Mass, 24 March 1982, ed. R. C. Reid, 14 pp.

21. Fay, J. A. and Ranck, D. (1981), Scale effects in liquified fuel gas vapor dispersion. Report for DOE Control No. DE-AC02-77EV04204, Fluid Dynamics Laboratory, Mass. Inst. of Technology, Cambridge, Mass., 95 pp.

22. Fay. J. A. (1980), Gravitational Spread and Dilution of Heavy Vapor Clouds, 2nd Intl. Symposium on Stratified Flows, Proceedings of, Trandheim, Norway, 24-27 June, pp. 471-494.

23. Feldbauer, G. F., Heigl, J., May, W., McQueen, W. and Whipp, R. (1972), Spills of LNG on Water-Vaporization and Downwind Drift of Combustible Mixtures, Report No. EE61E-62, ESSO Research and Engineering Co., Florham Park, N. J., 195 pp.

24. Germeles, A. E. and Drake, E. M. (1975), Gravity Spreading and Atmospheric Dispersion of LNG Vapor Clouds. Proceedings of 4th Intl. Symp. on Transport of Hazardous Cargoes by Sea and Inland Waterway, Jacksonville, Florida, USA, pp. 519-539.

25. Hall, D. J. (1979), Further Experiments on a Model of an Escape of Heavy Gas, Report LR(312) AP, Warren Springs Laboratory, Stenevage, Herts, U.K., 47 pp.

26. Hall, D. J., Barrett, C. F. and Ralph, M. O. (1974), Experiments on a Model of an Escape of Heavy Gas. Report LR217(AP), Warren Springs Laboratory, Dept. of Trade and Industry, Stenevage, Herts, U.K., 25 pp.

27. Hall, D. J., Hollis, E. J., and Ishaq, H. (1982), A Wind Tunnel Model of the Porton Dense Gas Spill Field Trials, Warren Springs Laboratory Report L394(AP), Dept. of Industry, Stevenage, Hertfordshire, U.K., 106 pp.

28. Hartwig. S. (1982), Heavy Gases and Risk Assessment, Proceedings of Second Symposium, 25-26 May 1982, Frankfurt, West Germany.

29. Hartwig, S. (1980), Heavy Gases and Risk Assessment, Proceedings of Proceedings of a Symposium, 3-4 September 1979, Frankfurt/Man, West Germany, D. Reidel Publishing Company, 306 pp.

30. Haugen, D. A. (editor), Workshop on Micrometeorology, American Meteorological Society, Boston, Mass., pp. 392.

31. Havens, J. A. (1980), An Assessment of the Predictability of LNG Vapor Dispersion From Catastrophic Spills on Water, J. Hazardous Materials, Volume 3, pp. 167-278.

32. Havens, J. A. (1979), A Description and Assessment of the SIGMET LNG Vapor Dispersion Model, Report No. CG-M-3-79, U. S. Coast Guard, Dept. of Transportation, Washington D. C., 215 pp.

33. Havens, J. A. (1977), Predictability of LNG Vapor Dispersion from Catastrophic Spills Onto Water: An Assessment, Office of Marshal Maine Safety, U. S. Coast Guard, Washington, D. C..

34. Hinze, J. O. (1975), Turbulence, McGrawHill Book Co., New York, 790 pp.

35. Humbert-Basset, R. and Montet, A. (1972), Dispersion dans l'atmosphere d'un nauge gazeus forme par epandage de G. N. L. sur le sol, 3rd Int. Conf. on Liquefied Natural Gas, September, Washington D. C., 23 pp.

36. Hunt, J. C. R. and Feinholz, H. (1975), Wind Tunnel Simulation of the Atmospheric Boundary Layer: A Report on Euromech 50, J. Fluid Mechanics, Volume 70, Part 3, August, pp. 543-559.

37. Huppert, H. E. and Simpson, J. E. (1980), The Slumping of Gravity Currents. J. Fluid Mechanics, Volume 99, Part 4, pp. 785 799.

38. Jagger, S. F. and Karsen, G. D. (1980), The Accidental Release of Dense Flammable and Toxic Gases From Pressurized Containment-Transition from Pressure Driven to Gravity Driven Phase, Proceedings 11th NATO/CCMS ITM Conference on Air Pollution Modeling and Its Applications, Amsterdam, 24-27 November 1980, 13 pp.

39. Kneebone, A. and Prew, L. R. (1974), Shipboard Jettison Tests of LNG Onto the Sea, 4th International Conference on LNG, Algeria, June.

40. Koopman, R. P., Kamppinen, L. M., Hogan, W. J., and Lind, C. D. (1981), Burro Series Data Report, LLNL/NWC 1980 LNG Spill Tests, Lawrence Livermore Laboratory, Livermore, Calif.

41. Koopman, R. P., Bowman, B. R. and Ermak, D. L. (1979), Data and Calculations of Dispersion of 5-m^3 LNG Spill Tests, UCRL-52876, Lawrence Livermore Laboratory, Livermore, Calif., 31 pp.

42. Lohmeyer, A., Meroney, R. N. and Plate, E. J. (1981), Model Investigations of the Spreading of Heavy Gases Released from an Instantaneous Volume Source at the Ground, Air Pollution Modeling and Its Application I, C. de Wispeloere, ed., Plenum Publishing Corp., pp. 433-448.

43. Martin, J. C. and Moyce, W. J. (1952), Part IV, An Experimental Study of the Collapse of Liquid Columns on a Rigid Horizontal Surface; Part V, In a Medium of Lower, but Comparable, Density, Physical Transactions of the Royal Society, Series A, Volume 244, pp. 312-334.

44. Maxworthy, T. (1980), On the Formation of Nonlinear Internal Waves From the Gravitational Collapse of Mixed Regions in Two and Three Dimensions, J. Fluid Mechanics, Volume 99, Part 1, pp. 47-64.

45. Meroney, R. N. and Neff, D. E. (1982), Dispersion of vapor from LNG Spills - Simulation in a Meteorological Wind Tunnel: Six Cubic Meter China Lake Spill Series, J. Wind Engineering and Industrial Aerodynamics, Volume 10, pp 1-19.

46. Meroney, R. N., Neff, D. E., and Cermak, J. E. (1978), Wind Tunnel Modeling of LNG Spills, American Gas Association Transmission Conference, Proceedings, 8-10 May 1978, Montreal, Canada, 25 pp.

47. Neff, D. E. and Meroney, R. N. (1982), The Behavior of LNG Vapor Clouds: Laboratory Tests on the Similarity of Heavy Plume Dynamics, Colorado State University Report, CER81-82DEN-RNM25, Gas Research Institute Contract No. 5014-352-0203, 135 pp.

48. Neff, D. E. and Meroney, R. N. (1981), The Behavior of LNG Vapor Clouds: Wind-Tunnel Simulations of 40 m^3 LNG Spill Tests at China Lake Naval Weapons Center, California, Colorado University Report CER81-82DEN-RNM1, Gas Research Institute Report No. 80/0094, 164 pp.

49. Picknett, R. G. (1981), Dispersion of Dense Gas puffs Released in the Atmosphere at Ground Level, Atmospheric Environment, Volume 15, pp. 509-525.

50. Raithby, G. D. (1976), A Critical Evaluation of Upstream differencing Applied to Problems Involving Fluid Flow, Computer Methods in Applied Mechanics and Engineering, Volume 9, pp. 75-103.

51. Raj, P. K. (1982), Heavy Gas Dispersion, A State of the art Review of the Experimental Results and Models, Lecture notes prepared by von Karman Institute Lecture Series 1982-1983 on Heavy Gas Dispersal, 8-12 March 1982, 73 pp.

52. Raj, P. K. (1981), Models for Cryogenics Liquid Spill Behavior on Land and Water, J. Hazardous Materials, Volume 5, pp. 111f.

53. Rosenzweig, J. J. (1980), A Theoretical Model for the Dispersion of Negatively Buoyant Vapor Clouds, Ph.D. Dissertation, Department of Mechanical Engineering, Mass. Inst. of Technology, September 1980, 162 pp.

54. Sandborn, V. A. (1972), Resistance Temperature Transducers, Metrology Press, Fort Collins, Colo., USA, 545 pp.

55. Simpson, J. and Britter, R. (1979), The Dynamics of the Head of a Gravity Current Advancing over a Horizontal Surface. J. Fluid Mechanics, Volume 94, No. 3, pp. 477-496.

56. te Riele, P. H. M. (1977), Atmospheric Dispersion of Heavy Gases Emitted at or Near Ground Level, 2nd Int. Loss Prevention Symp., Heidelberg, W. Germany, pp. 347-357.

57. van Ulden, A. P. (1979), The Unsteady Gravity Spread of a Dense Cloud in a Calm Environment, 10th International Technical Meeting on Air Pollution Modeling and its Application, NATO-CCMS, Rome, 26 October 1979, 9 pp.

58. van Ulden, A. P. (1974), On the Spreading of a Heavy Gas Released Near the Ground, Proceedings of First International Loss Prevention Symposium, the Hogue/Delft, Elsevier, Amsterdam, pp. 431-439.

59. Wilson, D. J. and Netterville, D. D. J. (1981), A Fast Response Heated Element Concentration Detector for Wind Tunnel Applications, J. of Wind Engineering and Industrial Aerodynamics, Volume 7, No.1, pp. pp. 55-64.

60. Yang, B. T. and Meroney, R. N. (1972), On Diffusion from an Instantaneous Point Source in a Neutrally Stratified Turbulent Boundary Layer with a Laser Light Scattering Probe, Project THEMIS Technical Report No. 20, Office of Naval Research Contract No. N00014-68-A-0493-0001, Colorado State University, Fort Collins, 219 pp.

61. Zeman, O. (1982), The Dynamics and Modeling of Heavier-than-air Cold Gas Releases, Atmospheric Environment, Volume 16, No. 4, pp. 741-751.

TABLES

Table 1
Source Cup Dimensions

Cup Number	Radius, R (cm)	Length, L (m)	Volume Calculated (cm^3)	Water Displacement Volume (cm^3)
1	5.20	10.3	437	450
2	3.75	7.4	163	165
3	2.25	4.4	35	35

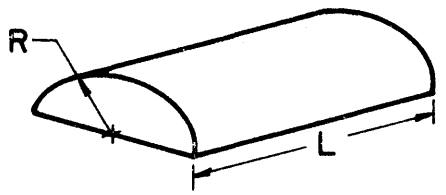

Table 2

Test Conditions

Freon-12 Releases in Air

Run No.	V_i (cm^3)	u_R (m/s)	L (m)	T (sec)	U (m/s)	u_L (m/s)	Re	Re_R	Re_*	Ri_*	Ri	t_s^*	$t_{I/B}^*$	t_v^*	u_R^*	u_L^*	$\tilde{z}_o$ x10^6
1	35	0.0	0.033	0.032	1.017	0.00	2226	0	0.000	∞	∞	~0	4.65	13.06	0.00	0.00	0.0
2		0.2	0.033	0.032	1.017	0.17	2226	440	0.015	11135	25.52	~0	4.65	13.06	0.20	0.17	6.7
3		0.4	0.033	0.032	1.017	0.35	2226	880	0.031	2784	6.38	~0	4.65	13.06	0.39	0.34	13.9
4		0.6	0.033	0.032	1.017	0.54	2226	1320	0.046	1237	2.84	~0	4.65	13.06	0.59	0.53	20.7
5		1.0	0.033	0.032	1.017	0.86	2226	2200	0.077	445	1.02	~0	4.65	13.06	0.88	0.85	34.6
6	165	0.0	0.055	0.042	1.316	0.00	4826	0	0.000	∞	∞	~0	4.65	16.90	0.00	0.00	0.0
7		0.2	0.055	0.042	1.316	0.18	4826	733	0.015	18559	42.77	~0	4.65	16.90	0.15	0.14	3.1
8		0.4	0.055	0.042	1.316	0.38	4826	1467	0.031	4640	10.69	~0	4.65	16.90	0.30	0.29	6.4
9		0.6	0.055	0.042	1.316	0.57	4826	2200	0.046	2062	4.75	~0	4.65	16.90	0.46	0.43	9.5
10		1.0	0.055	0.042	1.316	0.92	4826	3667	0.077	742	1.71	~0	4.65	16.90	0.76	0.68	16.0
11	450	0.0	0.077	0.049	1.554	0.00	7962	0	0.000	∞	∞	~0	4.65	19.97	0.00	0.00	0.0
12		0.2	0.077	0.049	1.554	0.19	7962	1027	0.015	25982	59.73	~0	4.65	19.97	0.13	0.12	1.9
$^{\Delta}$13		0.4	0.077	0.049	1.554	0.39	7962	2053	0.031	6496	14.93	~0	4.65	19.97	0.26	0.25	3.9
14		0.6	0.077	0.049	1.554	0.59	7962	3080	0.046	2887	6.64	~0	4.65	19.97	0.39	0.38	5.8
15		1.0	0.077	0.049	1.554	0.96	7962	5133	0.077	1039	2.39	~0	4.65	19.97	0.64	0.62	9.7

(Cont'd next page)

$^{\Delta}$This case chosen for 100 releases and measurements at x = 0.40, y = 0.0, z = 0.002 m

Table 2 (Continued)

Freon-12: SG = 4.17, MW = 120.1

$z_R \simeq 10\text{cm}$

$g = 9.81\ \text{m/sec}^2$

$\nu_a = 1.5 \times 10^{-5}\ \text{m}^2/\text{sec}$

$u_*/u_\delta = 0.048$

$z_o = 2.4 \times 10^{-5}\ \text{m}$

$t_s^* \lesssim$ Eq. (2-7)

$t_v^* \gtrsim$ Eq. (2-8)

$t_{I/B}^* \gtrsim C_z^{-2/3}$ where

$C_z \sim 0.1$

$\delta \simeq 20\ \text{cm}$

$\tilde{z}_o = z_o\, u_*/(g_i'\, V_i)^{1/2} = Re_*/Re$

$L = V_i^{1/3}$

$T = V_i^{1/6}/(g_i')^{1/2}$

$U = V_i^{1/6}\,(g_i')^{1/2}$

$Re = V_i^{1/2}(g_i')^{1/2}/\nu$

$Re_* = u_*\, z_o/\nu$

$Ri_* = \dfrac{g_i'\, V_i^{1/3}}{u_*^2}$, $Ri = \dfrac{g_i'\, V_i^{1/3}}{u_R^2}$

$Re_R = u_R\, V_i^{1/3}/\nu$

Table 3
Shear Layer Characteristics for Model Boundary Layers

x (m) / u_R (m/s)	(1) $\left(\frac{u_*}{u_\delta}\right)_{Slope}$			(2) $\left(\frac{u_*}{u_\delta}\right)_{Clauser}$			(3) $\left(\frac{u_*}{u_\delta}\right)_{Ludwig-Tillman}$			(4) θ/δ			(5) δ^*/δ		
	-0.5	0.5	1.5	-0.5	0.5	1.5	-0.5	0.5	1.5	-0.5	0.5	1.5	-0.5	0.5	1.5
0.2	0.059	0.052	0.053	0.059	0.054	0.054	0.047	0.048	0.046	0.115	0.116	0.109	0.171	0.175	0.177
0.4	0.050	0.047	0.046	0.053	0.052	0.052	0.051	0.048	0.049	0.081	0.085	0.088	0.113	0.123	0.129
0.6	0.046	0.039	0.046	0.053	0.050	0.050	0.052	0.048	0.049	0.092	0.083	0.083	0.121	0.118	0.118
1.0	0.033	0.047	0.047	0.051	0.046	0.046	0.050	0.047	0.049	0.074	0.072	0.072	0.103	0.099	0.097
Avgs Chosen	0.048			0.048			0.048			0.085			0.120		

x (m) / u_R (m/s)	(6) H (Shape Factor)			(7) u'/u at z = 1 cm			(8) u'/u_* z = 1 cm	(9) w'/u_* z = 1 cm	(10) $z_o \times 10^5$ (m)
	-0.5	0.5	1.5	-0.5	0.5	1.5	0.5	0.5	0.5
0.2	1.487	1.509	1.626	0.120	0.125	0.165	1.30	0.70	14.2
0.4	1.395	1.453	1.465	0.145	0.148	0.180	1.67	0.39	3.4
0.6	1.315	1.419	1.419	0.140	0.138	0.170	1.64	0.50	1.0
1.0	1.392	1.372	1.352	0.130	0.114	0.127	1.47	0.62	4.6
Avgs Chosen	1.40			0.15			1.55	0.55	2.4

(Cont'd. next page)

Table 3 (Continued)

u_R (m/s) \ x (m)	(11) (z_o) intercept $\times 10^5$ (m)		(12) z_{SL} (m)	(13) p			(14) $T_{E_1} = \int R dt$ * (sec)	(15) $T_{E_2} = (t)_{R=1/e}$ * (sec)	(16) Λ_1 * (m)	(17) Λ_2 * (m)	(18) k_p * (m^{-1})	(19) Λ_{k_p} * (m)
	-0.5	0.5	1.5	0.5	-0.5	0.5	2	0.5	0.5	0.5	0.5	0.5	0.5
0.2	14.2	11.8	5.9	0.0060	0.10	0.12	0.13	-	-	-	-	-	-
0.4	7.1	2.9	4.8	0.0040	0.13	0.12	0.13	0.26	0.220	0.072	0.062	-	-
0.6	3.2	0.6	3.0	0.0030	0.13	0.12	0.13	0.40	0.160	0.156	0.048	-	-
1.0	0.2	3.5	3.5	0.0015	0.13	0.12	0.13	0.15	0.124	0.088	0.107	2.80	0.052
Avgs		5.1		-	0.13			-	-	0.100	0.070	-	0.050

* at x = 0.5 m
z = 1 cm

(3) $\left(\frac{u_*}{u_\delta}\right)^2_{\text{Ludwig Tillman}} = 0.123(10^{-0.678H})\ (\frac{u_\delta\ \theta}{\nu})^{-0.268}$ if $10^3 < \frac{u_\delta\ \theta}{\nu} < 10^4$ with $\delta \simeq 20$ cm

(4) $\frac{\theta}{\delta} = \int_o^1 \frac{u}{u_\delta}(1 - \frac{u}{u_\delta})d\xi$

(5) $\frac{\delta_*}{\delta} = \int_o^1 (1 - \frac{u}{u_\delta})d\xi$

(6) $H = \delta^*/\theta$

(10) $z_o = z_r \exp\ (-k \frac{u_R}{u_*})$

Table 4

Mean Cloud Behavior: u_R = 0 m/s

V_i (cm^3)	u_R (m/s)	x^Δ (cm)	y (cm)	N	$\overline{t_a^*}$	$\sigma_{t_a^*}$	$\overline{t_m^*}$	$\sigma_{t_m^*}$	$\overline{t_d^*}$	$\sigma_{t_d^*}$	χ_m %	σ_{χ_m} %	x^*
35	0	5	0	4	1.58	1.3	13.6	4.6	–	–	33.20	7.60	1.52
		10	0	4	4.50	2.3	17.5	2.8	–	–	27.00	1.30	3.05
		15	0	5	13.90	2.6	22.9	1.5	–	–	10.60	4.20	4.57
		20	0	5	17.70	1.8	27.3	2.9	–	–	9.30	2.10	6.09
		25	0	5	31.80	7.5	43.8	6.1	–	–	5.00	1.30	7.61
		30	0	5	38.40	5.3	49.3	5.6	–	–	2.20	0.62	9.14
		40	0	4	109.60	31.7	150.2	61.5	–	–	0.83	0.74	12.20
		50	0	3	220.90	23.8	256.1	37.8	–	–	0.13	0.02	15.20
165	0	10	0	4	4.00	0.6	11.1	1.8	–	–	57.50	5.90	1.82
		20	0	5	12.30	1.0	19.0	2.2	–	–	15.90	3.40	3.64
		30	0	4	26.90	3.4	34.5	4.4	–	–	7.30	3.20	5.45
		40	0	6	45.20	12.9	54.4	13.8	–	–	2.60	1.70	7.27
		50	0	5	98.00	15.9	136.0	63.0	–	–	0.57	0.25	9.09
		60	0	4	297.50	88.1	397.1	59.9	–	–	0.24	0.09	10.90
450	0	10	0	5	6.00	0.7	15.7	2.2	–	–	66.90	3.60	1.30
		20	0	4	10.20	0.3	20.0	1.7	–	–	40.10	4.90	2.60
		30	0	5	17.30	0.9	27.0	2.4	–	–	18.90	3.80	3.91
		40	0	6	30.60	2.8	41.8	2.6	–	–	7.40	1.90	5.21
		50	0	5	47.30	2.0	60.2	3.0	–	–	2.70	0.50	6.51
		60	0	6	80.10	21.4	101.1	20.3	–	–	0.93	0.25	7.81
		80	0	3	80.60	36.0	214.0	96.0	–	–	0.67	0.14	10.40
		0	10	4	4.60	1.1	15.9	1.5	–	–	65.50	2.90	1.30
		0	20	4	10.00	1.1	22.7	3.1	–	–	28.00	5.70	2.60
		0	30	4	17.50	3.3	27.4	2.6	–	–	16.80	4.10	3.91
		0	40	3	28.10	1.5	38.7	3.1	–	–	7.40	0.30	5.21
		20	20	3	25.10	1.6	34.9	2.4	–	–	9.00	2.20	6.41
		40	45	3	46.00	0.3	59.7	3.4	–	–	2.80	0.30	7.83
		-10	0	3	4.60	0.6	16.4	2.9	–	–	71.80	5.60	-1.30

$^\Delta$ z = 2 mm all points

Table 5

Mean Cloud Behavior: u_R = 0.2 m/s

V_i (cm^3)	u_R (m/s)	x^{Δ} (cm)	z (mm)	N	$\overline{t_a^*}$	σ_{t_a}	$\overline{t_m^*}$	σ_{t_m}	$\overline{t_d^*}$	σ_{t_d}	χ_m %	σ_{χ_m} %	x^*
35	0.2	10	2	5	2.6	1.1	9.5	1.2	247	39	19.20	5.40	3.05
		15	2	5	7.6	2.6	15.9	2.3	257	43	11.40	2.00	4.57
		20	2	5	15.2	3.0	24.6	2.5	360	71	6.60	2.60	6.09
		25	2	3	16.7	1.6	26.2	3.6	348	57	3.10	1.40	7.62
		30	2	5	26.8	2.2	36.6	1.7	417	57	3.20	0.90	9.14
		40	2	5	46.2	9.5	90.6	67.0	466	38	1.50	0.70	12.20
		50	2	5	62.7	11.0	109.0	54.0	542	44	0.71	0.30	15.20
		75	2	5	127.0	38.0	280.0	66.0	654	36	0.40	0.20	22.90
		100	2	5	221.0	40.0	388.0	24.0	736	36	0.15	0.06	30.50
		150	2	4	271.0	13.0	557.0	56.0	987	33	0.13	0.04	45.70
165	0.2	10	2	5	4.5	1.40	11.9	2.1	356	37	45.60	8.40	1.82
		20	2	3	11.9	0.76	18.9	1.3	388	24	13.00	1.30	3.64
		30	2	4	23.9	1.50	39.5	4.7	461	108	11.20	1.20	5.45
		40	2	5	35.3	7.40	115.0	51.0	540	33	4.30	0.80	7.27
		50	2	5	58.0	7.70	157.0	17.0	605	40	1.78	0.20	9.09
		60	2	5	64.9	19.00	200.0	44.0	629	39	1.41	0.05	10.90
		80	2	5	103.0	13.00	290.0	221.0	755	19	0.88	0.08	14.50
		100	2	5	141.0	13.00	341.0	21.0	471	17	0.61	0.07	18.20
		150	2	5	242.0	29.00	481.0	64.0	633	32	0.37	0.08	27.30
		200	2	5	283.0	23.00	644.0	50.0	1228	81	0.32	0.05	36.40
450	0.2	20	2	5	8.2	0.7	13.6	1.7	351	17	38.00	4.2	2.60
		30	2	5	15.7	0.6	21.9	2.2	460	14	17.50	2.6	3.91
		40	2	5	24.1	0.9	31.4	3.0	467	10	6.10	1.2	5.21
		50	2	4	34.2	2.3	75.7	25.7	571	12	3.35	0.6	6.51
		60	2	5	45.2	5.2	142.0	38.0	592	6	2.75	0.1	7.81
		80	2	5	73.6	11.5	228.0	13.0	629	9	1.81	0.2	10.40
		100	2	5	112.0	23.0	293.0	7.0	703	12	1.31	0.1	13.00
		150	2	5	173.0	9.0	359.0	50.0	864	85	0.72	0.2	19.50
		200	2	4	259.0	34.0	500.0	54.0	675	10	0.50	0.1	26.00

$^{\Delta}$ y = 0 all points

Table 6

Mean Cloud Behavior: u_R = 0.4 m/s

V_i (cm^3)	u_R (m/s)	x^Δ (cm)	z (mm)	N	$\overline{t_a^*}$	$\sigma_{t_a^*}$	$\overline{t_m^*}$	$\sigma_{t_m^*}$	$\overline{t_d^*}$	$\sigma_{t_d^*}$	χ_m %	σ_{χ_m} %	x^*
35	0.4	10	2	5	6.2	1.8	15.5	2.5	104	17.0	24.60	9.00	3.05
		15	2	5	8.7	3.2	17.5	2.5	132	43.0	11.60	5.60	4.57
		20	2	5	14.4	4.9	26.3	6.1	145	25.0	7.10	2.40	6.09
		25	2	5	21.0	2.6	39.9	17.4	157	27.0	3.20	1.10	7.62
		30	2	5	21.2	9.5	41.0	27.0	225	32.0	3.50	1.70	9.14
		40	2	5	27.6	4.4	49.5	18.7	217	24.0	2.27	0.70	12.20
		50	2	5	45.2	8.5	94.2	44.2	276	28.0	1.00	0.20	15.20
		75	2	5	67.6	10.5	169.0	43.0	327	28.0	0.68	0.20	22.90
		100	2	5	91.7	5.1	233.0	20.0	381	48.0	0.40	0.05	30.50
		150	2	5	151.0	32.0	284.0	43.0	420	42.0	0.18	0.07	45.70
		200	2	5	207.0	39.0	343.0	43.0	525	43.0	0.12	0.07	60.90
165	0.4	10	2	5	5.5	0.7	12.8	2.2	169	13.0	42.70	7.00	1.82
		20	2	4	12.8	0.9	19.3	1.6	184	23.0	10.60	1.70	3.64
		30	2	5	18.9	2.0	28.7	5.1	222	24.0	5.90	1.80	5.45
		50	2	5	35.2	2.5	97.6	11.7	265	23.0	2.40	0.20	9.09
		60	2	5	39.3	1.1	120.0	11.0	270	20.0	2.00	0.30	10.90
		80	2	5	59.0	6.2	166.0	16.0	314	40.0	1.37	0.20	14.50
		100	2	5	70.9	4.8	189.0	13.9	357	20.8	1.08	0.20	18.20
		150	2	6	103.0	19.0	262.0	35.0	422	35.0	0.65	0.20	27.30
		200	2	5	156.0	27.0	304.0	21.0	452	24.0	0.35	0.05	36.40
450	0.4	10	2	5	2.2	0.5	8.5	0.8	191	13.0	75.80	3.00	1.30
		20	2	5	8.4	0.5	14.4	1.5	215	8.0	35.90	5.40	2.60
		30	2	5	14.0	1.0	20.7	1.9	245	9.0	13.90	3.70	3.91
		40	2	5	22.6	2.0	37.6	8.6	255	13.0	6.90	0.90	5.21
		50	2	5	30.0	0.6	48.1	11.5	278	13.0	4.00	1.10	6.51
		60	2	5	33.4	2.3	85.2	23.7	254	91.0	3.43	0.80	7.81
		80	2	5	45.4	3.6	140.0	8.6	332	18.0	2.97	0.20	10.40
		100	2	2	68.0	10.0	168.0	5.0	350	8.0	2.25	0.20	13.00
		150	2	5	93.0	13.9	223.0	15.0	416	13.0	1.27	0.10	19.50
		200	2	5	119.0	20.0	280.0	16.0	488	32.0	0.83	0.09	26.00
450	0.4	40	2	95	20.7	2.8	30.8	8.0	277	26.0	6.80	1.4	5.21

$^\Delta$ y = 0 all points

Table 7

Mean Cloud Behavior: u_R = 0.6 m/s

V_i (cm^3)	u_R (m/s)	x^{Δ} (cm)	z (mm)	N	$\overline{t_a^*}$	$\sigma_{t_a^*}$	$\overline{t_m^*}$	$\sigma_{t_m^*}$	$\overline{t_d^*}$	$\sigma_{t_d^*}$	χ_m %	σ_{χ_m} %	x^*
35	0.6	10	2	3	3.60	0.4	4.4	2.0	62.0	6.3	92.30	6.50	3.05
		15	2	5	5.87	1.4	14.2	2.3	86.2	11.3	11.90	3.30	4.57
		20	2	5	11.10	2.5	20.4	3.5	95.1	9.9	6.60	2.20	6.09
		25	2	5	16.10	4.1	32.2	12.1	101.0	11.0	4.50	1.80	7.62
		30	2	4	17.30	0.7	30.5	4.0	126.0	8.0	3.00	0.50	9.14
		40	2	5	24.00	4.4	42.6	13.4	131.0	9.0	2.52	1.20	12.20
		50	2	7	25.80	4.4	48.6	17.2	135.0	14.0	1.67	0.50	15.20
		75	2	5	43.80	9.6	88.1	15.9	188.0	13.0	0.76	0.25	22.90
		100	2	5	58.10	26.1	133.0	25.0	227.0	29.0	0.38	0.20	30.50
		150	2	4	71.10	15.0	159.0	26.0	251.0	33.0	0.18	0.07	45.70
		200	2	5	106.00	4.0	202.0	19.0	334.0	48.0	0.14	0.03	60.90
165	0.6	10	2	5	4.20	0.5	10.5	1.2	97.6	10.1	30.80	12.30	1.82
		20	2	5	10.50	2.1	18.3	1.7	110.0	5.0	12.40	4.70	3.64
		30	2	5	14.90	1.6	36.2	14.2	128.0	32.0	6.78	1.60	5.45
		40	2	5	19.50	2.0	34.8	7.1	135.0	8.0	5.69	1.60	7.27
		50	2	5	24.50	3.7	60.7	20.4	140.0	20.0	3.84	0.80	9.09
		60	2	5	32.40	3.8	55.9	17.1	157.0	18.0	2.74	0.50	10.90
		80	2	5	34.90	5.4	78.9	24.6	186.0	11.0	1.82	0.30	14.50
		100	2	5	46.90	2.6	116.0	14.0	212.0	8.0	1.48	0.20	18.20
		150	2	5	58.90	18.7	171.0	8.0	263.0	32.0	0.73	0.10	27.30
		200	2	5	92.40	11.2	195.0	14.0	301.0	25.0	0.54	0.06	36.40
450	0.6	10	2	5	3.50	0.7	10.5	1.6	130.0	9.0	73.20	.5	1.30
		20	2	5	8.60	0.3	14.2	1.5	137.0	12.0	25.70	7.80	2.60
		30	2	5	13.50	1.0	24.6	9.2	132.0	7.0	12.70	4.50	3.91
		40	2	5	18.50	0.8	32.0	8.7	157.0	5.0	7.76	1.50	5.21
		50	2	5	23.90	2.8	56.7	12.3	164.0	11.0	5.91	0.30	6.51
		60	2	5	27.80	1.2	68.4	9.0	196.0	8.0	4.55	0.40	7.81
		80	2	5	33.60	3.5	77.2	11.9	188.0	12.0	2.94	0.60	10.40
		100	2	5	39.60	3.9	87.0	21.7	213.0	6.0	2.06	0.60	13.00
		150	2	5	57.70	3.0	115.0	13.0	250.0	26.0	1.13	0.30	19.50
		200	2	5	79.20	3.9	153.0	25.0	268.0	11.0	0.86	0.20	26.00

$^{\Delta}$ y = 0 all points

Table 8

Mean Cloud Behavior: u_R = 1.0 m/s

V_i (cm^3)	u_R (m/s)	x^Δ (cm)	z (mm)	N	$\overline{t_a^*}$	$\sigma_{t_a^*}$	$\overline{t_m^*}$	$\sigma_{t_m^*}$	$\overline{t_d^*}$	$\sigma_{t_d^*}$	χ_m %	σ_{χ_m} %	x^*
35	1.0	10	2	5	6.8	1.5	7.4	2.6	48.2	6.3	16.2	3.50	3.05
		15	2	5	7.3	1.8	17.2	1.6	45.5	9.0	8.55	4.40	4.57
		20	2	5	10.9	0.7	21.1	1.5	53.1	7.3	3.19	0.80	6.09
		25	2	5	13.6	2.8	22.7	3.0	71.8	12.1	4.50	2.30	7.62
		30	2	5	15.0	2.6	25.1	2.4	65.2	1.9	2.81	0.80	9.14
		40	2	5	16.9	2.9	28.7	6.1	71.4	5.1	2.01	0.70	12.20
		50	2	5	21.9	2.8	37.7	7.5	85.7	7.4	1.59	0.40	15.20
		75	2	6	29.1	3.2	51.6	7.5	108.0	8.7	0.75	0.50	22.90
		100	2	5	38.0	2.5	66.8	10.7	117.0	7.0	0.50	0.20	30.50
		150	2	5	53.7	3.0	85.5	9.7	142.0	13.0	0.19	0.07	45.70
165	1.0	10	2	6	4.8	1.3	12.2	1.2	46.3	8.6	34.30	19.80	1.82
		20	2	5	10.0	2.5	19.4	5.8	54.4	12.3	22.10	12.50	3.64
		30	2	5	12.5	1.6	25.8	4.4	64.4	2.0	9.16	2.10	5.45
		40	2	5	15.5	1.9	32.0	6.6	81.3	8.4	6.52	1.80	7.27
		50	2	5	20.8	2.1	41.5	3.0	88.8	9.0	3.98	1.00	9.09
		60	2	5	22.3	2.3	49.0	4.0	93.1	2.1	4.05	0.50	10.90
		80	2	5	28.1	2.7	56.7	5.8	103.0	17.0	2.72	0.60	14.50
		100	2	5	30.9	0.9	59.8	10.1	116.0	6.0	1.43	0.40	18.20
		150	2	10	46.6	3.1	79.0	11.1	131.0	8.0	0.67	0.30	27.30
		200	2	5	61.2	4.7	92.5	8.7	152.0	10.0	0.44	0.09	36.40
450	1.0	20	2	3	7.2	0.9	18.6	4.6	64.9	0.8	13.80	1.40	2.60
		30	2	5	13.3	1.2	29.8	6.2	80.4	4.0	10.70	1.40	3.91
		40	2	5	15.1	1.8	33.9	5.5	81.0	6.0	7.32	1.00	5.21
		50	2	5	17.9	1.2	45.8	5.7	87.1	3.2	6.76	1.10	6.51
		60	2	6	21.2	1.5	46.0	3.4	94.9	5.8	5.40	1.20	7.81
		80	2	6	25.9	1.3	52.0	4.9	100.0	3.8	3.86	0.50	10.40
		100	2	5	28.8	1.7	62.7	2.6	122.0	7.0	3.24	0.50	13.00
		150	2	5	38.8	3.3	78.8	3.5	133.0	5.0	1.48	0.20	19.50
		200	2	5	50.3	5.0	93.3	13.0	141.0	7.0	0.97	0.20	26.00

$^\Delta$ y = 0 all points

Table 9

Vertical Concentration Profiles: u_R = 0.2 m/s

V_i (cm^3)	u_R (m/s)	x^Δ (cm)	z (mm)	χ_m %	σ_{χ_m} %	V_i (cm^3)	x (cm)	z (mm)	χ_m %	σ_{χ_m} %
35	0.2	10	2.0	19.20	5.40	165	20	2.0	13.00	3.00
		10	5.0	10.40	7.60		20	5.0	9.50	3.20
		10	7.5	11.90	3.20		20	7.5	5.30	1.40
		10	10.0	4.80	1.50		20	10.0	7.10	1.50
		10	15.0	4.40	2.00		20	15.0	1.25	0.80
		10	20.0	1.30	1.50		20	20.0	0.32	0.30
		10	25.0	0.09	0.03		20	25.0	0.13	0.10
							20	30.0	0.03	
35	0.2	25	2.0	3.10	1.40					
		25	7.5	4.50	1.70	165	50	2.0	1.78	0.20
		25	10.0	3.00	0.90		50	5.0	1.58	0.20
		25	15.0	3.90	1.70		50	7.5	1.25	0.10
		25	20.0	0.73	1.10		50	10.0	0.84	0.10
							50	15.0	0.24	0.08
35	0.2	50	2.0	0.71	0.30		50	20.0	0.22	0.10
		50	5.0	1.10	0.40					
		50	7.5	0.77	0.20	165	100	2.0	0.61	0.07
		50	10.0	0.56	0.40		100	5.0	0.60	0.00
		50	15.0	0.14	0.10		100	7.5	0.55	0.07
							100	10.0	0.52	0.08
							100	15.0	0.33	0.05
450	0.2	20	2.0	38.00	4.20		100	20.0	0.13	0.01
		20	5.0	23.00	3.90		100	25.0	0.08	0.08
		20	7.5	11.50	2.20					
		20	10.0	8.00	1.20					
		20	15.0	6.70	1.40					
		20	20.0	1.83	1.60					
450	0.2	50	2.0	2.47	0.80					
		50	5.0	2.26	0.90					
		50	7.5	1.62	0.13					
		50	10.0	1.09	0.41					
		50	15.0	0.42	0.30					
		50	20.0	0.15	–					
450	0.2	100	2.0	1.19	0.20					
		100	5.0	1.22	0.10					
		100	7.5	0.97	0.02					
		100	10.0	0.75	0.02					
		100	15.0	0.38	0.08					
		100	20.0	0.17	0.08					

$^\Delta$ y = 0 all points

V_i = 35 cm^3, L = 32.7 mm
= 165 cm^3, = 54.8 mm
= 450 cm^3, = 76.6 mm

Table 10

Vertical Concentration Profiles: u_R = 0.4 m/s

V_i (cm^3)	u_R (m/s)	x^{Δ} (cm)	z (mm)	χ_m %	σ_{χ_m} %	V_i (cm^3)	u_R (m/s)	x (cm)	z (mm)	χ_m %	σ_{χ_m} %
35	0.4	10	2.0	24.60	9.00	450	0.4	100	2.0	2.09	0.02
		10	5.0	13.00	8.90			100	5.0	2.17	0.30
		10	7.5	12.50	1.20			100	7.5	1.62	0.03
		10	10.0	8.30	4.00			100	10.0	0.83	-
		10	15.0	5.00	3.50			100	15.0	0.56	0.20
		10	20.0	2.17	1.50			100	20.0	0.11	0.05
		10	25.0	0.92	0.60						
		10	30.0	0.95	1.60						
		10	40.0	0.00	0.00						
35	0.4	25	2.0	3.21	1.10	165	0.4	20	2.0	10.6	1.70
		25	5.0	3.54	1.10			20	5.0	9.78	2.00
		25	7.5	2.67	1.60			20	7.5	7.10	2.20
		25	10.0	3.49	0.90			20	10.0	4.06	1.60
		25	15.0	0.93	0.50			20	15.0	1.18	1.00
		25	20.0	1.60	1.10			20	25.0	0.10	0.14
35	0.4	50	2.0	1.00	0.20	165	0.4	50	2.0	2.43	0.20
		50	5.0	1.11	0.40			50	5.0	2.35	0.30
		50	7.5	0.77	0.20			50	7.5	1.42	0.40
		50	10.0	0.60	0.10			50	10.0	1.16	0.20
		50	15.0	0.56	0.30			50	15.0	0.36	0.10
		50	20.0	0.15	0.05			50	20.0	0.15	0.10
		50	25.0	0.05	0.01			50	25.0	0.10	0.15
450	0.4	20	2.0	32.70	6.70	165	0.4	100	2.0	1.08	0.20
		20	5.0	11.10	1.00			100	5.0	0.96	0.03
		20	7.5	10.10	0.90			100	7.5	0.91	0.07
		20	10.0	6.77	0.60			100	10.0	0.70	0.01
		20	15.0	3.73	1.10			100	15.0	0.37	0.06
		20	20.0	1.23	0.40			100	20.0	0.11	0.07
		20	25.0	0.51	0.60			100	25.0	0.07	0.07
		20	30.0	0.62	0.30						
450	0.4	50	2.0	5.25	0.50						
		50	5.0	3.57	0.20						
		50	7.5	2.42	0.50						
		50	10.0	2.21	0.20						
		50	15.0	0.40	0.20						
		50	20.0	0.25	0.10						
		50	25.0	0.16	0.10						

$^{\Delta}$ y = 0 all points

Table 11
Vertical Concentration Profiles: u_R = 0.6 m/s

V_i (cm^3)	u_R (m/s)	x[Δ] (cm)	z (mm)	χ_m %	σ_{χ_m} %	V_i (cm^3)	u_R (m/s)	x (cm)	z (mm)	χ_m %	σ_{χ_m} %
35	0.6	10	2.0	92.30	37.00	450	0.6	100	2.0	2.06	0.60
		10	5.0	10.80	0.30			100	5.0	2.04	0.20
		10	7.5	8.45	5.00			100	7.5	0.91	0.10
		10	10.0	6.42	0.80			100	10.0	0.66	0.40
		10	15.0	1.52	0.90			100	15.0	0.34	0.20
		10	20.0	1.19	0.70			100	20.0	0.24	0.10
		10	25.0	1.48	0.90			100	25.0	0.17	0.10
		10	30.0	0.76	1.00			100	30.0	0.15	0.20
		10	40.0	0.73	1.50						
35	0.6	25	2.0	4.53	1.80	165	0.6	20	2.0	12.40	4.70
		25	5.0	2.71	2.60			20	5.0	7.04	2.40
		25	7.5	1.77	0.50			20	7.5	5.96	3.00
		25	10.0	2.55	0.40			20	10.0	7.70	1.40
		25	15.0	1.50	0.50			20	15.0	1.23	0.60
		25	20.0	0.22	0.10			20	20.0	2.06	0.60
		25	25.0	0.16	0.30			20	25.0	1.23	0.30
								20	30.0	0.15	0.20
35	0.6	50	2.0	1.67	0.50	165	0.6	50	2.0	3.85	0.80
		50	5.0	1.56	0.40			50	5.0	3.02	0.60
		50	7.5	0.91	0.50			50	7.5	1.69	0.20
		50	10.0	0.80	0.20			50	10.0	1.00	0.60
		50	15.0	0.33	0.20			50	15.0	0.59	0.37
		50	20.0	0.34	0.10			50	20.0	0.37	0.20
		50	25.0	0.21	0.10			50	25.0	0.34	0.20
		50	30.0	0.06	0.06						
450	0.6	20	2.0	25.70	7.80	165	0.6	100	2.0	1.48	0.20
		20	5.0	10.50	1.10			100	5.0	1.13	0.10
		20	7.5	6.02	1.80			100	7.5	0.96	0.10
		20	10.0	3.41	1.60			100	10.0	0.66	0.10
		20	15.0	2.02	0.20			100	15.0	0.38	0.06
		20	20.0	1.09	0.20			100	20.0	0.09	0.09
		20	25.0	1.37	0.30						
		20	30.0	0.90	0.60						
		20	40.0	0.25	0.40						
450	0.6	50	2.0	5.91	0.30						
		50	5.0	3.76	1.20						
		50	7.5	2.30	1.00						
		50	10.0	1.12	0.50						
		50	15.0	0.59	0.20						
		50	20.0	0.29	0.02						
		50	25.0	0.58	0.40						
		50	30.0	0.34	0.10						
		50	40.0	0.45	0.20						

[Δ] y = 0 all points

Table 12
Vertical Concentration Profiles: u_R = 1.0 m/s

V_i (cm^3)	u_R (m/s)	x^Δ (cm)	z (mm)	χ_m %	σ_{χ_m} %	V_i (cm^3)	u_R (m/s)	x (cm)	z (mm)	χ_m %	σ_{χ_m} %
35	1.0	10	2.0	16.20	3.50	165	1.0	20	2.0	22.10	12.50
		10	5.0	10.80	8.70			20	5.0	7.81	0.80
		10	7.5	5.14	1.30			20	7.5	6.53	0.80
		10	10.0	5.26	4.90			20	10.0	5.47	1.60
		10	15.0	2.23	1.20			20	15.0	2.51	1.30
		10	20.0	0.78	0.30			20	20.0	1.49	0.20
		10	25.0	0.77	0.70			20	25.0	1.63	0.50
		10	30.0	0.19	0.04			20	30.0	1.80	0.60
								20	40.0	0.80	0.10
35	1.0	25	2.0	4.50	2.34			20	50.0	0.72	0.30
		25	5.0	2.52	0.70			20	60.0	0.30	0.40
		25	7.5	1.16	0.50						
		25	10.0	1.09	0.70	165	1.0	50	2.0	3.98	1.00
		25	15.0	0.52	0.20			50	5.0	2.56	1.20
		25	20.0	0.56	0.40			50	7.5	2.42	0.10
		25	25.0	0.14	0.06			50	10.0	1.60	1.30
								50	15.0	0.77	0.40
35	1.0	50	2.0	1.59	0.40			50	20.0	0.67	0.30
		50	5.0	0.92	0.20			50	25.0	0.64	0.10
		50	7.5	0.73	0.30			50	30.0	0.12	0.03
		50	10.0	0.55	0.10						
		50	15.0	0.26	0.10	165	1.0	100	2.0	1.43	0.40
		50	20.0	0.21	0.10			100	5.0	1.64	0.80
		50	25.0	0.19	0.10			100	7.5	1.03	0.30
								100	10.0	1.01	0.40
								100	15.0	0.41	0.40
450	1.0	20	2.0	13.80	2.00			100	20.0	0.32	0.20
		20	5.0	12.30	2.00			100	25.0	0.32	0.03
		20	7.5	7.55	0.60			100	30.0	0.27	0.20
		20	10.0	5.43	1.20						
		20	15.0	3.70	0.90						
		20	20.0	2.77	0.30	450	1.0	100	2.0	3.24	0.50
		20	25.0	2.79	1.70			100	5.0	2.18	0.30
		20	30.0	2.51	0.80			100	7.5	2.12	0.03
		20	40.0	1.02	1.00			100	10.0	1.95	0.10
								100	15.0	1.24	0.20
450	1.0	50	2.0	6.76	1.10			100	20.0	0.76	0.20
		50	5.0	5.91	1.40			100	25.0	0.65	0.05
		50	7.5	4.23	0.90			100	30.0	0.63	0.10
		50	10.0	3.06	0.70			100	40.0	0.27	0.20
		50	15.0	2.21	0.40						
		50	20.0	1.70	0.40						
		50	25.0	1.25	0.40						
		50	30.0	0.60	0.40						
		50	40.0	0.84	0.40						

$^\Delta$ y = 0 all points

Table 13

Plume Behavior in Terms of Modified Dilution, $\tilde{\chi}$, and Dimensionless Distance, $\tilde{x}$.

○		◑		35 ◐		●	
0.2		0.4		0.6		1.0	
11135		2784		1237		445	
$\tilde{x}$ x10^{2}	$\tilde{\chi}$ x10^{-4}	$\tilde{x}$ x10^{2}	$\tilde{\chi}$ x10^{-4}	$\tilde{x}$ x10^{2}	$\tilde{\chi}$ x10^{-4}	$\tilde{x}$ x10^{2}	$\tilde{\chi}$ x10^{-4}
2.89	22.600	5.78	3.610	8.67	4.020	14.4	0.152
4.33	13.400	8.66	1.700	13.00	0.518	21.7	0.080
5.71	7.760	11.50	1.040	17.30	0.287	28.9	0.030
7.22	3.340	14.40	0.470	21.70	0.196	36.1	0.042
8.66	3.760	17.30	0.514	26.00	0.131	43.3	0.026
11.60	1.760	23.10	0.333	34.70	0.110	57.8	0.019
14.40	0.834	28.80	0.147	43.20	0.073	72.1	0.015
21.70	0.470	43.40	0.099	65.10	0.033	109.0	0.007
28.90	0.176	57.80	0.059	86.70	0.017	145.0	0.005
13.30	0.153	86.60	0.026	130.00	0.008	217.0	0.002
		115.00	0.018	173.00	0.006		

Table 13 (Continued)

□		◨	165	◧		■	
0.2		0.4		0.6		1.0	
18559		4640		2062		742	
$\tilde{x}$ $x10^{2}$	$\tilde{\chi}$ $x10^{-4}$	$\tilde{x}$ $x10^{2}$	$\tilde{\chi}$ $x10^{-4}$	$\tilde{x}$ $x10^{2}$	$\tilde{\chi}$ $x10^{-4}$	$\tilde{x}$ $x10^{2}$	$\tilde{\chi}$ $x10^{-4}$
1.34	115.000	2.67	13.500	4.01	2.880	6.68	0.693
2.67	32.900	5.34	3.350	8.02	1.160	13.40	0.447
4.00	28.300	8.00	1.870	12.00	0.635	20.00	0.185
5.34	10.900	13.30	0.759	16.00	0.533	26.70	0.132
6.67	4.500	16.00	0.632	20.00	0.360	33.40	0.080
8.00	3.570	21.30	0.433	24.00	0.257	40.00	0.082
10.60	2.230	26.70	0.341	31.90	0.170	53.20	0.055
13.40	1.540	40.10	0.205	40.10	0.139	66.80	0.029
20.00	0.936	53.40	0.111	60.10	0.068	100.00	0.014
26.70	0.809			80.20	0.051	134.00	0.009

Table 13 (Continued)

△		◭ 450		◭		▲		V_i (cm^3)
0.2		0.4		0.6		1.0		u_R (m/s)
25982		6496		2887		1039		$Ri^* = g_i' V_i^{1/3} u_*^2$
$\tilde{x}$ $x10^2$	$\tilde{\chi}$ $x10^{-4}$	$\tilde{x}$ $x10^2$	$\tilde{\chi}$ $x10^{-4}$	$\tilde{x}$ $x10^2$	$\tilde{\chi}$ $x10^{-4}$	$\tilde{x}$ $x10^2$	$\tilde{\chi}$ $x10^{-4}$	$\tilde{x} = x^* Ri_*^{1/2}$
1.61	159.00	1.61	39.700	2.42	11.400	8.07	0.462	$\tilde{\chi} = Ri_*^{3/2}$
2.43	73.30	3.23	18.800	4.84	3.990	12.10	0.358	
3.23	25.60	4.85	7.280	7.28	1.970	16.20	0.245	
4.04	14.20	6.46	3.610	9.70	1.200	20.20	0.226	
4.85	11.50	8.08	2.090	12.10	0.917	24.20	0.181	
6.45	7.58	9.69	1.800	14.50	0.706	32.30	0.129	
8.07	5.49	12.90	1.450	19.40	0.456	40.30	0.109	
12.10	3.01	16.10	1.180	24.20	0.320	60.50	0.050	
16.10	2.09	54.20	0.665	36.30	0.175	80.70	0.032	
		32.30	0.435	48.40	0.133			

$1.34 \times 10^{-2} < \tilde{x} < 2.17$

$2.0 \times 10^{1} < \bar{\chi} < 1.59 \times 10^{6}$

Table 14

Neutral Density Gas Cloud Behavior, $V_i = 35\ cm^3$

u_R (m/s)	x (cm)	x^*	χ %	t_a (sec)	t_a^*	$\approx t_a$	t_m (sec)	t_m^*	$\approx t_m$	t_d (sec)	t_d^*	$\approx t_d$	u_* (m/s)
0.2	10	3.05	12.80	0.16	4.92	0.064	0.568	17.7	0.228	2.09	69.9	0.84	.013
	15	4.57	3.12	0.62	19.40	0.249	1.260	39.2	0.504	3.08	95.5	1.23	
	20	6.09	2.48	0.99	30.70	0.395	1.670	51.8	0.668	3.69	115.0	1.48	
	25	7.62	1.19	1.21	35.40	0.455	2.100	65.2	0.084	3.83	119.0	1.53	
	30	9.14	1.12	1.12	34.70	0.447	2.090	64.9	0.840	4.54	141.0	1.82	
	40	12.20	0.71	1.74	53.90	0.693	2.610	81.0	1.040	5.87	182.0	2.34	
	50	15.20	0.44	2.27	70.30	0.905	4.350	135.0	1.730	6.87	213.0	2.74	
	75	22.90	0.42	3.05	94.70	1.220	4.060	126.0	1.630	9.33	289.0	3.72	
	100	30.50	0.24	3.70	115.00	1.480	4.720	146.0	1.880	8.05	250.0	3.22	
0.6	10	3.05	8.60	0.13	3.94	0.13	0.490	15.2	0.48	1.27	39.40	1.25	.032
	15	4.52	2.03	0.20	6.23	0.20	0.696	21.6	0.68	1.74	54.00	1.71	
	20	6.09	1.66	0.33	10.20	0.32	0.921	28.5	0.91	1.93	59.80	1.90	
	25	7.62	1.02	0.43	13.30	0.42	1.010	31.4	0.99	1.96	60.80	1.93	
	30	9.14	1.39	0.51	15.70	0.50	1.100	34.1	1.08	2.11	65.30	2.07	
	40	12.20	1.08	0.68	21.10	0.67	1.400	43.2	1.37	2.56	79.30	2.52	
	50	15.20	0.74	0.83	25.80	0.82	1.400	43.4	1.38	2.61	8.09	2.56	
	75	22.90	0.52	1.26	38.90	1.24	2.020	62.7	1.98	3.46	107.00	3.40	
	100	30.50	0.37	1.67	51.90	1.62	2.590	80.1	2.54	4.18	130.00	4.11	
	150	45.70	0.25	2.19	67.80	2.14	3.100	96.1	3.04	4.77	148.00	4.68	
	200	60.90	0.13	2.87	88.90	2.82	4.300	133.0	4.22	6.04	187.00	5.93	

APPENDIX A

APPENDIX A: Numerical Box Model Program:

Consider a dense cloud which is instantaneously released as a cylindrical box of radius, R_i, and height, H_i, that undergoes a slumping motion in which R increases with time. As the motion proceeds one may assume the box mixes with ambient air, but maintains uniform properties internally. The radial velocity is assumed to vary linearly from zero at the center to a maximum at the outer edge of the cloud. Such a dispersion scenario will proceed as sketched in Figure A-1. Sketches of how the experimental cloud was perceived to disperse are shown to the right of each box model sketch. Although the simplistic model may reproduce radial cloud dimensions and maximum concentrations measured, it cannot correctly reproduce the actual radial variation of height and concentration in time. Indeed, if the box model is calibrated to reproduce maximum concentrations measured at various radial locations, then the bulk average concentrations predicted will always be too low, and the entrainment rates used will actually be too high for the reality of local entrainment physics. Nonetheless, such a model has engineering value.

Conventional wisdom assumes that radial speed of the cloud front is proportional to the excess hydrostatic head within the cloud:

$$\frac{dR}{dt} = \propto (g'H)^{1/2} \qquad \text{(A-1)}$$

in which $\propto$ is a constant of order unity and $g' = g(\rho - \rho_a)/\rho_o$, ($\rho_o$ is sometimes chosen as local cloud density, ρ, and sometimes chosen as ambient air density, ρ_a). This expression is used in the models developed by van Ulden (1974), Germeles and Drake (1975), Cox and Carpenter (1980), Fay (1980), and Fay and Ranck (1981). This expression works well for stationary one-dimensional spread; however, it incorrectly suggests an initial cloud velocity at time equal zero.

An alternative approach was suggested by van Ulden (1979). He considered the total energy budget (potential, kinetic, turbulent, and internal energies) to calculate radial growth rates. He concluded for axisymmetric growth of a cylindrical disk, when entrainment is neglected, that

$$\frac{du^*}{dt^*} = 2\left(\frac{\rho_a}{\rho_i}\right)\frac{H^*}{R^*} - 2\beta_1\left(\frac{\rho_a}{\rho_i}\right)\frac{u^{*2}}{R^*} \qquad \text{(A-2)}$$

$$\frac{dR^*}{dt^*} = u^* \qquad \text{(A-3)}$$

where β_1 is a constant near one and starred quantities are dimensionless with time and length scales equal to $T = V_i^{1/6}/(g_i')^{1/2}$ and $L = V_i^{1/3}$.

The spread model used here is a revised version of van Ulden's approach. Specifically the influence of entrainment of mass on kinetic and potential energy was added, the Boussinesqu assumption was <u>not</u> made, and the total production of turbulence at the leading edge was assumed proportional to cloud density - not ambient density. The final expressions proposed are:

$$\frac{du_g^*}{dt^*} = \left[\frac{2}{\pi}\frac{1}{R^{*3}} - c_r\frac{u_g^{*2}}{R^*} - \frac{c_z u_g^{*2}}{2H^*}\right]\left[1 + \frac{\Delta\rho_i/\rho_a}{V^*}\right]^{-1} - 2\beta_1\frac{u_g^{*2}}{R^*} \qquad \text{for} \qquad t^* < Ri_*^{1/2} \qquad \text{(A-4)}$$

$$\frac{dR^*}{dt^*} = u_g^* \qquad \text{but never less than}$$

$$\frac{dR^*}{dt^*} = \frac{\alpha_7}{Ri_*^{1/2}} \qquad \text{(A-5)}$$

where $\beta_1 = 0.9$, $c_r = c_z = 0.1$, and $\alpha_7 = 3.5$.

Dilution of the gas cloud is assumed to occur by entrainment across the upper surface at a rate of $\pi R^2 u_z$ and by entrainment at the front at a rate of $2\pi RHu_r$, where u_z and u_r are appropriate entrainment speeds. The cloud volume will then increase at a rate:

$$\frac{d\Psi^*}{dt^*} = \pi R^{*2} u_z^* + 2\pi R^* H^* u_r^* \qquad \text{(A-6)}$$

where $\chi = (\Psi^*)^{-1}$ and $\pi R^{*2} H^* \chi = 1$.

At early times, when $Ri_*^{1/2} \gg 1$ and gravitational spreading dominates, the concensus is that u_r and u_z should be proportional to $(g'H)^{1/2}$; thus

$$u_r^* = c_r u_g^* \qquad \text{(A-7)}$$

$$u_z^* = c_z u_g^* \qquad \text{(A-8)}$$

where the constants c_r and c_z range from 0.0 to 1.0 depending upon the modeler's bias. (See Lohmeyer, Meroney, and Plate (1980).)

The behavior of the box model algorithms is critically dependent on the entrainment constants, c_r and c_z, selected. Figure A-2 displays the result of calculations using constants recommended by various authors. The van Ulden curves show little dilution; however his entrainment rates are based on overall plume dilution rather than local values. The curves produced by Cox and Carpenter or Picknett constants result from the high initial dilution perceived to occur during the Porton experiments. The low concentations may have resulted from source mechanism generated mixing or misplacement of concentration sensors. Data presented herein fall between the Lohmeyer et. al. and Germeles and Drake curves.

Notice that several sets of constants predict a plume height minimum. Fay in Reid (1982) questions whether potential and kinetic energy considerations permit cloud depth increase without an external source of energy such as wind shear.

In the later cloud development stage, when shear layer turbulence dominates, the entrainment velocities are generally related to friction velocity. In the present case u_z^* is modified following the approach of Eidsvik (1980) to:

$$u_z^* = c_z u_g^* + \frac{\alpha_4 / Ri_*^{1/2}}{\frac{\alpha_4}{\alpha_6} + \frac{Ri_*}{\pi R^{*2}} \left[1 + \frac{\Delta\rho_i / \rho_a}{*} \right]^{-1}} , \qquad \text{(A-9)}$$

where the constants are $\alpha_4 = 2.6$ and $\alpha_6 = 0.30$.

Fay and Ranck (1981) proposed that vertical entrainment behaves empirically as

$$u_z^* = f\, u_*^*$$

where $f^{-2} = C_1^{-2} + (C_2/Ri)^{-2}$ and

$$Ri = g'H/u_*^2 = Ri_*/\pi R^{*2}$$

When $Ri \gg 1$ then $f = C_z/Ri$ or

$$u_z^* = C_2\, u_*^*/Ri ,$$

and when $Ri \ll 1$ then $f \simeq C_1$ or

$$u_z^* = C_1\, u_*^* .$$

In terms of these constants the values used by various modelers are

Table A-1

Model Constants

Author (date)	C_1	C_2	Calibration data
Fay and Ranck (1980)	2.50	0.50	Hall (1974), Picknett (1978)
Cox and Carpenter (1980)	0.36	2.00	van Ulden (1974), Picknett (1978)
Eidsvik (1980)	0.39	4.55	Picknett (1978)
Zeman (1982)	0.64	12.50	Walljet and atmospheric boundary layer data
Present Results	0.30	2.60	---

Finally, although some models propose to relate drift distances to drift time by a nominal wind speed (ie. $x \simeq u_R t$), the current calculations use a cloud arrival time related to distance by a fraction of the average undisturbed wind speed over cloud depth, that is

$$\frac{dX^*}{dt^*} = u_g^* + \frac{Ri_*^{-1/2}}{k} \ln \beta_2 \frac{H^*}{z_o^*} \qquad \text{(A-10)}$$

where β_2 is chosen to give about one half the average velocity (ie. $\beta \simeq 0.1$).

Equations (A-4), (A-5), (A-6), and (A-10) were integrated by a fourth-order Runga-Kutta scheme. Entrainment rates were specified by Equations (A-7) and (A-9). Initial conditions were chosen as $V_i^* = 1.0$, $u_{g_i}^* = 0.0$, $x_i^* = \pi^{-1/3}$, $R_i^* = \pi^{-1/3}$, and $H_i^* = \pi^{-1/3}$. Additional data required are Ri_*, z_o^*, and cloud specific gravity or $\Delta\rho_i/\rho_a$. Constants found to fit the data most satisfactorily were

$c_r = 0.1$

$c_z = 0.1$ } ~ From calm release data

$\beta_1 = 0.9$

$\alpha_4 = 2.6$

$\alpha_6 = 0.30$ } ~ Eidsvik (1980)

$k = 0.4$

$\beta_2 \simeq (z_o/H)^{1/2}$ ~ 0.1 to 0.15 } From wind shear data

$\alpha_7 = 3.5$

From Equation (A-4) in the limit as R becomes large $\beta_1 = 0.9$ implies the constant α in Equation (A-1) equals one.

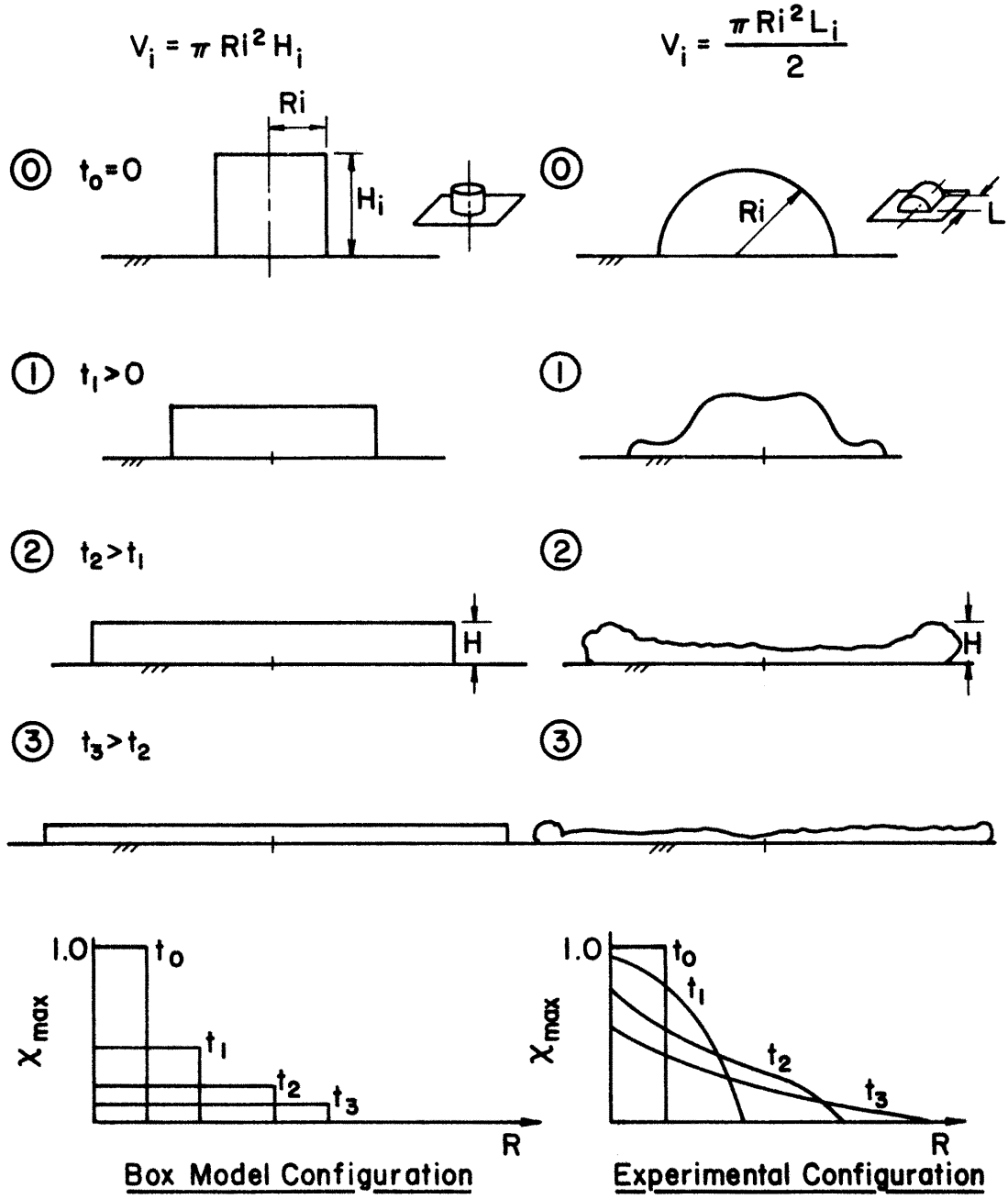
$V_i = \pi Ri^2 H_i$
$V_i = \frac{\pi Ri^2 L_i}{2}$
Ri
⓪ $t_0=0$
H_i
⓪
Ri
L_i
① $t_1>0$
①
② $t_2>t_1$
H
②
H
③ $t_3>t_2$
③
1.0
t_0
t_1
t_2
t_3
χ_{max}
R
Box Model Configuration
1.0
t_0
t_1
t_2
t_3
χ_{max}
R
Experimental Configuration
Note: $(\chi_{AVG})_{BOX} < (\chi_{AVG})_{ACTUAL}$
$H_{BOX} > H(R)_{ACTUAL}$
When constants are chosen such that $\chi_{max} = f(R)$ match.

Figure A-1.

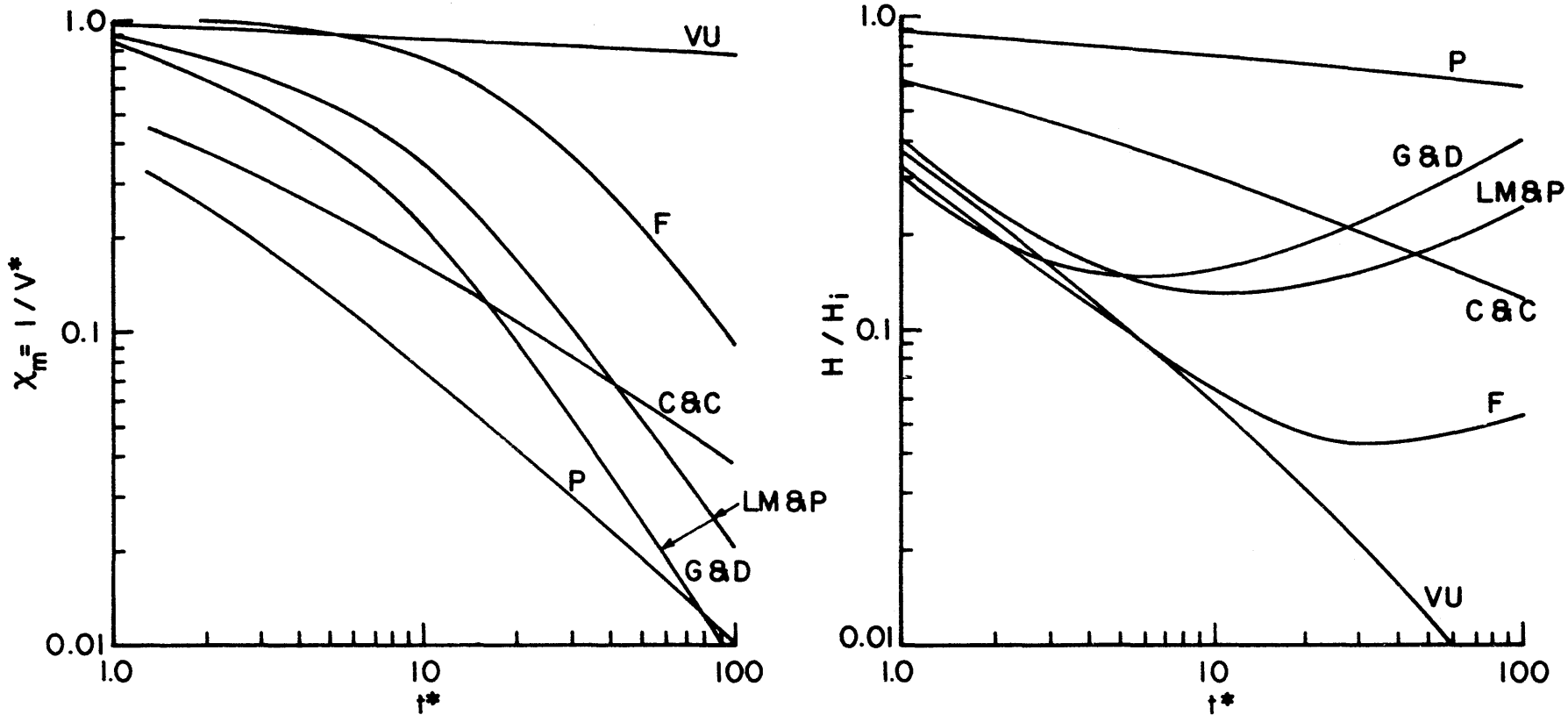

SG = 4.17 , $u_* = 0$

	C_r	C_z	a_1
Van Ulden (1974)	0.05	0	1.0
Germeles and Drake (1975)	0.0	0.1	$\sqrt{2}$
Fay (1980)	0.01	0.01	1.0
Cox and Carpenter (1980)	0.6	~0.00013	1.0
Picknett (1978)	0.82	~0.008	0.94
Lohmeyer, Meroney, and Plate (1980)	0.05	0.05	1.0

Figure A-2.

USERS GUIDE: BOX MODEL: DENSE 1

See Appendix A Meroney and Lohmeyer (1982) for general discussion. Model will calculate behavior of isothermal or cold dense gas plumes in calm or windy situations. The model does not

1) consider heat transfer from ground.
2) consider humidity effects.
3) treat continuous releases - only sudden.
4) adjust atmospheric boundary layer turbulence for stability.

Items 1), 2) and 4) could be easily added to this program. Contact Meroney for revised programs.

INPUT

The program requires 5 cards to run, it produces a table of cloud average behavior versus time.

Card 1 (8G10.3) SG, V, US, ZO, B1, B2, CR, CZ (similar to F10.3 but permits use of E format see Fortran manual)

* SG Specific gravity of dense cloud ie. ρ_o/ρ_a

* V Initial cloud volume (meter^3)

* US Friction velocity U_* (meters/sec)

* ZO Z_o - Roughness length (meters)

B1 Constant in energy equation use 0.9

B2 Fraction of height of cloud which is used in log law to compute convection velocity. Can be 0.1 to 1.0 (use 0.1 to convect cloud at 1/2 of average velocity over height of cloud).

CR C_r - Radial edge entrainment constant ranges from 0.01 - 0.8 use 0.1

CZ C_z - Top surface entrainment constant ranges from 0.00 - 0.1 use 0.1

Card 2 (8G10.3) A4, A6, VVII, RSI, HSI, USI, XSI, TSI

A4 Entrainment constant - ranges from 0.5 - 12.5 use 2.6

A6 Entrainment constant - ranges from 0.15 - 2.5 use 0.3

VVII Initial dilution - normally set to 1.0 for pure gas release

RSI Initial cloud radius

$$R^* = \frac{R}{V_i^{1/3}} = 0.682$$

HSI Initial cloud height

$$H^* = \frac{H}{V_i^{1/3}} = 0.682$$

[Note above values give a cylinder 1/2 as tall as it is wide, other choices are possible but

$$\frac{\pi R^2 H}{V_i} = 1 \quad \therefore \quad R_i^{*2} H_i^* = \frac{1}{\pi}$$

USI Initial cloud radial velocity = 0.0

XSI Initial cloud location - normally = 0.0

$$XSI = X_i^* = \frac{X_i}{V_i^{1/3}}$$

TSI Initial time

$$t^* = \frac{t}{T} = \frac{t\,(g_i')^{1/2}}{V_i^{1/3}} = 0.0$$

Card 3 (8G10.3) A7, VK, GAM

A7 Cloud growth rate constant due to background turbulence, ie.

$$\frac{dR}{dt} = A_7 U_* \quad \text{if}$$

buoyancy effects are small use 3.5

VK von Karmans' constant use 0.40

GAM Always set to 0.0

Card 4 (40A2)

Any name for program work you choose, do not use first space on card, otherwise 79 spaces are available.

Card 5 (8G10.3) BETA, SSTAR, THETA

* BETA

$$\beta = 1 - \frac{M_a}{M_i} = 1 - \frac{1}{SG}$$

example if SG = 4.17
$\beta = 0.760$

* SSTAR

$$S^* = \frac{C_{p\,o}^*}{C_{p\,a}^*} = 1$$

for isothermal release set to 0.0

where

$C_{p\,o}^*$ = molar specific heat capacity of source gas

$C_{p\,a}^*$ = molar specific heat capacity of air

* THETA

$$\Theta = 1 - \frac{T_i}{T_a}$$

where

T_i = initial temperature (°K) of source gas

T_a = initial temperature (°K) of air

Normally only starred quantities change from one run to another.

OUTPUT

All input quantities will be read out.

TIME SCALE:

$$T = V_i^{1/3}/(g_i')^{1/2}$$

LENGTH SCALE:

$$L = V_i^{1/3}$$

RICHARDSON NUMBER:

$$R_i = g_i' V_i^{1/3} / U_*^2$$

(Reynolds = $R_e = (g_i')^{1/2} V_i^{1/2} / 0.000015$ is calculated but not printed out - if you desire it change cards 43)

TSTAR:

$t^* = t/T$ (time)

XSTAR

$x^* = x/L$ (downward distance)

CONTENT:

χ = uncorrected dilution = V_i/V

RSTAR:

$R^* = R/L$ (radius)

HSTAR:

$H^* = H/L$ (height)

USTAR:

$V^* = U\ T/L$ (velocity of cloud front)

TIME:

t (seconds)

DIST:

x (meters)

DILUT: χ

except when THETA = 0.0, then it gives LNG concentration

RADIUS:

R (meters)

HEIGHT:

H (meters)

VELOCITY:

u (meters/sec)

To STOP program add three blank cards, or an end of file card at end of set of cases desired. Plot routines are on original version at CSU they can be modified or added as desired.

```
      PROGRAM DENS1(INPUT,OUTPUT,TAPE5=INPUT,TAPE6=OUTPUT)
C PROGRAM TO CALCULATE DENSE GAS DISPERSION
C OF AN INTANTANEOUS VOLUME IN TERMS OF A VAN ULDEN
C /FAY TYPE BOX MODEL WHICH INCLUDES U, ENTRAINMENT
C TO ACCOUNT FOR DILLUTION AND LOG LAW TO ACCOUNT
C FOR DILLUTION BY ADVECTION AND BACKGROUND TURBULENCE
C ENTRAINMENT IS DUE BOTH TO GRAVITY SPREADING AND
C BACKGROUND TURBULENCE ADJUSTED BY AN EIDSVIK TYPE RICHARDSON
C NUMBER .
C*********************
C
      DIMENSION K(4,4),YS(5),YY(5),Y(6,80)
     1 ,MTIT(8)
      REAL K
C      READ IN INPUT WRITE OUT INPUT
C*********************
C
5     READ(5,500) SG,V,US,ZO,B1,B2,CR,CZ,A4,A6,VVII,RSI,HSI,USI,
     1 XSI,TSI,A7,VK,GAM
      IF(SG.EQ.0.0) GO TO 200
      WRITE(6,501)
      WRITE(6,600) SG,V,US,ZO,B1,B2,CR,CZ,A4,A6
      WRITE(6,502)
      WRITE(6,600) VVII,RSI,HSI,USI,XSI,TSI,A7,VK,GAM
      READ(5,503) (MTIT(I),I=1,8)
      WRITE(6,602)(MTIT(I),I=1,8)
      READ(5,500) BETA,SSTAR,THETA
      WRITE(6,603) BETA,SSTAR,THETA
603   FORMAT(1X,//,* BETA = *,F10.6,5X,*SSTAR = *,F10.6,5X,*THETA = *
     1  F10.6,/)
C     CALCULATE RICHARDSON NUMBER,TIME SCALE,LENGTH
C     SCALE, AND REYNOLDS NUMBER
C*********************
C
      FI=3.1417
      RI=9.81*(SG-1.0)*V**0.333/US**2
      T=V**(1./6.)/(9.81*(SG-1.0))**0.5
      REY=(9.81*(SG-1.0))**0.5*V**0.5/0.000015
      FL=V**0.333
      RIS=RI**0.5
      AA=A7/RIS
      WRITE(6,601) T,FL,RI
      WRITE(6,700)
C     INITIALIZE
C*********************
C
      YS(1)=USI
      YS(2)=RSI
      YS(3)=VVII
      YS(4)=RSI+XSI
      YS(5)=HSI
      TS=TSI
      Y(1,1)=TS
      Y(2,1)=YS(4)
      Y(3,1)=1.0/YS(3)
```

```
      Y(4,1)=YS(2)
      Y(6,1)=YS(1)
      Y(5,1)=YS(5)
C      CALCULATION LOOP TO SOLVE FOR VELOCITY,RADIUS
C       DILUTION, AND X LOCATION SIMULTANEOUSLY
C*********************
C       SET TIME STEPS
C*********************
C
      DO 34 L=2,74
10    DO 20 I=1,4
      DO 20 J=1,4
20    K(I,J)=0.0
      IF(TS.LT.1.0) DTS=0.05
      IF ((TS.LT.10.0).AND.(TS.GE..99)) DTS=0.5
      IF((TS.LT.20.0).AND.(TS.GE.10.0)) DTS=1.0
       IF((TS.LT.100.0).AND.(TS.GE.20.0)) DTS=5.0
      IF((TS.LT.1000.0).AND.(TS.GE.100.0)) DTS=10.0
C      RUNGA KUTTA LOOP
C*********************
C
      DO 30 J=1,4
      GO TO (40,50,60,70),J
40    DO 41 I=1,4
41    YY(I)=YS(I)
      TPS=TS
      GO TO 80
50    DO 51 I=1,4
51    YY(I)=YS(I)+DTS*K(I,1)/2.0
      TPS=TS+DTS/2.0
      GO TO 80
60    DO 61 I=1,4
61    YY(I)=YS(I)+DTS*K(I,2)/2.0
      TPS=TS+DTS/2.0
      GO TO 80
70    DO 71 I=1,4
71    YY(I)=YS(I)+DTS*K(I,3)
      TPS=TS+DTS
80      CONTINUE
      IF((TPS.GT.1.0).AND.(YY(1).LE.AA))  YY(1)=AA
      BOY=(BETA*(1.0+SSTAR*YY(3))+(1.0+SSTAR)*(1.0-BETA)*THETA)/
     1  ((BETA+(1.0-BETA)*THETA)*(1.0+SSTAR*YY(3)))
      RHOR=((1.0+SSTAR*YY(3))-(1.0+SSTAR)*THETA*YY(3))*(1.0-BETA)/
     1 ((1.0+SSTAR*YY(3))*(1.0-BETA+BETA*YY(3)))
      YYY=(1.0+SSTAR*YY(3)-YY(3)*(1.0+SSTAR)*THETA)/
     1  (YY(3)*(1.0-THETA)*(1.0+SSTAR*YY(3)))
      SSSS=A4/RIS/(A4/A6+RI*RHOR*BOY/(FI*YY(2)**2))
      YY(5)=YYY/(FI*YY(2)**2)
      K(1,J)=(2.*BOY/(FI*YY(2)**3)-CR*YY(1)**2/YY(2)-CZ*YY(1)**2/(2.0
     1 *YY(5))-SSSS*YY(1)/(2.0*YY(5)))*RHOR-2.0*B1*YY(1)**2/YY(2)
     2  -4.0*GAM*YY(1)/(YY(5)**2*REY)
      K(2,J)=YY(1)
      K(3,J)=(FI*YY(2)**2*(CZ*YY(1)+SSSS)+
     1 2.0*FI*YY(2)*YY(5)*CR*YY(1))*(-YY(3)
     1  **2*(1.0-THETA))
      K(4,J)=1.0/(VK*RIS)*ALOG(B2*YY(5)*V**0.333/ZO)+YY(1)
```

```
       IF(TS.LT.10.0) K(4,J)=YY(1)
30     CONTINUE
       DO 100 I=1,4
100    YS(I)=YS(I)+DTS*(K(I,1)/6.0+K(I,2)/3.0+K(I,3)/3.0+K(I,4)/6.0)
       IF((TPS.GT.RIS).AND.(YY(1).EQ.AA)) YS(1)=AA
       YYYY=(1.0+SSTAR*YS(3)-YS(3)*(1.0+SSTAR)*THETA)/
      1   (YS(3)*(1.0-THETA)*(1.0+SSTAR*YS(3)))
       YS(5)=YYYY/(FI*YS(2)**2)
       TS=TS+DTS
       TR=TS*T
       XR=YS(4)*FL
       DIL=YS(3)
       IF(THETA.EQ.0.0) DIL=YS(3)/(YS(3)+(1.0-YS(3))*0.37)
       RR=YS(2)*FL
       HR=YS(5)*FL
       UR=YS(1)*FL/T
C       PRINT RESULTS
C*********************

       WRITE(6,701) TS,YS(4),YS(3),YS(2),YS(5),YS(1),TR,XR,DIL,RR,HR,UR
 34    CONTINUE
       GO TO 5
C       FORMAT STATEMENTS
C*********************
C
200    STOP
500    FORMAT(8G10.3)
501    FORMAT(1H1,3X,*SG*,8X,*INIT VOL*,2X,*USTAR*,5X,*ZO*,8X,*B1*,8X,
      1 *B2*,8X,*CR*,8X,*CZ*,8X,*A4*,8X,*A6*,//)
502    FORMAT(4X,*INIT DIL*,2X,,8X,*VON KAR*,3X,*GAMMA*,//)
503    FORMAT(8A10)
600    FORMAT(10G10.3,/)
601    FORMAT(1X,//,1X,*TIME SCALE = * ,F10.6,5X,*LENGTH SCALE = *,F10.6,
      1 5X,*RICHARDSON NUMBER = *,F10.2,/)
602    FORMAT(1X,/,1X,8A10)
700    FORMAT(1H1,1X,*T STAR*,6X,*X STAR*,6X,*CONCENT*,4X,*R STAR*,4X,
      1*H STAR*,6X,*U STAR*,6X,*TIME*,6X,*DIST *,4X,*DILUT*,4X,
      2 *RADIUS*,6X,*HEIGHT*,5X,*VELOCITY*,//)
1H ,12(1X,G9.3,1X))
       END
```

APPENDIX B

APPENDIX E: Numerical Depth-Averaged Model Program

A model for dense cloud dispersion is desired which reproduces the detailed nuances of behavior perceived during laboratory and field experiments. Three-dimensional calculations are very expensive of computer storage and time, especially when reverse flow regions are present which require the solution of the general three dimensional equations. Fortunately, when the flow situation is only weakly three dimensional, so that one dimension can be decoupled from the other two, a set of relations obtained by integrating the conservation equations over that dimension realistically describes fluid motions. To be accurate these "depth averaged" equations must have negligible vertical dynmamic pressure gradients in the vertical direction (ie. vertical velocities, w, are small and the hydrostatic pressure approximation is valid). Flow quantities are generally assumed to be constant, or at least have a similar distribution in the vertical as shown in Figure B-1.

Ponce and Yalusaki (1980) have reviewed the state of depth-averaged two-dimensional models. Three components of effective shear stresses were identified: (1) viscous stresses; (2) turbulent stresses; and (3) large scale momentum transfer due to the departure of the local velocity from the depth-averaged velocity. Clearly the main obstacle to reliable modeling by this method is the accurate physical description of the effective shear stresses. These stresses have been represented by a wide variety of approaches, ranging from total neglect, constant effective eddy diffusivity, and sophisticated three-dimensional turbulence models. One must also consider that the mechanism of energy transfer in two dimensional models is from small to larger scales, while the opposite is true for three-dimensional flow. Convective inertia terms which interact nonlinearly often lead to numerical stability problems. The

control of nonlinear instability by some artifice such as additional viscosity, smoothing, or numerical viscosity is generally necessary. Unfortunately, the artifice can sometimes cause the numerical solution to deviate from the physical solution.

Despite such calculation concerns a number of investigators have applied depth-averaged models to dense cloud dispersion. Brandeis and Kansa (1982) and Brandeis and Ermak (1982) examined the release of cylinders of liquids into diked areas or onto a water surface. They included no entrainment, ignored stress terms, and solved the difference equations using donor-cell differencing with flux-corrected transport as suggested by Book et. al. (1975).

Ermak et. al. (1981) used the same techniques to solve for LNG gas cloud dispersion behavior. They included a model for ambient air entrainment and vertical variation of properties based on a similarity profile use of depth averaged quantities. Ermak et. al. compared model results with the dispersion patterns from spills of 40 m^3 LNG on a small pond. Comparisons were very good.

Doo (1979) solved for the assymptotic behavior of a two-dimensional, steady, line source of dense gas. He included a stability dependent entrainment model, but neglected effective stresses. Solution of his set of equations was by a fourth order Runga Kutta scheme. Subsequently Rosenzweig (1980) showed that any assumed similarity profiles can be rescaled to the uniform profile equations in the Boussinesq limit. He used a method of characteristics technique to solve a set of one dimensional equations and provided analytic solutions to the assymptotic equations for dense gas cloud behavior. Rosenzweig used the simple entrainment model

$$w_e = \alpha_2 |u_g| + \gamma \quad , \tag{B-1}$$

where α_2 is a constant to account for shear entrainment and γ provides for background turbulent flow entrainment. When gravitationally generated movement is yet significant he suggests ($\alpha \neq 0$, $\gamma \neq 0$)

$$\begin{aligned} R &\sim t^{1/2} \quad , \\ u_g &\sim \left(\frac{r}{R}\right) t^{-1/2} \quad , \\ H &\sim \left(\frac{r}{R}\right) t^{1/2} \quad , \text{ and} \\ \chi &\sim \left(\frac{r}{R}\right)^{-2} t^{-1/2} \quad ; \end{aligned} \tag{B-2}$$

whereas when only background turbulence is effective ($\alpha = 0$, $\gamma \neq 0$);

$$\begin{aligned} H &\sim t \quad , \text{ and} \\ \chi &\sim \{a(1 - \left(\frac{r}{R}\right)^2) + b\} t^{-2} \quad . \end{aligned} \tag{B-3}$$

Comparisons to field and laboratory data produced values of γ ranging from 0.002 to 0.13. Rosenweig limited radial growth rate by also specifying that frontal velocity obey

$$\frac{dR}{dt} = (u_g)_R = \sqrt{\lambda}\ [g'H]^{1/2} \quad . \tag{B-4}$$

No turbulent stresses were considered since a boundary layer approximation was assumed.

Zeman (1982) solved a set of radially-symmetric depth-averaged equations by a centered-difference numerical scheme. His equations included the Boussinesq assumption and neglected added shear stress terms. He proposed an entrainment model based on experience with stratified atmospheric flows to be

$$w_e = \frac{[0.56(1 - Ri) + C_F]}{1 + 2Ri}\ C_F\ u_g(r) \tag{B-5}$$

where $Ri = \frac{1}{2}\ g \left[\frac{\Delta\rho\ H(r)}{\rho_a\ u_g(r)^2}\right]$ and $C_F \simeq 0.08$.

The dimensionless depth-averaged non-Boussenesq, unsteady, radially-symmetric symmetric equations were derived for the current model. The entrainment equation specified is

$$\frac{\partial(\rho^* h^*)}{\partial t^*} + \frac{1}{r^*}\frac{\partial}{\partial r^*}(\bar{\rho}^*\bar{u}^* r^* h^*) = w_e^* \qquad \text{(B-6)}$$

where depth averaged quantities are defined by

$$\overline{\phi}^* = \frac{1}{H^*}\int_o^{H^*} \phi^* \, dz^* \quad .$$

Starred quantities are scaled in the manner discussed in Section 2.2.1.

The radial momentum equation is

$$\frac{\partial(\bar{\rho}^*\bar{u}^* h^*)}{\partial t^*} + \frac{1}{r^*}\frac{\partial}{\partial r^*}(\bar{\rho}^*\bar{u}^{*2} r^* h^*) = u_\infty^*(h^*)w_e^* +$$

$$-\frac{\beta_1}{2}\frac{\partial}{\partial r^*}(h^{*2}(\bar{\rho}^* - 1)) + \tau_o^* - \frac{1}{r^*}\frac{\partial(h^* r^* \bar{T}_{rr}^*)}{\partial r^*} \qquad \text{(B-7)}$$

where τ_o^* is retarding surface shear stress, say

$$\tau_o^* = -\bar{\rho}^*\bar{u}^*|\bar{u}^*| C_F^2 \quad , \qquad \text{(B-8)}$$

and $\bar{T}_{rr}^*$ is effective shear stress,

$$\bar{T}_{rr}^* = \bar{\tau}_{rr}^* + \frac{1}{\bar{h}^*}\int_o^{h^*} \rho^* \Delta u^* dz^* \quad , \qquad \text{(B-9)}$$

and $u^*(z) = \bar{u}^* + \Delta u^*(z)$. One may replace the effective shear stress term by an effective eddy diffusivity, which is this case is chosen as

$$\bar{T}_{rr}^* = -\rho^* \nu_r^* \frac{\partial \bar{u}^*}{\partial r^*} \qquad \text{with} \quad \nu_r^* = 0.15\left(\frac{u_*}{u_R}\right)\bar{u}^* \quad . \qquad \text{(B-10)}$$

Finally, a conservation equation for the mass fraction of the source gas is

$$\frac{\partial(\bar{\rho}^{*}\bar{C}h^{*})}{\partial t^{*}} - \frac{1}{r^{*}}\frac{\partial}{\partial r^{*}}(\bar{\rho}^{*}\bar{C}\,\bar{u}^{*}r^{*}h^{*}) = 0 , \qquad \text{(B-11)}$$

and

$$\bar{\rho}^{*} = \frac{1}{1 - \bar{C} - \frac{\rho_a}{\rho_o}\bar{C}} \qquad \text{(B-12)}$$

where ρ_o/ρ_a is the source gas specific gravity.

When the cloud is released in a wind field it is assumed that the center of gravity is advected to a new location x_o^{*} given by the equation

$$x_o^{*} = \int_o^{t^{*}} \frac{u_{*}^{*}}{k} \ln \beta_2\left(\frac{H_o^{*}}{z_o^{*}}\right) dt^{*} \qquad \text{(B-13)}$$

and the effective entrainment rate is

$$w_e^{*} = \alpha_2 |\bar{u}^{*}| + \gamma u_{*}^{*} \qquad \text{(B-14)}$$

Equations (B-6), (B-7), and (B-12) were developed in a difference form using an implicit, second-upwind-difference, donor-cell approach. The difference equations were solved by the Thomas algorithm. Step sizes in time were limited to

$$\Delta t^{*} \leq \frac{0.25\,\Delta r^{*}}{|\bar{u}_{max}^{*}| + c_{max}^{*}}$$

where c^*_{max} is the maximum local wave speed, and wave speed is defined as $c = (g'H)^{1/2}$ See Table 16, Section 5.2.1 for the constants specified.

The algorithm maintained conservatism of the original cloud mass. It lost less then 0.5 % of the mass over integration periods out to $t^* = 300$. Raithby (1976) suggests that upwind-difference schemes introduce damping due to transient behavior as well as spatial variations. Alternative schemes were examined, such as the flux-connected-transport scheme of Book et. al. (1976) and the smoothing algorithm by P. E. Long (Techniques Development Laboratory of the US National Weather Service); however, the extra complication resulted in only small improvement in the results.

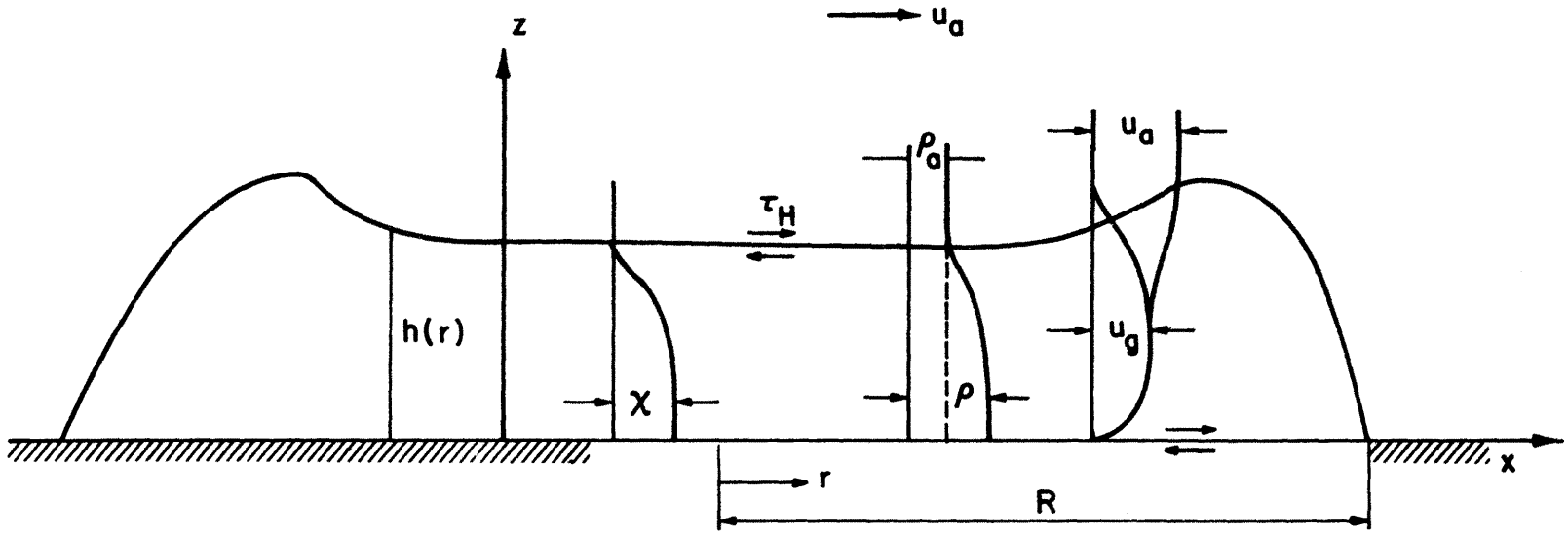

a) Side View of Depth-averaged Unsteady Dense Gas Cloud

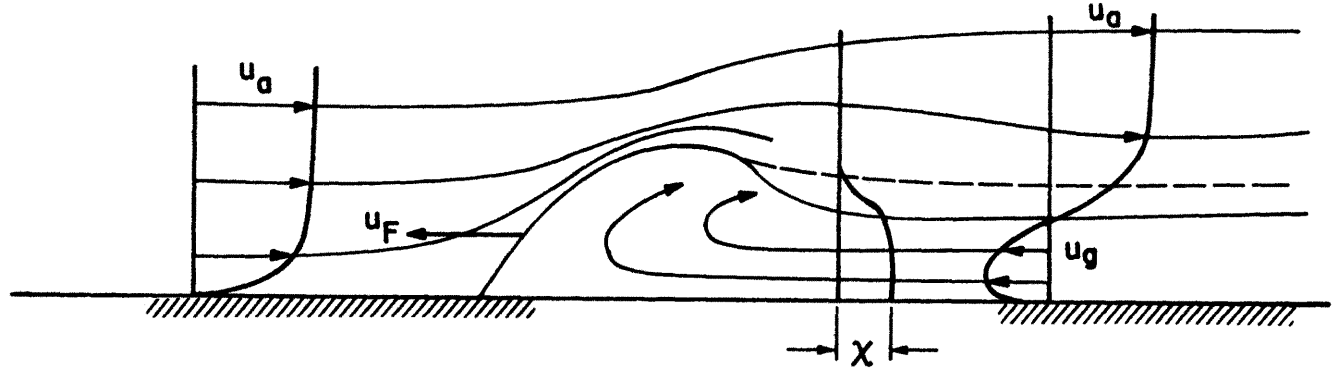

b) Character of Dense Vapor Intrusion

Figure B-1.

USERS GUIDE: SLAB MODEL: DENSE 8

See Appendix B Meroney and Lohmeyer (1982) for general discussion. Model will calculate behavior of a symmetric isothermal cylindrical dense cloud source in calm or windy situations. The model does not

1.) consider thermal or humidity effects.
2.) treat continuous releases - only sudden.
3.) adjust atmospheric boundary layer conditions for stability.

Items 1), 2), and 3) could be included with program changes. Contact Meroney for revised programs.

INPUT

The program requires 4 cards to run, it produces a series of tables and plots describing the momentary cloud description.

Card 1 (8G10.3) SG, HI, RI, UF, ZO, GAMMA, CF, BETA

*	SG	Specific gravity of source gas ie ρ_o/ρ_a
*	HI	Initial cloud height (meters)
*	RI	Initial cloud radius (meters)
*	UF	Friction velocity, U_*, (meters/sec)
*	ZO	Roughness height, Z_o, (meters)
	GAMMA	Entrainment constant for background turbulence use 0.4
	CF	Drag coefficient of boundary use 0.25
	BETA	Hydrostatic pressure adjustment constant for vertical distribution of $\Delta\rho$ use 0.333

Card 2 (8G10.3) DT, CFF, BM, B1, STEP, TOTAL, WIDTH, AMULT

DT	Starting time step, $\hat{\Delta t}$, use 0.10
CFF	Surface entrainment coefficient use 0.05
BM	3d or 2d Selector
	Use BM = 1.0 if want cylindrical cloud Use BM = 0.0 if want 2d cloud

B1 — Viscous Damper - use only if cloud goes unstable, normally use 0.0

* STEP — Incremental value of $\hat{t}$ for which program prints out results, common values for examining early cloud behavior are 1.0, 2.0, 5.0 for examining late cloud behavior use 10.0, 20.0, 100.0, etc.

* TOTAL — Total number of steps or printouts, generally you get Total + 1, typically use 10.0, 20.0, 30.0

* WIDTH — Determines increment in radius data is calculated and total grid size. ie. DR = RI/(HI * WIDTH) and Maximum R = 100 DR, use 3.0, 5.0, but be careful here sometimes even numbers give program integration problems

AMULT — Constant which determines what value of Courant number is not exceeded, ie. AMULT = Courant max, use 0.5 or less

Card 3 (8G10.3) B2, DELTA, CZ2

B2 — Fraction of cloud height at cloud center at which convection velocity is calculated in cylindrical coordinates use 0.10

DELTA — Entrainment coefficient at early spreading rates use 0.0

CZ2 — An adhoc corrector to use to keep waves from growing too big; if you use given constants use 0.05, (do not set to zero)

Card 4 (40A2)

Any name for case you desire, do not use first column on card, otherwise 79 spaces are available.

OUTPUT

All input quantities are read out.

TIME SCALE:

$$T = HI/(g_i')^{1/2}$$

VELOCITY SCALE:

$$U \quad (g_i' \; HI)^{1/2}$$

VOLUME:

$$V_i = \pi \; (RI + DR \cdot \frac{HI}{2})^2 * HI$$

REYNOLDS NUMBER:

$$R_e = U \cdot HI / \nu_a$$

FRICTION VELOCITY:

$$U_* = UF$$

RICHARDSON NUMBER:

$$R_i = (g_i' \; HI)/U_*^2$$

TIME:

$$\hat{t} = t/T$$

TIME INCREMENT:

$$\hat{\Delta t} = \Delta t/T$$

COURANT NUMBER:

$$= \frac{\Delta t \cdot U_{max}}{\Delta R}$$

PHASE COURANT NUMBER:

$$= \frac{\Delta t \cdot C_{max}}{\Delta R} = \frac{\Delta t(\sqrt{g_i' \; H})_{max}}{\Delta R}$$

CONS: Check on cloud integration:

Should be very near 1.00 (example 0.994)

AVG MASS FRACTION:

$$\bar{C}_{\text{avg over cloud}} = AMS$$

AVG MOLE FRACTION:

$$\bar{\chi}_{\text{avg over cloud}} = DIL$$

XSTAR: Distance in stored variables

$$X^* = X/V_i^{1/3}$$

TSTAR: Time in starred variables

$$t^* = t\,(g_i')^{1/2}/V_i^{1/3}$$

RADIUS:

$$\hat{R} = R/HI$$

HEIGHT:

$$\hat{H} = H/HI$$

SPEC GRAVITY:

$$\hat{\rho} = \bar{\rho}/\rho_a \quad \text{(depth averaged)}$$

MASS FRACTION:

$$\bar{C} \quad \text{(depth averaged)}$$

VELOCITY:

$$\hat{u} = \bar{u}\ T/L \quad \text{(depth averaged)}$$

RADIUS 1:

$$R^* = R/V_i^{1/3}$$

HEIGHT 1:

$$H^* = H/V_i^{1/3} \quad \text{(depth averaged)}$$

VOL FRACT:

$$\chi = \bar{C}/(\bar{C} + (1 - \bar{C})\ \ SG)$$

TMAX:

t^*_{max} when χ is maximum for a given radius R^*

CHIMAX:

χ_{max} = maximum χ at a given R^*

To stop program type 999.0 in first 10 spaces of one card and add two blank cards.

GOOD LUCK

```
Cƒ      DEBUG
Cƒ      ARRAYS
Cƒ      GOTOS
        PROGRAM DENS8(INPUT,OUTPUT,TAPE5=INPUT,TAPE6,DEBUG=OUTPUT)
C       PROGRAM TO CALCULATE DENSE PLUME BEHAVIOR UTILIZING A SLAB
C       MODEL APPROACH WHICH ALLOWS FOR VARIATION IN HEIGHT AND
C       RADIAL CONCENTRATION. RADIAL COORDINATES ARE UTILIZED.
C       WIND EFFECTS ARE ACCOUNTED FOR BY SHEAR ENTRAINMENT
C       AND TURBULENCE ENTRAINMENT.  LOG LAW VELOCITY PROFILE
C       IS USED IN 2D VERSION, AXISYMETRIC VERSION DRIFTS WITH
C       NO ADDITIONAL VELOCITY EFFECTS.
C**********************
C
       DIMENSION RHO(100),H(100),U(100),C(100), UW(100),
      1   MTIT(8),R(100),HA(100),HB(100),HC(100),RW(100)
      2 ,A(100),B(100),CC(100),D(100),E(100),F(100)
      3 ,CHI(100),H1(100),R1(100),CHIM(100),TMAX(100),H2RH(100)
       REAL PI
        PI=3.1417
C       INPUT DATA
C**********************
C       SPECIFIC GRAVITY, INITIAL HEIGHT, INITIAL RADIUS, CONSTANTS
C       FRICTION VELOCITY,SURFACE ROUGHNESS, CFF(0.01),GAMMA(0.3)
C       CF(0.25) ,DELTA(0.30),CZ2(0.010),AND BETA (0.10), AND TIME STEP
C       FORMAT (8F10.3)
C       TITLE TO GRAPHS, FORMAT (8A10)
C
1       CONTINUE
        READ(5,100) SG,HI,RI,UF,ZO,GAMMA,CF,BETA,DT,CFF,BM,B1
      1 ,STEP,TOTAL,WIDTH,AMULT,B2,DELTA,CZ2
        IF(SG.EQ.999.) STOP
        WRITE(6,200) SG,HI,RI,UF,ZO,GAMMA,CF,BETA,DT,CFF,BM,B1
        WRITE(6,209) STEP,TOTAL,WIDTH,AMULT,B2,DELTA,CZ2
        READ(5,101) (MTIT(I),I=1,8)
        WRITE(6,201) (MTIT(I),I=1,8)
C            INITIALIZE
C**********************
C       SET ALL SPACE UNOCCUPIED BY DENSE GAS TO AMBIENT CONDITIONS
C       CREATE RADIAL GRID
C
        DR=RI/(HI*WIDTH)
        XS=0.0
        DO 10 I=1,100
        AI=I
        R(I)=(AI-1.0)*DR
        RHO(I)=1.0
        H(I)=0.0
        U(I)=0.0
        C(I)=0.0
        CHI(I)=0.0
        CHIM(I)=0.000001
        TMAX(I)=0.0
        UW(I)=0.0
        HA(I)=0.0
        HB(I)=0.0
```

```
      HC(I)=0.0
10    CONTINUE
      DO 11 I=2,100
11    RW(I)=R(I-1)+DR/2.0
      M=WIDTH+1.0
C      SET ALL SPACE IN CLOUD TO DENSE GAS CONDITIONS
C*********************
C
      IF(BM.EQ.0.0) GO TO 21
      DO 20 I=1,M
      RHO(I)=SG
      H(I)=1.0
      C(I)=1.0
      CHI(I)=1.0
      HA(I)=SG
      HC(I)=SG
20    CONTINUE
      GO TO 22
21    CONTINUE
      LB=26-M+1
      LE=LB+M+M-2
      DO 23 I=LB,LE
      RHO(I)=SG
      H(I)=1.0
      C(I)=1.0
      CHI(I)=1.0
      HA(I)=SG
      HC(I)=SG
23     CONTINUE
22     CONTINUE
C      CALCULATE VOLUME, REYNOLDS NUMBER, TIME AND VELOCITY SCALES
C*********************
C
      VOL=PI*(RI+DR*HI/2.0)**2*HI
      IF(BM.EQ.0.0) VOL=(FLOAT(M)*2.0-1.0)*DR*HI**2
      REY=(9.81*(SG-1.0) *HI)**0.5/0.000015*HI
      FRUD=UF*UF/(9.81*(SG-1.)*HI)
      IF(UF.GT.0.0)  RICH=1.0/FRUD
      SFRUD=SQRT(FRUD)
      TS=(HI/(9.81*(SG-1.0)))**0.5
      US=(9.81*(SG-1.0)*HI)**0.5
      WRITE(6,202) TS,US,VOL,REY
      IF(UF.GT.0.0)  WRITE(6,203) UF,ZO,RICH
      BBB=HI/VOL**0.3333
      DO 25 I=1,100
25    R1(I)=R(I)*BBB
      ZO=ZO/HI
C          CALCULATE
C*********************
C
      K=0
      LCNT=0
      T=0.0
      CAUCH=0.0
      COUR=0.0
      T1=0.0
```

```
      DT1=DT
      GO TO 61
29    K=K+1
30    CONTINUE
      LCNT=LCNT+1
C     CALCULATE A,B,C,D,TO PERMIT CALCULATION OF HA
C*********************
C
      DO 305 I=2,100
305   UW(I)=(U(I)+U(I-1))*RW(I)**BM/2.0
      DO 301 I=2,99
      CFP=CFF+DELTA*ABS(U(I))
      DA=B1*RHO(I)*ABS(U(I+1)-U(I))*RW(I+1)**BM
      DC=B1*RHO(I)*ABS(U(I)-U(I-1))*RW(I)**BM
      A(I)=AMAX1(-UW(I+1),DA-UW(I+1)/2.0,0.0)*DT/DR/R(I)**BM
      CC(I)=AMAX1(UW(I),DC+UW(I)/2.0,0.0)*DT/DR/R(I)**BM
      B(I)=1.0+A(I)+CC(I)+(UW(I+1)-UW(I))*DT/DR/R(I)**BM
      D(I)=HA(I)
      IF(BM.EQ.0) GO TO 43
       IF(U(I).LT.0.0) CFP=CZ2
      IF(C(I).GT.1.E-3) D(I)=D(I)+DT*CFP
     1 *ABS(U(I))+DT*GAMMA*SFRUD
      GO TO 300
43     CONTINUE
      IF(C(I).GT.1.E-3)D(I)=D(I)+DT*CFP
     2 *ABS(U(I)-2.5*SFRUD*ALOG(H(I)/ZO+1.0))+DT*GAMMA*SFRUD
300   CONTINUE
301   CONTINUE
C     CALL SUBROUTINE TO CALCULATE HA BY TRI DIAGONAL MATRIX METHOD
C*********************
C
      CALL   TRIG(A,B,CC,D,100,E,F,HA,2,0.0,0.0,2,0.0,0.0)
C     CALCULATE D  TO PERMIT CALCULATION OF HB
C*********************
C
      ABC=DT/DR*BETA/16.0
      ABD=CF*CF*DT
      DO 700 I=2,100
      H2RH(I)=(H(I-1)+H(I))**2*(RHO(I-1)+RHO(I)-2.0)
700   CONTINUE
      IF(BM.EQ.0.0) GO TO 310
      DO 302 I=2,99
      D(I)=HB(I)-RHO(I)*U(I)*ABS(U(I))*ABD
      IF(C(I).LT.1.E-3) GO TO 303
      D(I)=D(I)+ABC*(H2RH(I)-H2RH(I+1))
303   CONTINUE
302   CONTINUE
      GO TO 311
310   CONTINUE
      DO 312 I=2,99
      USH=2.5*SFRUD*ALOG(H(I)/ZO+1.0)
      D(I)=HB(I)-RHO(I)*U(I)*ABS(U(I))*ABD
     1 +USH*DT*(CFP*ABS(U(I)-USH)+GAMMA*SFRUD)
      IF(C(I).LT.1.E-3) GO TO 313
      D(I)=D(I)+ABC*(H2RH(I)-H2RH(I+1))
313   CONTINUE
312   CONTINUE
311   CONTINUE
C      CALL SUBROUTINE TO CALCULATE HB BY TRI DIAGONAL MATRIX METHOD
C*********************
C
      IF(BM.EQ.0.0)GO TO 500
      CALL   TRIG(A,B,CC,D,100,E,F,HB,1,0.0,0.0,2,0.0,0.0)
```

```
      GO TO 501
500   CALL TRIG(A,B,CC,D,100,E,F,HB,2,0.0,0.0,2,0.0,0.0)
501    CONTINUE
C     CALCULATE D TO PERMIT CALCULATION OF HC
C*********************
C
      DO 323 I=2,99
      D(I)=HC(I)
323   CONTINUE
C     CALL SUBROUTINE TO CALCULATE HC BY TRI DIAGONAL MATRIX METHOD
C*********************
C
      CALL   TRIG(A,B,CC,D,100,E,F,HC,2,0.0,0.0,2,0.0,0.0)
      DO 304 I=1,100
      U(I)=HB(I)/(HA(I)+0.001)
      C(I)=HC(I)/(HA(I)+0.001)
      RHO(I)=1.0/(1.0-C(I)+C(I)/SG)
      H(I)=HA(I)/RHO(I)
      CHI(I)=C(I)/(C(I)+(1.0-C(I))*SG)
      IF(CHIM(I).GT.CHI(I)) GO TO 344
      CHIM(I)=CHI(I)
      TMAX(I)=T*SQRT(BBB)
344      CONTINUE
304   CONTINUE
      IF((BM.EQ.1).AND.(T.GT.10.)) XS=XS+2.5*UF/US*ALOG(B2*H(1)/ZO)*
     1 DT*SQRT(BBB)
C      STEP FORWARD IN TIME
C*********************
C
      T1=T
      TST=T1*SQRT(BBB)
      DT1=DT
C     FIND MAX VELOCITY AND MAX RHO(I)*H(I) IN FIELD
C*********************
C
      ROHMX=0.001
      UMAX=0.001
      DO 51 I=1,100
      ROHLCL=(RHO(I)-1.0)*H(I)
      IF(ROHMX.LT.ROHLCL) ROHMX=ROHLCL
51    IF(UMAX.LT.U(I)) UMAX=U(I)
      ROHMX=(ROHMX/(SG-1.0))**0.5
C      CALCULATE PHASE SPEED AND SPEED  COURANT PARAMETER
C*********************
C
      CAUCH=DT*UMAX/DR
      COUR=DT*ROHMX/DR
      DT2=AMULT*DR/UMAX
       DT3=AMULT*DR/ROHMX
       DT4=DR/(UMAX+ROHMX)
       IF(DT2.GT.DT3) DT2=DT3
      IF(DT2.GT.DT4) DT2=DT4
      DT=DT2
      T=T+DT
C      DECIDE WHETHER TO PRINT AND GRAPH
C*********************
C
```

```
      AK=K
      TSS=AK*STEP
      IF(T1.GT.TSS) GO TO 60
      GO TO 30
60    CONTINUE
C     CONSERVATION ESTIMATE
C*********************
C
61    CONS=0.0
      CONS1=0.0
      IF(BM.EQ.0.0) GO TO 600
      DO 99 I=2,99
      CONS2=RHO(I)*H(I)*R(I)
      CONS1=CONS2+CONS1
99    CONS=CONS2*C(I)+CONS
      CONS1=(2.0*CONS1*DR+DR*DR*H(1)*RHO(1)/4.0)/
     1 (SG*(R(M)+DR/2.0)**2)
      CONS=(2.0*CONS*DR+DR*DR*H(1)*C(1)*RHO(1)/4.0)/(SG*(R(M)+
     1 DR/2.0)**2)
      GO TO 601
600   CONTINUE
      DO 602 I=2,99
      CONS2=RHO(I)*H(I)
      CONS1=CONS2+CONS1
      CONS=CONS2*C(I)+CONS
602   CONTINUE
      CONS=CONS/SG/(2.0*FLOAT(M)-1.0)
      CONS1=CONS1/SG/(2.0*FLOAT(M)-1.0)
601    CONTINUE
      AMS=1.0/CONS1
      DILAVG=AMS/(AMS+(1.0-AMS)*SG)
C      PRINT RESULTS
C*********************
C
      DO 701 I=1,100
701   H1(I)=BBB*H(I)
      WRITE(6,204) T1,DT1,CAUCH,COUR,CONS,AMS,DILAVG,XS,TST,LCNT
      WRITE(6,208)
      WRITE(6,205) (R(I),H(I),RHO(I),C(I),U(I),R1(I),H1(I),CHI(I)
     1 ,TMAX(I),CHIM(I),I=1,100)
      [redacted]
      MTOT=TOTAL
      IF(K.GT.MTOT) GO TO 1[redacted]
      GO TO 29
      [redacted]
C      FORMAT STATEMENTS
C*********************
C
100   FORMAT(8G10.3)
101   FORMAT(8A10)
200   FORMAT(1X,*SG*,10X,*HI*,10X,*RI*,10X,*UF*,10X,*ZO*,10X
     1 ,*GAM*,4X,*CF*,4X,*BETA*,10X,*DT*,10X,*CFF*,10X,*BM*,10X,*B1*,
     2 //,12(1X,G9.3,1X))
203   FORMAT(1X,*FRICTION VELOCITY (M/S)=*,G10.3,*Z0 = *,
     1 G10.3,*RICHARDSON NUMBER = *,F10.3)
```

```
201   FORMAT(1X,8A10)
202   FORMAT(1X,*TIME SCALE =*,1X,F10.3,* SEC   VELOCITY SCALE = *,
     1  F10.3,* M/SEC  VOLUME = *,E15.3,*  REYNOLDS NUMBER = *,F10.3)
204   FORMAT(1H1,*TIME = *,F10.3,*  TIME INCREMENT = *,F10.3,
     1  *  COURANT NUMBER = *,F10.3,*PH COUR NUMB = *,F10.3,
     2 *CONS = *,F10.3,/,*  AVG MASS FRACTION = *,F10.3,
     3 *  AVG MOLE FRACTION = *,F10.3,* X-STAR = *,F10.3,
     4 *T-STAR = *,F10.3,*LCNT =*,I5,//)
205   FORMAT( 10(1X,F10.3,2X))
208   FORMAT(1X,//,* RADIUS*,9X,*HEIGHT*,9X,*SPEC.GRAV.*,
     1 4X,*MASS FRAC*,4X,*VELOCITY*,4X,*RADIUS1*,4X
     2 ,*HEIGHT1*,4X,*VOL FRAC*,5X,*TMAX*,5X,*CHIMAX*,//)
209   FORMAT(1X,*STEP*,6X,*TOTAL*,6X,*WIDTH*,6X,*MULT*,6X.*B2*,
     18X,*DELTA*,7X,*CZ2*,//,7(1X,G9.3,1X))
      END
C
C
      SUBROUTINE TRIG(A,B,C,D,MD,E,F,W,L1,A1,Q1,LM,AM,QM)
C*********************
C
C     GENERAL TRI-DIAGONAL SOLVER
      DIMENSION A(MD),B(MD),C(MD),D(MD),E(MD),F(MD),W(MD)
      IF(L1.EQ.1) E(1)=0.0
      IF(L1.EQ.1) F(1)=W(1)
C     ABOVE OVERWRITTEN IF LM.NE.2
C*********************
C
      IF(L1.EQ.2) E(1)=1.0
      IF(L1.EQ.2) F(1)=-A1
      IF(L1.EQ.3) E(1)=A1/(A1-1.0)
      IF(L1.EQ.3) F(1)=Q1/(1.0-A1)
      MM=MD-1
      DO401 M=2,MM
      DEN=B(M)-C(M)*E(M-1)
      E(M)=A(M)/DEN
401   F(M)=(D(M)+C(M)*F(M-1))/DEN
      IF(LM.EQ.1) W(MD)=AM
      IF(LM.EQ.2) W(MD)=(F(MM)+AM)/(1.0-E(MM))
      IF(LM.EQ.3) W(MD)=(F(MM)+QM/AM)/((1.0+AM)/AM-E(MM))
      DO 402 M(M)=E(M)*W(M+1)+F(M)
      RETURN
      END
```

APPENDIX C

APPENDIX C: Examples of Research Implications for a Hazardous Gas: Propane

This section uses the numerical box model program described in Appendix A to calculate a range of hazard distances for instantaneous releases of gas clouds produced from the sudden vaporization of Propane or L.P.G. The results are limited to situations where

1) The terrain in the vicinity of the plume source and downwind is flat.

2) Nearby building structures, tanks or pipelines are small enough not to influence plume dispersion.

3) The wind field is neutrally stable (ie. Pasquill-Gifford Category D).

4) The field height at which the reference speed is evaluated is 10 meters.

5) The local surface roughness is of the order of z_o = 2 cm, such that $u_*/u_{10} = 0.05$.

6) The duration of the spill is essentially instantaneous (ie. $t_{\text{end spill}} \leq 10\ T$, where $T = V_i^{1/6}/(g(SG-1)^{1/2})$.

Properties of Propane (C_3H_8) used during these calculations were chosen to be:

Molecular Weight = 44.1 g/g-mole ,

$T_{\text{boil off}} = -42.07^{\circ}C$,

$H_o/R_o = 0.25$ (Initial cloud dimensions) ,

$SG_{\text{boil off}} = 1.94$,

$\beta = 0.342$,

$s^* = 1.465$, and

$\theta = 0.215$.

For near calm situations the experimental data, numerical box program , and numerical depth integrated program produce similar results as summarized in Figure C-1. For Propane (SG_o effective = 1.94, MW_o effective = 56) one obtains

$$x(C = 1\%) = 9.5\ V_i^{1/3}\ (m)$$

$$t_a(C = 1\%) = 32\ V_i^{1/3}\ (sec)$$

where V_i is initial plume volume at boiloff temperature of -42°C.

Eidsvik (1980) provided hazard calculations for Propane for a variety of size spills at a wind speed of 0.5 m/sec. Similar calculations produced Figure C-2 from the Appendix A model. As noted the Eidsvik results are quite different. Eidsvik proposes that

$$\chi_m \sim V_i^{2/5} \quad \text{and} \quad t_a \sim V_i^{1/3} .$$

These values are not consistent with the basic physics of the box model he used. In addition Eidsvik's model suggests

$$\chi_m = u_R\ t_a + R(t_a) .$$

As noted by Fay (1980) this will produce exaggerated plume transport for a logarithmic velocity profile.

For an instantaneous spill of 10^5 kg of Propane the downwind extent, width and arrival times are plotted in Figure C-3 as they vary with increasing wind speed. Maximum plume width and arrival time at C = 1% vary only slightly below 10 m/sec. Distance to the location value where C = 1% steadily increases. Eidsvik (1980) predicts a slight decrease in downwind distance to the 1% level as wind speed increases. His result is not consistent with the presence of plume advection by the background wind field.

The most widely used hazard assessment and response tool currently used by fire departments and other emergency response organizations is the Chemical Hazard Response Information System (CHRIS) prepared by the Department of Transportation, Coast Guard. This methodology calculates LFL (Lower Flammability Limit), regions based on a neutral density gaussian plume model approach. Table C-1 compare CHRIS predictions for various spill situations against the Appendix A box model approach.

Table C-1

Propane (L.P.G.) Hazard Assessment*

Spill Sizes (short tons)	CHRIS Distance LFL (m)	CHRIS Half Width (m)	CHRIS Arrival Time (min)	BOX Distance LFL (m)	BOX Half Width (m)	BOX Arrival Time (min)
0.1	18	8	0.1	30	28	0.50
1.0	152	18	1.0	66	60	1.00
10.0	602	38	4.0	450	127	1.25
100.0	1389	98	9.0	300	275	2.00
1000.0	3195	200	21.0	650	600	2.67

* $u \simeq 5$ knots, D stability

The CHRIS model assumes the plume is convected as $X = u_R t$, but the sudden collapse of a cold cloud will place the majority of the gas near the ground, where the wind speeds are very low. The CHRIS model overestimates plume transport, but it underestimates plume width substantially.

References Appendix (C)

CHRIS (1974), A Condensed Guide to Chemical Hazards, CG-446-1; Hazardous Chemical Data, CG-446-2; Hazard Assessment Handbook, CG-446-3; and Response Methods Handbook, CG-446-4, Department of Transportation, U.S. Coast Guard, COMDTINST M 16465.11,12,13, and 14, USGPO, Washington, D.C.

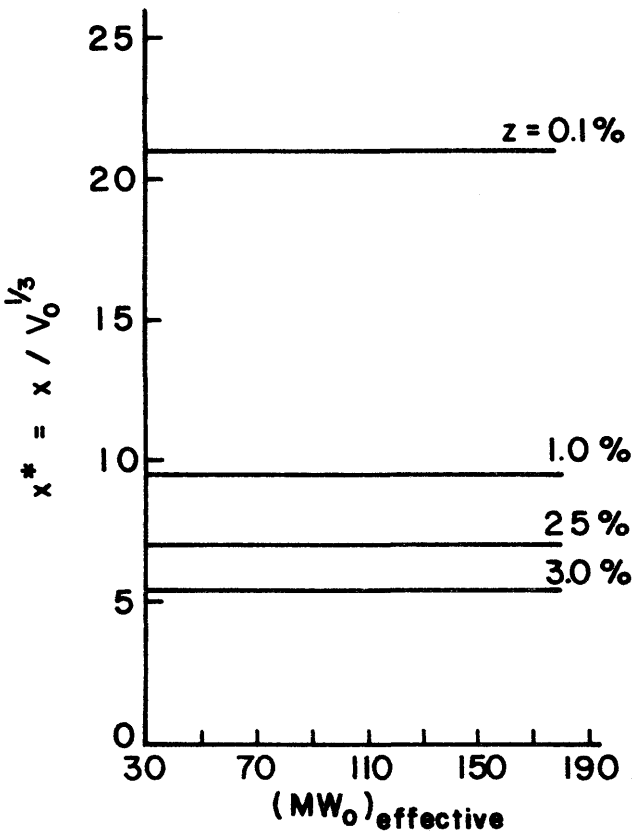
25
20
15
10
5
0
z = 0.1%
1.0 %
2.5 %
3.0 %
30
70
110
150
190
$(MW_o)_{effective}$
$x^* = x / V_o^{1/3}$

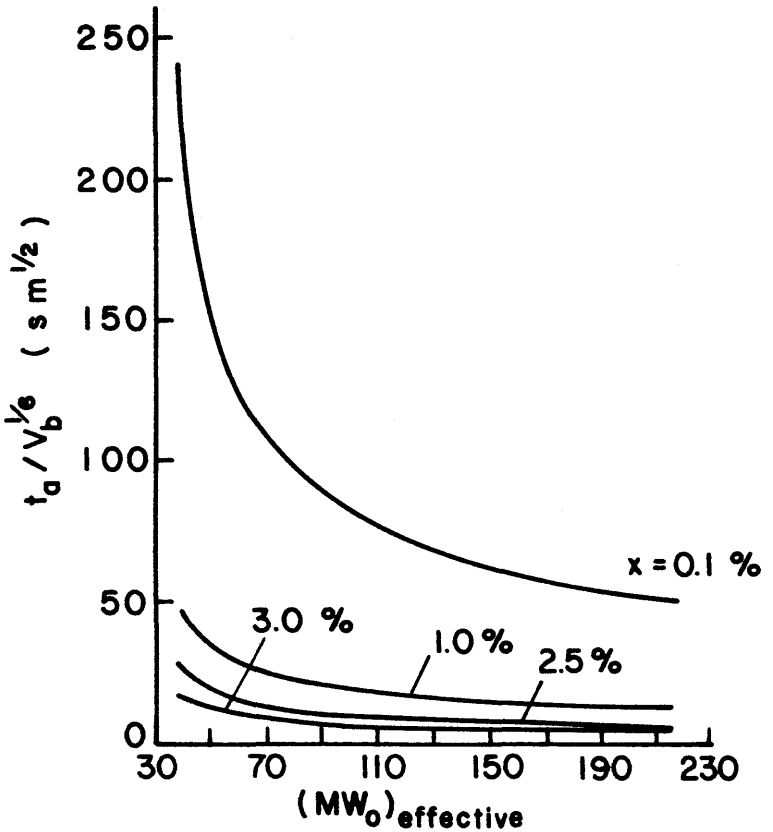
250
200
150
100
50
0
x = 0.1 %
3.0 %
1.0 %
2.5 %
30
70
110
150
190
230
$(MW_o)_{effective}$
$t_a / V_b^{1/6}$ (s $m^{1/2}$)

Figure C-1.

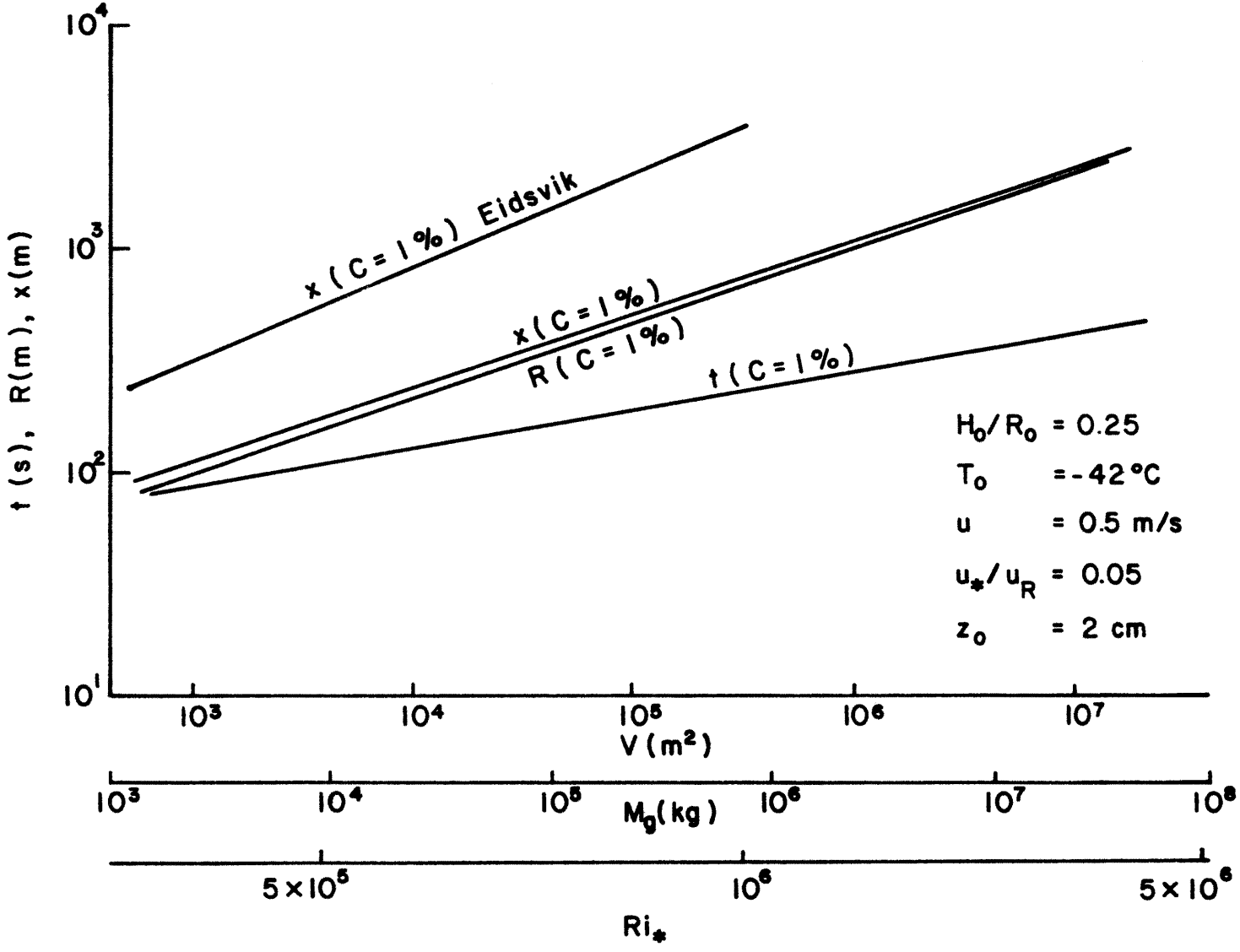
t (s), R(m), x(m)
10^4
10^3
10^2
10^1
x (C = 1 %) Eidsvik
x (C = 1 %)
R (C = 1 %)
t (C = 1 %)
H0/R0 = 0.25
T0 = -42 °C
u = 0.5 m/s
u*/uR = 0.05
z0 = 2 cm
10^3
10^4
10^5
10^6
10^7
V (m^2)
10^3
10^4
10^5
Mg(kg)
10^6
10^7
10^8
5x10^5
10^6
5x10^6
Ri*

Figure C-2.

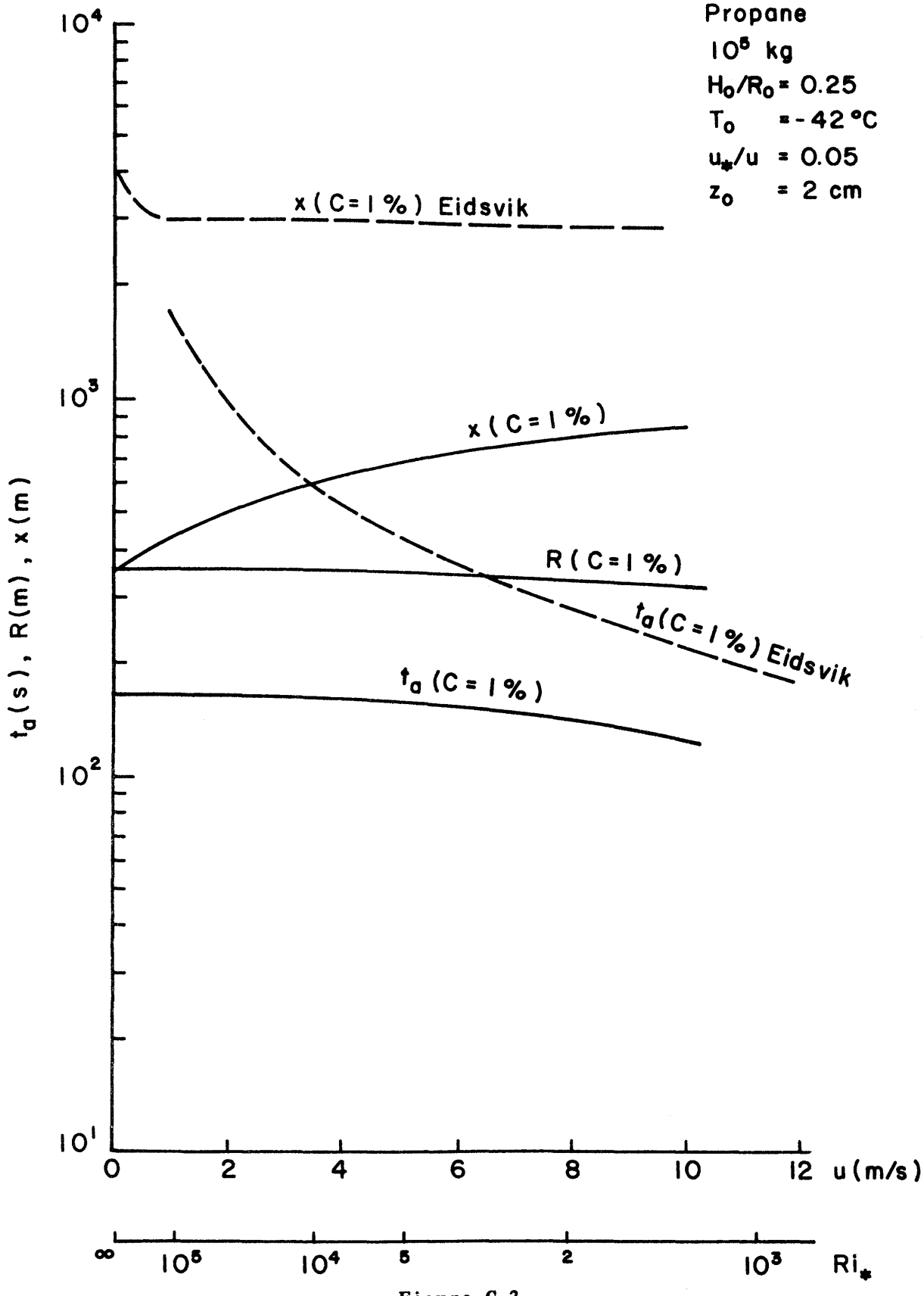
Propane
10^5 kg
H0/R0 = 0.25
T0 = -42 °C
u*/u = 0.05
z0 = 2 cm
x (C=1 %) Eidsvik
x (C=1 %)
R (C=1 %)
ta (C=1 %) Eidsvik
ta (C=1 %)
ta(s), R(m), x(m)
10^4
10^3
10^2
10^1
0
2
4
6
8
10
12
u (m/s)
∞
10^5
10^4
5
2
10^3
Ri*

Figure C-3.